Ph.D. Dissertation

Symmetry Breaking in Complex, Disordered, and Nonlinear Optical Potentials for the Manipulation of the Flow of Light

복소, 무질서 및 광학적 비선형 퍼텐셜에서의 대칭성 붕괴를 통한 빛의 흐름 제어

BY

Sunkyu Yu

August 2015

DEPARTMENT OF ELECTRICAL ENGINEERING AND
COMPUTER SCIENCE
COLLEGE OF ENGINEERING
SEOUL NATIONAL UNIVERSITY

Abstract

Symmetry Breaking in Complex, Disordered, and Nonlinear Optical Potentials for the Manipulation of the Flow of Light

Sunkyu Yu

DEPARTMENT OF ELECTRICAL ENGINEERING AND COMPUTER SCIENCE

COLLEGE OF ENGINEERING

SEOUL NATIONAL UNIVERSITY

The flow of light in matters is usually defined by macroscopic Maxwell's equations. In ideal media with homogeneous, isotropic, linear, and time-invariant optical material parameters, the aspect of light wave dynamics is simple and intuitive: propagating straight with oscillated electromagnetic fields, as the direct example of Fermat's principle. This planewave dynamics, the basis of geometric optics, originates from the conservation of various symmetries of the Schrodinger-like wave equation, including translational and chiral symmetry, Hermitian symmetry, Lorentz reciprocity, and time-reversal symmetry.

To control the flow of light even in a classical manner such as lens,

mirror, and prism, some parts of the symmetries in optics should be broken. Breaking the translational symmetry with inhomogeneous materials is the traditional method of controlling light by scattering such as refraction, reflection, and diffraction. The dissipation or amplification of optical energy during the propagation is quantified by the non-Hermitian Hamiltonian of the wave equation. The materials composed of chiral molecules allow the rotation of the polarization of light, i.e. optical activity. The optical Doppler effect, which has been employed in astronomy for the observation of the motion of stars and galaxies, is based on the time-varying position of light sources, breaking Lorentz reciprocity.

Recent achievements in optics, including counterintuitive theoretical results and improved fabrication technologies, have now been pioneering unprecedented regimes of controlling optical potentials which derive non-classical flow of light. Nano-scale technologies linked with the concept of metamaterials have opened a path to the design of theoretically-demonstrated artificial media supporting extraordinary light flows: such as unidirectional light flow, modified Snell's law, negative index, cloaking, and perfect absorption. The development of optical amplification techniques has been applied to the realization of the quantum-mechanical notion of parity-time symmetry: stimulating a new class of optics in complex potentials. Because these achievements have been based on broader and drastic forms of symmetry breaking in Maxwell's equations, in-depth investigation of various symmetry breakings is now imperative to realize designer manipulation of light flow.

In this dissertation, we explore symmetry breakings in various platforms: complex, disordered, and nonlinear optical potentials. The

investigation is focused on unconventional flows of light linked with the notions of parity-time symmetry, chirality, causality, supersymmetry, biomimetics, mode junction photonics, and slow-light. We believe that our results including counterintuitive concepts and novel design methods for optical devices will be the foundation of future development in optics based on non-classical flow of light.

Keywords: Symmetry Breaking, Parity-Time Symmetry, Disorder, All-Optical Device, Optics, Wave

Student Number: 2007-21026

Table of Contents

Abstract ..... **i**

Table of Contents ..... **iv**

List of Figures ..... **ix**

Chapter 1 Introduction 1

1.1 Why should we break the symmetry of light?. 1

1.2 Outline of the dissertation 2

Chapter 2 Parity-Time Symmetric Optics 4

2.1 Introduction to PT-symmetric optics 5

2.2 PT-symmetric waves in the spatial domain. 1 1

2.2.1 2-level chirped system 1 1

2.2.2 *N*-level photonic molecule 2 4

2.3 PT-symmetric waves in momentum domains 4 3

2.3.1 Optical chirality in low-dimensional eigensystems .. 4 4

2.3.2 Interpretation of PT-symmetry in *k*-space 6 3

2.4 Conclusion..... 75
Chapter 3 Disordered Optics 76
3.1 Introduction to disordered optics..... 77
3.2 Supersymmetric bandgap in disorder..... 78
3.2.1 Wave dynamics in random-walk potentials 79
3.2.2 Supersymmetric transformation for isospectrality.. 83
3.2.3 Bloch-wave family with tunable disorder 86
3.3 Biomimetic disordered surface..... 91
3.4 Conclusion..... 98
Chapter 4 All-Optical Devices with Nonlinearity 99
4.1 Introduction to all-optical devices..... 100
4.2 Mode junction photonics..... 101
4.2.1 Photonic Junction Diode..... 105
4.2.2 Multi-Junction Half Adder 113
4.3 Slow-light enhanced optical functionalities 115
4.3.1 Multiband slow light 116
4.3.2 Optical A/D converter..... 126
4.3.3 All-optical A/D converter 137
4.3.4 Travelling-wave all-optical isolator..... 143
4.4 Conclusion..... 149
Chapter 5 Conclusion 150

Appendix A Eigenvalues in PT-Meta-molecules 152

Appendix B Supplements for Section 2.3.1 157

B.1 Planewave solution of a PT-symmetric optical material 157

B.2 Density of optical chirality for complex eigenmodes 158

B.3 Effect of imperfect PT symmetry on the modal chirality 159

B.3.1 Broken symmetry in the real part of permittivity ... 159

B.3.2 Broken anti-symmetry in the imaginary part of the permittivity 161

B.4 Transfer between RCP and LCP modes in the PT-symmetric chiral material 162

B.4.1 Propagation of complex eigenmodes 162

B.4.2 Strength of chiral conversion C_{CS} before the EP 163

B.5 The state of polarization (SOP) at the EP: Optical spin black hole 164

B.6 Giant chiral conversion in the resonant structure 165

B.7 Detailed information of fabrication and experiment in THz chiral polar metamaterials 166

B.7.1 Fabrication process of THz chiral polar metamaterials 166

B.7.2 THz-TDS system for the measurement of intermodal chirality 167

B.8 Realization of PT-symmetric permittivity in metamaterial platforms 167

B.9 Design parameters of chiral waveguides 171

B.10 Low-dimensional linear polarization 171

Appendix C Detailed Derivation for Section 2.3.2 173

C.1 Detailed derivation of Eq. (2.20) 173

C.2 Serial calculation of discretized coupled mode equations 175

Appendix D Analytical Methods for Section 3.2 177

D.1 Details of the FDM and FGH method 177

D.2 Calculation of the Hurst exponent 177

Appendix E Supplements for Section 4.2 179

E.1 Details of the device structures and numerical method used in the study 179

E.2 Coupled mode theory for the di-atomic photonic junction diode 181

E.2.1 Analytical model and coupled mode equations 181

E.2.2. Solution of resonator field (a_1, a_2, a_3) 183

E.2.3 Implementation of Kerr nonlinearity and calculation of diode throughput 185

Bibliography 187

Abstract in Korean..... 203

List of Figures

Figure 2.1. The classification of Hamiltonians in wave physics, in terms of eigenspectra related to pseudo-Hermiticity. Pseudo-Hermiticity [48], supporting real or complex-conjugate (c.c.) eigenspectra, contains the notion of PT symmetry. The boundary between real and c.c. eigenspectra corresponds to the exceptional point (EP). The non-PT-symmetric potentials with pseudo-Hermiticity can be achieved with mathematical methods such as supersymmetric (SUSY) transformation [50]. 6

Figure 2.2. Symmetries related to P and T operators: (a) parity symmetry with space inversion, (b) time-reversal symmetry with counter-flow of time, and (c) parity-time symmetry based on the PT operator. 7

Figure 2.3. Eigenspectra of the PT-symmetric Hamiltonian $H = p^2 - (ix)^N$ [33]. The spectrum is real and positive when $N \geq 2$. We note that $N = 2$ corresponds to the harmonic oscillator. The coalescence of eigenstates is observed as N decreases. 9

Figure 2.4. Examples of early PT-symmetric optics: (a) double refraction from modal skewness [57], (b) asymmetrically-steered waves in Bloch oscillating potentials [12], (c) passive PT-symmetric potentials with loss-induced transparency [41], and (d) distinctive propagations for the degrees of PT symmetry [43]. 10

Figure 2.5. Wave dynamics in spatially-varying PT-symmetric potentials [44]. (a) Schematics of the spatially varying potential. (A_k, B_k) denote the

field amplitude of supermode (*A*,*B*) in k^{th} segment, where +/- sign represents the propagation direction. (b) Spatial evolution of λ_1 (normalized to k_0; blue: Re[λ_1/k_0]; and red: *Im*[λ_1/k_0]). (c) Spatial evolution of power in waveguide 1 (blue) and 2 (red). Cases of Hermitian ($n_{i1,2}$ = 0) and uniform PT potential (n_{r0} = 3.4, $n_{i1,2}$ = -/+0.006·n_{r0}) are compared to the spatially-varying PT structure ($n_{r0}(x)$ = 2+x/100). Black arrows mark the spatial EP from the CMT. The wave is excited at waveguide 1 (marked in blue). f_0=200THz and the unit cell length Δx=200nm. …… 16

Figure 2.6. Wave dynamics in spectrally-dispersive PT-symmetric potentials [44]. (a) Dispersion curves of coupled nanopillar waveguides in air. Pillar radius r = 40 nm (blue, upper); 70 nm (red, middle); and 100 nm (green, lower). L = 700 nm; d = 220 nm; and pillar index n_r = 3.5. (b) Effective index of a waveguide n_{eff} and coupling coefficients between waveguides as a function of frequency and radius. (c,d) Difference of effective index Δn_{eff} (blue: real-part; red: imaginary-part) between supermodes in coupled nanopillar waveguides (c: r = 80 nm; d: r = 100nm). Cases of Hermitian (dotted lines, n_1 = n_2 = 3.5) and passive PT-symmetric (solid lines, n_1 = 3.5, n_2 = 3.5+i·0.02) potentials are compared. Green arrows denote the spectral EP as obtained analytically from the CMT. All results are obtained with COMSOL Multiphysics, by applying Floquet-Bloch boundary conditions for the in-plane TE polarization. …… 18

Figure 2.7. Wave dynamics in rainbow PT-symmetric potentials [44]. (a) Coupled nanopillar waveguides for the PT chirped potential (n_r = 3.5; n_{i1} = 0; and n_{i2} = 0.02). The pillar radius r increases from 40 nm to 100 nm. r = 1nm per unit cell (each cell composed of 8 identical pillars). (b) The spatial distribution of n_{eff} = β_{r0}/k_0 and κ/k_0 plotted for frequencies from 170THz (red) to 231THz (blue). (c–e) Evolution of modal indices $n_{eff}^{A,B}$=$\beta_{A,B}/k_0$ for supermodes at different frequencies, along the PT chirped potential. The blue and red arrows each

represent low- (*A*) and high- (*B*) loss supermode. (f) Evolution of the interaction parameter λ_1/k_0 from 195 THz (red) to 231THz (blue). Points of $\lambda_1 = 0$ define Spatio-Spectral EPs (x_{EP}, ω_{EP}). (g) Asymmetry factor for intermodal coupling $|S_{32}/S_{41}|^2$ between supermodes *A* and *B*. The dotted line represents the locus of Spatio-Spectral EPs (x_{EP}, ω_{EP}). All results are obtained with COMSOL Multiphysics. 20

Figure 2.8. Propagation features along rainbow PT-symmetric potentials [44]. Skewness of supermodes in the PT-symmetric rainbow potential: for supermode (a) *A* (low loss) and (b) *B* (high loss). The evolution of power ratio and the field amplitudes are shown for different excitation frequencies of (c, d) 231 THz and (e, f) 195 THz, and for different input excitation ports (blue: lossless waveguide 1 and red: lossy waveguide 2). EPs are marked with black lines. Theoretical (S-matrix analysis, Lines) and numerical (COMSOL, symbols) results are overlaid with excellent fit, showing asymmetric wave propagation along the potential. To minimize the reflection at the input port, all sources of COMSOL simulation are given by the eigen-modal field obtained from COMSOL eigenvalue results in Fig. 2.6. 23

Figure 2.9. Examples of photonic molecules for novel optical functionalities: (a) coupled resonators for optical supermodes [75], (b) perfect absorbing meta-molecules composed of electric and magnetic meta-atoms [74], and (c) Fano meta-molecules composed of coupled plasmonic dipoles [73]. 24

Figure 2.10. Eigenmodes in PT-symmetric metamolecules [46]. (a) Schematic of a PT-symmetric meta-molecule composed of an odd number *N* of atomic waveguides (corresponding to $\beta_{i0} > 0$; red: gain, blue: loss, gray: normal). (b) Real and (c) imaginary part of each eigenvalue for the PT meta-molecule as a function of the phase angle θ=arctan(β_{i0}/β_{r0}), for the case *N*=23. Curves from left to right

correspond to decreasing value of p. Green labels denote the modal index p. The intensity distribution of supermodes in the PT meta-molecule (N=23) are shown as a function of θ, for (d) p=1, (e) p=11, and (f) p=12. (g) Beam center of mass of supermodes (red: gain mode, blue: loss mode). The coupling coefficient κ_o is $\beta_{r0}/200$. . . 3 0

Figure 2.11. Propagation features in PT-symmetric metamolecules [46]. (a,d,g) Modal excitation, (b,e,h) beam propagation, and (c,f,i) evolution of beam CM (blue solid line) are presented for (a-c) p=11 complex ($\beta_{i0}=\kappa_o/2$), (d-f) p=9-11 complex phase-coexistent ($\beta_{i0}=\kappa_o$), and (g-i) entirely collapsed meta-molecules ($\beta_{i0}=2\kappa_o$). The field intensity in (b,e,h) is normalized across the waveguide array at each position (X). Blue and black dotted lines in (c,f,i) denote the dominant (p=11) and trapping (p=1–10) modes. The frequency f_0=193.4THz, $\beta_{r0}=3.5\cdot(2\pi f_0/c)$, and $\kappa_o=\beta_{r0}/200$. 3 3

Figure 2.12. Eigenmodes tuned by the weighted imaginary potentials [46]: (a) Weighting factor applied to the imaginary potential (cyan and yellow: side-enhanced and center-enhanced imaginary potential). The intensity of supermodes with the center-enhanced weighting are presented for (b) p=1, (c) p=11, and (d) p=12. The beam centers of mass of supermodes are shown for the (e) center-enhanced and the (f) side-enhanced imaginary potential. $\kappa_o=\beta_{r0}/200$. 3 6

Figure 2.13. Beam evolution tuned by the weighted, spatially-varying imaginary potentials [46]: (a) Spatially-varying weighting factor for the imaginary potential. (b) The beam evolution along the dynamic meta-molecule excited at the center atom, expressed as the beam center of mass. Blue dotted line shows only the p=11 supermode. (c) Spatial variations of modal excitation. The imaginary potential of gain and loss atoms before the weighting is $\beta_{i0}=\kappa_o/2$, and the coupling coefficient κ_o is $\beta_{r0}/200$. 3 7

Figure 2.14. Schematics of PT-symmetric meta-molecules [46] (a) before and (b) after the inversion of PT symmetry. (c) Real and (d) imaginary

part of each eigenvalue, and (e) the beam CM of supermodes for the inverted PT meta-molecule as a function of θ (N=23). Green labels denote the modal index p..... 39

Figure 2.15. Inversion of asymmetric light transfer in PT-symmetric optical potentials [46]. (a,d) Modal excitation, (b,e) beam propagation, and (c,f) evolution of beam CM (blue solid line) are presented for (a-c) p=11,13 complex phase-coexistent ($\beta_{i0}=\kappa_o/2$), and (d-f) entirely collapsed molecules ($\beta_{i0}=2\kappa_o$), with the inverted PT symmetry (Fig. 3b). (Movie 2 in [46]) The field intensity in (b,e) is normalized across the waveguide array at each position (X). Blue and black dotted lines in (c,f) denote the dominant (p=11) and the trapping (p=2–10) modes. The frequency f_0 = 193.4THz, β_{r0} = 3.5·($2\pi f_0/c$), and $\kappa_o=\beta_{r0}/200$..... 40

Figure 2.16. Numerical confirmation for Fig. 2.11 and 2.15, utilizing COMSOL Multiphysics [46]: (a,d) Imaginary potential and (b,c,e,f) beam dynamics are presented for (b,e) p=11 complex (Δn_{i0}=0.01), and (c,f) entirely collapsed meta-molecules (Δn_{i0}=0.042) in the case of complex molecules (a-c) before PT inversion, and (d-f) after PT inversion. The field intensity in (b,c,e,f) is normalized across the waveguide array at each position (X). Black dotted lines in (b,c,e,f) denote the beam center of mass. The frequency f_0=193.4THz.... 42

Figure 2.17. Eigenvalues and spatial evolution of eigenmodes in PT-symmetric chiral material [45]. The real and imaginary parts of the effective permittivity $\varepsilon_{eig1,2}$ are shown in (a) and (b) with respect to ε_{i0}. (c) The density of chirality χ, normalized by the product of the electric field intensity U_e and β_{r0} (orange: $\varepsilon_{\kappa 0}= \varepsilon_{r0}/10^3$, blue: $\varepsilon_{\kappa 0}= -\varepsilon_{r0}/10^3$, line: eigenmode 1, symbol: eigenmode 2). (d)-(h). Spatial evolution of eigenmodes corresponding to points *d*-*h* marked in a-c. The red and blue arrows represent the axes of E_y (amplifying mode) and E_z (decaying mode). At the EP f, the complex eigenmode has the singular form of a modal helix. ε_{r0} = 12.25 for (a)-(h), and $\varepsilon_{\kappa 0}$ =

$\varepsilon_{r0}/10^3 > 0$ for (a), (b), and (d)-(h)..... 48

Figure 2.18. Chiral dynamics within PT-symmetric optical material [45]. (a) C_{IM} and (b) C_{CS} as functions of ($\varepsilon_{i0}/\varepsilon_{\kappa 0}$). The output power ratio of LCP over RCP ($I_L/I_R = |E_{LT}/E_{RT}|^2$ in dB) is shown for the case of (c) LCP and (d) RCP incidence as a function of the imaginary permittivity ($\varepsilon_{i0}/\varepsilon_{r0}$) and the interaction length ($L_{eff} = \varepsilon_{r0}^{1/2} \cdot d/\Lambda_0$). The black dotted lines in c and d represent the EPs, where the dimensionality reduces to one..... 53

Figure 2.19. Chiral polar metamaterial for low-dimensional chirality [45]. (a) Schematics of a PT-symmetric, point-wise anisotropic permittivity material for Eq. (2.14). (b) Metamaterial realization of Fig. 2.19a using crossed I-shaped gold structures (tilted by θ) inside the polyimide. (c) Lorentz model for an I-shaped patch with different material regimes..... 56

Figure 2.20. Observation of EP dynamics in chiral polar metamaterials [45]. The experimental (a,b) and the simulated (c,d) results of C_{IM} are shown in a spectral regime for dielectric (a,c) and metallic (b,d) realizations. The peak value of the C_{IM} as a function of θ is shown in e and f for each realization. The black dotted lines in (a)-(d) represent the condition of EPs in spectral and θ domains. All simulated results were obtained using COMSOL Multiphysics. . 59

Figure 2.21. Chiral waveguides supporting bases of modal helices [45]. (a) Cross sections of a complex-strip waveguide using isotropic materials (graded color: Si for a lossless medium; purple: Ti for a lossy medium; green: silica substrate; graded color represents the effective loss by the Ti layer). The red and blue arrows describe a corresponding point-wise anisotropic permittivity. (b) The intensity profile and the polarization (in arrows) of the eigenmodes for the structure (ε_{yz}=0, Δ=0). (c) shows the modal chirality by I_L/I_R as a function of Δ and t_{Ti}. (d) The absolute value of the difference between eigenvalues as a function of Δ and t_{Ti}. The intensity profile

and the local chirality ($I_L(y,z)$ / $I_R(y,z)$) at the EP are shown in e. All results were obtained using COMSOL Multiphysics with an optical wavelength of Λ_0=1500 nm. …… 61

Figure 2.22. Schematics of one-way transitions [51] along (a, b) elliptic, (c) hyperbolic, and (d) quasi-linear IFCs. (a) Counterclockwise and (b) clockwise transitions; dotted lines denote the direction of the flow of light for beam steering. (c) High-*k* and (d) low-*k* excitations. Blue (or purple) circles denote the initial (or excited) state for each IFC. (e) Schematic linking one-way optical transition with causality. Red (or gray) arrows show allowed (or forbidden) transitions along the IFC in (a-e). …… 65

Figure 2.23. Potential momentum spectra for degrees of PT symmetry [51]: (a) at the EP ($\Delta\varepsilon_{sr0} = \Delta\varepsilon_{si0}$), (b) before the EP ($\Delta\varepsilon_{sr0} > \Delta\varepsilon_{si0}$), and (c) after the EP ($\Delta\varepsilon_{sr0} < \Delta\varepsilon_{si0}$). Lower figures illustrate the corresponding coupling between momentum states for each degree. Green (purple) solid line denotes the momentum state that corresponds to the 'cause' ('effect'). As shown, causality is only maintained at the EP. Gaussian spectra with σ = 0.25 and $p_0 = q_0 = 1$ are assumed, without loss of generality. …… 69

Figure 2.24. Discretization of (a) spatial and (b) momentum domains for the derivation of Eq. (2.23) [51]. S_L and S_R present the left and right surfaces, respectively, of the unit volume V (in blue). A wave with a unit amplitude (at the (k_{x0},k_{y0}) state, shown by red arrows in (a)) is incident on the left side of the spatial domain. Circles in (b) represent discretization in momentum space. Blue circles denote states that participate in the coupling to the calculated state (k_x,k_y). 71

Figure 2.25. High-*k* excitations along the hyperbolic IFC (ε_{x0} = –9, ε_{y0} = 2.25) [51]. (a) Design strategy with 5-stage transitions. (b) Normalized real-valued momentum spectra of $\Delta\varepsilon_{pq}$ (Gaussian bandwidth of $\sigma_{x,y}$ = k_0/100 for each spectrum). (c) Normalized amplitude and (d) phase

of the corresponding complex potential in the spatial domain. The profile of momentum spectra in (b) is assigned to both $\Delta\varepsilon_{xpq}$ and $\Delta\varepsilon_{ypq}$. The amplitude of the envelopes in momentum space at $x = 100\lambda_0$ are shown for different bandwidths of (e) $\sigma_{x,y} = k_0/200$ and (f) $\sigma_{x,y} = k_0/100$. (g) Variation in the effective index along the x-axis for different bandwidths (solid lines show $\sigma_{x,y} = k_0/100$, and dotted lines show $\sigma_{x,y} = k_0/200$). The phase of the magnetic field at each position (red circles in 4 g) is also shown in the right panel of (g). Maximum values of modulations are $\Delta\varepsilon_x(x, y)/\varepsilon_{x0} = \Delta\varepsilon_y(x, y)/\varepsilon_{y0} = 0.04$, 0.12, and 0.20. Discretization parameters at the deep-subwavelength scale are $\Delta x = \lambda_0/50$, $\Delta k_y = k_0/100$, and $\Delta p = \Delta q = \sigma_{x,y}/10$ for all cases. 7 3

Figure 2.26. Asymmetric beam steering and collimation in the elliptic IFC ($\varepsilon_{x0} = 9$, $\varepsilon_{y0} = 2.25$) [51]. (a) IFC with 5-stage transitions. Red (gray) squares denote allowed (forbidden) states for the transition. (b) Beam trajectories (solid lines) for different incidences of $n_y > 0$ (blue dotted lines) and $n_y < 0$ (orange). $\varepsilon_x(x, y)/\varepsilon_{x0} = \varepsilon_y(x, y)/\varepsilon_{y0} = 0.2$ and $\sigma_{x,y} = k_0/200$. All other parameters of the potential are the same as those presented in Fig. 2.25..... 7 4

Figure 3.1. The examples of disordered optics: (a) broadband and efficient optical absorbers based on wideband k-spectra [141]. (b) Anderson localization based on large k components which originate from the random-walk interference [142]..... 7 8

Figure 3.2. Wave dynamics in crystals, quasicrystals, and Bernoulli random potentials [140]. (a) Definitions of elements, illustrated for an example of a 1D Fibonacci quasicrystal ($N = 8$). $g_A = 600$ nm, $g_B = 200$ nm, $w = 120$ nm, $s = 140$ nm, and the wavelength is $\lambda_0 = 1500$ nm. (b) Hurst exponent H for each potential as a function of the sequence length N. The sequence lengths N are selected to be equal to those of Fibonacci quasicrystals. The H of the Bernoulli random potential is plotted with error bars for 200 statistical ensembles. The black dashed line represents the Hurst exponent of ideal Brownian

motion (H = 0.5). (c)-(e). Eigenstates of each potential. The blue curve represents the ground state of each potential, and the colored lines represent the spectral (n_{eff}) distributions of the eigenstates. (f)-(h). Evolutions of the band structures for different sequence lengths N: (c),(f) for crystals, (d),(g) for quasicrystals, and (e),(h) for Bernoulli random potentials. …… 82

Figure 3.3. Effects of SUSY transformation on the generation of quasi-isospectral potentials [140]. A 1D Fibonacci quasicrystal (N = 5) is considered as an example. (a) Original potential. (b)-(f). 1st - 5th SUSY-transformed potentials. The orange (or black) dotted lines represent the preserved (or annihilated) eigenstates. All eigenstates are calculated using both the FDM and FGH method, the results of which are in perfect agreement.…… 85

Figure 3.4. Potentials and band structures of SUSY-transformed crystal and quasicrystal (N = 144) [140]. The 10th SUSY-transformed potentials and their eigenstates are depicted for (a) a crystal potential and (b) a quasicrystal potential. (c) and (d) show the eigenvalues of the SUSY-transformed potentials as a function of the modal numbers of the crystal and quasicrystal potentials, respectively. The 0th SUSY-transformed potential corresponds to the original potential. …… 87

Figure 3.5. Correlation features of SUSY-transformed potentials for N = 144 with bandgaps maintained [140]. The evolutions of the potential profiles following the successive application of SUSY transformations (0th, 6th, 12th, and 18th) for a. a crystal and e. a quasicrystal. b-d and f-h present magnified views (at x_L, x_C, x_R) of the potentials for even numbers of SUSY transformations (overlapped, up to the 20th transformation; the blue arrows indicate the direction of potential modulation).…… 89

Figure 3.6. Microscopic SEM views of the wing of Morpho butterfly [124]: in (a) a few μm scale and (b) its enlarged picture. The measurement is carried out by K. Chung in J. H. Shin's group in KAIST [124].. 92

Figure 3.7. Schematics of biomimetic reflecting surfaces [124]: (a) with disorders and (b) without disorders. Dark grey: Cr layers to block the retro-reflection from spheres. Blue: Silica, Pink: TiO_2. 93

Figure 3.8. Reflection property of biomimetic reflecting surfaces [124]: (a) the example of the reflected eiectric field. 94

Figure 3.9. Images of fabricated films [124]. (a) Comparison of the fabricated reflector (PDMS encased thin film) with Morpho rhetenor (above) and Morpho didius (below). The size of the reflector is 6 inches in diameter. (b) Various colors ranging from deep blue through green to coppery red realized by controlling the layer thicknesses. (c) Image of deep blue reflector (shown in Fig. 3.9b), wrapped around a rod with diameter of 1 cm. Note that the color appears the same throughout, even though the reflector is bent, and thus presents a viewing angle that varies from 0 to 90°. The fabrication and experiment are carried out by K. Chung in J. H. Shin's group in KAIST [124]..... 97

Figure 4.1. The examples of all-optical switching devices based on optical nonlinearity: (a) ring-resonator-based switch [193], (b) Kerr-effect switch based on a photonic crystal waveguide crossing structure [192], and (c) Fano-based efficient switch with coupled photonic crystal resonators [203]..... 101

Figure 4.2. Dynamics of photonic mode junction [125]. (a) Examples of orthogonal mode junctions constructed between two orthogonal modes, providing different frequency separation and modal overlap properties. (b) Examples of molecular modes, which could be used to construct a variety of molecular mode junction (S, D, T: Single-, Di-, Tri- atomic molecular modes). A *T-* / *T0* mode junction, for example, can be constructed between two structures providing orthogonal modes of *T-* and *T0* (composed of optical atoms in single mode, sharing an identical polarization). Dashed circles in Fig. 4.2(a,b) represent optical atoms. (c) Operation principles of the

mode junction. Excited modes at the operation frequency are marked with filled curves. N_T(E) and N_{T0}(E) axis represents the density of states for *T*- and *T0* mode. Adjusting the optical potential, the dominant mode of the controlled region can be switched between *T*- (non-shifted, yellow) and *T0* (potential ΔE-shifted, pink) modes, to give a junction throughput of either a '0' (yellow) or '1' (pink). The coupling across the junction is determined by the inner product between eigenmodes of the left/right structures (equivalently, multiplying spatial mode profiles at the same frequency along the *identical mode axis* (*T*- or *T0*)). 104

Figure 4.3. Operation of a mode junction diode [125]: under (a) Forward bias below threshold, (b) Forward bias above threshold, and (c) Reverse bias..... 106

Figure 4.4. Comparison between a mode junction structure and an ordinary asymmetric structure [125]. (a) Impedance matched ($1/\tau_L = 1/\tau_{R1} + 1/\tau_{R2}$) low reflection design is achieved with a junction diode, by adjusting τ_L. Mode-dependent field intensity inside resonators (even: $|a_1+a_2|^2$, odd: $|a_1-a_2|^2$) for structures in (a) are shown for; (b) - forward bias before threshold, (c) - forward bias after threshold, (d) - under reverse bias. For two-band operation (b) at the operation frequency ω_{op} (dashed line), on resonance feeding and low power excitation of the resonator is achieved. $\kappa = 0.003\omega_{op}$, and $Q = 200$. Coupled-mode-theory was used for the calculation. 108

Figure 4.5. Photonic mode junction diode operation [226]. (a) Numerically (FDTD, blue lines, Appendix E.1), and analytically (CMT, red lines, Appendix E.2) obtained response curve of the $\Psi_{e\text{-}o}$-ψ_o junction diode. 110

Figure 4.6. Multi-junction realization of monolithic half-adder [125]; (a) coupling to *S* (*XOR*) port with a single logic input (I_A or I_B) power below the threshold. (b) coupling to *C* (*AND*) port under two input signals ($I_A \cdot I_B$) for their total power above the threshold. Even (state

1)- / Odd (state 2)- mode excitation for the central di-atomic resonator and couplings to the even- / odd- mode coupler at the *S* / *C* port (left / right) of the half-adder is evident from the FDTD generated field amplitude plot. Figure (c) shows the logic operations of *AND* & *XOR*, under the two input signals at 50Gbps (de-correlated, PRBS). Figure (d) and (e) show the optical eye patterns for AND & XOR outputs. To note, for the generation of phase / time synchronized two input signals (I_A and I_B) for the proper logic operation, a single source was assumed, which are power divided and then separately modulated [230]. …… 114

Figure 4.7. Coupled-mode theory model of a multi-atom, multi-band CROW [205]. $\kappa_{i,o,c}$: coupling constants between resonators; a_k^m : field amplitude in the *m*-th atomic resonator in molecule *k*. …… 118

Figure 4.8. Dispersion curves of a tri-atomic CROW [205]: in (a) a weak internal coupling regime ($\kappa_i = -0.04\omega_0$, $\kappa_o = 0.02\omega_0$) and (b) a strong internal coupling regime ($\kappa_i = -0.08\omega_0$, $\kappa_o = 0.02\omega_0$). Effect of cross coupling is evident by comparing $\kappa_c = 0$ (solid line) and $\kappa_c = 0.4\kappa_o$ (dashed line). (c) Group velocities for the dispersion curves in (b). Group velocities are normalized to v_g ($\omega = \omega_0$, $\kappa_c = 0$)…… 121

Figure 4.9. Band dynamics of MA-CROW [205]. (a) Band-dependent modification of molecular coupling strength for a di-atomic CROW; from constructive (even mode, $\kappa_{even} = \kappa_o + \kappa_c$) and destructive (odd mode, $\kappa_{odd} = \kappa_o - \kappa_c$) interferences. (b) Deviations in group velocity for each molecular mode, plotted for different *n*-atomic molecules. κ_c was set to $0.2\kappa_o$. v_g^{mono} denotes the group velocity of single atom CROW. (c) Intensity overlap between molecular modes *p* and *q* (marked as *np*:*nq*). Perfect intensity overlap can be obtained if $p+q=n+1$, for example, $p = 1$ and $q = 4$ for $n = 4$. …… 122

Figure 4.10. All-optical switching based on a MA-CROW Mach-Zehnder interferometer [205]. (a) Bandwidth limit of multi-atomic CROW, for different cross coupling coefficient κ_c. Blue and red lines show

the walk-off- and CROW dispersion-limited bandwidth respectively, for different MA-CROW structures (n = 2~5). A plot was made for the cases of p = 1 and q = n by assuming maximum band separation and a perfect intensity overlap between the signal and control waves. $\Delta\rho_{XPM}$=0.02%, $\lambda_0=2\pi c/\omega_0$=1550nm, σ=0.6, $\varphi=\pi$, and $\kappa_o=0.001\omega_0$. (b and c): A plot of the theoretically (lines) and FEM calculated (symbols) (b) walk-off parameter $\Delta n_g=c\cdot|1/v_{gp}-1/v_{gq}|$ and (c) Bandwidth limit, for di- and tri- atomic CROWs (Λ = 3a ~ 6a, for δ = 2a and 3a). Coupling coefficients for the CMT analysis were calculated from the isolated resonator modes. Switching operation of di-atomic CROW MZI for (d) On-State and (e) Off-State. Optical eye of the switched output, for PRBS control waves at (f) 100Gbps and (g) 200Gbps..... 125

Figure 4.11. Schematics of Taylor's PADC and its ideal output (for a 3-bit A/D converter. red line: decision threshold for the digital conversion) [204]. Bottom: slow-light implementation of 2 x 2 MZI. 128

Figure 4.12. The footprint and performance of the PADC [204]. (Up) Device length and (Down) ENOB of the PADC plotted for different coupling coefficients, at various target resolutions. (1550nm, σ=0.6, ρ=1.0%, and Λ=2μm). 132

Figure 4.13. Design strategies of elements in the PADC [204]. (a) CROW dispersion relation of the achieved design. (b) 3dB splitter (red rods tuned to r = 0.18a) (c) CROW-PC waveguide adapter (purple and red rods tuned to r=0.22a and 0.15a)..... 133

Figure 4.14. Demonstration of a 3-bit CROW PADC under a linear refractive index modulation (movie in [204]). For the figures on the right, the red dashed lines show the decision threshold. 134

Figure 4.15. The spectral response of the CROW PADC [204]. (Up) Plot of the digitized output (black) from a 3-bit CROW PADC compared with its analog sinusoid input signal (100GHz, yellow). (Down) ENOB of the 3-bit PADC at different frequencies of analog input signals. The

ENOB from the FDTD simulation (black) is compared to the ENOB values calculated from theory (in Section 2) showing excellent agreement. 136

Figure 4.16. Structure of travelling-wave, two-mode, 4-ports CROW MZI [198]: composed of 2 CROW waveguide arms, 6 directional coupler, and several waveguide bending and CROW-waveguide connectors. 138

Figure 4.17. Switching action of MSB MZI of the PADC [198]. (a) ON state (control signal power = 170mW/μm). (b) OFF state (control signal power = 0mW/μm). Zoomed-in images of the wave evolution, at the output ports of the MSB MZI, for (c) ON state, and (d) OFF state. 139

Figure 4.18. Spectral response of the two-mode CROW [198]. Response of (a) signal and (b) control wave from the two-mode CROW waveguide. (c) signal wave output from the MSB MZI, with sinusoidal control wave at 100GHz. 141

Figure 4.19. Error analysis of the all-optical PADC, based on the comparison with an electrically-modulated PADC [198]. ENOB of the travelling-wave, optically modulated PADC (solid lines, DGD = 10%) and electrically modulated PADC (dotted lines), plotted for different CROW dispersion (blue : linearized [259], red : diatomic CROW dispersion). 143

Figure 4.20. Schematics of travelling-wave all-optical isolator: (a) forward wave and (b) backward wave. 144

Figure 4.21. Design strategy of the travelling-wave all-optical isolator. (a) Travelling-wave all-optical isolator based on photonic crystal MA-CROWs. (b) Modulation signals for Path 1 and Path 2 in (a). T_m is a period of the square modulation and n_{pi} denotes the Kerr effect XPM for the π phase difference between two arms. 145

Figure 4.22. The operation of the travelling-wave all-optical isolator. (a) Forward wave, and (b) backward wave incidences. The simulation is

carried out by the 2D FDTD method with optical Kerr effect. 147

Figure 4.23. DC response of the travelling-wave all-optical isolator. Signal outputs for (left) 20mW/μm and (right) 40mW/μm signal powers, modulated by the ~25mW/μm modulation power. Blue lines for forward signals and red lines for backward signals. 147

Figure 4.24. Square pulse modulation for the all-optical isolator: (left) modulation power for each arm, (right) signal output with increased power. 148

Figure 4.25. $Sin^2(t)$ pulse modulation for the all-optical isolator: (left) modulation power for each arm, (right) signal output with increased power. 148

Chapter 1

Introduction

1.1 Why should we break the symmetry of light?

The property of light propagating in matters is usually defined by chargeless macroscopic Maxwell's equations, based on effective representations of matters [1]. If the matter is assumed to be ideal as homogeneous (in x- and k- domains), isotropic (in the polarization domain), conservative, non-dispersive and linear (in t- and ω- domains), Maxwell's equations are simplified to the Hermitian Schrodinger-like wave equation, representing the most fundamental property of light: propagating straight with constant amplitude, conserved frequency, momentum, and polarization, and identical phase and group velocities which is the simplest example of Fermat's principle [2]. This ideal feature originates from the conservation of various symmetries in the wave equation: translational and chiral symmetry, Hermitian symmetry, Lorentz reciprocity, and time-reversal symmetry.

Many of the impacts in classical optics have been carried out in the regimes of preserved symmetry. Classically, the straight propagation of light has enabled the successful application of geometric optics [2] which has also been extended to transformation optics [3] lately. Distortion-free and lossless propagation of light

has been the basis of optical communications [4]. Translational symmetry with periodic modulation in optical potentials has been applied to mimic the property of electronic solids, i.e. photonic crystal [5]. Recent researches in metamaterials [6], the foundation of many intriguing results in nanophotonics such as superlens [7], negative index [8], modified Snell's law [9], and cloaking [10], have begun with serious efforts to realize unnatural but homogeneous, linear, and Hermitian materials.

However, to exploit light as the mediator of information and impose the functionality, it is imperative to realize the designer manipulation of the flow of light. Recently, from active studies on innovative results of nanophotonics, there have been serious efforts to introduce symmetry breaking in various physical axes, in order to manipulate related optical quantities (e.g. spatial amplitude or momentum with translational symmetry or Hermitian symmetry, ω with time-reversal symmetry, $\dot{E}$ with chiral symmetry). One of the purposes of these researches has been focused on the realization of 'non-classical light' with broken symmetries, such as discretized wave dynamics [11-13], diffusive behaviors [14], adiabatic transports [15-18], Fano resonances [19-21], graphene optics [22-26], and topologically-protected propagations [27-29]. Such efforts not only provide in-depth understanding of light behaviors in the context of the symmetry, one of the most powerful mathematical frameworks in physics, but also enable fermionic wave dynamics which will be necessary for future optical functionalities toward photonic integrated circuits. In this context, the study of symmetry breaking in accordance with various physical quantities of photons (linear and angular momentum, polarization, and energy) will be the groundwork for a new class of wave dynamics and future optical devices.

1.2 Outline of the dissertation

In this dissertation, we focus on reviewing our achievements in symmetry breaking of light, in accordance with physical quantities of photons. In chapter 2, we

investigate parity-time (PT) symmetry breaking which allows unidirectional manipulation of optical linear and angular momenta. In chapter 3, we examine the disordered potentials with globally-broken translational symmetry, enabling the manipulation in momentum and spectral domains. In chapter 4, we explore the breaking of time-reversal symmetry based on optical nonlinearity, especially in terms of nonreciprocal and high-level all-optical device designs. Supporting information for the self-consistency is provided in Appendix A-E.

Chapter 2

Parity-Time Symmetric Optics

Due to the importance of observables with real eigenvalues, complex potentials which violate the Hermitian condition had been treated restrictively: e.g. for the description of a nonequilibrium process [30, 31] or for the rigorous explanation of phenomenological constitutive relations based on nonlocal complex potentials [32]. However, since the pioneering work of Bender [33], it has been widely accepted that the condition of parity-time (PT) symmetry allows real eigenvalues and thus physical observables, even for complex potentials of non-Hermitian Hamiltonians.

Among various fields of adopting the notion of PT symmetry [34-40], optics has been one of the most active fields in realizing PT-symmetric wave dynamics. It originates from the feasibility of complex potentials with gain and loss optical materials and the bosonic property of non-interacting photons, enabling the effective test bed of quantum-mechanical PT-symmetric potentials [41]: in terms of the analogy between the paraxial wave equation and the Schrodinger wave equation for a single electron [42]. However, to demonstrate the sufficient impact of PT-symmetric optics, it is now imperative to find original and distinctive features of PT-symmetric optical potentials not restricted to the effective form of

quantum-mechanical PT symmetry, by employing intriguing properties of PT symmetry: such as modal skewness [43, 44], low-dimensionality [45], and localization [46].

In this chapter, we investigate the flow of light in PT-symmetric optical potentials, especially focusing on the breaking of PT symmetry linked with asymmetric wave dynamics. After the brief review beginning with the operator-based description (section 2.1), we explore PT-symmetric potentials in two aspects: wave evolutions in the spatial domain (section 2.2) and the manipulation of linear or angular momenta (section 2.3).

2.1 Introduction to PT-symmetric optics

In the problems of quantum mechanics and optics using linear Hamiltonians, the Hermitian condition has guaranteed real eigenspectra successfully [47]. However, the Hermitian condition (yellow circle in Fig. 2.1) is just the sufficient condition for real eigenspectra [47], and there exist much broader regimes of non-Hermitian Hamiltonians with real eigenvalues (Indian-red regions in Fig. 2.1). After the Bender's finding [33], PT symmetry which corresponds to the *PT*-transformation-invariant Hamiltonian H ($H = PTH(PT)^{-1}$ where P: parity operator and T: time-reversal operator) has been employed to achieve non-Hermitian Hamiltonians with real eigenspectra. Although there has been a broader boundary of pseudo-Hermiticity based on antilinear symmetries [48] (blurred regions in Fig. 2.1), including non-PT-symmetric potentials with real eigenvalues (e.g. potentials designed by supersymmetric (or Darboux) transformation [49, 50]), in this chapter we focus on the wave dynamics in PT-symmetric optical potentials which not only can be designed by the simplest condition of $V(\boldsymbol{x}) = V^*(-\boldsymbol{x})$ but also provide intuitive understanding of spectral properties of complex potentials, linked with causality [51].

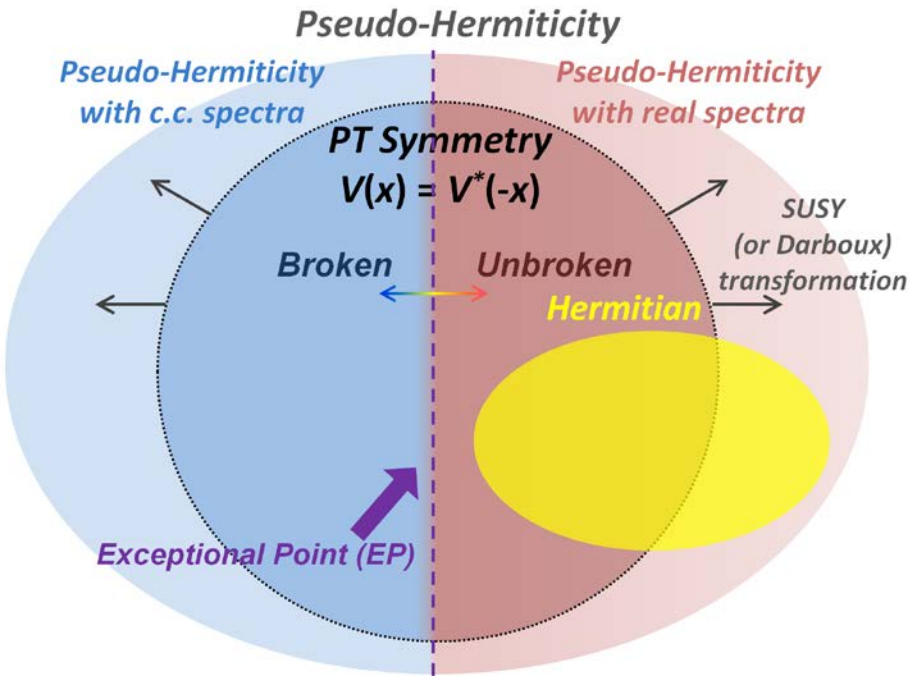

Figure 2.1. The classification of Hamiltonians in wave physics, in terms of eigenspectra related to pseudo-Hermiticity. Pseudo-Hermiticity [48], supporting real or complex-conjugate (c.c.) eigenspectra, contains the notion of PT symmetry. The boundary between real and c.c. eigenspectra corresponds to the exceptional point (EP). The non-PT-symmetric potentials with pseudo-Hermiticity can be achieved with mathematical methods such as supersymmetric (SUSY) transformation [50].

For a better understanding, we begin with the description for each operator (Fig. 2.2). Firstly, parity operator P is utilized to describe the action of space inversion ($\boldsymbol{x} \rightarrow -\boldsymbol{x}$, Fig. 2.2a), simultaneously deriving the inversion of linear momentum ($\boldsymbol{p} \rightarrow -\boldsymbol{p}$) and the handedness. Time-reversal operator T is applied to the counter-flow of time ($t \rightarrow -t$, Fig. 2.2b), also naturally inducing the inversion of linear momentum ($\boldsymbol{p} \rightarrow -\boldsymbol{p}$). Note that in the spectral domain ω for harmonic problems, the inversion of time ($t \rightarrow -t$) is replaced by the complex-conjugate

action ($i \rightarrow -i$). Therefore, from the serial change by T and P, PT operator (Fig. 2.2c) results in the change of $\boldsymbol{x} \rightarrow -\boldsymbol{x}$ and $i \rightarrow -i$.

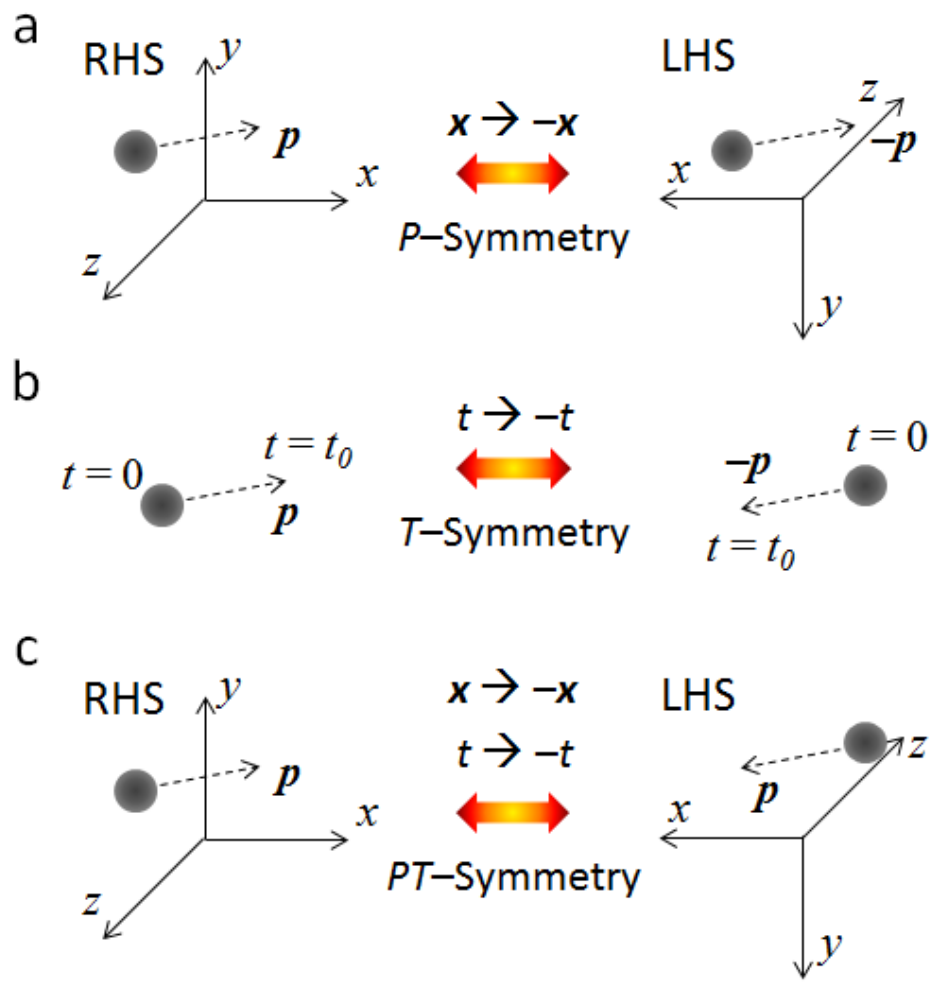

Figure 2.2. Symmetries related to P and T operators: (a) parity symmetry with space inversion, (b) time-reversal symmetry with counter-flow of time, and (c) parity-time symmetry based on the PT operator.

Before introducing Hamiltonians, look into the eigenstate of PT operator [52]. If $PT\varphi = \lambda\varphi$, because $(PT)^2 = I$ due to $\boldsymbol{x} \rightarrow -(-\boldsymbol{x})$ and $i \rightarrow -(-i)$, $PT(PT\varphi) = \varphi =$

$\lambda(PT\varphi) = \lambda^2\varphi$, giving $\lambda^2 = 1$. Because there is the action of $i \rightarrow -i$, λ has a complex value, and then, now we can estimate the mathematical form of eigenvalues by the PT operator: $\lambda = e^{i\theta}$.

Now, consider the Hamiltonian $H = p^2 + V(x)$ for the eigenvalue problem of $H\psi = E\psi$, where p^2 corresponds to the kinetic energy operator and $V(x)$ is the potential energy operator. When H is PT-symmetric, $H = PTH(PT)^{-1}$ which gives $PTH = HPT$. Note that from $PTH\psi = PT(p^2\psi(x) + V(x)\psi(x)) = p^2\psi^*(-x) + V^*(-x)\psi^*(-x)$ and $HPT\psi = (p^2 + V(x))\cdot(PT\psi(x)) = p^2\psi^*(-x) + V(x)\psi^*(-x)$, PT symmetry gives the potential satisfying $V(x) = V^*(-x)$ which has been considered as 'PT-symmetric potentials' (e.g. $V_1(x) = ix^3 + ix$ is PT-symmetric and $V_2(x) = ix^3 + x$ is non-PT-symmetric). Following the result in classical quantum mechanics [47], 'suppose' that when PT and H are commute ($PTH = HPT$), ψ is also the eigenstate of PT with the eigenvalue of $\lambda = e^{i\theta}$ [52]. This assumption then gives the following simple relations of $PT(H\psi) = PT(E\psi) = E^*(PT\psi) = E^*e^{i\theta}\psi$ and $H(PT\psi) = H(e^{i\theta}\psi) = e^{i\theta}(H\psi) = Ee^{i\theta}\psi$, surprisingly deriving real eigenspectra as $E = E^*$ from $H(PT\psi) = PT(H\psi)$.

However, we should remember that the case is not as simple as above. The above assumption (the sharing of eigenstates by PT and H, when $PTH = HPT$) holds only when both PT and H are linear operators. Unfortunately, PT operator is nonlinear due to the complex-conjugation ($i \rightarrow -i$) by the T operator, as shown in the antilinear relation of $PT(c_1 p) = c_1^* p$. Therefore, we can roughly say that 'PT-symmetric potentials *can* get real eigenspectra at *certain* conditions' (see Fig. 2.1). In 1998, Bender firstly found a huge class of non-Hermitian Hamiltonians with real eigenspectra [33], i.e. PT-symmetric Hamiltonians satisfying the condition of $V(x) = V^*(-x)$ such as $H = p^2 - (ix)^N$ (Fig. 2.3), in sharp contrast to complex eigenspectra in non-PT-symmetric potentials such as $V_2(x) = ix^3 + x$.

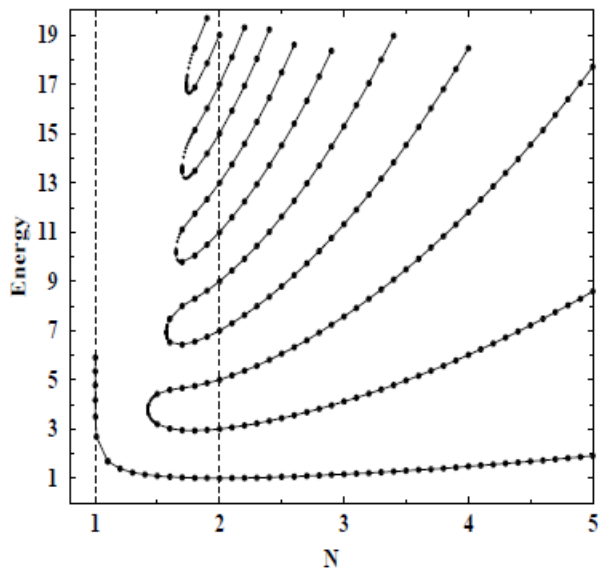

Figure 2.3. Eigenspectra of the PT-symmetric Hamiltonian $H = p^2 - (ix)^N$ [33]. The spectrum is real and positive when $N \geq 2$. We note that $N = 2$ corresponds to the harmonic oscillator. The coalescence of eigenstates is observed as N decreases.

The concept of PT symmetry has opened a pathway for handling complex potentials, overcoming traditional Hermitian restrictions, and stimulating the field of complex quantum mechanics [40]. In sharp contrast to Hermitian potentials, PT-symmetric potentials support regimes in which some eigenvalues are complex (Fig. 2.3, $N < 2$) due to the nonlinearity of the *PT*. Accordingly, the phase of eigenvalues can be divided into a real and a complex regime - with a border line called the exceptional point (EP), marking the onset of PT symmetry breaking (Fig. 2.1). It is emphasized that at the EP the given eigensystem becomes supporting a 'lower' dimension [45], resulting in the 'singularity' in the eigensystem.

Despite those interesting features of PT-symmetric Hamiltonians, the difficulty in the realization of complex electrical potentials (even almost impossible in a microscopic level!) has hindered the demonstration of complex quantum mechanics. Therefore, due to more accessible implementation of optical complex

potentials utilizing optical gain and loss [43], serious research has focused on optical analogues of PT-symmetric dynamics (Fig. 2.4). Based on the equivalence of the Schrodinger and paraxial wave equations, the classical simulation of complex quantum mechanics has been tested [53, 54]. More importantly, although Lorentz reciprocity cannot be broken only with spatially-varying complex potentials [55, 56], exotic behaviors of light have been implemented by the use of complex optical potentials; such as asymmetric conversion of optical modes [44, 46], abnormally-diffracted beams (Fig. 2.4a,2.4b, [57]), loss-induced transparency (Fig. 2.4c, [41]), unidirectional invisibility [58, 59], and the spectral realization of PT-symmetry exploiting nonequilibrium resonances [60]. Note that all these phenomena originate from the dynamics of complex eigenmodes in relation to their modal skewness and asymmetric intermodal transfer [44, 46], especially near the EP with a singularity (Fig. 2.4d, [43]). Recently, there have also been intriguing efforts to apply the physics of PT symmetry to metamaterials [61, 62].

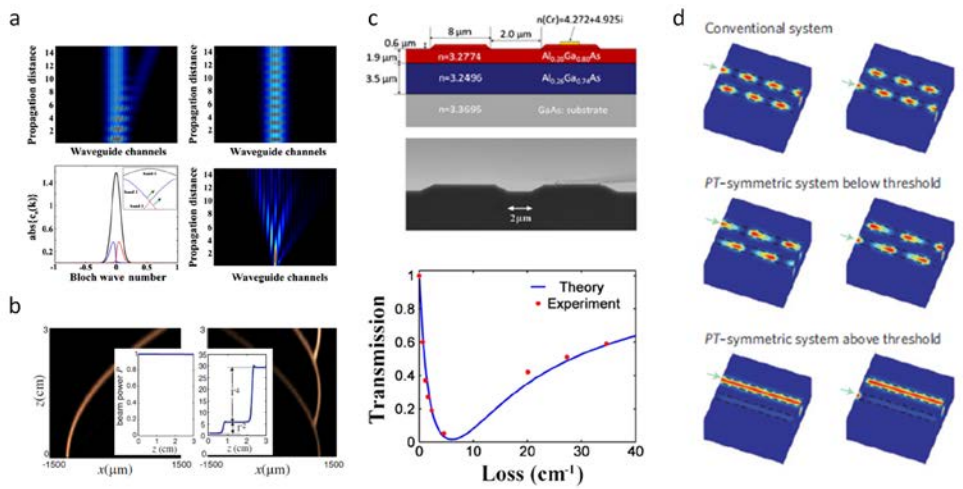

Figure 2.4. Examples of early PT-symmetric optics: (a) double refraction from modal skewness [57], (b) asymmetrically-steered waves in Bloch oscillating potentials [12], (c) passive PT-symmetric potentials with loss-induced transparency [41], and (d) distinctive propagations for the degrees of PT symmetry [43].

2.2 PT-symmetric waves in the spatial domain

In the section 2.2, we investigate PT-symmetric wave dynamics in the spatial domain. We begin with the simplest example of a two-level optical system including the spatial-/spectral- dispersions [44] for the understanding of PT-symmetric optical potentials, by introducing the interaction parameter defining the EP in eigenspectra. We then consider the wave dynamics in *N*-atomic photonic molecular systems [46], analyzing the degree of asymmetry in propagation related to modal skewness and observing the competition between local and global PT symmetry. These results will be the foundation of unconventional flow of light in complex optical potentials: by harnessing nonorthogonal, skewed eigenmodes.

2.2.1 2-level chirped system

In optics, the necessary condition for PT-symmetric Hamiltonians is fulfilled with a media of symmetric-real and antisymmetric-imaginary refractive index profile [43]. In various structures, interesting behaviors of photons around an EP have been investigated both theoretically [12, 57] and experimentally [41, 43, 61]. While past studies of PT symmetry may have opened new routes to photon manipulation in terms of its directivity and spatial profile, the complex interaction parameter λ [63], that defines the EP, had been still interpreted in a narrow sense as only a quantity related to the imaginary refractive index.

Here we introduce the generalized condition of PT-induced EP by employing the multi-dimensional interaction parameter $\lambda(x,\omega)$ of spatial and spectral freedoms [44]. By introducing dispersive variations in the PT-symmetric potentials along the propagation axis of the wave, EPs of Spatio-Spectral separation are obtained. As a result of the EP separation, spatially-adjustable and frequency-dependent asymmetric wave propagation is predicted analytically and confirmed with an example of "Rainbow EP", using an adiabatically chirped optical potential.

Before studying the behavior of the PT-induced EP with a Spatio-Spectral interaction parameter $\lambda(x,\omega)$, we start our discussion with the simple case of a

spatially uniform potential having real and imaginary indices $n_{1,2} = n_{r1,2} + in_{i1,2}$. Using the coupled mode theory (CMT) [64] we may write,

$$\frac{d}{dx}\begin{bmatrix}\psi_1(x)\\ \psi_2(x)\end{bmatrix} = i\begin{bmatrix}\beta_1 & \kappa_{12}\\ \kappa_{21} & \beta_2\end{bmatrix}\begin{bmatrix}\psi_1(x)\\ \psi_2(x)\end{bmatrix}, \tag{2.1}$$

where $\psi_{1,2}(x)$ are the amplitudes of waves propagating along waveguides 1 and 2; $\beta_{1,2} = \beta_{r1,2} + i\beta_{i1,2}$ are the complex wave numbers of the uncoupled waveguides 1 and 2; and $\kappa_{12,21}$ are the coupling coefficients (for small $|n_{i1}| - |n_{i2}|$, $|\kappa_{12}| \sim |\kappa_{21}| \sim \kappa$). Postulating the plane-wave solution $\psi_{1,2}(x) = \psi_{1,2}(0)\cdot e^{i\beta x}$ and separating real and imaginary parts of $\beta_{1,2}$, Eq. (2.1) may be cast in the form of the eigenvalue equation,

$$\beta_{A,B}\Psi = \begin{bmatrix}\beta_{r1} & 0\\ 0 & \beta_{r2}\end{bmatrix}\Psi + \begin{bmatrix}i\beta_{i1} & \kappa_{12}\\ \kappa_{21} & i\beta_{i2}\end{bmatrix}\Psi, \tag{2.2}$$

where $\Psi = [\psi_1(x), \psi_2(x)]^T$, and $\beta_{A,B}$ are the eigenvalues (propagation constants) of supermodes (A,B). It is convenient to express Eq. (2.2) in Hamiltonian form for the derivation of λ which defines the EP [63]. Upon diagonalizing the second term of Eq. (2.2), we obtain,

$$\beta_{A,B}\Psi = \left[H_0 + i\lambda_0 UIU^+ + \lambda_1 U\sigma_3 U^+\right]\Psi \quad , \tag{2.3}$$

where H_0 is the unperturbed, real Hamiltonian $[H_0]_{pq} = \beta_{rp}\cdot\delta_{pq}$; I is the identity matrix; σ_3 is a Pauli matrix [65]; U is a unitary matrix; $\lambda_0 = (\beta_{i1} + \beta_{i2})/2$ is an interaction parameter for the gain/loss equalization; and $\lambda_1 = \{|\kappa|^2 - [(\beta_{i1} - \beta_{i2})/2]^2\}^{1/2}$ is an interaction parameter for band repulsion. For a PT structure ($n_{1,2}=n_{r0}$, $\beta_{r1,2}=\beta_{r0}$), the eigenvalues of supermodes (A,B) are then given by $\beta_{A,B}=\beta_{r0}+i\lambda_0\pm\lambda_1$, A,B corresponding to the +,– sign, respectively. The existence of an EP is entirely determined by λ_1, the condition $\lambda_1 = 0$ (or $|\kappa| = |\beta_{i1} - \beta_{i2}|/2$) marking the transition to differential loss/gain between supermodes A and B, while λ_0 denotes the average

gain/loss of supermodes, being zero in the case of ideal PT symmetry ($\beta_{i1}+\beta_{i2}=0$), and becoming non-zero through a gauge transformation into passive PT symmetry ($\beta_{i1}>\beta_{i2}>0$) [41]. We note that, as the degree of intermodal asymmetry after the EP is determined by the difference of the absorption coefficients $2\cdot Im(\lambda_1)$ between skewed supermodes A and B, it is expected that the generalization of the constant λ_1 to $\lambda_1 = \lambda_1 (x,\omega)$ would enable intermodal asymmetry of both spatial and spectral-dependence.

To impose the *spatial* variation on $\lambda_1 = \lambda_1 (\kappa, \beta)$, here we introduce a spatial dependence on both real and imaginary parts of $\beta_{1,2}=\beta_{1,2}(x)$ by cascading unit cells of "instantaneous" potential. Figure 2.5a shows the schematics of two coupled waveguides composed of cascaded unit cells for the scattering matrix (S-matrix) analysis [66]. The k^{th} cell supports the supermode pair (A_k, B_k), with the local dielectric potential (effective index) $n_{1k,2k}(x)$ and coupling $\kappa_{12k,21k}(x)$ between waveguides. The wave amplitudes of supermodes in the k^{th} cell is then denoted as $v_k = [A_k^+, A_k^-, B_k^+, B_k^-]^{\text{T}}$. The field of waveguides 1 and 2 in the k^{th} cell, composed of the linear combination of supermodes, can then be expressed as,

$$\begin{aligned}\psi_{(1,2)k}(x) &= \rho_{(1,2)A,k}\left(A_k^{+}e^{i\beta_{A,k}(x-x_k)} + A_k^{-}e^{-i\beta_{A,k}(x-x_k)}\right)\\ &+ \rho_{(1,2)B,k}\left(B_k^{+}e^{i\beta_{B,k}(x-x_k)} + B_k^{-}e^{-i\beta_{B,k}(x-x_k)}\right)\\ &= A_k^{+}\eta_{(1,2)A+,k}(x) + A_k^{-}\eta_{(1,2)A-,k}(x)\\ &+ B_k^{+}\eta_{(1,2)B+,k}(x) + B_k^{-}\eta_{(1,2)B-,k}(x)\end{aligned} \tag{2.4}$$

where $\beta_{(A,B),k}$ and $[\rho_{1,(A,B),k}\ ,\ \rho_{2,(A,B),k}]$ are the eigenvalue and normalized eigenvector of each supermode (A,B) which can be derived in the k^{th} unit cell from Eq. (2.2), and x_k is the left side position of the cell. From the continuity condition of the wave across the boundary ($\psi_{(1,2)k}=\psi_{(1,2)k+1}$, $\partial_x\psi_{(1,2)k}=\partial_x\psi_{(1,2)k+1}$ for both waveguide 1 and 2), the transfer matrix M_k for $v_{k+1}=M_k\cdot v_k$ is obtained as $M_k=C_{k+1}(x=x_{k+1})^{-1}C_k(x=x_{k+1})$, where

$$C_k = \begin{bmatrix} \eta_{1A+,k} & \eta_{1A-,k} & \eta_{1B+,k} & \eta_{1B-,k} \\ \eta_{2A+,k} & \eta_{2A-,k} & \eta_{2B+,k} & \eta_{2B-,k} \\ i\beta_{A,k}\eta_{1A+,k} & -i\beta_{A,k}\eta_{1A-,k} & i\beta_{B,k}\eta_{1B+,k} & -i\beta_{B,k}\eta_{1B-,k} \\ i\beta_{A,k}\eta_{2A+,k} & -i\beta_{A,k}\eta_{2A-,k} & i\beta_{B,k}\eta_{2B+,k} & -i\beta_{B,k}\eta_{2B-,k} \end{bmatrix}. \quad (2.5)$$

In the problems of Hermitian Hamiltonians, the S-matrix S_k can be obtained by rearranging the transfer matrix relation, where the scattered output field vector $u^O{}_k = [A_k^-, B_k^-, A_{k+1}{}^+, B_{k+1}{}^+]^T$ is related to the input vector $u^I{}_k = [A_k{}^+, B_k{}^+, A_{k+1}{}^-, B_{k+1}{}^-]^T$ by $u^O{}_k = S_k \cdot u^I{}_k$. The wave propagation along the coupled waveguides of $\lambda_1(x)$ can then be solved using $M_{tot} = M_n M_{n-1} \cdots M_1$, and its scattering matrix representation. However, for non-Hermitian Hamiltonians with complex potentials, S-matrix formulation is different from the above formulation [66]: the matrix formulation should be modified to prevent diverging exponential terms.

It should also be noted that special attention is needed in the treatment of the EP. At the EP, as supermodes coalesce (A_k=B_k), and since waveguides are effectively decoupled, the amplitude vector needs to be redefined for each waveguide as $v_k = [A^1{}_k{}^+, A^1{}_k{}^-, A^2{}_k{}^+, A^2{}_k{}^-]^T$ to maintain the same degrees of freedom (e.g., $k+1^{th}$ cell in Fig. 2.5a). From the S-matrix analysis, we can now relate the EP and the associated intermodal asymmetry to parameters of the *unit cell* at the EP. Worth mentioning that the effective decoupling will be the basis of novel phenomena (such as drastic asymmetric transfer and inverted PT symmetry) in *N*-atomic PT-symmetric molecule in section 2.2.2.

For the case of slowly-varying potential (effective index of a single uncoupled waveguide is $n_{r0}(x) = 2 + x/100$, x in μm) with $\kappa = 0.02 \cdot k_0$ (k_0: free space wave number), the CMT-obtained spatial EP ($\lambda_1(x_{EP}) = 0$, arrow), and the S-matrix-calculated power evolution are shown in Fig. 2.5b and 2.5c, comparing the Hermitian ($n_{i1,2} = 0$) and PT-symmetric ($n_{i1,2} = -/+0.006 \cdot n_{r0}(x)$) waveguides. We note the behavior of λ_1 around the spatial EP (Fig. 2.5b) which describes the variation of

the degree of PT symmetry (at y=0) along the x axis. Prior to the spatial EP obtained from the CMT, λ_1 being real describes the effective coupling and allows *Hermitian-like* power exchange between waveguides (Fig. 2.5c). Meanwhile, after the spatial EP, λ_1 being imaginary affects the absorption coefficient ($\alpha_{A,B}=\lambda_0 \pm Im(\lambda_1)$) and enables PT-*like* power amplification of the supermode. We stress that this sharp *spatial phase transition* across the spatial EP for a spatially varying $\lambda_1(x)$ is in sharp distinction when compared to the cases of a Hermitian or a *uniform* PT (λ_1 = constant; $n_{r0} = 3.4$, $n_{i1,2} = -/+ 0.006 \cdot n_{r0}$) (Fig. 2.5b,2.5c, left).

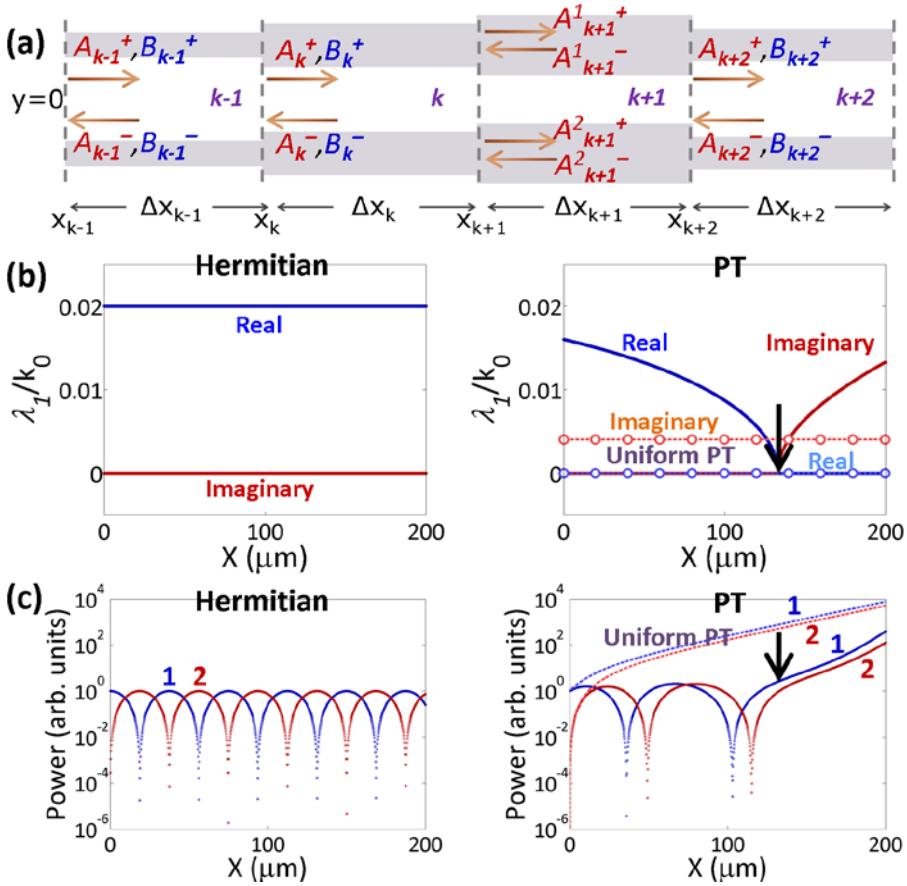

Figure 2.5. Wave dynamics in spatially-varying PT-symmetric potentials [44]. (a) Schematics of the spatially varying potential. (A_k , B_k) denote the field amplitude of supermode (A,B) in k^{th} segment, where +/- sign represents the propagation direction. (b) Spatial evolution of λ_1 (normalized to k_0; blue: Re[λ_1/k_0]; and red: *Im*[λ_1/k_0]). (c) Spatial evolution of power in waveguide 1 (blue) and 2 (red). Cases of Hermitian ($n_{i1,2}$ = 0) and uniform PT potential (n_{r0} = 3.4, $n_{i1,2}$ = -/+0.006·n_{r0}) are compared to the spatially-varying PT structure ($n_{r0}(x)$ = 2+x/100). Black arrows mark the spatial EP from the CMT. The wave is excited at waveguide 1 (marked in blue). f_0=200THz and the unit cell length Δx=200nm.

The behavior of a PT-induced EP, now with a *spectrally varying* λ_1, is investigated through the relation of $\lambda_1 = \lambda_1(\kappa(\omega))$ by employing a dispersive

potential made of dielectric nanopillar waveguides [67]. Figure 2.6a shows the dispersion relation of Hermitian coupled waveguides. For reference, since the 3rd supermode has a dipolar field in each nanopillar which is orthogonal to the first 2 supermodes (monopole), the coupling to the 3rd mode can be neglected. Approaching the band edge ($\beta_{r0}=\pi/\Lambda$), as coupling between waveguides becomes weaker with the reduced mode-envelop decay length $\delta \sim 1/\beta_{r0}$ (Fig. 2.6b), the two supermodes are *nearly* degenerate. For comparison, Figs. 2.6c,d show the spectral behavior of the EP in passive *dispersive* PT structures (n_{i1}=0, n_{i2}=0.02) of coupled nanopillar waveguides. Similar to the case of the spatial EP ($\lambda_1(x_{EP}) = 0$), *a sharp phase transition* across the *spectral* EP ($\lambda_1(\omega_{EP}) = 0$, green arrows, Figs. 2.6c and 2.6d) was observed. In a low-frequency regime prior to the spectral EP, the effective index difference between supermodes $\Delta n_{eff} = (\beta_A - \beta_B)/k_0$ having a real term, allows *Hermitian-like* coupling between waveguides. We note that when increasing the frequency, for the *dispersive* PT, the band coalesce ($Re(\Delta n_{eff}) = 0$) occurs *before* the band edge but *at the spectral EP* ($\lambda_1(\omega_{EP}) = 0$), in sharp contrast to Hermitian structures where the bands asymptotically approach a degenerate point *at* the band edge. Passing the spectral EP and entering into a high-frequency regime, a discontinuous and sharp increase in $Im(\Delta n_{eff})$ promotes PT-*like* differential loss between supermodes. It is worth noting that as $\partial_\omega\kappa(n_{r0}) >> \partial_\omega\beta$ for the dispersive PT structure (Fig. 2.6b), the transition between Hermitian- and PT-operation with the control of the *real part* of the index n_{r0} (or pillar size, Fig. 2.6c,2.6d), instead of the conventional tuning of *imaginary* index n_i [41, 43, 57, 59], should be possible.

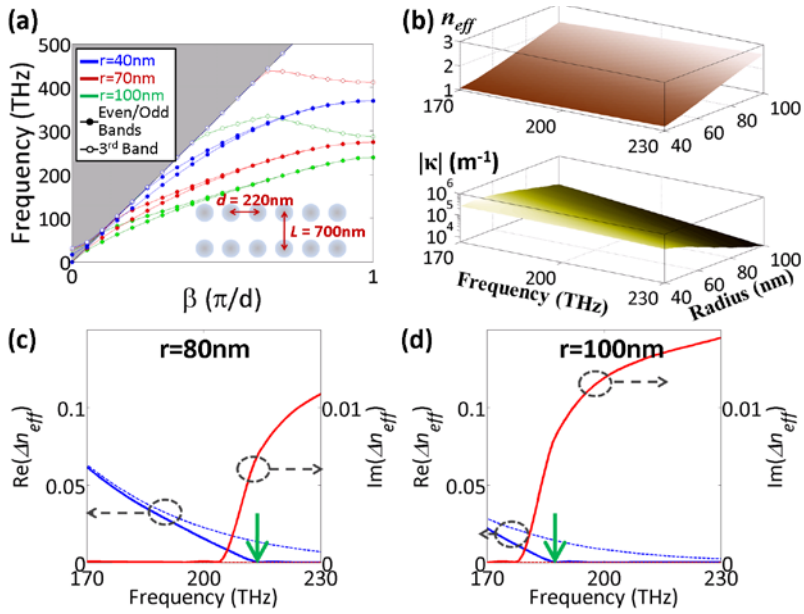

Figure 2.6. Wave dynamics in spectrally-dispersive PT-symmetric potentials [44]. (a) Dispersion curves of coupled nanopillar waveguides in air. Pillar radius r = 40 nm (blue, upper); 70 nm (red, middle); and 100 nm (green, lower). L = 700 nm; d = 220 nm; and pillar index n_r = 3.5. (b) Effective index of a waveguide n_{eff} and coupling coefficients between waveguides as a function of frequency and radius. (c,d) Difference of effective index Δn_{eff} (blue: real-part; red: imaginary-part) between supermodes in coupled nanopillar waveguides (c: r = 80 nm; d: r = 100nm). Cases of Hermitian (dotted lines, $n_1 = n_2 = 3.5$) and passive PT-symmetric (solid lines, $n_1 = 3.5$, $n_2 = 3.5+i\cdot0.02$) potentials are compared. Green arrows denote the spectral EP as obtained analytically from the CMT. All results are obtained with COMSOL Multiphysics, by applying Floquet-Bloch boundary conditions for the in-plane TE polarization.

Chirped optical (Rainbow) potentials [68-71] have been one of the foci of recent research efforts in photonic crystals [68], metamaterials [69, 70], and plasmonics [71]. Constructed of a dispersive waveguide with adiabatic spatial variation, the rainbow structure (here, as a pair) provides an ideal test-bed for the

impact of generalized interaction parameters $\lambda(x,\omega)$ in PT symmetry. Figures 2.7a and 2.7b show the schematics and numerically-calculated structural parameters (n_{eff} = β_{r0}/k_0, κ/k_0) of a PT-symmetric rainbow potential constructed of nanopillar waveguides. It is worth mentioning that care was taken in the design of the adiabatic potential (∂_x $(1/\beta_{r0})$ ~0.01 << 1, [72]) to achieve an ideal (~0.99) throughput. Shown in Fig. 2.7c–2.7e are the evolution of effective indices $n_{eff}^{A,B}(x)=\beta_{A,B}/k_0$ for supermodes along the PT chirped potential. After the Spatio-Spectral EP ($\lambda_1(x_{EP}, \omega_{EP}) = 0$), the position *and* wavelength dependent split of each supermode is evident, as can be seen from $Im(n_{eff})$. The interaction parameter for band repulsion $\lambda_1(x, \omega)$ is also plotted in Fig. 2.7f as a function of position and frequency. The spatial EP x_{EP} and spectral EP ω_{EP} interrelated by $\lambda_1(x_{EP}, \omega_{EP}) = 0$ form the "rainbow EP", which has to be defined in *two*-dimensional parameter space. We note that this *Spatio-Spectral* dependency of λ_1 also enables the "rainbow intermodal asymmetry". From the S-matrix calculation, the intermodal coupling between supermodes (*A*,*B*) can be calculated at each cell boundary, to establish the degree of intermodal asymmetry. Figure 2.7g shows the intermodal asymmetry factor ($|S_{32}/S_{41}|^2$, S_{32}: $B_{k-1}^{+} \rightarrow A_k^{+}$, S_{41}: $A_{k-1}^{+} \rightarrow B_k^{+}$) across the cell boundary, *quantitatively*-evaluated for the first time in this paper, using the S-matrix approach.

In a Hermitian structure with mutually-orthogonal supermodes, the coupling between supermodes is naturally prohibited, as $S_{32} = S_{41} = 0$. In contrast, $S_{32} \cdot S_{41} \neq 0$ is achieved for the PT-symmetric potential, where the intermodal coupling between skewed supermodes exists. For the rainbow PT structure, both the PT-like asymmetry $|S_{32}/S_{41}|^2 \neq 1$ and Hermitian-like symmetry $|S_{32}/S_{41}|^2 = 1$ exist, each regime respectively being defined in the two-dimensional parameter space by the locus of ($x = x_{EP}$, and $\omega = \omega_{EP}$) (Fig. 2.7g, dotted line). In short, the locus of EP defines the transition boundary between real (symmetric modal coupling) and complex (asymmetric modal coupling) phase, which is set by the spatial / spectral dispersion. It is also notable that the increase of asymmetry factor $|S_{32}/S_{41}|^2 >> 1$ in

the PT-like regime implies that the dominant mode of this regime is the low-loss supermode *A*.

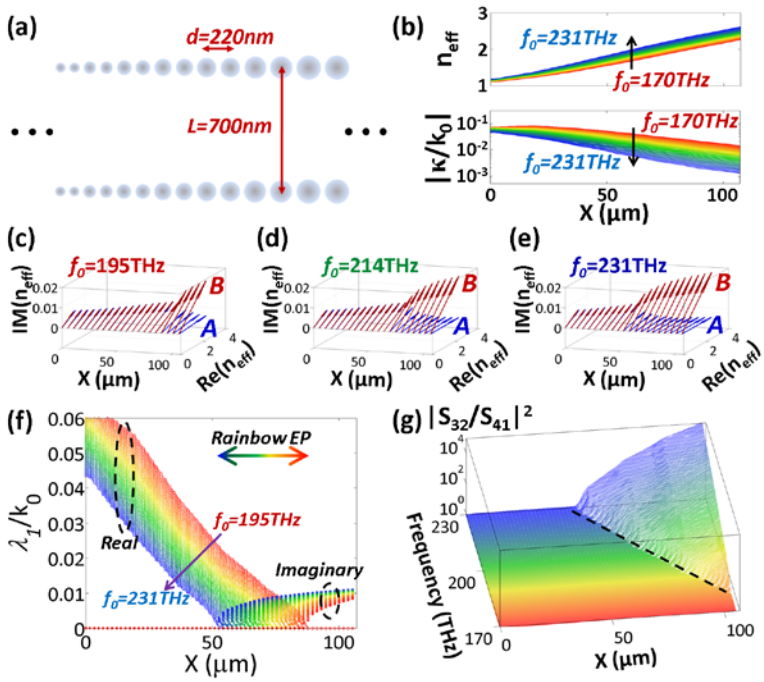

Figure 2.7. Wave dynamics in rainbow PT-symmetric potentials [44]. (a) Coupled nanopillar waveguides for the PT chirped potential (n_r = 3.5; n_{i1} = 0; and n_{i2} = 0.02). The pillar radius *r* increases from 40 nm to 100 nm. *r* = 1*nm* per unit cell (each cell composed of 8 identical pillars). (b) The spatial distribution of $n_{eff} = \beta_{r0}/k_0$ and κ/k_0 plotted for frequencies from 170THz (red) to 231THz (blue). (c–e) Evolution of modal indices $n_{eff}^{A,B} = \beta_{A,B}/k_0$ for supermodes at different frequencies, along the PT chirped potential. The blue and red arrows each represent low- (*A*) and high- (*B*) loss supermode. (f) Evolution of the interaction parameter λ_1/k_0 from 195 THz (red) to 231THz (blue). Points of $\lambda_1 = 0$ define Spatio-Spectral EPs (x_{EP}, ω_{EP}). (g) Asymmetry factor for intermodal coupling $|S_{32}/S_{41}|^2$ between supermodes *A* and *B*. The dotted line represents the locus of Spatio-Spectral EPs (x_{EP}, ω_{EP}). All results are obtained with COMSOL Multiphysics.

Intermodal asymmetry can be transformed into the port-to-port asymmetry with the skewness of supermodes, as shown in a uniform PT potential. From the intermodal asymmetry, the dominantly excited port is determined only by the skewness of dominant supermode. Figures 2.8a,b show the skewness of supermodes $|A^1{}_k{}^+/A^2{}_k{}^+|^2$ and $|B^1{}_k{}^+/B^2{}_k{}^+|^2$ (1 and 2 denote the waveguides) for a PT-symmetric rainbow potential. Modal skewness ($|A^1{}_k{}^+/A^2{}_k{}^+|^2 \neq 1$, $|B^1{}_k{}^+/B^2{}_k{}^+|^2 \neq 1$) is observed in the PT-like regime ($x > x_{EP}$, $\omega > \omega_{EP}$); while in the Hermitian-like regime, the symmetry ($|A^1{}_k{}^+/A^2{}_k{}^+|^2 = 1$, $|B^1{}_k{}^+/B^2{}_k{}^+|^2 = 1$) is evident. The direction of skewness for supermode *A* and *B* ($|A^1{}_k{}^+/A^2{}_k{}^+|^2 > 1$, $|B^1{}_k{}^+/B^2{}_k{}^+|^2 < 1$) also shows that lossless (or lossy) waveguide 1 (or 2) will be dominantly excited for low- (or high) loss mode *A* (or *B*). Figures 2.8c–2.8f show the port-to-port asymmetric propagation for the PT-symmetric rainbow potential. As can be seen, comparing the cases of wave input to lossless- port 1 (Fig. 2.8c,e) and the lossy-port 2 (Fig. 2.8d,f), PT-like asymmetric wave propagation is observed after the spatial EP (black-dotted line), in contrast to Hermitian-like, symmetric wave propagation prior to the spatial EP. Note that dominantly-excited port (waveguide 1) after the EP is determined only by the skewness of supermode *A*. With the strong spectral and spatial dependency of the EP, different degrees of asymmetry can be achieved for different input frequencies (Fig. 2.8c and 2.8d vs. Fig. 2.8e and 2.8f) for a fixed structure, or for a fixed input frequency, with different waveguide designs.

In this section we presented a generalization to PT- symmetry physics by introducing a multi-dimensional interaction parameter λ_1, and have investigated its impact on the behavior of EPs and intermodal asymmetry [44]. Depending on the functional dependency of λ_1 upon space (x) and/or frequency (ω), it is shown that a sharp phase transition between Hermitian-like and PT-like behavior across the spatial- and/or spectral-EP (x_{EP}, ω_{EP}) results, in contrast to the case of constant λ_1. Applying PT symmetry to the case of a chirped optical potential, a rainbow-like spatio-spectral separation of EP is achieved, enabling port-to-port asymmetry with two degrees of freedom (x,ω). The intermodal asymmetry was derived for the first

time, *quantitatively*, from the S-matrix method. We believe these results can be applied directly to electric potentials from the similarity between the Schrodinger and paraxial wave equations, and by establishing the generalized definition of an EP, we envisage more wide-open applications of PT symmetry in diverse platforms and spectra, such as one-way devices using optical nonlinearity based on slow light structures (see section 4.3.4).

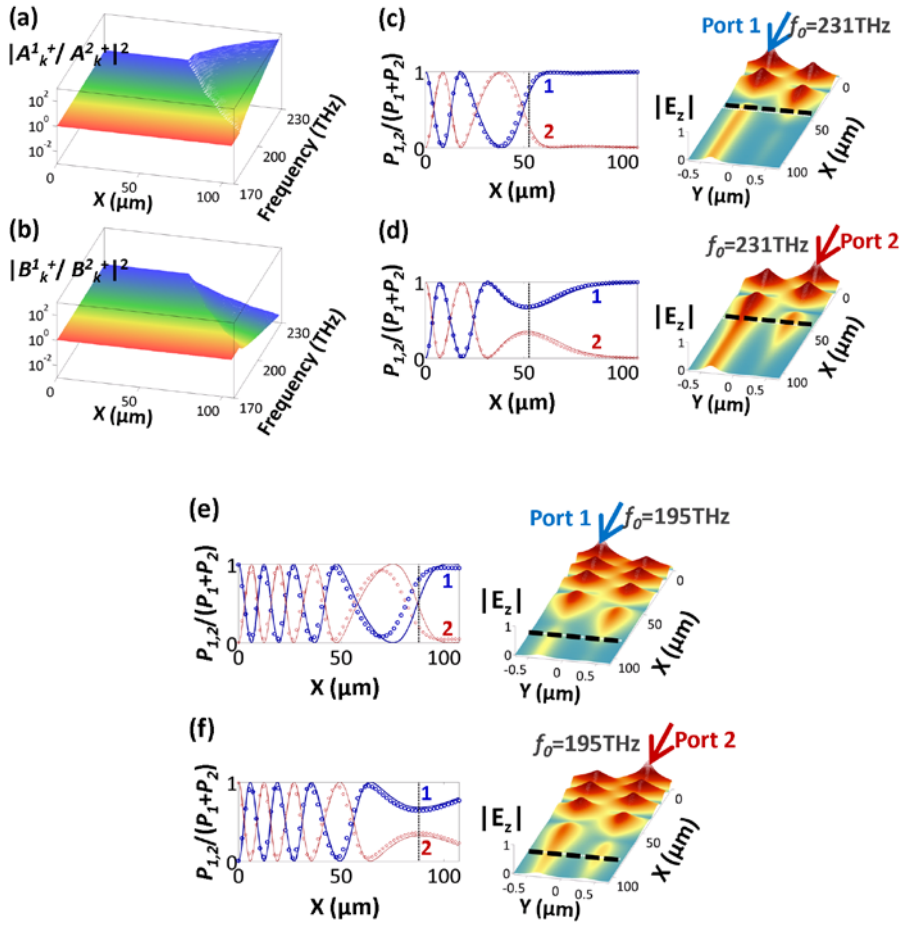

Figure 2.8. Propagation features along rainbow PT-symmetric potentials [44]. Skewness of supermodes in the PT-symmetric rainbow potential: for supermode (a) *A* (low loss) and (b) *B* (high loss). The evolution of power ratio and the field amplitudes are shown for different excitation frequencies of (c, d) 231 THz and (e, f) 195 THz, and for different input excitation ports (blue: lossless waveguide 1 and red: lossy waveguide 2). EPs are marked with black lines. Theoretical (S-matrix analysis, Lines) and numerical (COMSOL, symbols) results are overlaid with excellent fit, showing asymmetric wave propagation along the potential. To minimize the reflection at the input port, all sources of COMSOL simulation are given by the eigen-modal field obtained from COMSOL eigenvalue results in Fig. 2.6.

2.2.2 *N*-level photonic molecule

To achieve novel optical functionalities overcoming basic features of isolated optical elements, the physics of *meta-molecules* has become a topic of intensive research (Fig. 2.9) [73-77]. A range of novel phenomena, originating from collective interactions between the constituent *meta-atoms* placed in close proximity with each other, have been demonstrated in acoustics [78, 79], quantum mechanics [80, 81], and optics [73-75]. For example, molecular modal properties have been investigated as a pathway to meta-materials with exotic refractive index upon the appropriate design and arrangement of photonic meta-atoms [82]. Yet, while such meta-molecular phenomena arising solely due to the passive interaction between meta-atoms is interesting in itself, a whole new range of phenomena is revealed when *complex* potentials (or refractive index $n=n_r+in_i$) with gain or loss are introduced.

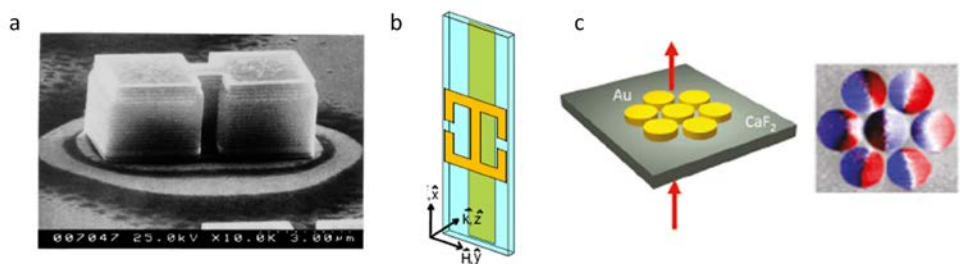

Figure 2.9. Examples of photonic molecules for novel optical functionalities: (a) coupled resonators for optical supermodes [75], (b) perfect absorbing meta-molecules composed of electric and magnetic meta-atoms [74], and (c) Fano meta-molecules composed of coupled plasmonic dipoles [73].

Notably, strong intermodal asymmetry has been demonstrated around the EP in a photonic molecule composed of two atoms (N=2, section 2.2.1). Extending this concept into multi-level (N>2) meta-molecular systems has further led to the discovery of a range of interesting behaviors - including unidirectional invisibility [58, 59], double refraction [57], an optical tachyon [83], and solitons [84] – all the

while focusing on the dynamics of *completely broken* PT symmetry where all eigenvalues are complex. Yet, not only does this completely complex eigenvalue regime ignore states of partial collapse of PT symmetry, but it relies on large values of gain and large device footprints that would hinder the practical realization of feasible devices.

In this section, we investigate the intermodal asymmetry of complex meta-molecules [46], including the unexplored regime of phase co-existence; where the real and complex phases co-exist in a partially collapsed PT-symmetry. Contrary to the intuitive expectation, we demonstrate that the rapidity of onset of asymmetry is drastically increased, not in the entirely complex phase regime with the largest modal skewness, but in the real-complex phase coexistent regime, at significantly reduced imaginary value of potential (i.e. gain and loss). We explain this paradoxical behavior through the concept of '*spatial trapping modes*' which support complex eigenvalues and atomized modal profiles (with negligible effective coupling between waveguides), resulting in the hindrance of the energy transfer within the molecule. From the condition of PT symmetry for each trapping mode, we also demonstrate *reversible asymmetry* – control over the directionality of spatial asymmetry – simply by removing the imaginary potential of two meta-atoms: demonstrating the competition between local and global PT symmetry.

As an example platform, we consider individual optical waveguides as 'atoms' arranged in a periodic array that forms a meta-molecule (waveguide array). Figure 2.10a shows an example of a PT-symmetric meta-molecule with an odd number N of atoms characterized by either gain ($n_i<0$), loss ($n_i>0$), or normal ($n_i=0$) waveguides arranged such that $n(y) = n^*(-y)$ along the direction perpendicular to the waveguide axes. As in previous works [41, 43, 57], the imaginary part of n is assumed to be much smaller than the real part of n, allowing the use of the conjugated form of reciprocity theory for the modal coupling. In practice, control over the gain and loss of individual waveguides could be achieved through spatial modulation of the optical pump intensity [43]. The governing equation based on the

coupled mode theory for this molecule with identical nearest-neighbor coupling κ_o between atoms is:

$$\frac{dA_N}{dx} = i\beta_N^T I_N A_N + i\kappa_o C_N A_N, \tag{2.6}$$

where β_N and A_N are column vectors with their m-th component being the wavevector and field amplitude of the m-th atom ($[\beta_N]_m=\beta_m$, $[A_N]_m=a_m$) respectively, I_N is the identity matrix, and C_N is the nearest-neighbor coupling matrix ($C_{N(p,q)}=1$ for $|p-q|=1$, $C_{N(p,q)}=0$ otherwise, $1\le p,q\le N$). Postulating the solution $A_N(x)=A_N(0)\cdot e^{i\beta x}$ of the eigenvalue β, Eq. (2.6) may be cast in the form of the eigenvalue equation as,

$$\beta I_N A_N = \beta_N^T I_N A_N + \kappa_o C_N A_N. \tag{2.7}$$

Equation (2.7) can be expressed as $M_N A_N=0$, where the tri-diagonal matrix $M_N = (\beta-\beta_N^T)I_N-\kappa_o C_N$ has components of $M_{N(p,p)} = \beta-\beta_p$, $M_{N(p,q)} = -\kappa_o$ for $|p-q|=1$, and $M_{N(p,q)} = 0$ otherwise. If identical atoms are assumed ($\beta_p = \beta_0$), the determinant of the tri-diagonal matrix M_N has the following recurrence relation,

$$\det(M_N) = (\beta-\beta_0)\cdot\det(M_{N-1}) - \kappa_o^2\cdot\det(M_{N-2}) \tag{2.8}$$

Utilizing the above relation, the characteristic equation for identical atoms ($\beta_p = \beta_0$) can be expressed as (See Appendix A),

$$\prod_{s=1}^{N}\left[(\beta-\beta_0) - 2\kappa_o\cos\frac{s\pi}{N+1}\right] = 0, \tag{2.9}$$

where the solutions are given by $\beta_s=\beta_0+2\kappa_o\cos(s\pi/(N+1))$ with each s representing one of the N number of supermodes (each supermode defined as an individual eigenmode of the entire meta-molecule). Since $\cos[s\pi/(N+1)] = -\cos[(N+1-$

$s)\pi/(N+1)]$, there exists $[N/2]$ pairs of β-$\beta_0\pm 2\kappa_0\cdot\cos[s\pi/(N+1)]$ in the product terms of Eq. (2.9). In this regard, it is illustrative to express Eq. (2.9) as,

$$(\beta-\beta_0)^{N(\mathrm{mod}\,2)}\cdot\prod_{p=1}^{[N/2]}\left[(\beta-\beta_0)^2-4\kappa_o{}^2\cos^2\frac{p\pi}{N+1}\right]=0, \qquad (2.10)$$

where the eigenvalues with smaller p evidently support a larger deviation from the intrinsic atomic eigenvalue β_0 (due to $\cos(p_1\pi/(N+1)) > \cos(p_2\pi/(N+1))$ when $1 \le p_1 < p_2 \le [N/2]$).

From Eq. (2.10), the solution for a PT-symmetric meta-molecule can be derived. The matrix M_N for the odd number N-atomic PT-symmetric molecule has components of $M_{N(p,p)} = \beta$-β_{r0}+$i\cdot(-1)^{|(p-[N/2]-1)|(\mathrm{mod}2)}\cdot\beta_{i0}$ for $p<[N/2]+1$, $M_{N(p,p)} = \beta$-β_{r0}-$i\cdot(-1)^{|(p-[N/2]-1)|(\mathrm{mod}2)}\cdot\beta_{i0}$ for $p>[N/2]+1$, $M_{N(p,p)} = \beta$-β_{r0} for $p=[N/2]+1$, $M_{N(p,q)} = -\kappa_o$ for $|p-q|=1$, and $M_{N(p,q)} = 0$ otherwise, where β_{r0} and $\pm\beta_{i0}$ are the real and imaginary parts of the wavevectors of the isolated atoms. In this case, the term $(\beta-\beta_0)^2$ in Eq. (2.10) becomes $|\beta-\beta_{r0}+i\beta_{i0}|^2$ such that (See Appendix A),

$$(\beta-\beta_{r0})^{N(\mathrm{mod}\,2)}\cdot\prod_{p=1}^{[N/2]}\left[\left|\beta-\beta_{r0}+i\beta_{i0}\right|^2-4\kappa_o{}^2\cos^2\frac{p\pi}{N+1}\right]=0. \qquad (2.11)$$

Equation (2.11) gives sets of eigenvalues and the conditions of EPs for the PT molecule. The eigenvalues are classified as $[(N+1)/2]$ sets by their deviations from the atomic state β_{r0}. In contrast to purely real solutions in Eq. (2.9), the $[N/2]$ eigenvalue sets, consisting of pairs $\beta_p=\beta_{r0}-\lambda_p$ and $\beta_q=\beta_{r0}+\lambda_p$ ($p<q$, $p+q=N+1$) except one permanently real eigenvalue ($\beta=\beta_{r0}$), are real if $\lambda_p{}^2>0$ and complex if $\lambda_p{}^2<0$, where the interaction parameter λ_p defining the EP is,

$$\lambda_p=\left(4\kappa_o{}^2\cos^2\frac{p\pi}{N+1}-\beta_{i0}{}^2\right)^{\frac{1}{2}}. \qquad (2.12)$$

Equation (2.12) shows that the condition of the EP (λ_p=0) for (β_p,β_q) varies dependent on p as $\cos[p\pi/(N+1)]=|\beta_{i0}/(2\kappa_o)|$. This originates from the variation of effective coupling $\kappa_{eff}=\kappa_o\cos(p\pi/(N+1))$, depending on the modal index p and corresponding molecular mode profile. Strong interaction between atoms (small p) provides increased deviation from the original mode and thus is more robust to the onset of PT symmetry collapse (requiring an increased β_{i0}). We further point out that due to only the square of β_{i0} entering Eq. (2.12), an identical set of eigenvalues is also obtained for the inverted sign of β_{i0} ($n_{GL\text{-}inverted}(y)=n^*(y)$), which follows directly from the mirror symmetric arrangement of the PT potential ($n_{GL\text{-}inverted}(y)=n^*(y)=n(-y)$).

Figures 2.10b (2.10c) presents the real (imaginary) parts of eigenvalues for an N=23 molecule, demonstrating the phase transition of eigenvalues from the real to the complex phase. As the interaction parameter λ_p changes from a real to an imaginary value with the increase of β_{i0}, the real part of eigenvalues coalesce sequentially (in order of decreasing p from 11 to 1, Fig. 2.10b) to β_{r0}, while the imaginary part splits with a same magnitude though opposite sign for each eigenvalue in a given (p,q) pair (compare curves 11-1 with curves 13-23 in Fig. 2.10c). Consequently, the number of real eigenvalues is reduced to N-2, N-4, …, 1 as the EPs are sequentially crossed (when each Re(λ_p) = 0). The resulting pairs (p,q) of complex eigenvalues support different amplifying (p) and decaying (q) levels (Im(λ_p)) that become saturated with further increase in β_{i0}. It is important to note that there is the regime of *phase coexistence* between λ_1=0 and $\lambda_{[(N+1)/2]}$=0, which supports the coexistence of both real and complex eigenvalues.

The asymmetry of the PT-symmetric potential around the EP is characterized not only by the phase transition of eigenvalues but also by modal skewness which allows the inter-modal coupling between mutually non-orthogonal supermodes. Figures 2.10d-10f shows the intensity distribution of amplifying supermodes in the PT-symmetric meta-molecule (N=23) obtained from substitution of a particular β_p into M_NA_N=0 (for reference, the intensity profile of each decaying mode has mirror

symmetry with the corresponding amplifying mode). As can be seen, all supermodes except that with a permanently real eigenvalue ($\beta=\beta_{r0}$, Fig. 2.10f) exhibit asymmetric intensity distributions after the EP. The degree of skewness shows strong modal dependency according to the difference in effective coupling κ_{eff} (Fig. 2.10d,e). As p approaches $[N+1]/2$ where κ_{eff} is small, the PT symmetry becomes fragile, and the intensity of the supermode leans to the boundary of the molecule, deriving huge skewness. This p-dependent skewness is presented explicitly with the evolution of beam center of mass (CM) $\langle m\rangle=\Sigma_m m|a_m|^2/\Sigma_m|a_m|^2$ (Fig. 2.10g). We note that supermodes are transformed drastically after the EP, exhibiting *atomized intensity profiles* where the field becomes mainly localized to a particular gain (loss) atom characteristic to that particular amplifying (decaying) mode ($p<[N+1]/2$ for a gain atom and $p>[N+1]/2$ for a loss atom). Conversely, the spatial profiles of eigenmodes in the case of inverted sign of β_{i0} are mirror-symmetric to their original form (not shown).

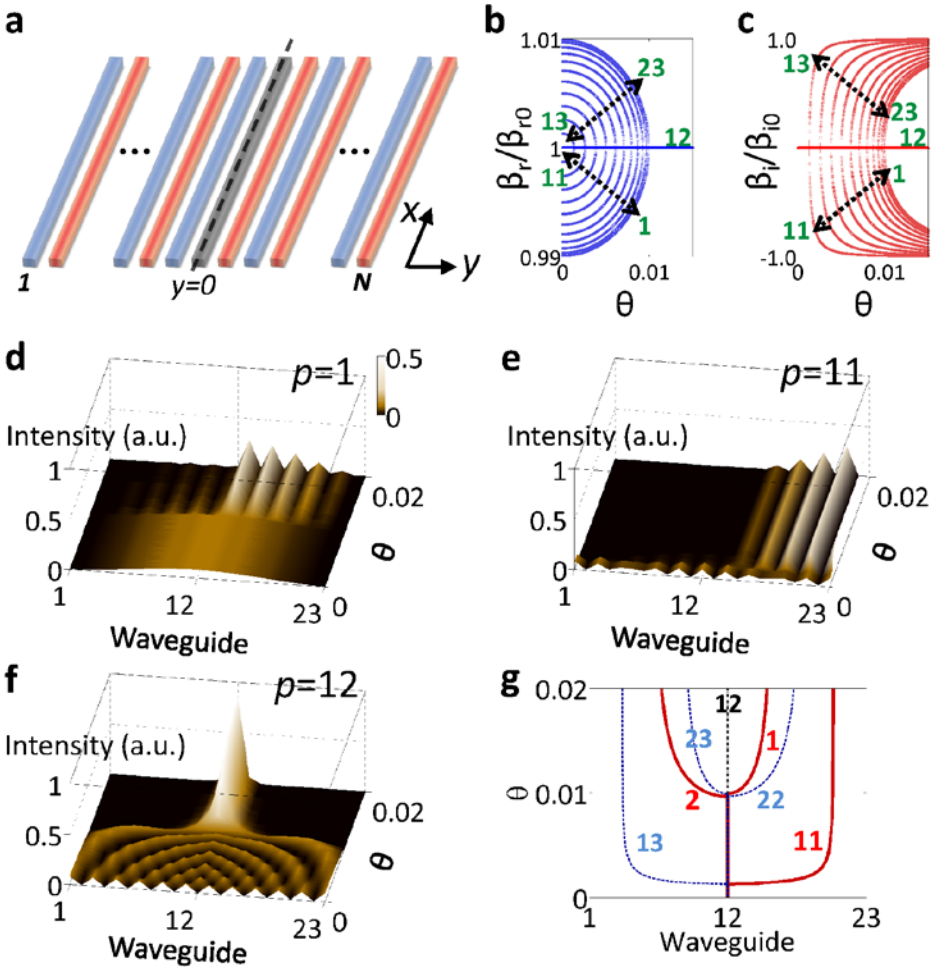

Figure 2.10. Eigenmodes in PT-symmetric metamolecules [46]. (a) Schematic of a PT-symmetric meta-molecule composed of an odd number N of atomic waveguides (corresponding to $\beta_{i0} > 0$; red: gain, blue: loss, gray: normal). (b) Real and (c) imaginary part of each eigenvalue for the PT meta-molecule as a function of the phase angle θ=arctan(β_{i0}/β_{r0}), for the case N=23. Curves from left to right correspond to decreasing value of p. Green labels denote the modal index p. The intensity distribution of supermodes in the PT meta-molecule (N=23) are shown as a function of θ, for (d) p=1, (e) p=11, and (f) p=12. (g) Beam center of mass of supermodes (red: gain mode, blue: loss mode). The coupling coefficient κ_o is $\beta_{r0}/200$.

To assess the dynamics of a PT molecule, the wave propagation is analyzed

with the S-matrix method [66]. For the potential composed of cascaded N-atomic molecules, the field in the m-th unit cell is expressed as,

$$\psi_m = \sum_{p=1}^{N} u_{p,m} \cdot \left[A_{p,m} e^{i\beta_p (x - x_m)} + B_{p,m} e^{-i\beta_p (x - x_m)} \right] = 0, \tag{2.13}$$

where $u_{p,m}$ and β_p are the eigenvector and the eigenvalue of the p-th supermode, $A_{p,m}$ (or $B_{p,m}$) is the amplitude of the forward (or backward) propagating wave, and x_m is the center position of the unit cell. From the boundary condition ($\psi_m = \psi_{m+1}$, $\partial_x \psi_m = \partial_x \psi_{m+1}$), the $2N \times 2N$ S-matrix is obtained. From the S-matrix it is possible to calculate the beam evolution in a PT meta-molecule (waveguide array) upon arbitrary excitation. Figure 2.11 shows the beam dynamics calculated by S-matrix, for the weakly (2.11a-2.11c, complex only for p=11) and strongly (2.11d-f, complex only for p=9–11) collapsed phase-coexistent molecules, as well as the entirely collapsed (2.11g-2.11i) molecule, under excitation of the central atom. Note that the required β_{i0} for varying degrees of collapse follows directly from the result presented in Fig. 2.10b,c. Asymmetric inter-modal coupling to the maximally amplifying mode (p=11) is clearly observed, in sharp contrast to the symmetric behavior in a real (or Hermitian) potential (Movie 1 in [46]).

The critical aspect to note here is the differing degrees to which the rapidity of asymmetry in propagation occurs among phase-coexistent and entirely collapsed molecules. For the entirely collapsed molecule with a large imaginary potential ($\beta_{i0} = 2\kappa_o$), there exist [N/2] number of amplifying supermodes each supporting modal skewness (Fig. 2.10g). As the beam CM of the dominant mode (p=11, maximally amplifying mode) lies furthest from the excited center atom, the beam should successively couple into all of the other amplifying modes (p=1–10, Fig. 2.11g) until its eigen-spectrum finally becomes dominated by the p=11 mode. Yet, due to their atomized intensity profile after the respective EPs, the inter-modal coupling between amplifying modes is much weaker than the coupling between modes of real phases (prior to their EP). Accordingly, these intermediate

amplifying modes act as *spatial trapping modes*, which hinder the efficient energy transfer within the molecule. Conversely, the more rapid asymmetric transfer with only a small imaginary potential ($\beta_{i0}=\kappa_o/2$) in the phase-coexistent molecule (Fig. 2.11c) can be explained by the absence of trapping modes, thus allowing for the p=11 mode to rapidly dominate the eigen-spectrum as compared to the gradual behavior of the entirely collapsed molecule (Fig. 2.11i). This phase-dependent asymmetry is apparent by comparing weakly- (Fig. 2.11a-2.11c) and strongly-collapsed (Fig. 2.11d-2.11f) molecules. It is important to note that the rapid asymmetric transfer is achieved in tandem with a reduction of the required gain; exceeding one order of magnitude in the case of an $N \geq 63$ molecule, the threshold values of β_{i0} given by $\sim 2\kappa_0 \cdot cos[\pi/2 - 2\pi/(N+1)]$ and $2\kappa_0 \cdot cos[\pi/(N+1)]$ for the phase-coexistent and entirely collapsed molecule respectively.

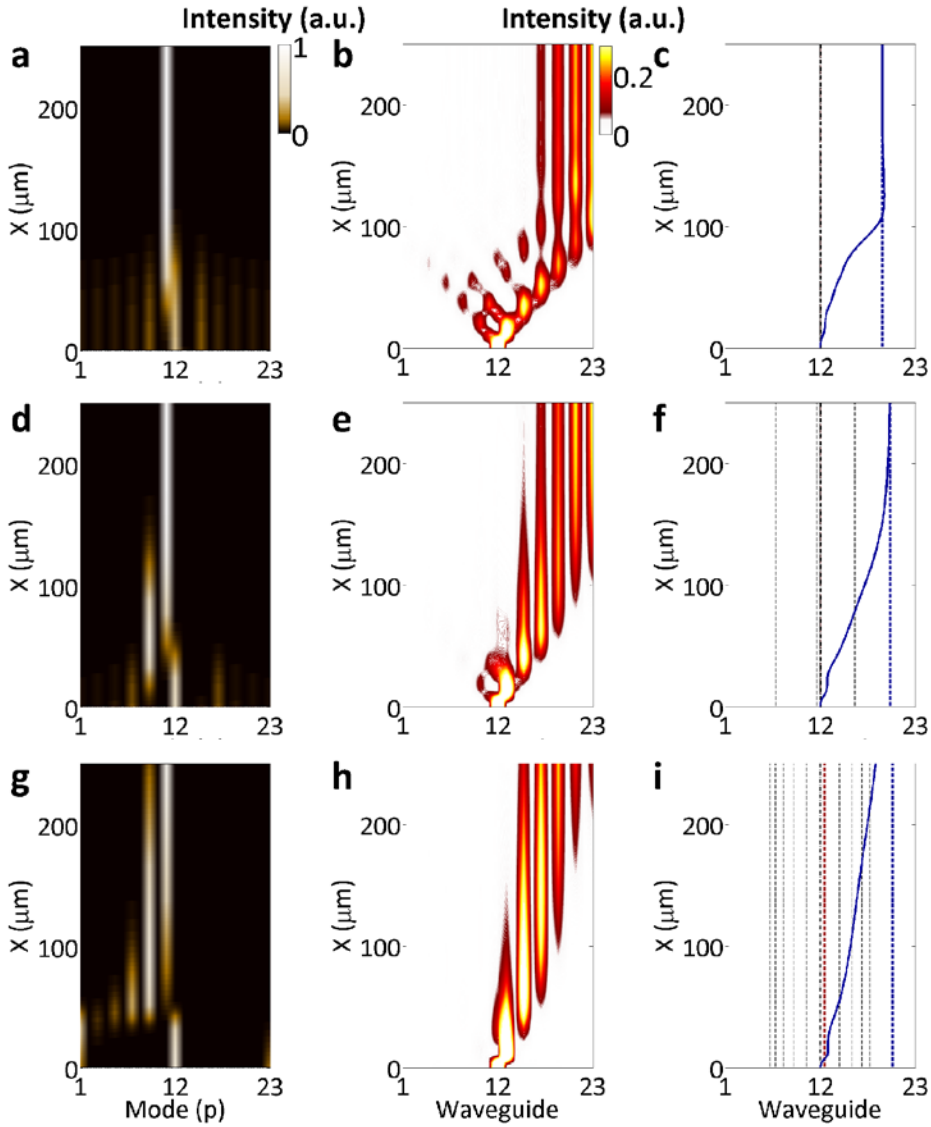

Figure 2.11. Propagation features in PT-symmetric metamolecules [46]. (a,d,g) Modal excitation, (b,e,h) beam propagation, and (c,f,i) evolution of beam CM (blue solid line) are presented for (a-c) p=11 complex ($\beta_{i0}=\kappa_o/2$), (d-f) p=9-11 complex phase-coexistent ($\beta_{i0}=\kappa_o$), and (g-i) entirely collapsed meta-molecules ($\beta_{i0}=2\kappa_o$). The field intensity in (b,e,h) is normalized across the waveguide array at each position (X). Blue and black dotted lines in (c,f,i) denote the dominant (p=11) and trapping (p=1–10) modes. The frequency f_0=193.4THz, $\beta_{r0}=3.5\cdot(2\pi f_0/c)$, and $\kappa_o=\beta_{r0}/200$.

Further, the phase-coexistent molecule in the absence of trapping modes (Fig. 2.11a-2.11c) provides the opportunity for flexible manipulation of asymmetry based on spatial variation of $\beta_{i0}=\beta_{i0}(x)$. In detail, while the phase-coexistent state itself provides a means of control over the relaxation of the non-reciprocity dynamics toward the dominant supermode (p=11), there is still lacking a mechanism through which the final extent of asymmetric transfer can be controlled. Here we demonstrate that spatially weighting the imaginary part of the molecular potential provides a route to flexible manipulation of asymmetric transfer in the phase-coexistent regime.

In Figure 2.12, we show the skewness of supermodes in a PT-symmetric meta-molecule with the potential adjustment. Figure 2.12a shows the multiplying factor applied to the imaginary part of the potential for a given atom in the molecule from Fig. 2.10. For the center-enhanced molecule (yellow in Fig. 2.12a), the intensity of supermodes (p=1,11,12) is shown in Fig. 2.12b-2.12d. While the supermode of robust PT symmetry with small $Im[\lambda_p/\beta_{r0}]$ (p=1) is skewed insignificantly in the case of uniform imaginary part of potential (unity weighting factor - Fig. 2.10d), the skewness of this mode increases drastically (Fig. 2.12b) in the center-enhanced imaginary potential, showing the modal energy concentrated in the region of low amplitude imaginary potential.

In contrast, though the dominant mode (p=11) leans to the outside immediately after the collapse, it is drawn again into the center region with increased amplitude imaginary potential (Fig. 2.12c). These results show that modes with smaller (or larger) imaginary effective index ($Im[\lambda_p/\beta_{r0}]$) tend to be pulled into the region with small (or large) imaginary potential. Also note that the center supermode (p=12, Fig. 2.12d) maintains spatial-symmetry regardless of the potential adjustment, as expected.

Figures 2.12e and 2.12f show the beam center of mass for the modified molecules of the center-enhanced (Fig. 2.12e) and side-enhanced (Fig. 2.12f)

imaginary potential. As can be seen, in the case of the large imaginary effective index of p=11, the skewness of the dominant mode (p=11) is intensified for the side-enhanced potential in contrast to the case of the center-enhanced potential, where remarkably there exists the regime of inverted skewness (where the beam center of mass shifts from right to left - Fig. 2.12e). In general, the loci of the beam center of mass for both cases can be changed dramatically compared to in Fig. 2.10i in the manuscript, considering that the gain or loss amplitude is changed by a factor of just 20% or less.

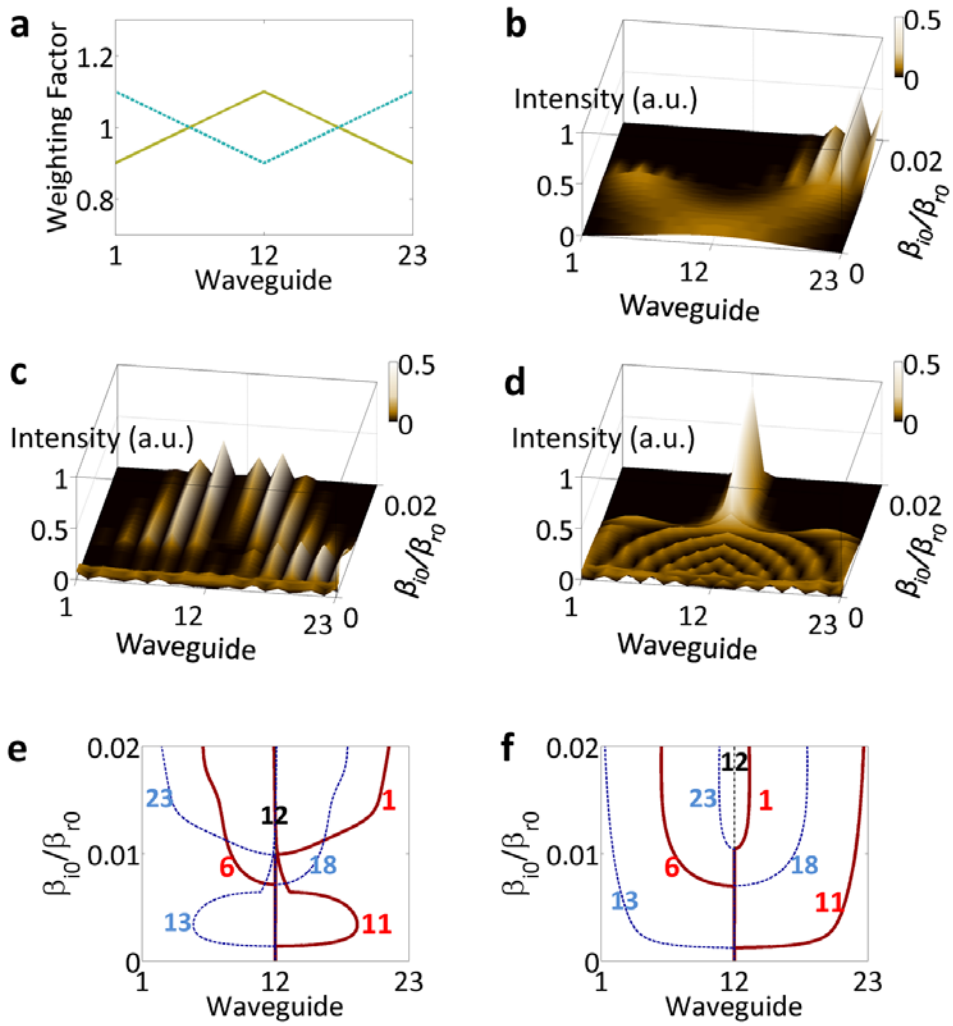

Figure 2.12. Eigenmodes tuned by the weighted imaginary potentials [46]: (a) Weighting factor applied to the imaginary potential (cyan and yellow: side-enhanced and center-enhanced imaginary potential). The intensity of supermodes with the center-enhanced weighting are presented for (b) p=1, (c) p=11, and (d) p=12. The beam centers of mass of supermodes are shown for the (e) center-enhanced and the (f) side-enhanced imaginary potential. $\kappa_o=\beta_{r0}/200$.

Figure 2.13 presents S-matrix calculations of the beam propagation along a dynamically center-enhanced molecule. For the sake of demonstrating more clearly the asymmetric transfer dynamics, the enhancement of the imaginary part of

potential is gradually introduced along the propagation direction (Fig. 2.13a). Further, the phase-coexistent state with only the collapse of the p=11,13 modes is selected to avoid the hindrance by spatial trapping states. The wave excited at the center exhibits an unconventional curved locus (Fig. 2.13b); strongly distinct from the previous works based on only plain asymmetry [41, 43, 44, 57]. This behavior can be attributed to the modal excitation in the PT-symmetric molecule (Fig. 2.13c). Along the x-axis, the supermode of p=11 is dominantly excited due to its largest gain. From the variation of the skewness of the p=11 mode by the potential adjustment (Fig. 2.12a), the beam evolution is altered (compare Fig. 2.11c in the manuscript and 2.13b). This effect is confirmed by the evolution of beam center of mass (Fig. 2.13b, blue solid line), compared with the modal center of mass in p=11 (blue dotted line).

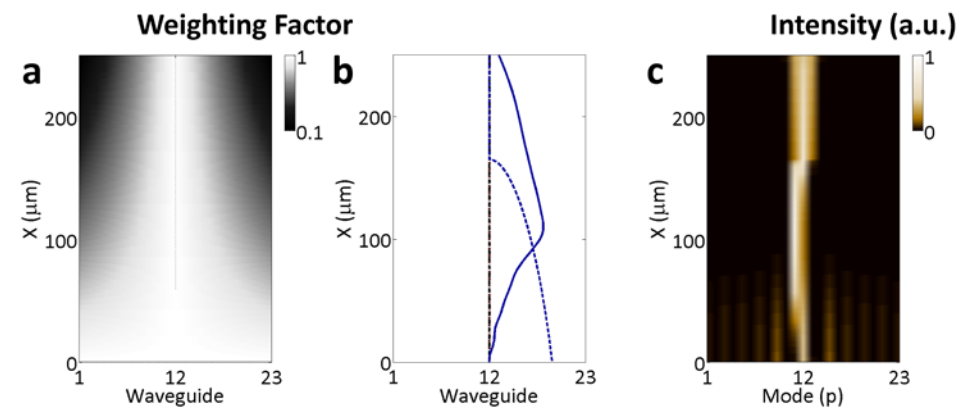

Figure 2.13. Beam evolution tuned by the weighted, spatially-varying imaginary potentials [46]: (a) Spatially-varying weighting factor for the imaginary potential. (b) The beam evolution along the dynamic meta-molecule excited at the center atom, expressed as the beam center of mass. Blue dotted line shows only the p=11 supermode. (c) Spatial variations of modal excitation. The imaginary potential of gain and loss atoms before the weighting is $\beta_{i0}=\kappa_o/2$, and the coupling coefficient κ_o is $\beta_{r0}/200$.

While a much higher degree of asymmetry is achieved in the *absence* of trapping modes, at the same time, the trapping modes provide a pathway to realize

the novel phenomenon of '*reversible asymmetric transfer*' based on the local inversion of PT symmetry. For example, consider the center nearest-neighbor trapping mode (p=1) which has the beam CM leaned to the right side (Fig. 2.10g). This skewness is determined mainly by the condition of PT symmetry in the center nearest-neighbor atoms ($\{[N+1]/2\pm1\}^{th}$ waveguides, Fig. 2.14a) due to the center-focused eigenmode (Fig. 2.10d). Therefore, by turning off the gain and loss (e.g. amplitude masking of the pump [43]) of the center nearest-neighbor atoms (Fig. 2.14b), the condition of PT symmetry for the center nearest-neighbor trapping mode is inverted (which is determined by the arrangement of center next-nearest-neighbor atoms of $\{[N+1]/2\pm2\}^{th}$ waveguides), deriving a reversal of skewness.

Eigenvalues and the evolution of beam CM of the inverted PT meta-molecule are shown in Fig. 2.14c-2.14e, revealing the reversed beam CM of the nearest-neighbor trapping mode (from right to left, p=1 in Fig. 2.10g vs p=2 in Fig. 2.14e). As can be seen, the skewness of the p=2 amplifying mode (to the left of the center atom) in the inverted PT molecule is determined by the PT symmetric condition of center next-nearest-neighbor atoms of 10^{th} (for gain, left) and 14^{th} (for loss, right) waveguides. It is worth noting that, since the three real atoms at the center compose three real split modes (dotted lines, Fig. 2.14b), p=1 and p=23 modes maintain real eigenvalues, supporting symmetric beam CMs.

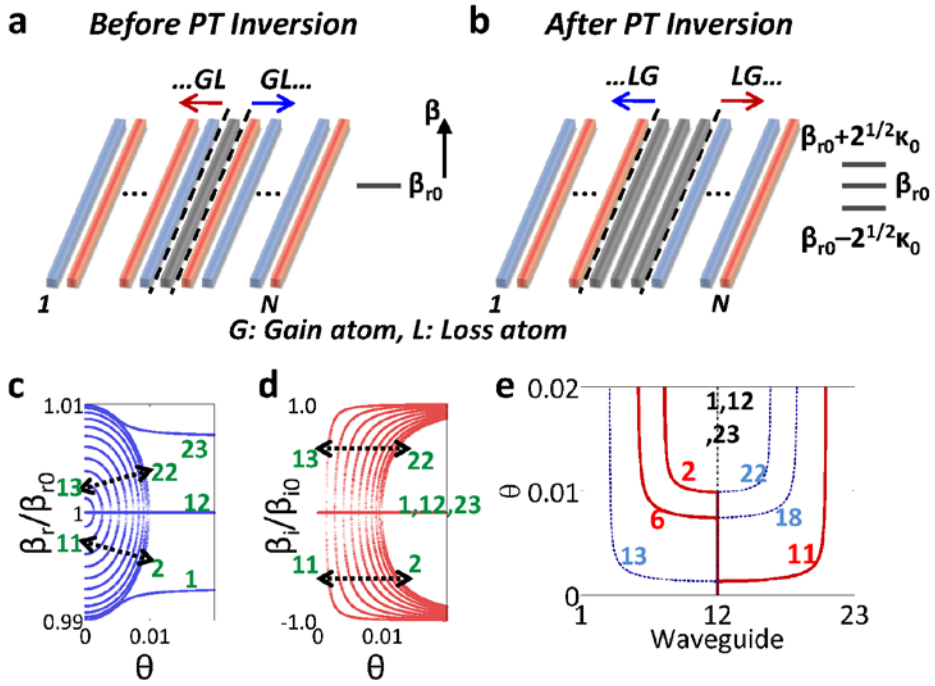

Figure 2.14. Schematics of PT-symmetric meta-molecules [46] (a) before and (b) after the inversion of PT symmetry. (c) Real and (d) imaginary part of each eigenvalue, and (e) the beam CM of supermodes for the inverted PT meta-molecule as a function of θ (N=23). Green labels denote the modal index p.

Figure 2.15 shows the beam dynamics of phase coexistent and entirely collapsed meta-molecules after the inversion of PT symmetry for the center nearest-neighbor atoms (Fig. 2.14b). For the weakly-collapsed phase-coexistent molecule (θ=arctan(β_{i0}/β_{r0})=0.0025, complex only for p=11), a similar evolution of beam CM is achieved with the comparable efficiency of asymmetric coupling to that of the non-inverted case (Fig. 2.14a, Fig. 2.10g). In contrast, for the entirely collapsed molecule, the direction of asymmetry is reversed (from right to left) due to the reversed skewness of the nearest-neighbor trapping mode (p=2, Fig. 2.14e). Although the final route of coupling is saturated to the dominant mode (p=11, rightward skewness) due to its largest amplification, the reversed asymmetry is clearly exhibited until $X \sim 200\mu m$.

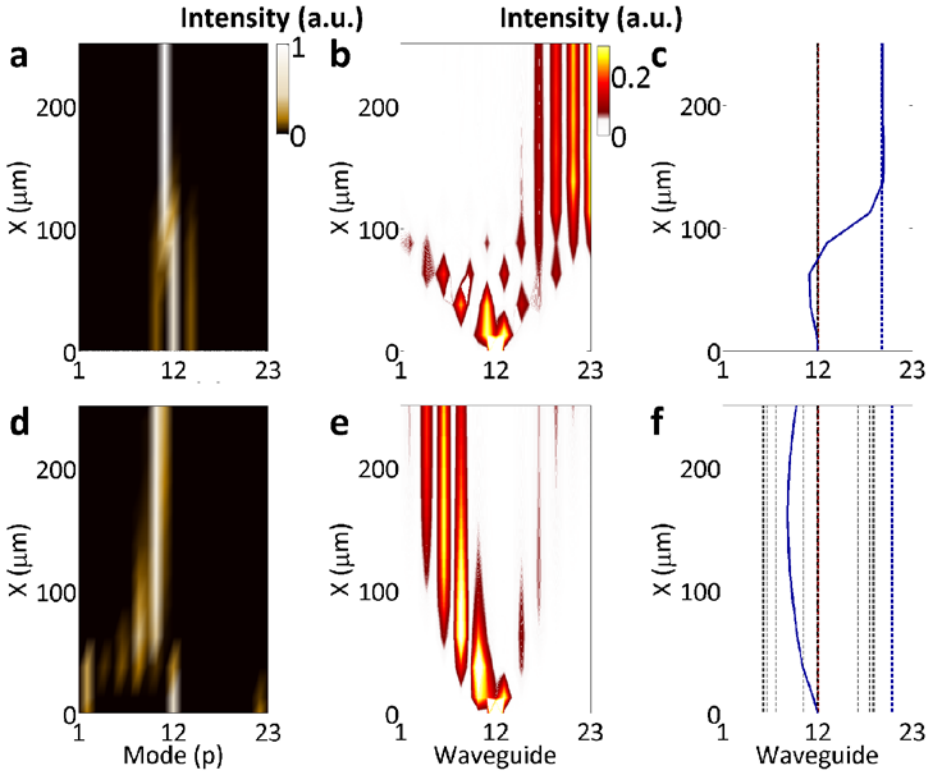

Figure 2.15. Inversion of asymmetric light transfer in PT-symmetric optical potentials [46]. (a,d) Modal excitation, (b,e) beam propagation, and (c,f) evolution of beam CM (blue solid line) are presented for (a-c) p=11,13 complex phase-coexistent ($\beta_{i0}=\kappa_o/2$), and (d-f) entirely collapsed molecules ($\beta_{i0}=2\kappa_o$), with the inverted PT symmetry (Fig. 3b). (Movie 2 in [46]) The field intensity in (b,e) is normalized across the waveguide array at each position (X). Blue and black dotted lines in (c,f) denote the dominant (p=11) and the trapping (p=2–10) modes. The frequency f_0 = 193.4THz, $\beta_{r0} = 3.5\cdot(2\pi f_0/c)$, and $\kappa_o=\beta_{r0}/200$.

To confirm our results based on coupled mode theory and the scattering matrix method in Fig. 2.11 and Fig. 2.15, we provide the numerical verification for the dynamic behavior inside the complex meta-molecule, based on using an electromagnetic solver based on the finite element method (COMSOL, 2-dimensional, in-plane TE-polarization model). For the numerical stability and the proper design for experiments, the passive complex meta-molecule with dielectric atomic waveguides is applied which is achieved through a gauge transformation

into passive PT symmetry [41, 44]. It should be noted that the passive complex molecule is composed of atoms characterized by either low-loss ($n_i=n_{i0}$ - Δn_{i0}, orange in Fig. 2.16a and 2.16d), high-loss ($n_i=n_{i0}$ + Δn_{i0}, blue in Fig. 2.16a and 2.16d), or middle-loss ($n_i=n_{i0}$, gray in Fig. 2.16a and 2.16d) waveguides.

The design of PT-symmetric meta-molecule is equivalent to that specified in the theoretical analysis. The atomic waveguide has 200nm width composed of the material of refractive index n_{r0} = 3.8 for β_{r0}~3.5·($2\pi f_0/c$) where f_0=193.4THz. The air gap between waveguides is 230nm to achieve κ_o~β_{r0}/200. Figure 2.16a-2.16c show the imaginary potential (Fig. 2.16a), and beam dynamics for the weakly collapsed (Fig. 2.16b, complex only for p=11) and the entirely collapsed (Fig. 2.16c) molecules, under excitation of the central atom. To note, for the passive realization, the center of the imaginary potential is set to be n_{i0} = 0.042. As observed in Fig. 2.11a-2.11c and Fig. 2.11g-2.11i, the more rapid asymmetric transfer with only a small imaginary potential in the phase-coexistent molecule is also observed in this numerical verification (Fig. 2.16b vs Fig. 2.16c).

Figure 2.16d-2.16f show the imaginary potential (Fig. 2.16d), and beam dynamics of phase coexistent (Fig. 2.16e) and entirely collapsed meta-molecules (Fig. 2.16f) after the inversion of PT symmetry for the center nearest-neighbor atoms. The reversible asymmetric transfer in the entirely collapsed regime is also demonstrated by this numerical analysis (Fig. 2.16f, compared with Fig. 2.15f), by imposing Δn_{i0}=0 only for center nearest-neighbor atoms.

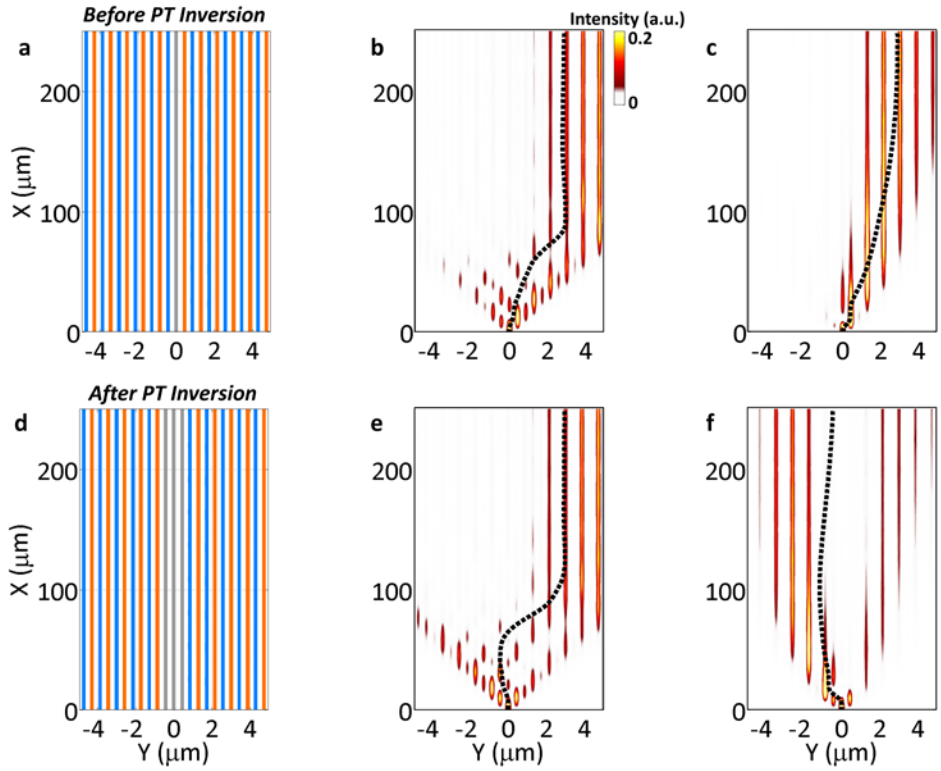

Figure 2.16. Numerical confirmation for Fig. 2.11 and 2.15, utilizing COMSOL Multiphysics [46]: (a,d) Imaginary potential and (b,c,e,f) beam dynamics are presented for (b,e) p=11 complex (Δn_{i0}=0.01), and (c,f) entirely collapsed meta-molecules (Δn_{i0}=0.042) in the case of complex molecules (a-c) before PT inversion, and (d-f) after PT inversion. The field intensity in (b,c,e,f) is normalized across the waveguide array at each position (X). Black dotted lines in (b,c,e,f) denote the beam center of mass. The frequency f_0=193.4THz.

In conclusion, in this section we investigated the phase-dependent asymmetric transfer inside a complex meta-molecule. Contrary to the intuitive expectation based on the skewness of eigenmodes, highly-drastic asymmetric coupling was observed in the phase-coexistent molecule with smaller imaginary potentials (θ=0.0025) as compared to the case of entirely collapsed meta-molecules (θ=0.01). We demonstrated that this unusual phenomenon is due to the absence of 'spatial trapping modes' in the phase-coexistent regime, which hinder the energy transfer

inside the molecule. Reversing the skewness of the center nearest-neighbor trapping mode through removal of the imaginary potentials of only two atoms, we demonstrated reversible asymmetry in the entirely collapsed regime. These fascinating phenomena further the understanding of the physics of complex meta-molecules, and provide a pathway to implement the novel physics of non-Hermitian potentials in meta-material structures with feasible gain and loss values (θ=0.0025 which is within the limits of semiconductor-based gain media, e. g. θ_{max}~0.005 for GaInAsP [85]).

Especially, the realization of reversible asymmetric transfer based only on the local inversion of PT symmetry will enable the development of sensitive and switchable asymmetric optical devices, implemented with techniques for precise control over imaginary potentials. The dynamic and selective control over the imaginary potential (gain/loss, only for two waveguides) can be easily implemented in the fiber-based system with the electrical pump [58] or longitudinally-coupled optical pump; such as selective current injections to the semiconductor optical amplifier [86], or selective excitations of optical pumps to Erbium-doped fiber amplifiers [87]. Yet, the control can also be achieved with the vertically-coupled optical pump technique [43], from the modulated spatial profile of the pump with amplitude masking, as demonstrated in the previous work of the PT symmetry [43].

2.3 PT-symmetric waves in momentum domains

The concept of parity-time (PT) symmetry has been used to identify a novel route toward unidirectional dynamics in optical k-space: imposing asymmetry on the flow of light as shown in section 2.2. Although PT-symmetric potentials have been implemented under the requirement of $V(x) = V^*(-x)$ [33], this precondition has only been interpreted within the mathematical framework for the symmetry of Hamiltonians and has not been directly linked to unidirectionality induced by PT symmetry. Within the context of light-matter interactions, in this section we

interpret the notion of PT-symmetry in *k*-space: manipulating linear [51] and angular [45] momenta of light. We demonstrate that PT-symmetric potentials produce unidirectional transitions of optical modes inside the *k*-continuum, which corresponds to an exceptional point on the degree of PT symmetry. Our analysis reveals not only a novel class of optical chirality based on low-dimensional eigensystems [45] – also operating as an optical spin black hole – but also a critical link between non-Hermitian problems and spectral theory [51], enabling multi-dimensional designer manipulation of optical modes in contrast to the one-dimensional approach in previous PT-symmetric optics.

2.3.1 Optical chirality in low-dimensional eigensystems

Chirality is a universal feature in nature, as observed in fermion interactions [88] and DNA helicity [89]. Much attention has been given to the chiral interactions of light, not only regarding its physical interpretation [90, 91] but also regarding the intriguing phenomena it displays in excitation [92-94], absorption [95-97], generation [98, 99], and refraction [100-102]. Although recent progress in metamaterials [102-109] and 3-dimensional writing technology [110, 111] has spurred artificial enhancements of optical chirality, most approaches are founded on the same principle of the mixing of electric and magnetic responses. However, due to the orthogonal form of electric and magnetic fields, intricate designs are commonly required for mixing.

In this section, we introduce novel nonmagnetic chiral interactions of light based on a low-dimensional eigensystem [45]. In contrast to previous approaches, we derive the optical chirality from the mixing of amplifying and decaying electric responses, not from the mixing of electric and magnetic responses. Most importantly, we demonstrate that the dimensionality of PT-symmetric chiral material is reduced to one at the EP, leading to a single, perfectly circular modal helix. Unique chiral behaviors arising from the low-dimensionality, such as one-way chiral *conversion* between circular polarizations (CP) and chirality reversal for linear polarization (LP) state change, are theoretically predicted through

experimental demonstration in a metamaterial platform. It is also shown that any arbitrarily polarized incidences of PT-symmetric chiral material converge to a single chiral eigenstate without reflections, corresponding to spin black hole dynamics, as which cannot be realized with conventional (Hermitian) approaches using polarizers and retarders. Our proposal opens, for the first time, the domain of low-dimensional chirality utilizing PT-symmetric compositions of isotropic materials and, thus, will provide new insights into active chirality [98, 99] and metamaterials in the complex domain [62], overcoming the limit of existing chiral metamaterials based upon 2-dimensional eigensystems.

First, we assume a homogeneous and anisotropic hypothetical optical material that is PT-symmetric with respect to the $(\boldsymbol{y}\pm\boldsymbol{z})/2^{1/2}$ axis. The relative permittivity tensor, satisfying the necessary condition of PT symmetry (symmetric real and anti-symmetric imaginary potentials defined as $\varepsilon(\boldsymbol{r}) = \varepsilon^{*}(-\boldsymbol{r})$), is then characterized as

$$\bar{\bar{\varepsilon}}_r = \begin{pmatrix} \varepsilon_{r0} & 0 & 0 \\ 0 & \varepsilon_{r0} + i\varepsilon_{i0} & \varepsilon_{\kappa 0} \\ 0 & \varepsilon_{\kappa 0}^{*} & \varepsilon_{r0} - i\varepsilon_{i0} \end{pmatrix}, \tag{2.14}$$

where ε_{r0} and ε_{i0} have real values (for $\varepsilon_{i0} \geq 0$, $\boldsymbol{y}$: gain axis, $\boldsymbol{z}$: loss axis). Here, $\varepsilon_{\kappa 0}$ is also set to a real value, assuming a nonmagnetic material without gyrotropic effects. Note that all the material parameters are defined 'locally', in sharp contrast to the case of nonlocal complex materials utilized for the reinterpretation of optical chirality [32]. For a planewave (E_y, E_z) propagating along the $\boldsymbol{x}$-axis (E_x=0), there exist two eigenstates, each with an eigenvalue (or effective permittivity) $\varepsilon_{eig1,2} = \varepsilon_{r0} \pm \lambda_{PT}$ and a corresponding eigenmode $\boldsymbol{v}_{eig1,2} = \eta_{1,2}\cdot(\varepsilon_{\kappa 0}, -i\varepsilon_{i0} \pm \lambda_{PT})^{\mathrm{T}}$, where $\eta_{1,2} = [1/(|\varepsilon_{\kappa 0}|^2 + |-i\varepsilon_{i0} \pm \lambda_{PT}|^2)]^{1/2}$ is a normalization factor and $\lambda_{PT} = (\varepsilon_{\kappa 0}^{\,2} - \varepsilon_{i0}^{\,2})^{1/2}$ is a complex interaction parameter defining the EP ($\lambda_{PT} = 0$, see Appendix B.1, [44, 46]). These complex eigenmodes are generally nonorthogonal ($\boldsymbol{v}_{eig1}\cdot\boldsymbol{v}_{eig2}^{\,*} \neq 0$), except for the case of a Hermitian potential ($\varepsilon_{i0} = 0$). It is critical to note that

because the handedness of $\eta_{1,2}\cdot(\varepsilon_{\kappa 0}, -i\varepsilon_{i0} \pm \lambda_{PT})^{T}$ resembles that of the LCP (left CP) basis, $v_L = (1/2)^{1/2}\cdot(1, -i)^{T}$, the PT-symmetric potential becomes naturally chiral, favoring the LCP mode, as will be detailed in later discussions.

Figure 2.17a (2.17b) presents the real (imaginary) part of the effective permittivity $\varepsilon_{eig1,2}$ for each eigenstate of PT-symmetric systems ***d*** to ***h***, which have different values of ε_{i0}. Similar to other PT-symmetric potentials [41, 43, 44], the variation of ε_{i0} derives the generic square-root curve from the definition of λ_{PT} and results in the apparent phase transition of eigenvalues from the real to the complex phase across the EP (point ***f***, $\varepsilon_{i0} = \varepsilon_{\kappa 0}$ or $\lambda_{PT} = 0$). The normalized density of optical chirality $\chi/(\beta_{r0}U_e)$ for each eigenstate ***d***-***h*** is shown in Fig. 2.17c ($\chi = [\varepsilon_0\varepsilon_r\cdot\boldsymbol{E}\cdot(\nabla \mathrm{x}\boldsymbol{E}) + (1/\mu_0)\cdot\boldsymbol{B}\cdot(\nabla \mathrm{x}\boldsymbol{B})]/2$, $U_e = |\boldsymbol{E}|^2$ and $\beta_{r0} = \varepsilon_{r0}^{1/2}\cdot 2\pi/\Lambda_0$, Appendix B.2, [90]), along with the corresponding profiles of eigenpolarization (Figs. 2.17d-2.17h, $\varepsilon_{\kappa 0} > 0$). For the Hermitian case ($\varepsilon_{i0} = 0$, Fig. 2.17d), the eigenmodes take the form of linearly polarized, coupled modes (even and odd, $\chi = 0$, Fig. 2.17c), constituting 2-dimensional orthogonal bases. As the magnitude of the imaginary potential ε_{i0} increases ($0 < \varepsilon_{i0} < \varepsilon_{\kappa 0}$, Fig. 2.17e), the eigenmodes begin to converge and take the chiral form of left-handed elliptical polarizations, resulting in nonorthogonality $\boldsymbol{v}_{eig1}\cdot\boldsymbol{v}_{eig2}^{*} \neq 0$ and increased chirality (Fig. 2.17c, points ***d***→***f***). At the EP ($\varepsilon_{i0} = \varepsilon_{\kappa 0}$, Fig. 2.17f), two chiral eigenmodes coalesce to a left-circular helical basis due to the reduced geometric multiplicity (=1 for $\varepsilon_{eig1} = \varepsilon_{eig2}$) of Eq. (2.14). This *low-dimensional* existence of a chiral eigenmode in the form of a *modal helix* - distinguished from the structural helix of electric and magnetic mixing [110, 111] and from plasmonic chiral films of co- / counter- rotating currents [96, 97, 112] - yields perfect modal chirality with a pure handedness (Fig. 2.17c, point ***f***). After the EP ($\varepsilon_{i0} > \varepsilon_{\kappa 0}$, Figs. 2.17g,h), the 2-dimensional eigensystem is recovered, and the chirality decreases again (Fig. 2.17c, points ***f***→***h***) as each chiral eigenmode is saturated to a linear mode (***y***, amplifying; ***z***, decaying). It is noted that the handedness of the chiral eigenmodes can be reversed by changing the sign of $\varepsilon_{\kappa 0}$ based on the form of the eigenmode $\boldsymbol{v}_{eig1,2} = \eta_{1,2}\cdot(\varepsilon_{\kappa 0}, -i\varepsilon_{i0} \pm \lambda_{PT})^{T}$ (Fig. 2.17c,

orange for left-handedness with $\varepsilon_{\kappa 0} > 0$, blue for right-handedness with $\varepsilon_{\kappa 0} < 0$). For completeness, we also analyze the effect of the imperfection in PT symmetry ($\mathrm{Re}[\varepsilon_y] \neq \mathrm{Re}[\varepsilon_z]$ or $\mathrm{Im}[\varepsilon_y] \neq -\mathrm{Im}[\varepsilon_z]$) with respect to the modal chirality (see Appendix B.3), which shows the experimental tolerance ($\mathrm{Re}[\varepsilon_y] \neq \mathrm{Re}[\varepsilon_z]$) and the possibility of active and passive realizations ($\mathrm{Im}[\varepsilon_y] \neq -\mathrm{Im}[\varepsilon_z]$).

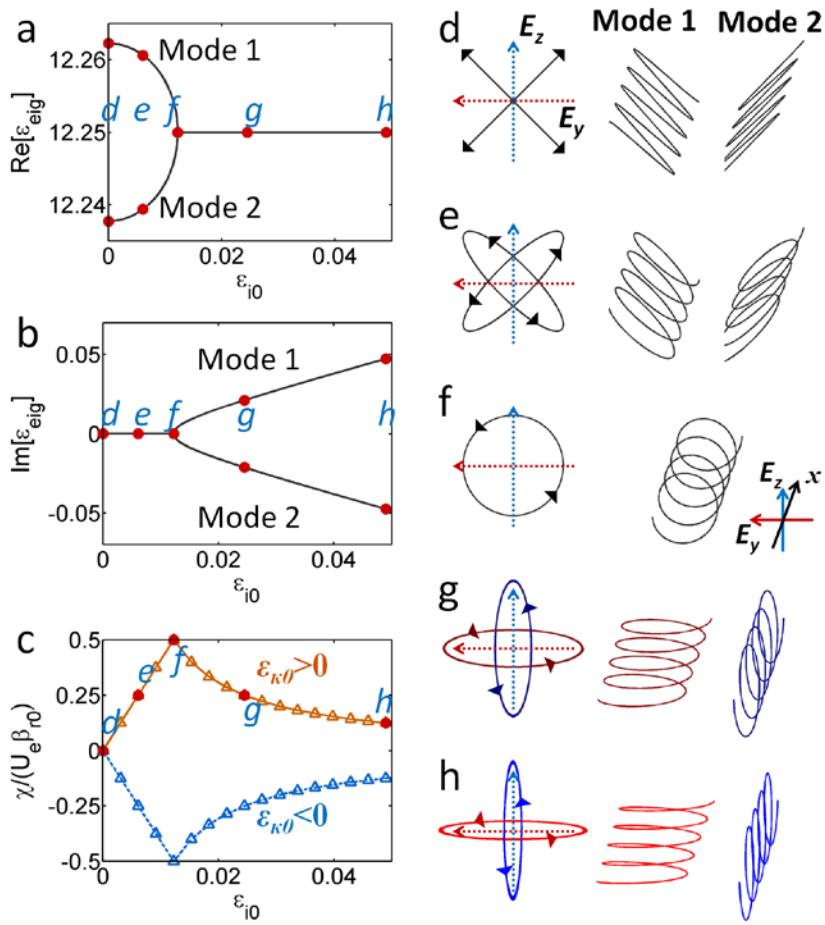

Figure 2.17. Eigenvalues and spatial evolution of eigenmodes in PT-symmetric chiral material [45]. The real and imaginary parts of the effective permittivity $\varepsilon_{eig1,2}$ are shown in (a) and (b) with respect to ε_{i0}. (c) The density of chirality χ, normalized by the product of the electric field intensity U_e and β_{r0} (orange: $\varepsilon_{\kappa 0}= \varepsilon_{r0}/10^3$, blue: $\varepsilon_{\kappa 0}= -\varepsilon_{r0}/10^3$, line: eigenmode 1, symbol: eigenmode 2). (d)-(h). Spatial evolution of eigenmodes corresponding to points *d*-*h* marked in a-c. The red and blue arrows represent the axes of E_y (amplifying mode) and E_z (decaying mode). At the EP *f*, the complex eigenmode has the singular form of a modal helix. ε_{r0} = 12.25 for (a)-(h), and $\varepsilon_{\kappa 0} = \varepsilon_{r0}/10^3 > 0$ for (a), (b), and (d)-(h).

To further examine the general behavior of chiral eigenstates in PT-symmetric chiral material, we study the modal transfer between two CP modes through

propagation. Utilizing the eigenmodes and eigenvalues obtained from Eq. (2.14) and employing the CP bases of $v_{R,L} = (1/2)^{1/2}\cdot(1, \pm i)^{\mathrm{T}}$, the transfer relation between the incident $E_{inc} = (E_{RI}, E_{LI})_{\mathrm{CP}}{}^{\mathrm{T}}$ and transmitted field $E_{trn} = (E_{RT}, E_{LT})_{\mathrm{CP}}{}^{\mathrm{T}}$ is written as $\boldsymbol{E}_{trn} = \boldsymbol{M}_{PT}\boldsymbol{E}_{inc}$ (see Appendix B.4.1 for the detailed derivation), where

$$M_{PT} = \begin{bmatrix} t_{R\to R} & t_{L\to R} \\ t_{R\to L} & t_{L\to L} \end{bmatrix} = \frac{1}{2}\begin{bmatrix} \varphi_1 + \varphi_2 & -i\dfrac{\varepsilon_{\kappa 0} - \varepsilon_{i0}}{\lambda_{PT}}(\varphi_1 - \varphi_2) \\ i\dfrac{\varepsilon_{\kappa 0} + \varepsilon_{i0}}{\lambda_{PT}}(\varphi_1 - \varphi_2) & \varphi_1 + \varphi_2 \end{bmatrix}; \tag{2.15}$$

$\beta_{1,2} = 2\pi\varepsilon_{eig1,2}{}^{1/2}/\Lambda_0$ is the propagation constant of each chiral eigenmode, $\varphi_{1,2} = exp(-i\beta_{1,2}d)$ is the modal phase evolution, d is the propagation distance, and Λ_0 is the free-space wavelength.

A closer investigation of the transfer matrix M_{PT} provides a straightforward understanding of chiral interactions. First, the inequality between off-diagonal terms ($|t_{R\to L}| > |t_{L\to R}|$) leads to an asymmetric intermodal transfer between the right CP (RCP) and left CP (LCP) modes. Meanwhile, because the self-evolutions of the RCP and LCP modes are identical ($t_{R\to R} = t_{L\to L}$), the chiral response of the system is governed by the *intermodal chirality*, which we define as

$$C_{IM} = \left|\frac{t_{R\to L}}{t_{L\to R}}\right| = \left|\frac{\varepsilon_{\kappa 0} + \varepsilon_{i0}}{\varepsilon_{\kappa 0} - \varepsilon_{i0}}\right| = \left|\frac{1 + \dfrac{\varepsilon_{i0}}{\varepsilon_{\kappa 0}}}{1 - \dfrac{\varepsilon_{i0}}{\varepsilon_{\kappa 0}}}\right|. \tag{2.16}$$

It is important to note that the intermodal chirality C_{IM} is solely determined by the ratio of ε_{i0} and $\varepsilon_{\kappa 0}$, which is directly related to the degree of PT symmetry, i.e., the interaction parameter of $\lambda_{PT} = (\varepsilon_{\kappa 0}{}^2 - \varepsilon_{i0}{}^2)^{1/2}$. Accordingly, at the EP ($\lambda_{PT} = 0$), a one-way chiral conversion $C_{IM} \to \infty$ from the RCP to LCP mode is achieved, as

expected from the reduction of the eigensystem to a 1-dimensional pure LCP modal helix (Fig. 2.17f). Before and after the EP, the intermodal chirality decreases (Fig. 2.18a) with the existence of two eigenmodes of elliptical polarization (Figs. 2.17e,g).

While the *intermodal chirality* C_{IM} defines the unique origin of chirality in PT-symmetric material, the '*strength' of the chiral conversion* C_{CS} is determined by the competition between the intermodal transfer and the self-evolution ($C_{CS}^{R\to L} = |t_{R\to L} / t_{R\to R}|$, $C_{CS}^{L\to R} = |t_{L\to R} / t_{L\to L}|$). After the EP ($\varepsilon_{i0} \geq \varepsilon_{\kappa 0}$), $C_{CS}^{R\to L}$ and $C_{CS}^{L\to R}$ can be expressed as

$$C_{CS}^{R\to L} = \left(\frac{\varepsilon_{i0}+\varepsilon_{\kappa 0}}{\varepsilon_{i0}-\varepsilon_{\kappa 0}}\right)^{1/2} \cdot \tanh\left[\frac{2\pi d}{\Lambda_0}\cdot\left(\frac{\sqrt{\varepsilon_{r0}^{\,2}+\varepsilon_{i0}^{\,2}-\varepsilon_{\kappa 0}^{\,2}}-\varepsilon_{r0}}{2}\right)^{1/2}\right], \quad (2.17)$$

$$C_{CS}^{L\to R} = \left(\frac{\varepsilon_{i0}-\varepsilon_{\kappa 0}}{\varepsilon_{i0}+\varepsilon_{\kappa 0}}\right)^{1/2} \cdot \tanh\left[\frac{2\pi d}{\Lambda_0}\cdot\left(\frac{\sqrt{\varepsilon_{r0}^{\,2}+\varepsilon_{i0}^{\,2}-\varepsilon_{\kappa 0}^{\,2}}-\varepsilon_{r0}}{2}\right)^{1/2}\right]. \quad (2.18)$$

In agreement with the observations made for C_{IM}, $C_{CS}^{R\to L}$ is always larger than $C_{CS}^{L\to R}$ and results in LCP-favored chiral conversion (plotted in Fig. 2.18b; for the regime before the EP with oscillatory behavior, see Appendix B.4.2). In addition, because $C_{CS}^{R\to L} \sim 2\pi L_{eff}\cdot(\varepsilon_{\kappa 0}/\varepsilon_{r0})$ and $C_{CS}^{L\to R} \sim 0$ near the EP, the chiral conversion becomes unidirectional, and its strength can be controlled by the material and structural parameters, namely, $(\varepsilon_{i0}/\varepsilon_{r0})$ and $L_{eff} = \varepsilon_{r0}^{\,1/2}\cdot d/\Lambda_0$. Figures 2.18c and 2.18d show the chirality of the transmitted wave for RCP and LCP incidences as a function of $(\varepsilon_{i0}/\varepsilon_{r0})$ and L_{eff}. For large L_{eff} values, strong LCP chirality from the one-way chiral conversion is apparent near the EP, which emphasizes the role of the singularity. It is critical to note that this chiral singularity acts as the *optical spin black hole* (Fig. 2.18e), where all the states of polarization (SOP) converge toward

the south pole of the Poincaré sphere [2] during the propagation (see Appendix B.5 for details in the incidence condition and the Stokes parameter expression and Supplementary Movie S1 in [45] for the dynamic LCP-convergent behavior at the EP). Notably, a giant chiral conversion (I_L/I_R=20 dB within a small range of values near L_{eff} = 1.4) can also be achieved in the *resonant structure* (see Appendix B.6). We emphasize that this drastic increase in chiral interactions as a result of the low-dimensional PT-chiral system is fundamentally distinct from conventional chirality, which exploits the mixing of electric and magnetic responses in a 2-dimensional eigensystem of unequal self-evolutions (or circular birefringence, $t_{R\to R} \neq t_{L\to L}$) and zero intermodal coupling ($t_{L\to R} = t_{R\to L} = 0$).

Focusing on the vicinity of the EP, chirality reversal can be achieved for the SOP of linear polarization (LP) incidences. For the LP incidence $\boldsymbol{E}_{inc} = (E_{RI}, E_{LI})_{\mathrm{CP}}{}^{\mathrm{T}} = (1/2)^{1/2}\cdot E_0\cdot(e^{-i\theta}, e^{i\theta})_{\mathrm{CP}}{}^{\mathrm{T}}$ of an arbitrary polarized angle θ, the transmitted field $\boldsymbol{E}_{trn}$ at the EP is obtained from the transfer matrix M_{PT} as

$$E_{trn} = \begin{pmatrix} E_{RT} \\ E_{LT} \end{pmatrix} = \frac{E_0}{\sqrt{2}} \cdot e^{-i\cdot 2\pi \frac{\sqrt{\varepsilon_{r0}}\cdot d}{\Lambda_0}} \cdot \begin{pmatrix} e^{-i\theta} \\ e^{i\theta} + C_{CS}{}^{R\to L}\big|_{EP} \cdot e^{-i\theta} \end{pmatrix}. \qquad (2.19)$$

From Eq. (2.19), it is clear that LCP transmission can be controlled by the polarized angle θ of LP and $C_{CS}{}^{R\to L}|_{\mathrm{EP}}$ (Fig. 2.18f), whereas RCP transmission is invariant (see Supplementary Movie S2 in [45] for the SOP evolutions by the degree of PT symmetry with LP incidences; θ = 0, π/2, π, and 3π/2). In the strong chiral conversion regime of $C_{CS}{}^{R\to L}|_{\mathrm{EP}} > 2$ (outside the dotted circle in Fig. 2.18f), the transmitted wave is *always* left-handed ($|E_{LT}| > |E_{RT}|$) for all angles of θ. In contrast, in the regime of $C_{CS}{}^{R\to L}|_{\mathrm{EP}} \leq 2$, *chirality reversal* to a right-handed output is permitted for input angles of $cos(2\theta) < -C_{CS}{}^{R\to L}|_{\mathrm{EP}}/2$. It is interesting to note that a pure RCP transmission can also be achieved in the special case of $C_{CS}{}^{R\to L}|_{\mathrm{EP}} = 1$ and *z*-LP (θ = 90°, on the solid circle in Fig. 2.18f), which is counterintuitive regarding the singular existence of the LCP modal helix. This paradoxical result

arises from the unidirectional ($R \rightarrow L$) intermodal transfer, which leads to a completely destructive interference for the LCP mode only ($e^{i\theta} + C_{CS}^{R\rightarrow L}|_{\mathrm{EP}} \cdot e^{-i\theta}$). It is worth mentioning that the observed phenomena of CP interference and chirality reversal are absent in conventional chiral materials, which are based on *uncoupled* LCP and RCP modes ($t_{L\rightarrow R} = t_{R\rightarrow L} = 0$), and thus, they maintain the LP state with natural optical rotation during propagation. In practice, the regime of chirality reversal can be controlled by changing L_{eff} or $\varepsilon_{\kappa 0}$ (Fig. 2.18g) based on the definition of $C_{CS}^{R\rightarrow L}|_{\mathrm{EP}}$ ($=2\pi L_{eff} \cdot (\varepsilon_{\kappa 0}/\varepsilon_{r0})$).

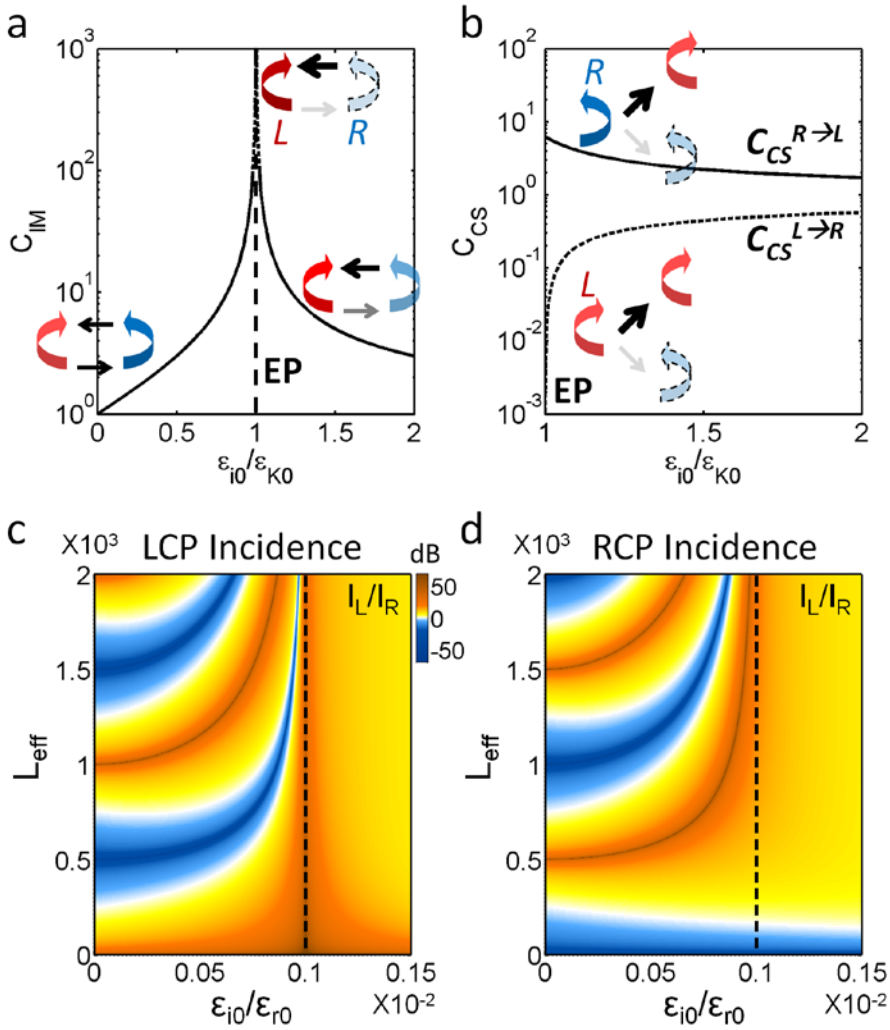

Figure 2.18. Chiral dynamics within PT-symmetric optical material [45]. (a) C_{IM} and (b) C_{CS} as functions of ($\varepsilon_{i0}/\varepsilon_{\kappa 0}$). The output power ratio of LCP over RCP ($I_L/I_R = |E_{LT}/E_{RT}|^2$ in dB) is shown for the case of (c) LCP and (d) RCP incidence as a function of the imaginary permittivity ($\varepsilon_{i0}/\varepsilon_{r0}$) and the interaction length ($L_{eff} = \varepsilon_{r0}^{1/2} \cdot d/\Lambda_0$). The black dotted lines in c and d represent the EPs, where the dimensionality reduces to one.

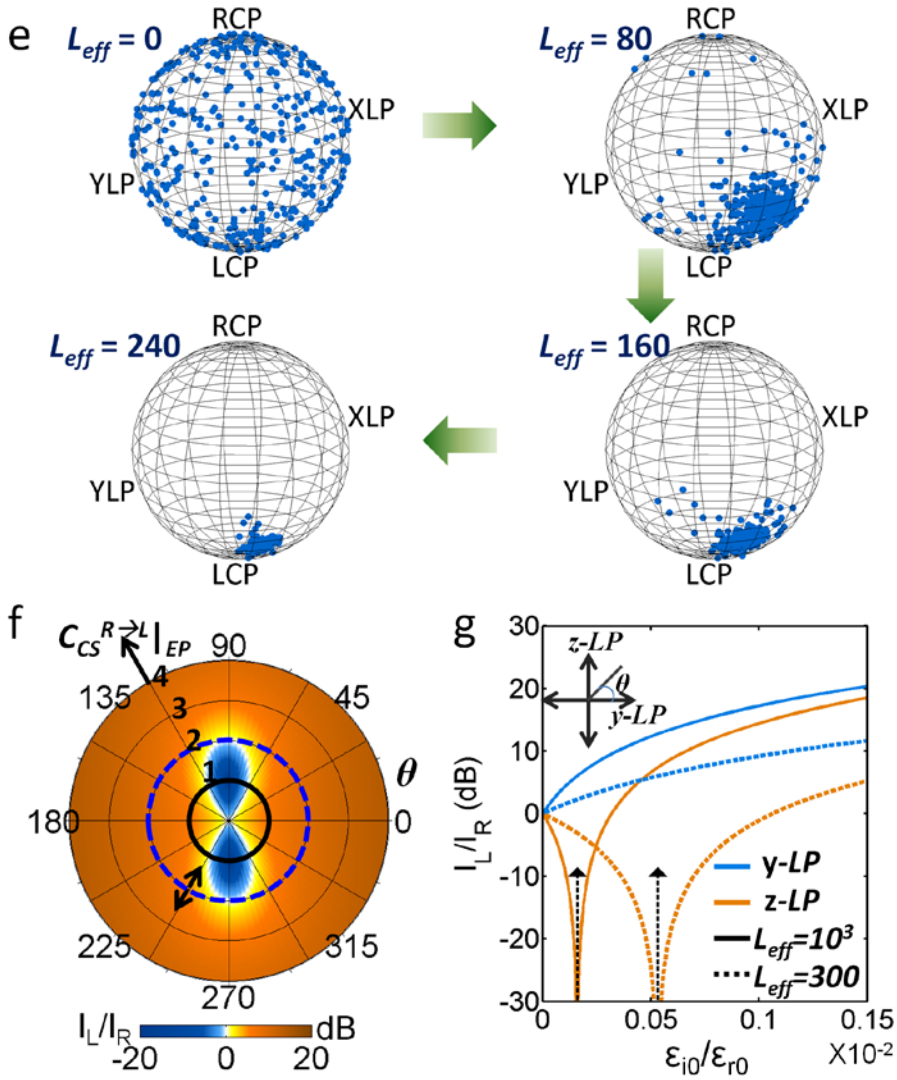

Figure 2.18 (continue). (e) LCP-convergent spin black hole dynamics on the Poincaré sphere at the EP, demonstrated with randomly polarized incidences. The interaction lengths are L_{eff} = 0, 80, 160, and 240, clockwise from the upper left. The movie is shown in Supplementary Movie S1 in [45]. The ratio of I_L/I_R at the EP for LP incidences is shown in (f) as a function of $C_{CS}^{R\to L}|_{EP}$ and the polarized angle θ of LP and in (g) as a function of coupling permittivity ($\varepsilon_{\kappa 0}/\varepsilon_{r0}$). The black dotted arrows denote the points at which $C_{CS}^{R\to L}|_{EP}$ = 1. All the results are based on the transfer matrix method. ε_{r0}=6.5 in (b)-(g), $\varepsilon_{\kappa 0}=\varepsilon_{r0}/10^3$ in (b)-(d), $\varepsilon_{\kappa 0}=\varepsilon_{r0}/200$ in (e), and $L_{eff}=10^3$ for (b) and (f).

We now investigate the experimental realization of the hypothetical medium considered thus far, focusing on observation of the one-way chiral conversion (quantified by C_{IM}), which is clear and direct evidence of the low-dimensionality. To obtain the complex anisotropic permittivity of Eq. (2.14) with feasible isotropic media, especially satisfying the locality, it is natural to employ the principle of metamaterials, which will not only enable the 'local' material parameter defined for planewaves from the subwavelength limit [113-115] but will also allow the satisfaction of PT-symmetry through the designer separation of real and imaginary permittivity based on the Lorentz model.

Figure 2.19 shows the experimental realization of low-dimensional chirality, transplanting the ideal point-wise anisotropic permittivity (Fig. 2.19a for Eq. (2.14)) into the THz metamaterial structure with *isotropic electric materials* (see Appendix B.7 for the fabrication process and the THz measurement). To increase purely electrical light-matter interaction in the THz regime without diamagnetic behaviors, magnetic moments induced by the current loop should be suppressed [116]. Therefore, the I-shaped metamaterial [82] with an ultrahigh refractive index ($\varepsilon_r >> 1$ and $\mu_r \sim 1$) is applied as a *polarized metamaterial platform* each for $\boldsymbol{y}$ and $\boldsymbol{z}$ mode (Fig. 2.19b). Because the I-shaped patch supports effective permittivity following the Lorentz model [82] with a permeability approaching unity, its spectral response (Fig. 2.19c) is divided into dielectric ($\mathrm{Re}[\varepsilon] \geq 0$) and metallic ($\mathrm{Re}[\varepsilon] < 0$) states, both of which can be subdivided into low-loss ($|\mathrm{Re}[\varepsilon]| >> |\mathrm{Im}[\varepsilon]|$) and high-loss ($|\mathrm{Re}[\varepsilon]| \sim |\mathrm{Im}[\varepsilon]|$) regimes.

To compose the *PT-symmetric polar metamaterial* in a passive manner, we utilize the low- and high-loss regimes for $\boldsymbol{y}$ and $\boldsymbol{z}$ polarization for both dielectric (Figs. 2.19d,e) and metallic (Figs. 2.19f,g) realizations utilizing propagating and evanescent waves, respectively (see Appendix B.8). Figures 2.19d and 2.19f show the real and imaginary values of anisotropic permittivity ε_y and ε_z (at $\theta = 0$ in Fig. 2.19b) for the fabricated samples of dielectric and metallic realizations (Figs. 2.19e and g, respectively). These figures prove the spectral overlap between low- and

high-loss regimes for the ***y***- and ***z***-axis patches and the existence of EP with Re[ε_y] = Re[ε_z] and Im[ε_y] ≠ Im[ε_z]. Note that our single-layered structure, when symmetrically embedded in a subwavelength-thick polyimide ($t < \lambda_0/100$), can be considered a homogenized metamaterial guaranteeing local material parameters [82]. To introduce the coupling $\varepsilon_{\kappa 0}$ (=ε_{yz}), we apply the oblique alignment with a tilted angle θ (Fig. 2.19b).

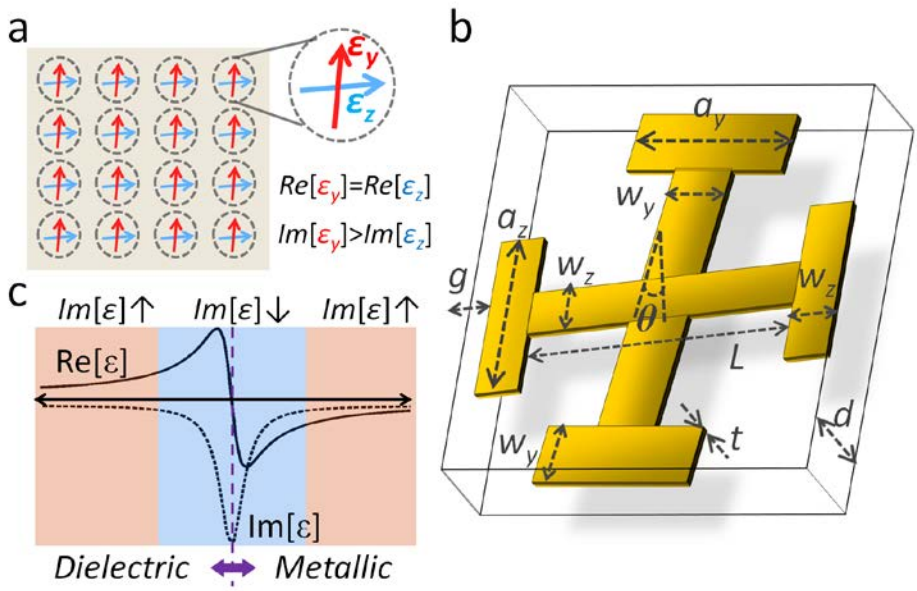

Figure 2.19. Chiral polar metamaterial for low-dimensional chirality [45]. (a) Schematics of a PT-symmetric, point-wise anisotropic permittivity material for Eq. (2.14). (b) Metamaterial realization of Fig. 2.19a using crossed I-shaped gold structures (tilted by θ) inside the polyimide. (c) Lorentz model for an I-shaped patch with different material regimes.

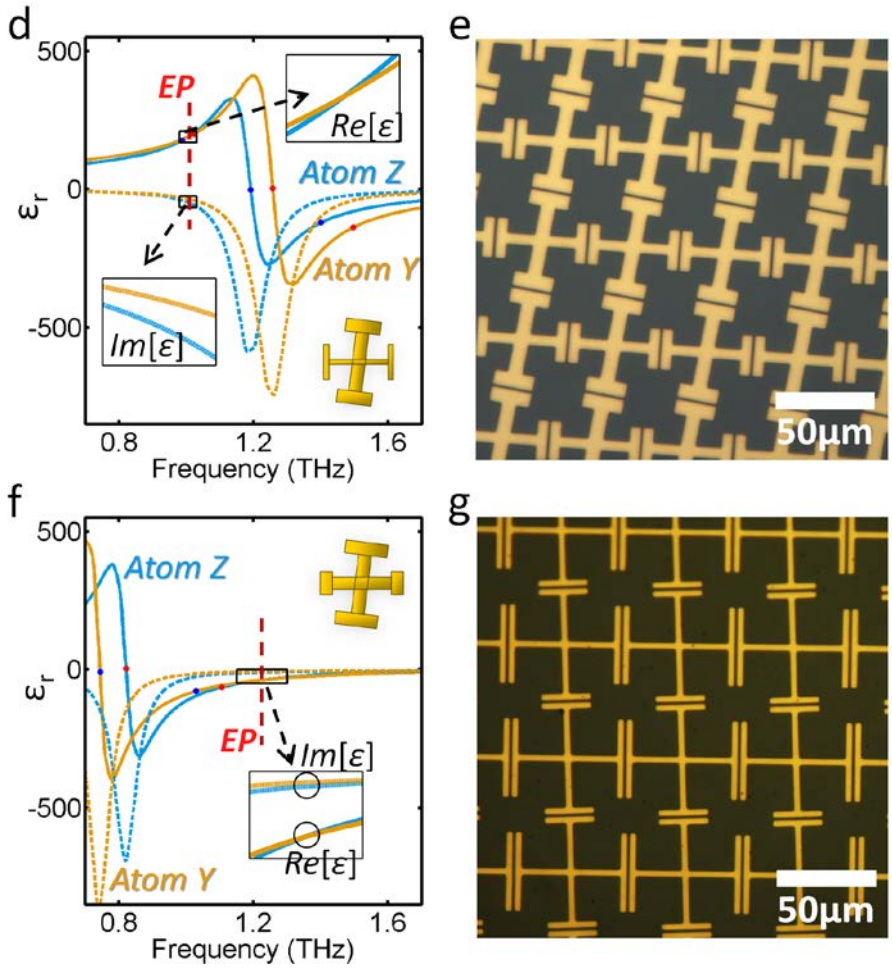

Figure 2.19 (continue). The effective anisotropic permittivity of chiral metamaterials: (d) the dielectric realization with propagating mode, and (f) the metallic realization with evanescent mode. The fabricated samples of a chiral metamaterial are shown in (e) and (g), respectively. Insets of (d) and (f) are the expanded images of the real and imaginary parts near the EP (red dotted line). The width of each polarized patch in (d),(e) is set unequally to w_y = 5.5 μm and w_z = 7.5 μm, and the other structural parameters are g = 1.0 μm, L = 34.5 μm, a = 20.5 μm, t = 100 nm, and d = 2 μm. The arm length of each polarized patch in f,g is set unequally to a_y = 25 μm and a_z = 40 μm, and the other structural parameters are g = 1.5 μm, L = 50 μm, w = 3.0 μm, t = 100 nm, and d = 2 μm. The fabrication and THz experiment are carried out by H. S. Park in B. Min's group in KAIST [45].

By controlling the value of θ, we can obtain the θ_{EP}, where the one-way chiral conversion occurs with $\varepsilon_{\kappa 0} = |\mathrm{Im}[\varepsilon_y - \varepsilon_z]|$, also known as the breaking of PT symmetry. The experimentally measured intermodal chirality $C_{IM}(\theta,\omega)$ is shown each for dielectric (Fig. 2.20a) and metallic (Fig. 2.20b) state design realization, and it is well-matched with the result given by COMSOL simulation (Figs. 2.20c and 2.20d, respectively). In both fabricated samples, θ_{EP} satisfying the one-way chiral conversion for the extremely sensitive EP are observed, as expected in simulation results (black dotted lines). For the dielectric state with propagating waves inside the metamaterial, the large C_{IM} = 17.4 dB is observed at $\theta_{EP} = 2.0^{\circ}$ (Fig. 2.20e), and from its tendency, we can expect a much higher C_{IM} value with the increased resolution in θ and with the sacrificed bandwidth. In the design in the metallic state with evanescent waves inside the metamaterial, the C_{IM} = 16.4 dB is observed at $\theta_{EP} = 1.6^{\circ}$. It is noted that despite the different propagating features of the two regimes, the exceptional point design derives the chiral interaction of light in terms of 'one-way chiral conversion' for both regimes, confirming the role of low-dimensionality with a singular chiral eigenstate. It is also worth mentioning that in both cases, the separated ***y*** and ***z*** local modes that are highly-concentrated within the gaps are well-converted to a single planewave-like beam due to the deep-subwavelength scale of the structure, conserving the pure spin angular momentum (or chirality) without additional orbital angular momentum.

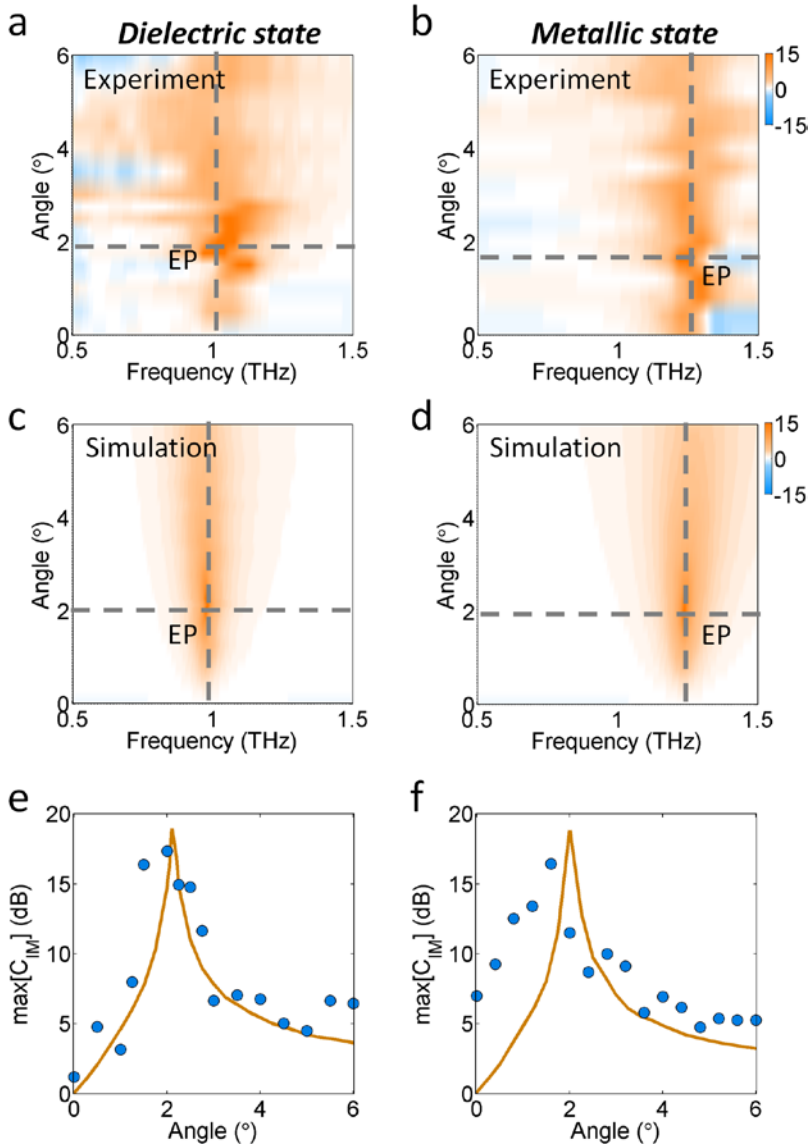

Figure 2.20. Observation of EP dynamics in chiral polar metamaterials [45]. The experimental (a,b) and the simulated (c,d) results of C_{IM} are shown in a spectral regime for dielectric (a,c) and metallic (b,d) realizations. The peak value of the C_{IM} as a function of θ is shown in e and f for each realization. The black dotted lines in (a)-(d) represent the condition of EPs in spectral and θ domains. All simulated results were obtained using COMSOL Multiphysics.

Extending the discussion to the guided-wave and the optical frequency, we propose a modal helix in an optical waveguide platform utilizing isotropic materials. The point-wise permittivity (Fig. 2.19a) is transplanted into the complex-strip waveguide as a passive form (Fig. 2.21a), where the lossy Ti layer (grey region, thickness t_{Ti}) under a lossless Si-strip waveguide imposes the selective decay of the $\boldsymbol{z}$ mode, which is well-separated from the $\boldsymbol{y}$ mode (Fig. 2.21b, ε_y for low-loss and ε_z for high-loss). The structural parameters are designed to satisfy $Re[\varepsilon_y] = Re[\varepsilon_z]$, and the coupling ε_{yz} is achieved with the deviation Δ, which breaks the orthogonality between the $\boldsymbol{y}$ and $\boldsymbol{z}$ polarized modes (see Appendix B.9 for detailed parameters). It is worth mentioning that the sign change of $\varepsilon_{\kappa 0}$ ($=\varepsilon_{yz}$) can also be controlled by the mirror offset of $-\Delta$ for the deterministic control of the handedness (Fig. 2.17c). Therefore, the chirality of the proposed modal helix has *directionality* from the sign reversal of Δ for the backward ($-\boldsymbol{x}$) view, which is absent in the structural helicity.

Figures 2.21c and 2.21d show the COMSOL-calculated modal chirality and the difference between eigenvalues as a function of the structural parameters (t_{Ti} and Δ). Because the control of the Ti layer alters the complex part of ε, the two structural parameters provide three degrees of freedom (Re[ε], Im[ε], and $\varepsilon_{\kappa 0}$), resulting in the single EP in the 2D parameter space (t_{Ti} = 19 nm, Δ = 91 nm, I_L/I_R = 21 dB, and 18 dB for modes 1 and 2). The finite modal chirality (~20 dB) originates in the separated intensity profiles of the $\boldsymbol{y}$ and $\boldsymbol{z}$ modes (Fig. 2.21b), resulting in the non-uniform local chirality (82 dB maximum, Fig. 2.21e). Therefore, the chiral guided-wave includes the additional orbital angular momentum from the varying wave-front, in contrast to the case of the subwavelength structure (Fig. 2.19), which supports a planewave. With an experimentally accessible geometry ($I_L/I_R \geq 10$ dB in Δ = 80~100 nm) and the coalescence of eigenmodes (Fig. 2.21d), the complex-strip waveguide will be an ideal building block for chiral guided-wave devices and for the utilization of active materials such as GaInAsP [85].

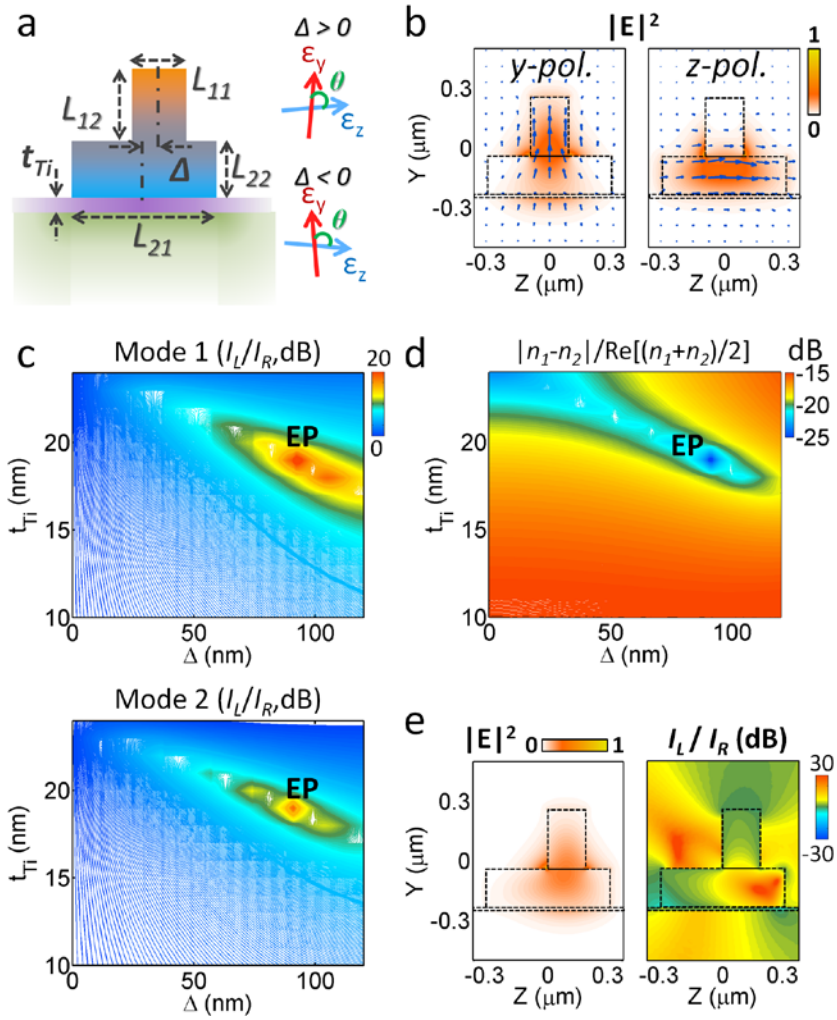

Figure 2.21. Chiral waveguides supporting bases of modal helices [45]. (a) Cross sections of a complex-strip waveguide using isotropic materials (graded color: Si for a lossless medium; purple: Ti for a lossy medium; green: silica substrate; graded color represents the effective loss by the Ti layer). The red and blue arrows describe a corresponding point-wise anisotropic permittivity. (b) The intensity profile and the polarization (in arrows) of the eigenmodes for the structure (ε_{yz}=0, Δ=0). (c) shows the modal chirality by I_L/I_R as a function of Δ and t_{Ti}. (d) The absolute value of the difference between eigenvalues as a function of Δ and t_{Ti}. The intensity profile and the local chirality ($I_L(y,z)$ / $I_R(y,z)$) at the EP are shown in e. All results were obtained using COMSOL Multiphysics with an optical wavelength of Λ_0=1500 nm.

In this section, we proposed and investigated a new class of optical chirality based on the physics of complex potentials [45] without any bi-anisotropic mixing of electric and magnetic dipoles. Based on the mixing of amplifying and decaying responses and on the presence of the low-dimensional eigenmode at the EP, exotic chiral behaviors such as one-way CP convergence and chirality reversal are observed, which cannot be observed in conventional chiral [110, 111] or gyrotropic [117] materials. It is noted that the reduced dimensionality also enables reflectionless CP generation following the dynamics of optical spin black holes, which is impossible in conventional approaches based on Hermitian elements [93]. We also emphasize that our result, supporting the saturation of linear polarizations to a single circular polarization, is distinct from the reinterpretation of chirality [32] using nonlocal complex potentials, which maintains optical activity for linear polarizations.

We demonstrated the physics of low-dimensional chirality by using ultrahigh index polar metamaterial with two design strategies: utilizing propagating and evanescent waves. The results prove the existence of EP and the one-way chiral conversion in the spectral regime, and the manipulation of the angular property is achieved. As an application, a chiral waveguide using isotropic materials is also proposed, which can be achieved by transplanting the point-wise anisotropic permittivity of an ideal complex-potential.

Our findings of low-dimensional chirality will pave a new route toward chiral devices, such as on-chip guided-wave devices for chiral lasers, amplifiers, and absorbers as well as complex chiral metamaterials and topological phases. Based on the general framework of non-Hermitian physics [118], we note that our work can be further extended using different polarization bases (Appendix B.10) to enable SOP collection for the arbitrary designer polarization. We can also envisage the manipulation of orbital angular momentum of light, based on PT-symmetric configuration.

2.3.2 Interpretation of PT-symmetry in *k*-space

Optical modes are one of the critical features for defining the flow of light by determining the 'momentum' (or wavevector k) of photons for a given spatial distribution of optical potentials. In the context of light-matter interactions, the manipulation of optical modes and wavevectors through the modulation of refractive index landscapes (or optical potentials) is not only a classical subject, as observed in a diffraction grating [119], but is also an emerging area of research involved in recent discoveries in the field of optics, e.g., subwavelength plasmonics [120] and indefinite metamaterials [121, 122] with high-k components, optical Bloch oscillations [13, 123] based on a graded-k design, bio-mimic reflective surface [124] with randomly-distributed k, and drastic optical manipulation [125] using modal orthogonality. Although extremely encouraging, all of these achievements were obtained by controlling only the real-valued optical potentials within the well-known restriction of Hermiticity [47] in quantum mechanics and optics for real eigenvalues. Because real potentials correspond only to double-sided spectra in Fourier space, the considerable opportunities afforded by complex potentials of generalized spectra have been overlooked.

Because PT-symmetric optics were initially developed as an effective model of quantum-mechanical problems [33], optical potentials in subsequent PT-symmetric applications have been designed to simply fulfill the condition of $V(x) = V^*(-x)$, which is derived from the commutative relation between PT and the Hamiltonian operators for a Schrödinger-like equation [42]. Interestingly, however, investigations of the PT-symmetric potential $V(x)$ in the Fourier domain, which has the intriguing consequence that the *potential momentum of* $F\{V(x)\}$ *is real-valued*, for example, have not been attempted. Because the directional shift in *momentum* space is the underlying physics of PT-symmetric optical phenomena, a more thorough investigation of the potential momentum $F\{V(x)\}$ will provide new insight into PT-symmetric optics in terms of momentum interactions between light and potentials.

In this section, we propose a novel pathway toward *unidirectional coupling* in *k*-space in the context of light-matter momentum interactions to demonstrate the role of potential momentum $F\{V(x)\}$ [51]. We start from the general problem of light excursions in *k*-space, focusing on 'unidirectional modal transitions' along the isofrequency contour (IFC). Under the weak-coupling regime, we then demonstrate that 'causality' in potential momentum space, *i.e.*, causal potential momentum, produces a unidirectional *k*-transition of light inside the IFC *k*-continuum, corresponding to exceptional point (EP) dynamics on the degree of PT symmetry. Our results provide a logical mechanism for understanding PT symmetry through spectral analysis and enable the 'design' of momentum shifts through potential modulations rather than the 'observation' of momentum shifts at given PT-symmetric potentials, thereby providing designers control of optical modes, such as for collimated beam steering or excitations in the extreme regime of low- or high-*k* states.

Figure 2.22 shows examples of light excursions in *k*-space. Because the wavevector *k* affects the direction and effective wavelength of wave propagation, applications such as beam steering (controlling the direction, Figs. 2.22a and 2.22b) and high- / low-*k* excitation (controlling the wavelength, Fig. 2.22c and Fig. 2.22d, respectively) could be enabled through modification of wavevectors. To tailor the evolution of the optical state in *k*-space, we address the unidirectionality for the modal transition along the IFC (red arrows in Fig. 2.22), which suppresses the back transfer (gray arrows in Fig. 2.22) to the initial state, thereby efficiently delivering optical energy into the targeted mode. Notably, the unidirectional modal transition can be understood in the context of the relation between 'cause' (the initial state excited with incident waves) and 'effects' (the directionally excited states from the serial and unidirectional coupling) along the IFC, which naturally leads to the concept of *causality* (Fig. 2.22e). Note that in the following discussions, we employ the notion of causality in the *k*-axis (red arrows in Fig. 2.22e) rather than the time axis, *i.e.*, causal momentum, as used in non-temporal applications in

image processing and mathematics.

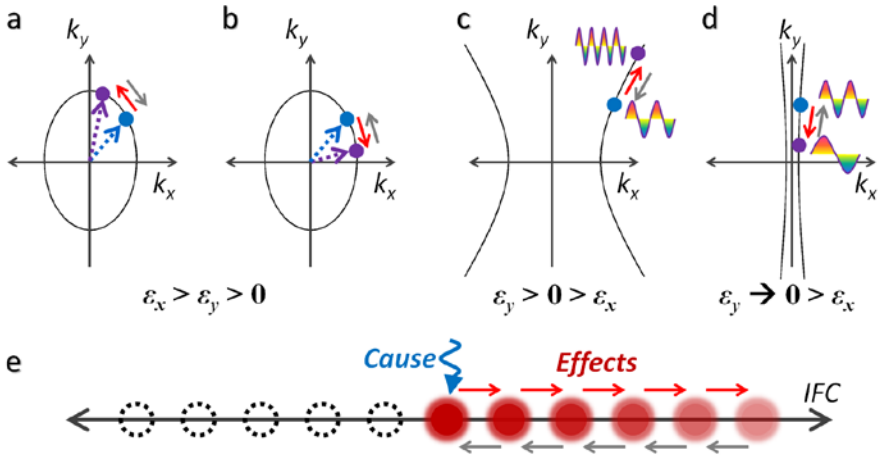

Figure 2.22. Schematics of one-way transitions [51] along (a, b) elliptic, (c) hyperbolic, and (d) quasi-linear IFCs. (a) Counterclockwise and (b) clockwise transitions; dotted lines denote the direction of the flow of light for beam steering. (c) High-k and (d) low-k excitations. Blue (or purple) circles denote the initial (or excited) state for each IFC. (e) Schematic linking one-way optical transition with causality. Red (or gray) arrows show allowed (or forbidden) transitions along the IFC in (a-e).

To investigate the relationship between one-way transitions and causality, by generalizing the continuous coupled mode theory [72] to 2-dimensional anisotropic materials, we derive the coupled mode equation for analyzing the coupling and energy transfer between optical modes. Without loss of generality, we consider a TM-polarized wave in a nonmagnetic anisotropic material (H_z, E_x, and E_y with $\varepsilon_{x,y}$) that produces a k-continuum for an elliptic IFC [2] (Figs. 2.22a and 2.22b), a hyperbolic IFC [126] (Fig. 2.22c), or a quasi-linear IFC with extreme anisotropy [127] (Fig. 2.22d) in k-space. Here, we apply two standard approximations to the time-harmonic wave equation at a frequency ω: a weak ($|\Delta\varepsilon_{x,y}(x,y)| << |\varepsilon_{x0,y0}|$, where $\varepsilon_{x,y}(x,y) = \varepsilon_{x0,y0} + \Delta\varepsilon_{x,y}(x,y)$) and a slowly-varying modulated potential ($|\Delta\varepsilon_y^{-1}\cdot\partial_x\Delta\varepsilon_y| << |k_x|$ and $|\Delta\varepsilon_x^{-1}\cdot\partial_y\Delta\varepsilon_x| << |k_y|$). We use the IFC relation of $k_0^2 = k_x^2/\varepsilon_{y0} + k_y^2/\varepsilon_{x0}$,

where $k_0 = \omega/c$ is the free-space wavenumber, to derive the following expression (see Appendix C.1)

$$\iint (\vec{\beta}_{\vec{k}} \cdot \vec{\sigma}_{\vec{k}}(x,y))\psi_{[k_x,k_y]} e^{-i(k_x x + k_y y)} dk_x dk_y = 2i \cdot \iint \nabla \cdot (\vec{\beta}_{\vec{k}} \psi_{[k_x,k_y]}) e^{-i(k_x x + k_y y)} dk_x dk_y , \tag{2.20}$$

where $\psi_{[kx,ky]}$ is the spatially varying envelope of the magnetic field imposed on the planewave solution $exp(-ik_x \cdot x - ik_y \cdot y)$ as $H_z(x,y) = \iint \psi_{[kx,ky]}(x,y) \cdot exp(-ik_x \cdot x - ik_y \cdot y) dk_x dk_y$, $\boldsymbol{\beta_k} = (k_x \cdot \varepsilon_{y0}^{-1})\boldsymbol{x} + (k_y \cdot \varepsilon_{x0}^{-1})\boldsymbol{y}$ is the ε-normalized wavevector, and $\boldsymbol{\sigma_k}(x,y) = (k_x \cdot \Delta\varepsilon_y(x,y)/\varepsilon_{y0})\boldsymbol{x} + (k_y \cdot \Delta\varepsilon_x(x,y)/\varepsilon_{x0})\boldsymbol{y}$ is the local modulation vector. Equation (2.20) clearly shows the source of the modal transitions $\boldsymbol{\beta_k} \cdot \boldsymbol{\sigma_k}(x,y)$ that induce the locally modulated envelope $\nabla\psi$. Additionally, note that $\psi_{[kx,ky]}$ corresponds to the amplitude of the k-space optical mode $\boldsymbol{k} = (k_x, k_y)$.

With the Fourier expansion ($\Delta\varepsilon_{pq}(p,q)$) of the modulated potential $\Delta\varepsilon(x,y)$ and the use of the divergence theorem, the 2-dimensional coupled mode equation between the optical modes of $\boldsymbol{k} = (k_x, k_y)$ and (k_{x-p}, k_{y-q}) is obtained as

$$\begin{aligned} &8\pi^2 i \cdot \oint_S \psi_{[k_x,k_y]} \vec{\beta}_{\vec{k}} \cdot d\vec{s} \\ &= \int_V \iiint_{-\infty}^{\infty} \left(\frac{(k_x - p)^2 \Delta\varepsilon_{ypq}}{\varepsilon_{y0}^2} + \frac{(k_y - q)^2 \Delta\varepsilon_{xpq}}{\varepsilon_{x0}^2} \right) \psi_{[k_x - p, k_y - q]} dp dq dv \end{aligned} . \tag{2.21}$$

Equation (2.21) defines the coupling *along* the IFC $k_0^2 = k_x^2/\varepsilon_{y0} + k_y^2/\varepsilon_{x0}$ (including the multipath coupling through $\Delta\varepsilon_{pq}(p,q)$ with a finite bandwidth) and can be used to derive the criterion for the *directional* coupling that prohibits back transfers (gray arrows in Fig. 2.22). Note that the potential momentum $\Delta\varepsilon_{pq}$ in Eq. (2.21) mediates the coupling between states, and a highly efficient unidirectional modal transition can be obtained by enforcing a restriction in potential momentum space (p,q), such as $\Delta\varepsilon_{pq} \neq 0$ only for a single quadrant, to achieve a zero value for

the integral of the back transfer. Such a restriction can indeed be realized with the causality condition in multi-dimensions by replacing the axis condition $k > 0$ with the quadrant condition $k_x > 0$ and $k_y > 0$, defined by the multi-dimensional Hilbert transform for single orthant spectra [128, 129]. The selection of a nonzero quadrant is also clearly determined by the transition direction, e.g., the high-k excitation toward larger k (the red arrow in Fig. 2.22c) is produced by restricting the potential momentum to the 1st quadrant ($p,q \geq 0$), whereas the low-k excitation toward smaller k (red arrow in Fig. 2.22d) is produced by selecting the 3rd quadrant spectrum ($p,q \leq 0$). The implementation of the aforementioned conditions in the momentum and spatial domains can easily be achieved by employing the multi-dimensional Hilbert transform for single orthant spectra, such as $\Delta\varepsilon_{pq} = [1 \pm sgn(p) \pm sgn(q) + sgn(p)\cdot sgn(q)]\cdot\Delta\varepsilon_{rpq}(p,q)/4$, where the upper (lower) sign refers to the high- (low-) k excitation, $\Delta\varepsilon_{rpq}^{*}(-p,-q) = \Delta\varepsilon_{rpq}(p,q)$, where $\Delta\varepsilon_r(x,y) = (1/4\pi^2) \cdot \iint\Delta\varepsilon_{rpq}(p,q) \cdot exp(-ipx-iqy)dpdq$ is a real function. In the spatial domain, the "unidirectional coupling potentials" for the low-k and high-k excitations then become

$$\Delta\varepsilon_{L,H}(x,y) = \frac{1}{4}\left(\Delta\varepsilon_r(x,y) - \frac{1}{\pi^2}\int_{-\infty}^{\infty}\int_{-\infty}^{\infty}\frac{\Delta\varepsilon_r(x',y')}{(x-x')(y-y')}dx'dy'\right) \pm \frac{i}{4\pi}\left(\int_{-\infty}^{\infty}\frac{\Delta\varepsilon_r(x',y)}{x-x'}dx' + \int_{-\infty}^{\infty}\frac{\Delta\varepsilon_r(x,y')}{y-y'}dy'\right), \quad (2.22)$$

or simply $\Delta\varepsilon_{L,H} = \{[\Delta\varepsilon_r - H_T(\Delta\varepsilon_r)] \pm i[H_{px}(\Delta\varepsilon_r) + H_{py}(\Delta\varepsilon_r)]\}/4$, where $\Delta\varepsilon_L$ ($\Delta\varepsilon_H$) is the potential for the low- (or high-) k excitation with the upper (or lower) sign, and H_T (or H_p) is the total (or partial) Hilbert transform. We emphasize that Eq. (2.22) not only reveals that complex potentials in the spatial domain are essential for producing unidirectional modal transitions but also that the PT-symmetric complex potentials of $\Delta\varepsilon_0\cdot exp(-ip_0x)$ that have been previously studied are only a manifestation of a special case, i.e., pointwise unidirectional coupling ($\Delta\varepsilon_{rp} = \Delta\varepsilon_0\cdot\pi[\delta(p-p_0) + \delta(p+p_0)]$) in a 1-dimensional problem. Note that our formalism

based on potential momentum causality allows the deterministic design of potentials for unidirectional modal transitions: from the $\Delta\varepsilon_{rpq}$ in potential momentum space. This condition in 2-dimensional space can easily be extended to isofrequency 'surfaces' in 3-dimensional problems by employing a 3-dimensional Hilbert transform [128, 129].

Most importantly, Eq. (2.22) offers the link between PT symmetry and causality in potential momentum space, which, to the best of our knowledge, has not been previously elucidated. The unidirectional coupling potentials of Eq. (2.22) from causality satisfy the necessary condition for PT symmetry $\Delta\varepsilon_{L,H}(x,y) = \Delta\varepsilon_{L,H}^{*}(-x,-y)$ and also guarantee real-valued spectra in momentum space (p,q). Because 'perfect' modal unidirectionality in PT-symmetric potentials is achieved only at the EP [43, 44] where PT symmetry breaking occurs, we note that the causality potentials of Eq. (2.22) that have unidirectionality correspond to the EP on the degree of PT symmetry (within the approximations of weak and slowly varying modulation; see Appendix C.1). Accordingly, the regimes before and after the EP correspond to *noncausal*, real-valued spectra in potential momentum space.

We illustrate the aforementioned results with a PT-symmetric potential $\Delta\varepsilon_s(x,y)$ in space, where $Re[\Delta\varepsilon_s]$ (or $Im[\Delta\varepsilon_s]$) is an even (or odd) real-valued function that satisfies the precondition $\Delta\varepsilon_s(x,y) = \Delta\varepsilon_s^{*}(-x,-y)$. The potential momentum $\Delta\varepsilon_m(p,q) = F\{\Delta\varepsilon_s(x,y)\}$ is then expressed by the sum of real-valued functions as $\Delta\varepsilon_m(p,q) = \Delta\varepsilon_{m\text{-}even}(p,q) + \Delta\varepsilon_{m\text{-}odd}(p,q)$, where $\Delta\varepsilon_{m\text{-}even} = F\{Re[\Delta\varepsilon_s(x,y)]\}$ is an even function and $\Delta\varepsilon_{m\text{-}odd} = -Im[F\{Im[\Delta\varepsilon_s(x,y)]\}]$ is an odd function. To clarify the relation between the degree of PT symmetry and the potential momentum, we assume a potential for which the real and imaginary parts of $\Delta\varepsilon_s(x,y)$ with a Gaussian envelope $\Delta\varepsilon_s(x,y) = [\Delta\varepsilon_{sr0} \cdot cos(p_0x + q_0y) + i\Delta\varepsilon_{si0} \cdot sin(p_0x + q_0y)] \cdot exp(-(x^2+y^2)/(2\sigma^2))$, where both $\Delta\varepsilon_{sr0}$ and $\Delta\varepsilon_{si0}$ are real values and $\Delta\varepsilon_{sr0} = \Delta\varepsilon_{si0}$ at the EP. Figure 2.23 shows the calculated potential momentum at each different degree of PT symmetry. Although the spectrum of the potential momentum satisfies causality ($p,q \geq 0$) at the EP (Fig. 2.23a), the potentials of the

regimes before (Fig. 2.23b) and after (Fig. 2.23c) the EP break causality. In this respect, the concept of PT symmetry breaking can be interpreted as a phase transition from an *in-phase* potential momentum spectrum to an *out-of-phase* potential momentum spectrum (Fig. 2.23b vs. 2.23c) separated by the causal phase (Fig. 2.23a). Note that this interpretation provides an intuitive understanding of the degree of PT symmetry, providing a perspective not restricted to the relative magnitude between the real and imaginary parts of the potentials but rather from a direct spectral analysis of the 'degree of the causality' for the real-valued potential momentum. Furthermore, with the multi-dimensional expression of Eq. (2.22), our results allow the multi-dimensional extension of the PT-symmetric condition to overcome the one-dimensional effective model based on the paraxial wave equation that is commonly used in the description of PT-symmetric optics [57].

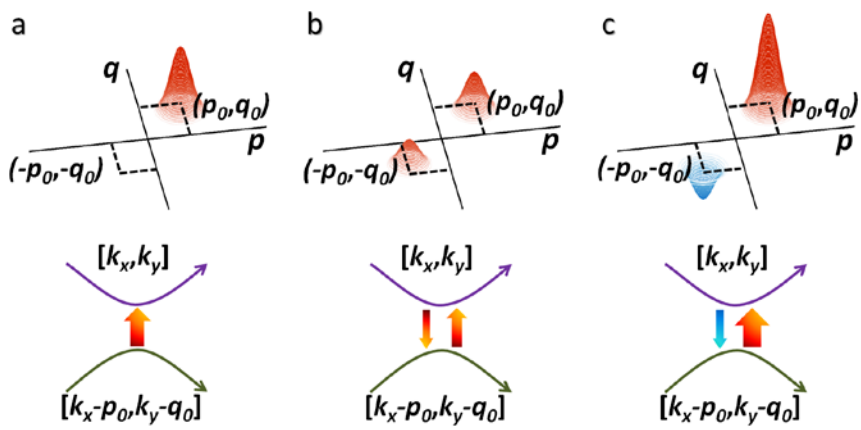

Figure 2.23. Potential momentum spectra for degrees of PT symmetry [51]: (a) at the EP ($\Delta\varepsilon_{sr0} = \Delta\varepsilon_{si0}$), (b) before the EP ($\Delta\varepsilon_{sr0} > \Delta\varepsilon_{si0}$), and (c) after the EP ($\Delta\varepsilon_{sr0} < \Delta\varepsilon_{si0}$). Lower figures illustrate the corresponding coupling between momentum states for each degree. Green (purple) solid line denotes the momentum state that corresponds to the 'cause' ('effect'). As shown, causality is only maintained at the EP. Gaussian spectra with $\sigma = 0.25$ and $p_0 = q_0 = 1$ are assumed, without loss of generality.

Without loss of generality, we investigate a case of high-*k* excitations along

the hyperbolic IFC ($p,q \geq 0$, Fig. 2.22c). Although high-k features of hyperbolic metamaterials provide an ideal template for subwavelength imaging [121] or light confinement [130], the large mismatch in k-vector hinders the excitation of high-k modes in the indefinite IFC [131]. Here, we apply the unidirectional modal transition for the adiabatic transfer of optical energy to the high-k state. A y-axis-invariant wave incident on a unidirectional potential ($x \geq 0$) from the left side ($k_{x0} > 0$) is considered, as illustrated in Fig. 2.24a. Note that potentials of arbitrary shape can be accommodated by discretizing the potential in both the spatial (Fig. 2.24a) and momentum (Fig. 2.24b) domains. By setting the y-infinite unit volume V with a deep-subwavelength spatial discretization Δx, the surface integral of Eq. (2.21) is determined on the $S_L(x_L)$ and $S_R(x_R)$ surfaces, and the volume integral can be evaluated from the average of the values in S_L and S_R. The discretization for the momentum states was also performed on the IFC (circles in Fig. 2.24b) from the phase-matching condition. The discretized form of Eq. (2.21) is then expressed as

$$\int_{S_R} \psi_m(x_R, y)dy = \int_{S_L} \psi_m(x_L, y)dy + \sum_{n=1}^{m} \frac{\varepsilon_{y0}\Delta x \cdot \Delta p_n \Delta q_n}{16\pi^2 i k_{xm}} \cdot \left(\frac{{k_{xn}}^2 \Delta\varepsilon_{ypq}}{\varepsilon_{y0}^2} + \frac{{k_{yn}}^2 \Delta\varepsilon_{xpq}}{\varepsilon_{x0}^2} \right) \cdot \int_{S_L+S_R} \psi_n dy, \quad (2.23)$$

where the subscript m denotes the m-th momentum state of (k_{xm},k_{ym}); $n = 1$ is the incident state; $p = k_{xm} - k_{xn}$; $q = k_{ym} - k_{yn}$; $\Delta p_n = k_{x(n+1)} - k_{xn}$; and $\Delta q_n = k_{y(n+1)} - k_{yn}$. Equation (2.23) can be used to perform a serial numerical calculation for the integral of the envelope, starting from the left boundary (detailed procedure for the serial calculation is provided in the Appendix C.2). As a result of the causality condition that is imposed on $\Delta\varepsilon_{pq}$, only the eigenstates on the bounded region of the IFC (blue circles in Fig. 2.24b) participate in the coupling to the (k_x,k_y) state.

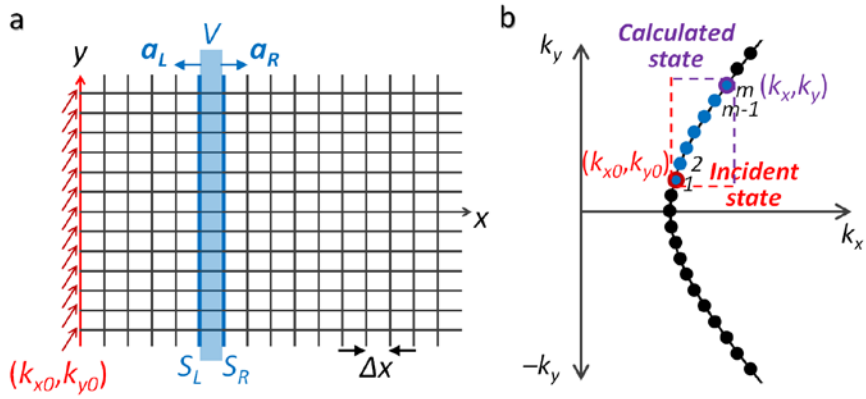

Figure 2.24. Discretization of (a) spatial and (b) momentum domains for the derivation of Eq. (2.23) [51]. S_L and S_R present the left and right surfaces, respectively, of the unit volume V (in blue). A wave with a unit amplitude (at the (k_{x0},k_{y0}) state, shown by red arrows in (a)) is incident on the left side of the spatial domain. Circles in (b) represent discretization in momentum space. Blue circles denote states that participate in the coupling to the calculated state (k_x, k_y).

The high-k excitation process is shown in Fig. 2.25. For general curvilinear IFCs, the transition through the multiple linear-path coupling should be adopted, as shown in the example presented in Fig. 2.25a. In this specific example, we assume a potential modulation that provides five real-valued momentum spectra (Fig. 2.25b) for multiple transitions. A finite bandwidth is used for each spectrum to accommodate quasi-phase matching. Figures 2.25c and 2.25d show the amplitude and phase of the complex potential given by Eq. (2.22) and present the confinement in space from the finite bandwidth and the mixed phase evolution from the multi-harmonics.

Figures 2.25e and 2.25f present the results for high-k excitations in k-space at the point $x = 100\lambda_0$ for different bandwidths of the potential momentum spectra. The variation in the effective index along the x-axis is illustrated in Fig. 2.25g, using $n_{eff}(x) = \iint n(k_x,k_y)\cdot|\psi_{[kx,ky]}(x)|^2 dk_x dk_y \;/\; \iint|\psi_{[kx,ky]}(x)|^2 dk_x dk_y$ and the excited envelopes at each x value. For all cases, successful multistage delivery of optical energy to the high-k regime is observed and is found to be more efficient for larger

modulation depths (Fig. 2.25g). Notably, even the higher-k states are excited above the targeted final (5^{th}) state (black dotted line in Fig. 2.25g), which results from the linear asymptotic behavior of the hyperbolic IFC ($k_y \sim (-\varepsilon_x/\varepsilon_y)^{1/2} \cdot k_x$) that alleviates the phase-matching condition in the high-k regime. This result indicates that a perpetual transition to higher-k states becomes possible for the hyperbolic IFC, provided that the minor phase-mismatch is compensated by the bandwidth of the modulation spectra, as evidenced by the superior excitations in the high-k regime with the application of broadband potentials (solid vs. dotted lines after the arrows in Fig. 2.25g).

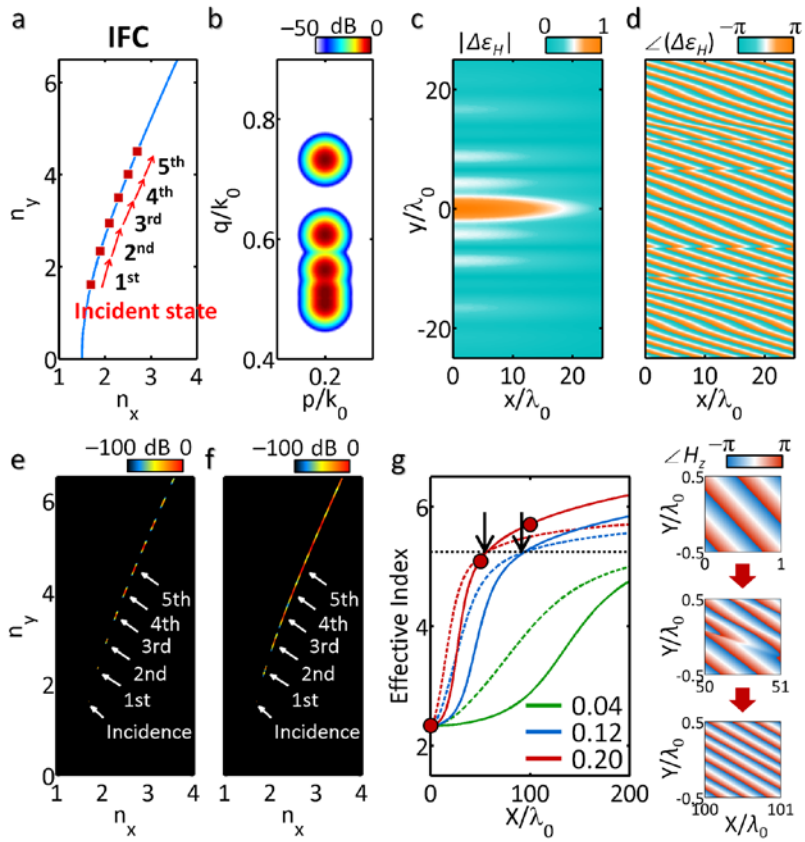

Figure 2.25. High-k excitations along the hyperbolic IFC ($\varepsilon_{x0} = -9$, $\varepsilon_{y0} = 2.25$) [51]. (a) Design strategy with 5-stage transitions. (b) Normalized real-valued momentum spectra of $\Delta\varepsilon_{pq}$ (Gaussian bandwidth of $\sigma_{x,\,y} = k_0/100$ for each spectrum). (c) Normalized amplitude and (d) phase of the corresponding complex potential in the spatial domain. The profile of momentum spectra in (b) is assigned to both $\Delta\varepsilon_{xpq}$ and $\Delta\varepsilon_{ypq}$. The amplitude of the envelopes in momentum space at $x = 100\lambda_0$ are shown for different bandwidths of (e) $\sigma_{x,\,y} = k_0/200$ and (f) $\sigma_{x,\,y} = k_0/100$. (g) Variation in the effective index along the x-axis for different bandwidths (solid lines show $\sigma_{x,\,y} = k_0/100$, and dotted lines show $\sigma_{x,\,y} = k_0/200$). The phase of the magnetic field at each position (red circles in 4 g) is also shown in the right panel of (g). Maximum values of modulations are $\Delta\varepsilon_x(x, y)/\varepsilon_{x0} = \Delta\varepsilon_y(x, y)/\varepsilon_{y0} = 0.04$, 0.12, and 0.20. Discretization parameters at the deep-subwavelength scale are $\Delta x = \lambda_0/50$, $\Delta k_y = k_0/100$, and $\Delta p = \Delta q = \sigma_{x,\,y}/10$ for all cases.

Figure 2.26 shows another application to definite materials, in which selective

transitions are determined by the lateral component k_y of the wavevector. For clockwise beam steering along the elliptic IFC (Fig. 2.26a, with the nonzero 4th quadrant of (p,q) space), the transition is allowed only within the 1st quadrant of the IFC, as can be clearly observed from the transition states (red squares) along the IFC. Figure 2.26b shows the beam trajectories in spatial domain calculated from Eq. (2.23) and confirms that strong, selective beam steering occurs only with lateral positive wavevector components k_{y0}, as predicted. In contrast to the high-k excitation example with asymptotic behavior (Figs. 2.25e-2.25g), we note that in this case, selective convergence toward the final k state is obtained, facilitating asymmetric steering and collimation of the beam (blue solid lines, angular bandwidth from 44° to 17°).

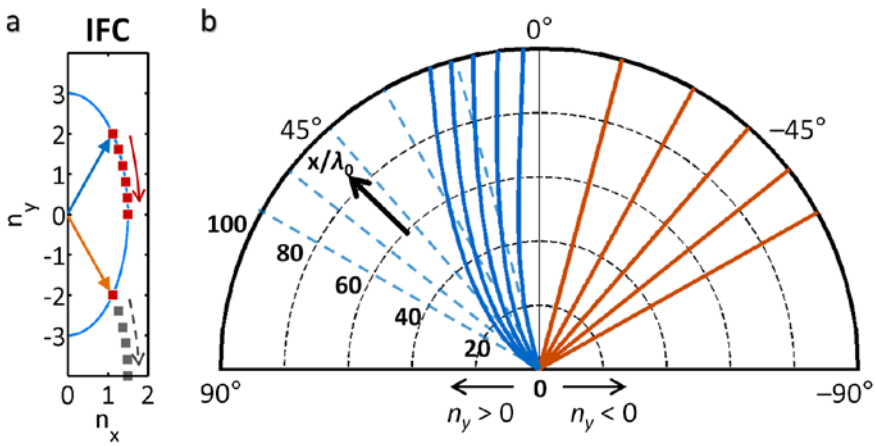

Figure 2.26. Asymmetric beam steering and collimation in the elliptic IFC (ε_{x0} = 9, ε_{y0} = 2.25) [51]. (a) IFC with 5-stage transitions. Red (gray) squares denote allowed (forbidden) states for the transition. (b) Beam trajectories (solid lines) for different incidences of $n_y > 0$ (blue dotted lines) and $n_y < 0$ (orange). $\varepsilon_x(x, y)/\varepsilon_{x0} = \varepsilon_y(x, y)/\varepsilon_{y0}$ = 0.2 and $\sigma_{x,y} = k_0/200$. All other parameters of the potential are the same as those presented in Fig. 2.25.

In this section, we developed and analyzed the unidirectional excursion of excited states along the k-continuum to extend the engineering of optical potentials into the complex domain of generalized spectra [51]. We derived the condition for

unidirectional k-transitions within the context of optical and potential momentum interactions, and then we expand the interpretation of a singular PT-symmetric potential as the causal potential of real-valued momentum spectra.

Our approach offers a fundamental understanding of the degree of PT symmetry in terms of *causal momentum interactions* between light and potentials to allow the multi-dimensional extension of the PT-symmetric condition, and provides us with the ability to tailor optical evolution in k-space via *unidirectional* complex potentials directly designed in k-space. We have demonstrated novel applications, such as excitations in the extreme k regime and asymmetric beam steering and collimation. A further application for complex potentials could be made in the frequency ω domain, i.e., using time-varying complex potentials for temporal non-Hermitian dynamics. It is envisaged that the relation between causality and a *complex* potential momentum may also provide a clue to the physical interpretation of *non*-PT-symmetric potentials with real spectra [50].

2.4 Conclusion

In this chapter 2, we reviewed our researches in the field of PT-symmetric optics. Through our 4 subjects – (1) chirped potential [44], (2) N-level potential [46], (3) optical spin-angular momentum [45], and (4) causality in k-space [51], – we have tried to understand intriguing phenomena in PT-symmetric potentials in the context of distinctive eigensystems: skewness, low-dimensionality, chirality, and unidirectional intermodal conversion. In recent works, there have been serious efforts to constitute the originality of PT-symmetric optics compared to PT-symmetric quantum mechanics: such as optical potentials including permeability and permittivity [132], PT-symmetric metasurfaces [62], and plasmonic PT-symmetric potentials [133]. Our generalized frameworks can not only be helpful for the understanding of these works, but also allow the connection with recent topics on eigenvalue problems in optics: such as supersymmetry [50, 134, 135] or the topology of eigenstates [27].

Chapter 3

Disordered Optics

The investigation of periodic systems based on Bloch's theorem [136, 137] has enabled the intuitive understanding of solids in wave physics. The analysis of Bloch waves had explained the existence of bandgaps in electronic crystals, allowing the classification of materials in solid state physics: insulators, semiconductors, and metals, according to the width of the bandgap. This result has also been applied to optics in the context of optical analogy of quantum mechanics: especially devising the notion of photonic crystals [5].

However, the finding of quasicrystals [138] and amorphous materials [139] derived the paradigm shift, due to the existence of newly-folded diffraction patterns [138] and bandgaps [139] without any help of the periodicity. These surprising results demonstrated that the periodicity is a narrow notion to cover all the 'ordered' wave dynamics. We should focus on the notion of the 'order' itself, the concept of not only including the periodicity but also containing determined actions without the periodicity (e.q. quasicrystals [138]) and probabilistic tendencies (e.g. amorphous materials [139]). This extension of the concept enables the design of ordered wave dynamics in disordered potentials (such as aperiodic

potentials without long-range correlations).

In this chapter, we introduce our researches in disordered optics; which treats intriguing phenomena in disordered optical potentials. After the brief review of previous works (section 3.1), we introduce the design of bandgap dynamics with tunable disorder, based on the notion of supersymmetry (section 3.2, [140]). We then show the biomimetic example of disordered optics: the analogy of Morpho butterfly (section 3.3, [124]).

3.1 Introduction to disordered optics

The physical origin of intriguing phenomena in disordered optics is fundamentally based on the Fourier relation between spatial and momentum space. Due to the disorder in space, various k components of optical potentials are obtained, being spread out in a whole system. Therefore, in the context of light-matter interactions, the spatial and spectral distribution of k components is the underlying physics determining the degree of disorder, which can also be quantified by the spatial correlation of optical potentials.

Using the spread k components, there are two categories in disordered optics: wideband operation in spatial and spectra domain (Fig. 3.1a, [141]) and Anderson localization exploiting high-k components (Fig. 3.1b, [142]). In both subjects, the performance of applications can be manipulated in terms of the degree of disorder: allowing the intermediate regime between ordered and disordered wave dynamics (Fig. 3.1a: distinctive absorption spectra in periodic, amorphous, and random potentials, Fig. 3.1b: tunable confinement as a function of the degree of disorder).

In the section 3.2, we propose a novel topic: bandgap design in disordered potentials with tunable degrees of disorder, by utilizing the notion of supersymmetry [140]. In the section 3.3, we show a new-type of disordered potentials: wideband k-space but narrowband ω-space, by employing the biomimetics of Morpho butterfly [124].

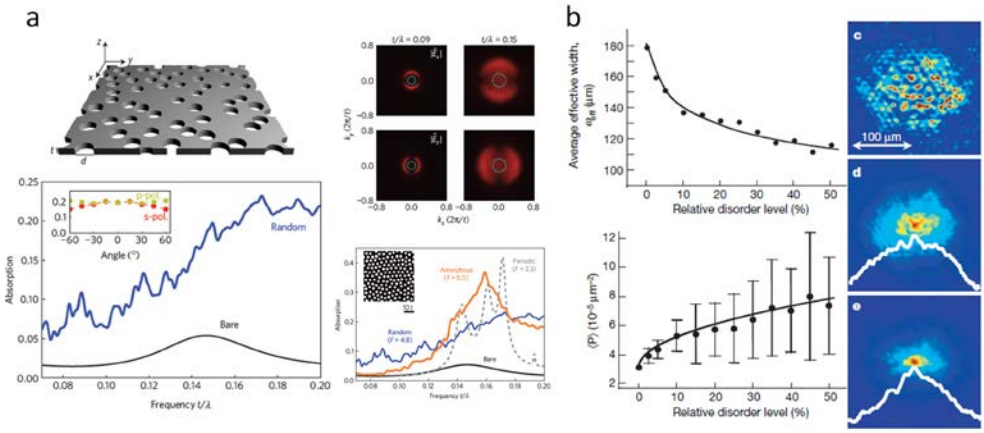

Figure 3.1. The examples of disordered optics: (a) broadband and efficient optical absorbers based on wideband *k*-spectra [141]. (b) Anderson localization based on large *k* components which originate from the random-walk interference [142].

3.2 Supersymmetric bandgap in disorder

The isospectral problem posed via the question "Can one hear the shape of a drum?" [143] introduced many fundamental issues regarding the nature of eigenvalues (sound) with respect to potentials (the shapes of drums). Following the demonstration presented in, it was shown that it is not possible to hear the shape of a drum because of the existence of different drums (potentials) that produce identical sounds (eigenvalues), *a.k.a.* isospectral potentials [144]. Although the isospectral problem has deepened our understanding of eigenstates with respect to potentials and raised similar questions in other physical domains [145], it has also resulted in various interesting applications such as the detection of quantum phases [146] and the modeling of anyons [147].

The field of supersymmetry (SUSY, [148]) shares various characteristics with the isospectral problem. SUSY, which describes the relationship between bosons and fermions [148], has been treated as a promising postulate in theoretical particle physics that may complete the Standard Model. Although the experimental

demonstration of this postulate has encountered serious difficulties and controversy, the concept of SUSY and its basis of elegant mathematical relations have given rise to remarkable opportunities in many other fields, e.g., SUSY quantum mechanics [149] and topological modes [150]. Recently, techniques of SUSY quantum mechanics have been utilized in the field of optics [49, 50, 134, 140, 151-159], thereby enabling novel applications in phase matching and isospectral scattering [151, 154, 159], complex potentials with real spectra [50], and complex Talbot imaging [49].

In this section, we propose a supersymmetric path to the generation of Bloch-like waves and bandgaps without the use of Bloch's theorem [140]. In contrast to approaches based on an iterative search for random networks with bandgaps [160-165], a deterministic route toward bandgap creation in the case of disordered potentials is achieved based on the fundamental wave equation. This result not only demonstrates that long-range correlation is a sufficient but not a necessary condition for Bloch-like wave dynamics but also enables the design of random-walk potentials with bandgaps. Such designs can facilitate the creation of a 'Bloch wave family' with identical bandgaps and tunable long-range correlations, even extending to conditions of extreme disorder comparable to Brownian motion. We demonstrate that the counterintuitive phenomenon of 'strongly correlated wave dynamics in weakly correlated potentials' originates from the ordered modulation of potentials based on spatial information regarding the ground state, which is the nature of SUSY.

3.2.1 Wave dynamics in random-walk potentials

To employ the supersymmetric technique, we investigate waves governed by the 1D Schrodinger-like equation, which is applicable to a particle in nonrelativistic quantum mechanics or to a transverse electric (TE) mode in optics. Without a loss of generality, we adopt conventional optics notations for the eigenvalue equation $H\psi = \gamma\psi$, where the Hamiltonian operator H is

$$\dot{H} = \frac{\dot{k}^2}{k_0^2} + V_o(\dot{x}), \tag{3.1}$$

$k = i\partial_x$ is the wavevector operator, k_0 is the free-space wavevector, $V_o(\dot{x}) = -[n(x)]^2$ is the optical potential, $n(x)$ is the refractive index profile, ψ is the transverse field profile, and n_{eff} is the effective modal index for the eigenvalue $\gamma = -n_{eff}^2$. Two independent methods are applied to Eq. (3.1) for verification, the Finite Difference Method (FDM) [166] and the Fourier Grid Hamiltonian (FGH) method [167], whereby both yield identical results for the determination of bound states (see the Appendix D.1).

To examine the relationship between wave dynamics and the correlations of potentials, three types of random-walk potentials are analyzed: crystals, quasicrystals, and disordered potentials, which are generated by adjusting the refractive index profile. Figure 3.2a represents a 1D binary Fibonacci quasicrystal (the 6th generation with an inflation number, or sequence length, of $N = 8$, substituting A→B and B→BA for each generation using A as the seed), where each element is defined by the gap between high-index regions: A (or B) for a wider (or narrower) gap. The crystal and the disordered potential are generated using the same definition of elements, while the crystal has an alternating sequence (BABABA…), and the disordered potential has equal probabilities of A and B for each element (*i.e.*, it is a Bernoulli random sequence [168] with the probability $p = 0.5$). To quantify the correlation, the Hurst exponent H [169, 170] is introduced (Fig. 3.2b; see the Appendix D.2). As N increases, both the crystal and the quasicrystal have H values that approach 0 (*i.e.*, they exhibit 'ballistic behavior' with strong negative correlations [169]), in stark contrast to the Bernoulli random potential, which has $H \sim 0.4$ (close to ideal Brownian motion, with $H = 0.5$).

Figures 3.2c-3.2h illustrate the wave dynamics for each potential, which are calculated using the FDM and the FGH method. Consistent with previous studies, Bloch-like wave dynamics with wide bandgaps are obtained for the ordered

potentials of the crystal (Fig. 3.2c) and the quasicrystal (Fig. 3.2d), and the Bloch-like nature becomes more apparent with increasing N (Fig. 3.2f,3.2g). By contrast, no bandgap is observed for the Bernoulli random potential, which lacks *any* correlations (Fig. 3.2e), especially for larger N (Fig. 3.2h); this lack of correlation originates from the broken coherence of this case, which hinders the destructive interference that is necessary for the formation of bandgaps. It should also be noted that many eigenstates are localized within this random potential, exhibiting a phenomenon that is widely known as Anderson localization [171].

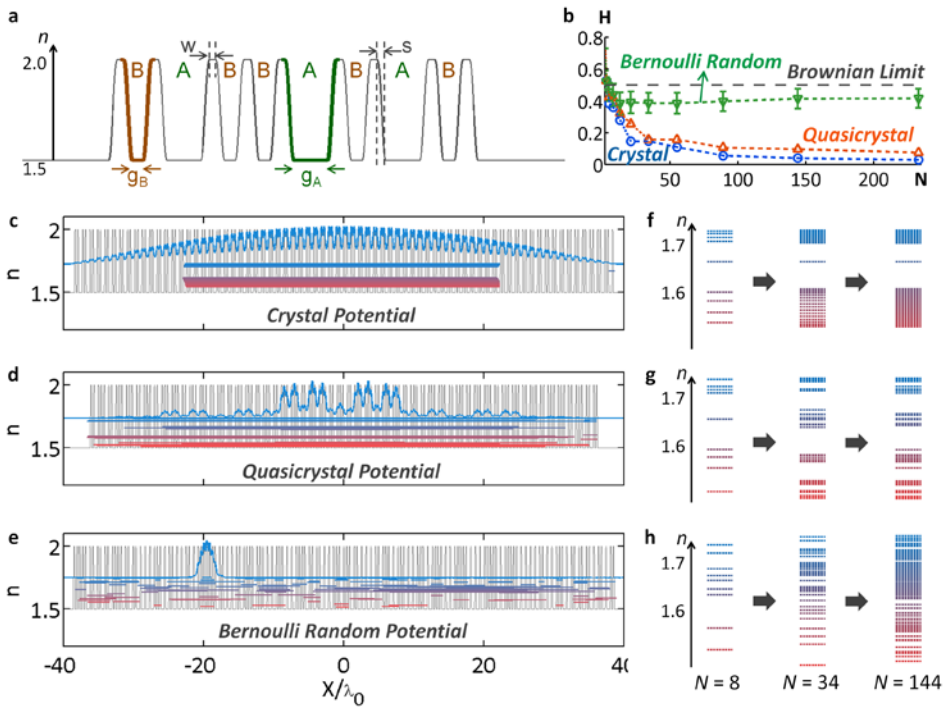

Figure 3.2. Wave dynamics in crystals, quasicrystals, and Bernoulli random potentials [140]. (a) Definitions of elements, illustrated for an example of a 1D Fibonacci quasicrystal (N = 8). g_A = 600 nm, g_B = 200 nm, w = 120 nm, s = 140 nm, and the wavelength is λ_0 = 1500 nm. (b) Hurst exponent H for each potential as a function of the sequence length N. The sequence lengths N are selected to be equal to those of Fibonacci quasicrystals. The H of the Bernoulli random potential is plotted with error bars for 200 statistical ensembles. The black dashed line represents the Hurst exponent of ideal Brownian motion (H = 0.5). (c)-(e). Eigenstates of each potential. The blue curve represents the ground state of each potential, and the colored lines represent the spectral (n_{eff}) distributions of the eigenstates. (f)-(h). Evolutions of the band structures for different sequence lengths N: (c),(f) for crystals, (d),(g) for quasicrystals, and (e),(h) for Bernoulli random potentials.

3.2.2 Supersymmetric transformation for isospectrality

In light of the results of Fig. 3.2, we now consider the following question: "*Is it possible to design nearly uncorrelated (or Brownian) potentials with H ~ 0.5 while preserving the original bandgaps?*". To answer this question positively, we exploit the SUSY transformation [49, 149, 154, 157, 159] to achieve quasi-isospectral potentials. In Eq. (3.1), it is possible to decompose the Hamiltonian operator as follows: $H - \gamma_0 = NM$, where $N = -ik / k_0 + W(\dot{x})$, $M = ik / k_0 + W(\dot{x})$, $W(\dot{x})$ is the superpotential that satisfies the Riccati equation $W(\dot{x})^2 - i[kW(\dot{x})]/k_0 + \gamma_0 = V_o(\dot{x})$, and γ_0 is the ground-state eigenvalue of $H\psi_0 = \gamma_0\psi_0$. Then, the inversion of the N and M operators yields the SUSY Hamiltonian H_s with the SUSY-partner potential $V_s(\dot{x})$: $H_s = MN + \gamma_0 = k^2 / k_0 + V_s(\dot{x})$. From the original equation $H\psi = \gamma\psi$, the relation $H_s \cdot (M\psi) = \gamma \cdot (M\psi)$ is obtained, thus proving isospectrality with γ and the transformed eigenstates of $M\psi$.

The solution $W(\dot{x})$ is simply obtained from the Riccati equation through $W(\dot{x}) = [\partial_x\psi_0(x)]/[k_0\psi_0(x)]$ for unbroken SUSY , which also provides the ground-state annihilation equation $M\psi_0 = [ik / k_0 + W(\dot{x})]\psi_0 = O$. Because $V_s(\dot{x}) = -[n_s(x)]^2$ is equivalent to

$$V_s(\dot{x}) = W^2 + i\frac{\dot{k}}{k_0}W + \gamma_0, \tag{3.2}$$

the index profile $n_s(\dot{x})$ after the SUSY transformation can finally be obtained as follows:

$$[n_s(\dot{x})]^2 = [n(\dot{x})]^2 + 2\frac{1}{{k_0}^2}\frac{d}{dx}\left(\frac{\psi_0'}{\psi_0}\right) = [n(\dot{x})]^2 + 2\frac{1}{{k_0}^2}\frac{d^2}{dx^2}\left(\log\psi_0\right). \tag{3.3}$$

Equation (3.3) demonstrates that the SUSY transformation can be achieved deterministically based solely on the ground-state-dependent functionality. Figure

3.3 illustrates an example of serial SUSY transformations applied to the 1D Fibonacci quasicrystal potential defined in Fig. 3.2, where the small value of $N = 5$ is selected for clarity of presentation. For each SUSY transformation, all eigenstates of each previous potential, except for the ground state, are preserved in the transformed spatial profiles, while the shape of the designed potential becomes 'disordered' through 'deterministic' SUSY transformations.

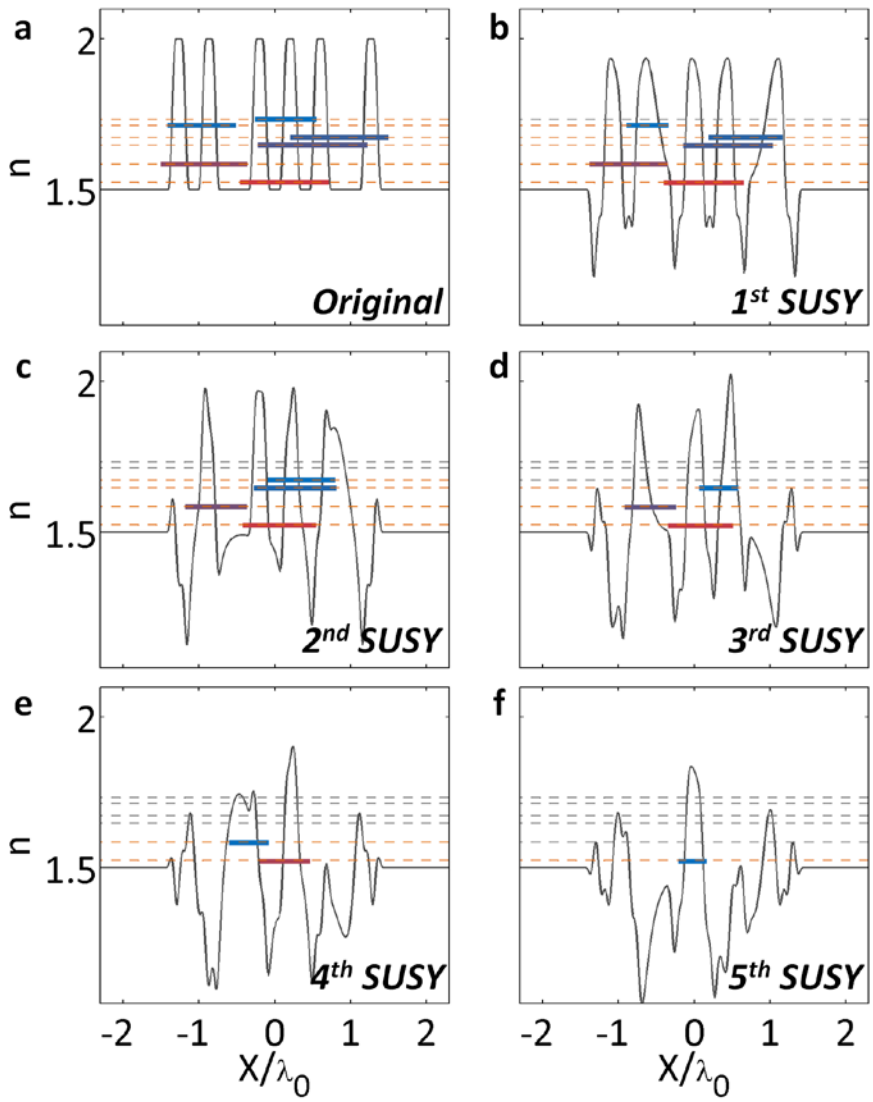

Figure 3.3. Effects of SUSY transformation on the generation of quasi-isospectral potentials [140]. A 1D Fibonacci quasicrystal (N = 5) is considered as an example. (a) Original potential. (b)-(f). 1st - 5th SUSY-transformed potentials. The orange (or black) dotted lines represent the preserved (or annihilated) eigenstates. All eigenstates are calculated using both the FDM and FGH method, the results of which are in perfect agreement.

3.2.3 Bloch-wave family with tunable disorder

Because the presence of deterministic order is essential for Bloch-like wave dynamics and bandgaps [138, 172], regardless of the presence of long-range correlations in their spatial profiles, the 'randomly shaped' potentials (Fig. 3.3) that can be 'deterministically' derived by applying SUSY transformations to ordered potentials offer the possibility of combining Bloch-like wave dynamics and disordered potentials. To investigate the wave dynamics associated with the SUSY transformation, we consider a larger-N regime in which the wave behaviors are clearly distinguished between ordered (Fig. 3.2f,3.2g) and disordered potentials (Fig. 3.2h). Figures 3.4a and 3.4b present the results obtained after the 10^{th} SUSY transformation for the crystal (Fig. 3.4a,c) and the quasicrystal (Fig. 3.4b,d) with N = 144. Although the shapes of the SUSY-transformed potentials and the spatial information of the eigenstates in Figure 3.4a and Figure 3.4b are quite different from those of the corresponding original potentials in Figure 3.2c and Figure 3.2d, the eigenspectrum of each potential is preserved, save for the annihilation of the 10 lowest eigenstates, which is consistent with the nature of SUSY transformations [149].

This eigenspectral conservation is apparent in Figure 3.4c and Figure 3.4d, which depict the variation in the effective modal index that occurs during the SUSY transformations (up through the 20^{th} SUSY transformation). As illustrated, the eigenspectrum of each potential is maintained from the original to the 20^{th} SUSY transformation, save for a shift in the modal number, and therefore, the bandgaps in the remainder of the spectrum are maintained during the serial SUSY transformations (~125 states after the 20^{th} SUSY transformation, following the loss of the 20 annihilated states). Consequently, bandgaps and Bloch-like wave dynamics similar to those of the original potentials are allowed in SUSY-transformed potentials with disordered shapes (Fig 3.4a,b) that can be classified as neither crystals nor quasicrystals.

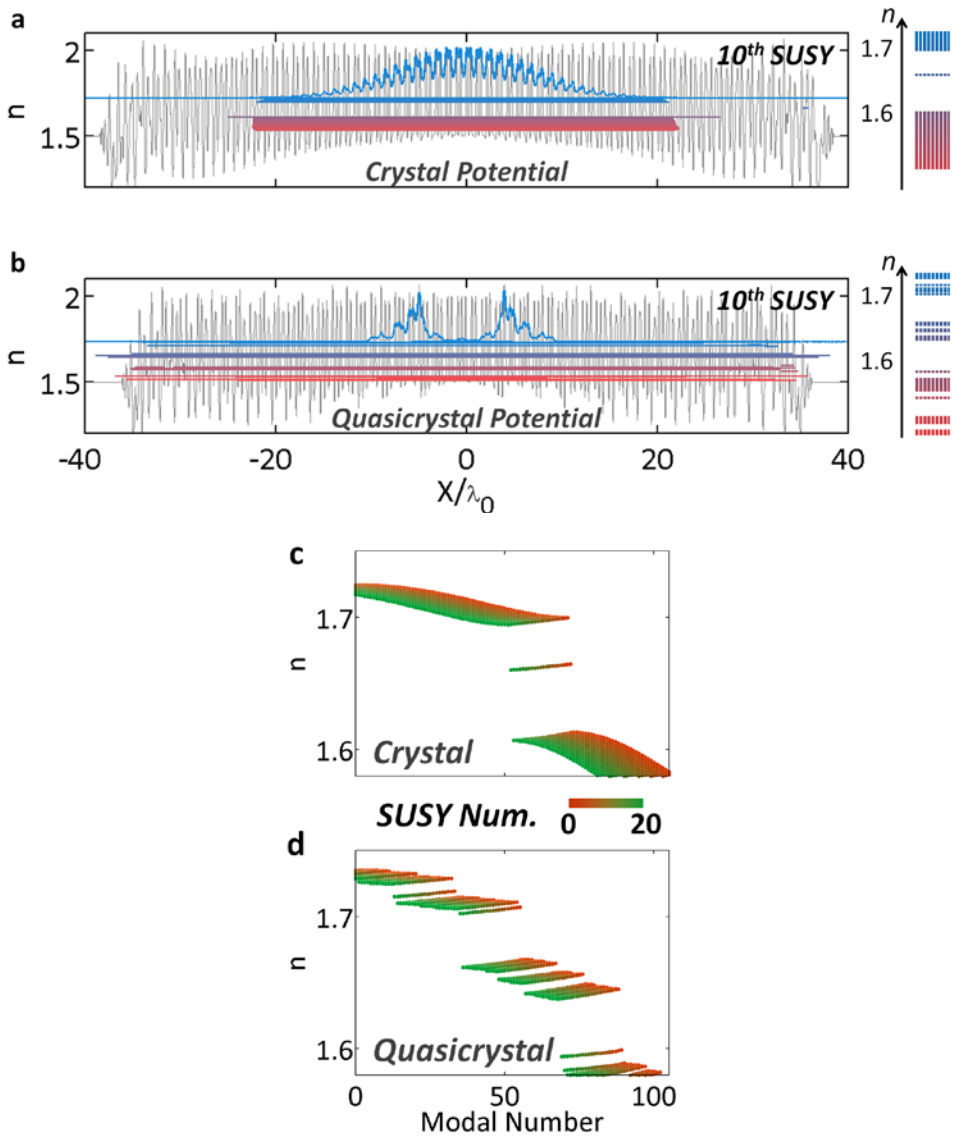

Figure 3.4. Potentials and band structures of SUSY-transformed crystal and quasicrystal (N = 144) [140]. The 10th SUSY-transformed potentials and their eigenstates are depicted for (a) a crystal potential and (b) a quasicrystal potential. (c) and (d) show the eigenvalues of the SUSY-transformed potentials as a function of the modal numbers of the crystal and quasicrystal potentials, respectively. The 0th SUSY-transformed potential corresponds to the original potential.

Figures 3.5a to 3.5h illustrate the shape evolutions of the crystal and

quasicrystal potentials that are induced through the SUSY process, demonstrating the increase in disorder for both potentials. Again, note that the SUSY-based modulation is determined by Eq. (3.3), starting from the ground-state profile $\psi_0(x)$, which is typically concentrated near the center of the potential (Fig. 3.4a,b). To investigate the correlation features of SUSY-transformed potentials with bandgaps, we again consider the Hurst exponent. Figure 3.5i shows the Hurst exponents for the transformed crystal and quasicrystal potentials as a function of the number of SUSY transformations.

The figure demonstrates that, for successive applications of SUSY transformations, the Hurst exponents of the crystal and quasicrystal potentials (H = 0 ~ 0.1) increase and saturate at H ~ 0.8. The negative correlations (H < 0.5) of the crystal and quasicrystal potentials (H = 0 ~ 0.1) become totally uncorrelated, with H = 0.51 after the 10th SUSY transformation; the correlations are even weaker than that of the Bernoulli random potential (H = 0.35~0.48, Figs 3.2b,3.5i) and approach the uncorrelated Brownian limit of H = 0.5. After the 10th SUSY transformation, the correlation begins to increase again into the positive-correlation regime ($H \geq$ 0.5, with long-lasting, *i.e.*, persistent, potential shapes), thereby exhibiting a transition between negative and positive correlations in the potentials. This transition from an 'anti-persistent' to 'persistent' shape originates from the smoothing of the original potential caused by the slowly varying term $\partial_x^2\{log[\psi_0(x)]\}$ in Eq. (3.3), which is derived from the nodeless ground-state wavefunction $\psi_0(x)$. This result reveals that the application of SUSY transformations to ordered (crystal or quasicrystal) potentials allows the remarkable control of the extent of disorders while preserving Bloch-like wave dynamics and bandgaps. Therefore, a 'Bloch wave family', whose members have identical bandgaps but tunable disorders, can be constructed through the successive application of SUSY transformations to each ordered potential, with a range of disorder spanning almost the entire regime of Hurst exponents indicating negative and positive correlations ($0 \leq H \leq 0.8$), including the extremely uncorrelated

Brownian limit of $H \sim 0.5$.

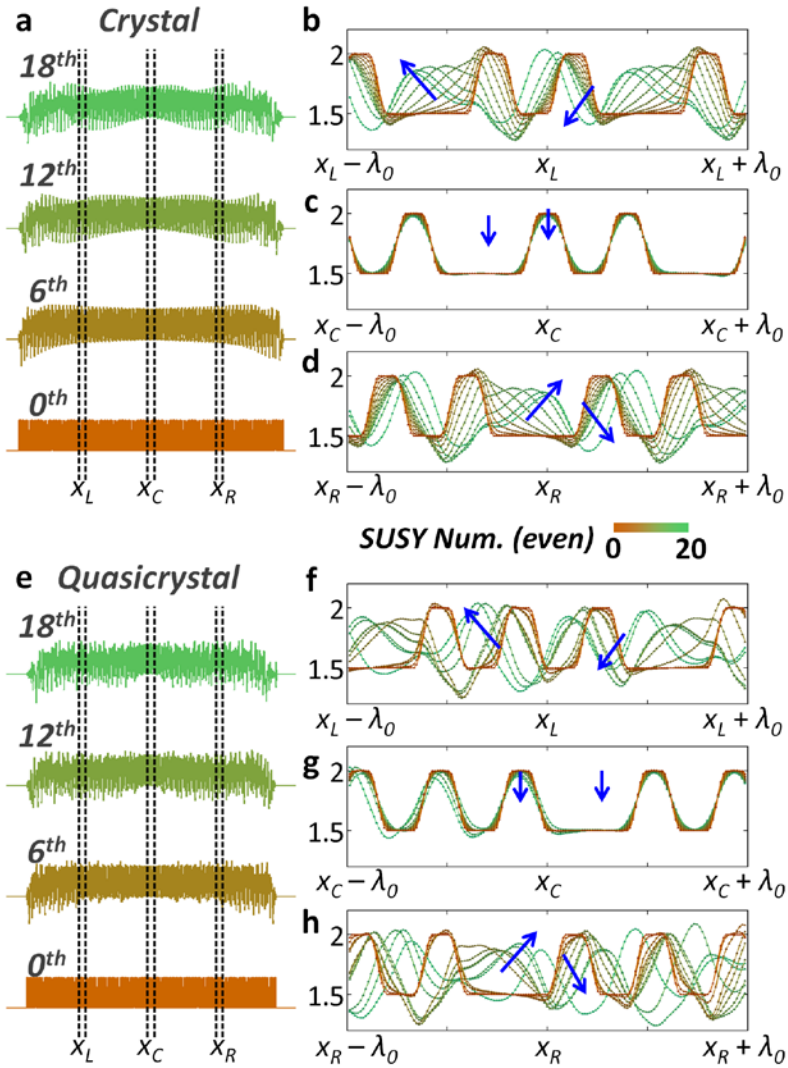

Figure 3.5. Correlation features of SUSY-transformed potentials for N = 144 with bandgaps maintained [140]. The evolutions of the potential profiles following the successive application of SUSY transformations (0^{th}, 6^{th}, 12^{th}, and 18^{th}) for a. a crystal and e. a quasicrystal. b-d and f-h present magnified views (at x_L, x_C, x_R) of the potentials for even numbers of SUSY transformations (overlapped, up to the 20^{th} transformation; the blue arrows indicate the direction of potential modulation).

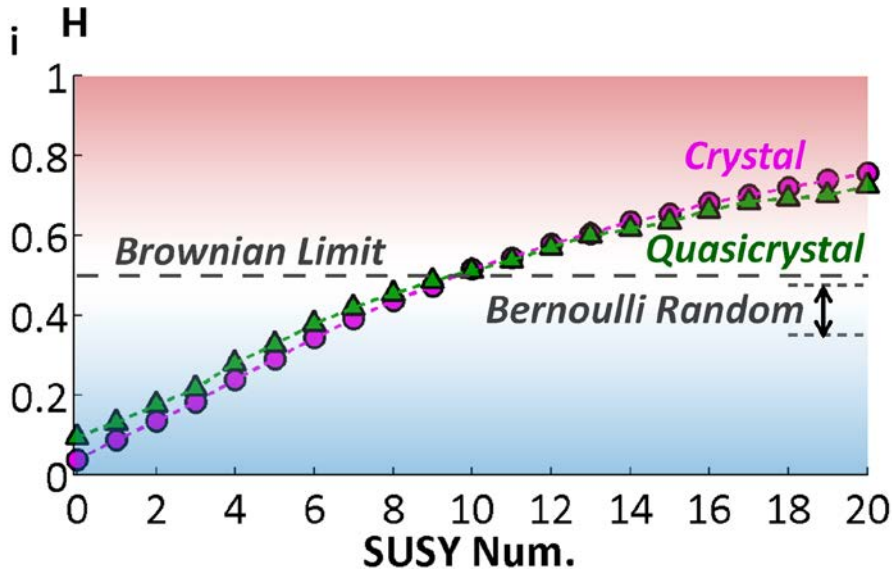

Figure 3.5 (continue). i. Hurst exponents *H* for each transformed potential as a function of the number of SUSY transformations. The red (or blue) region represents the regime of positive (or negative) correlation, whereas the white region corresponds to the uncorrelated Brownian limit. The arrow indicates the regime of the Bernoulli random potential (Fig. 3.2b).

To summarize, by employing supersymmetric transformations, we revealed a new path toward the deterministic creation of random-walk potentials with 'crystal-like' wave dynamics and tunable spatial correlations, extending the frontier of disorders for Bloch-like waves and identical bandgaps. Despite their weak correlations and disordered shapes, SUSY-transformed potentials retain the deterministic 'eigenstate-dependent order' that is the origin of bandgaps, in contrast to the hyperuniform disorder of pointwise networks [160-162, 164, 173-179] and deterministic aperiodic structures such as quasicrystals [138, 172] or the Thue-Morse [180] and Rudin-Shapiro sequences [181]. Our results, which were obtained based on a Schrodinger-like equation, reveal a novel class of Bloch-wave disorder that approaches the theoretical limit of Brownian motion while maintaining wide bandgaps identical to those of existing crystals or quasicrystals in both electronics and optics. We further envisage a novel supersymmetric relation, based on the

famous SUSY theory in particle physics, between ordered potentials and disordered potentials with coherent wave dynamics in solid-state physics.

3.3 Biomimetic disordered surface

Although disordered potentials allow wideband operations in k- and ω- domains desired in applications such as absorbers [182] and photovoltaics [183], in many other applications, selective bandwidth properties are useful. For example, the applications for the display require wideband k property (viewing angle) with narrowband ω property (color selectivity). In contrast, narrowband k with broadband ω is required for functional optical elements: manipulating the flow of light with wide bandwidth operation. Here we investigate the former case for reflective display, inspired by the structure in nature [124]: the wings of Morpho butterfly.

Morpho butterfly [184-186] is one of the most famous examples of the structural color [187-189], which has the wings with superior color stability for wide viewing angles (broadband k components). Such color stability seems to be counterintuitive to its excellent color purity (high-Q ω components), in the context of disordered optics which usually derives broadband operation in both domains due to diverse k and ω components. This exotic result can be explained by microscopic structures of the wings (Fig. 3.6). As can be seen, the surface of the wing has the periodicity guaranteeing the color selectivity, but the vertical and horizontal distribution of this periodicity is highly disordered, resulting in the broad viewing angle. Although many researches have been carried out to reproduce this fascinating result [190], most approaches have employed the lithography process, hindering the large-scale fabrication.

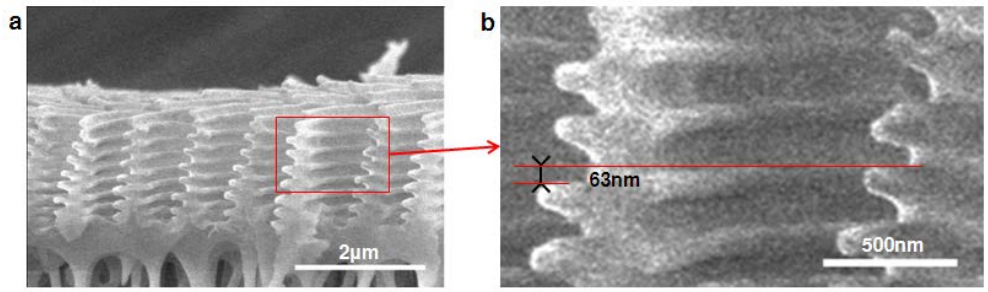

Figure 3.6. Microscopic SEM views of the wing of Morpho butterfly [124]: in (a) a few μm scale and (b) its enlarged picture. The measurement is carried out by K. Chung in J. H. Shin's group in KAIST [124].

To realize the large-scale fabrication, we apply the litho-less process: deposition of silica nanospheres and the following alternating deposition of dielectric 1D crystal. The following structure is shown in Fig. 3.7. By controlling the size distribution of nanospheres, the disorder of the structure can be controlled, while preserving the periodicity for the color purity.

To further investigate the mechanism, numerical analysis of the reflectivity was performed using 2-dimensional finite element method. Two model cases are considered. First, a *Morpho*-mimetic structure with a base layer of randomly sized silica microspheres was used (Fig. 3.7a). Second, a hypothetical reference structure with the same multilayer structure but with a base layer of mono-dispersive silica microspheres with a diameter of 300 nm was used (Fig. 3.7b). In all cases, the actual structural and optical parameters obtained from fabricated thin films were used.

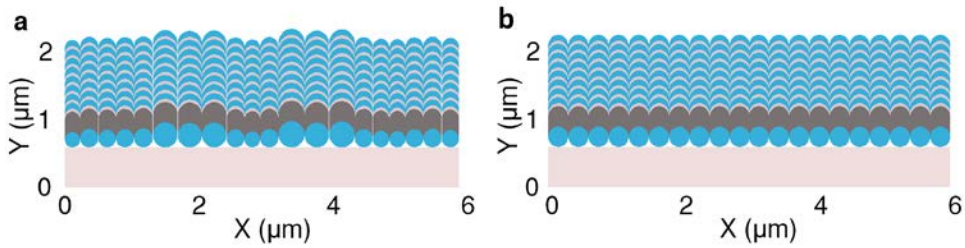

Figure 3.7. Schematics of biomimetic reflecting surfaces [124]: (a) with disorders and (b) without disorders. Dark grey: Cr layers to block the retro-reflection from spheres. Blue: Silica, Pink: TiO_2.

For the numerical assessment, finite element method (FEM, COMSOL) with perfectly-matched layer (PML) boundary condition is employed. A film that consists of 20 reflective elements (each composed of a Cr-deposited silica-ball and 8 SiO2 / TiO2 layers on top, with experimentally determined material parameters) were used. Incident light source defined by plane wave at an angle θ, normal to the film was assigned for calculation. Scattered field method is applied to measure reflected waves separate from the incident waves. The reflected power was measured along the far-field semicircle 10μm away from the center of the film (Fig. 3.8a). Calculations were performed for each incident wavelength (from 390 nm to 750 nm, with 5 nm interval), and incident angle (from 0° to 60 °, with 10 ° interval). In case of *Mopho*-mimetic structures, the results obtained from 40 independent realizations (20 for each polarization) - with each film randomly generated from the experimentally determined ball size distribution curve - were averaged to ensure sufficient randomness. Examples of *Morpho*-mimetic and reference structures, and a typical calculation result showing the reflected electric field from a *Morpho*-mimetic structure are shown in Fig. 3.8a.

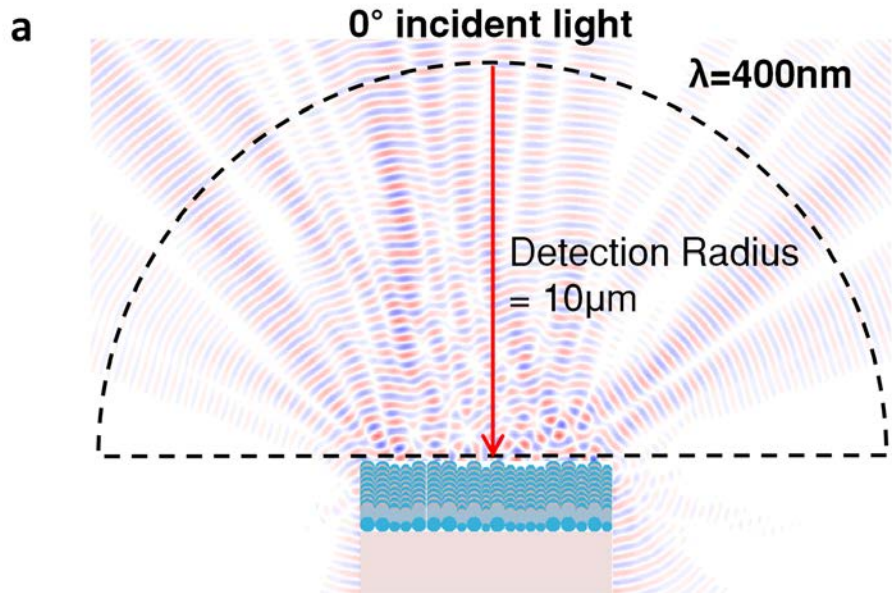

Figure 3.8. Reflection property of biomimetic reflecting surfaces [124]: (a) the example of the reflected eiectric field.

To calculate the total reflectivity for each wavelength and incident angle, the scattered power was integrated along the detection semicircle. The calculated angular distribution of reflected light intensity from *Morpho*-mimetic film under light incident at 0 °, -30 °, and -60 ° are shown in Figs. 3.8b-3.8d, respectively. We find that the overall shape of the distribution qualitatively similar to that from a single scale of *Morpho didius* [184-186, 190], being a single lobe with $1/e^2$ width of more than 90 ° even under normal incidence, and riddled with sharp spikes at irregular intervals. As the incidence angle is increased, the distribution becomes wider; in fact, there is significant retro-reflection at angles that even exceed the incidence angle, especially in the blue-green region from 400 to 500 nm. Consequently, the overall reflectivity, as shown in Fig. 3.8e, is highest in blue-green region from 400 to 500 nm at all incidence angles. Indeed, the reflectivity at a particular wavelength varies little with the incidence angle such that the reflectivity is uniformly low for wavelengths greater than ~550 nm.

A quite different behavior is observed from the reference film. As shown in Figs. 3.8f-3.8h, the angular distribution is quite narrow, with $1/e^2$ width of less than 40 ° even under normal incidence, and has well-defined peaks at regular intervals indicative of coherent diffraction. Such shape is maintained even under oblique incidence angles, with very little retro-reflection. Consequently, the overall reflectivity has several well-developed bands whose positions are clearly angle-dependent, as is shown in Fig. 3.8i. Furthermore, the main reflection band is much broader, ranging from 400 to ~600 nm.

We note that that the shape of the reflecting layers is spherical for both films, which is quite different from that of actual *Morpho* butterflies. Furthermore, due to the spherical shape, even the reference film has an intra-columnar difference in height of reflecting layers that is comparable to inter-columnar difference in the vertical offset of the reflecting columns in the *Morpho*-mimetic film. Thus, the fact that only the *Morpho*-mimetic film reproduces both the angular distribution and the angle-independence of reflectivity seems to indicate that while many aspects such as the shape of the reflecting layers contribute to the overall appearance of *Morpho* butterflies, it is the random (or disordered) variation in spatial location of 'each' reflecting multilayer elements that plays the major role in producing the angle-independent iridescence. The fabricated samples by KAIST (Prof. J. H. Shin group) are also shown in Fig. 3.9.

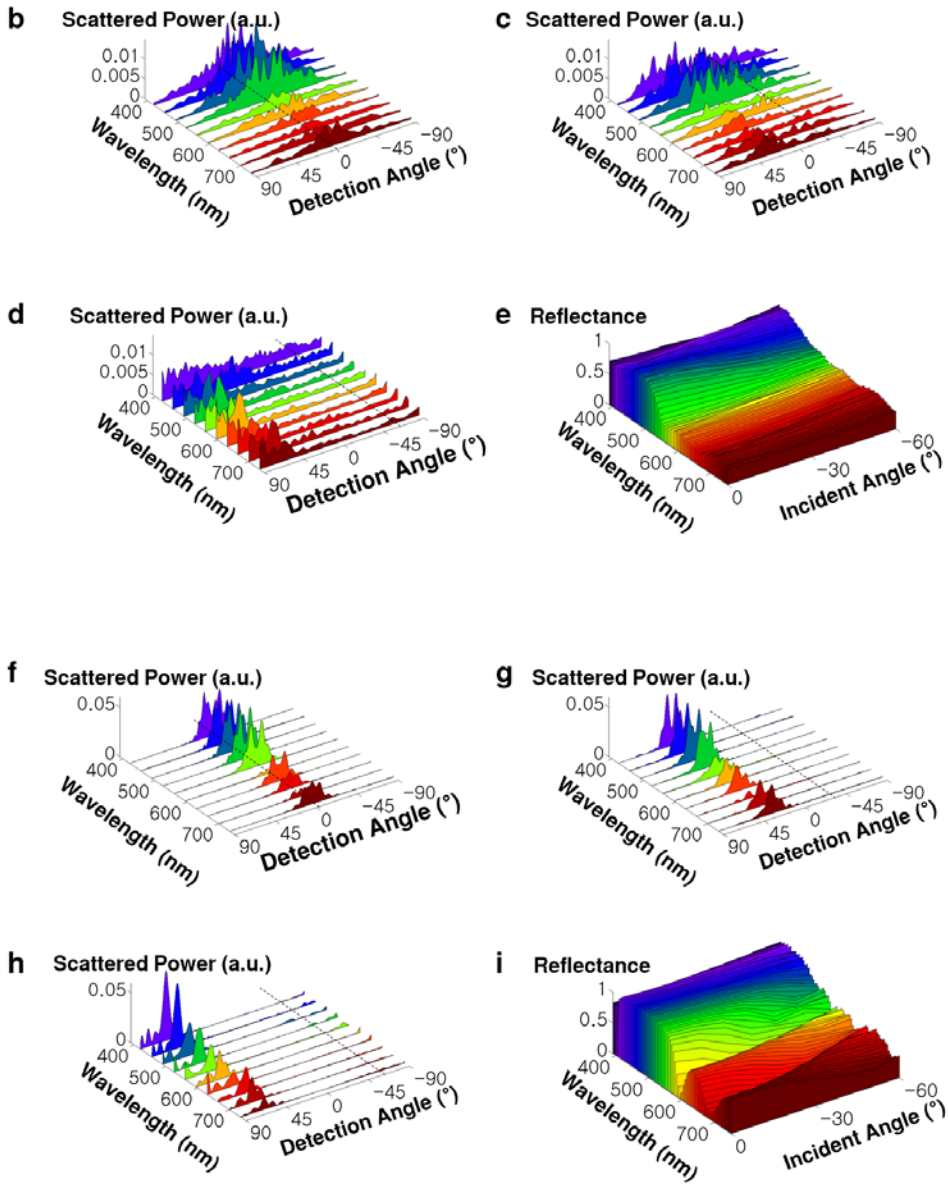

Figure 3.8 (continue). The calculated angular distribution of reflected light intensity from (b-d) *Morpho*-mimetic films and (f-h) reference films under light incident at (b,f) 0 °, (c,g) -30 °, and (d,h) -60 °. The overall reflectance as a function of wavelength and incident angle is shown in (e, for Morpho films) and (i, for reference films).

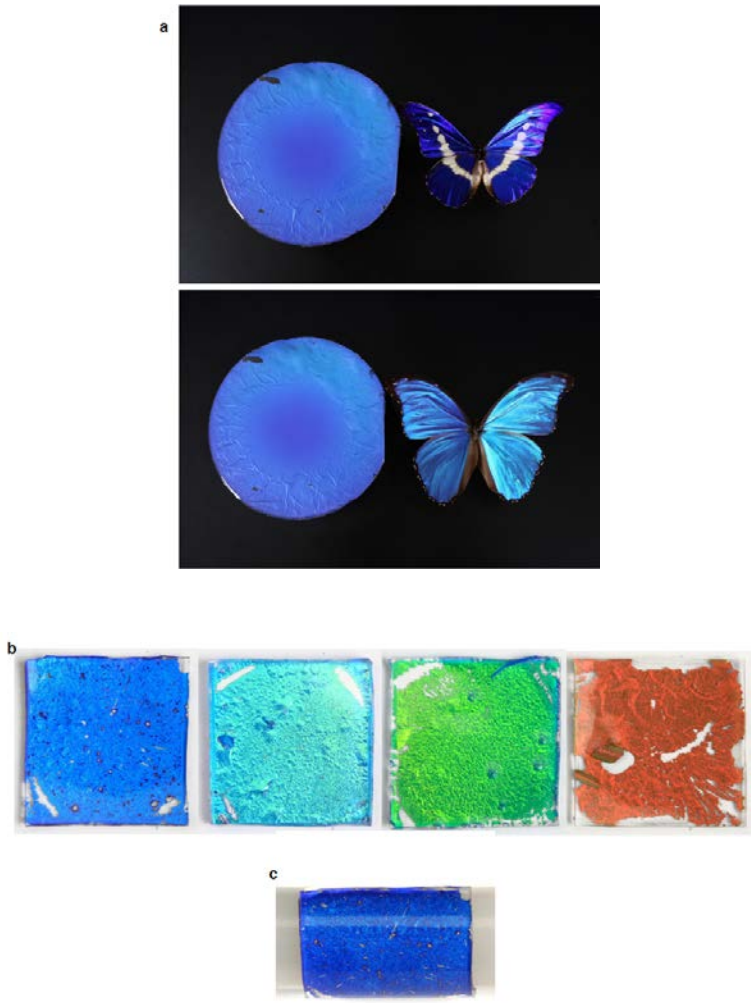

Figure 3.9. Images of fabricated films [124]. (a) Comparison of the fabricated reflector (PDMS encased thin film) with Morpho rhetenor (above) and Morpho didius (below). The size of the reflector is 6 inches in diameter. (b) Various colors ranging from deep blue through green to coppery red realized by controlling the layer thicknesses. (c) Image of deep blue reflector (shown in Fig. 3.9b), wrapped around a rod with diameter of 1 cm. Note that the color appears the same throughout, even though the reflector is bent, and thus presents a viewing angle that varies from 0 to 90°. The fabrication and experiment are carried out by K. Chung in J. H. Shin's group in KAIST [124].

3.4 Conclusion

In this chapter 3, we reviewed our researches in the field of disordered optics. We showed two examples of disordered potentials which derive counterintuitive dynamics: (1) bandgaps in disordered potentials which is identical to those in ordered potentials [140], and (2) broadband k- and narrowband ω- reflecting films [124]. In contrast to periodic structures which have been studied intensively through Bloch's theorem, there are many fascinating but unexplored wave dynamics in disordered potentials which will enable new types of wave flows.

Chapter 4

All-Optical Devices with Nonlinearity

As the footprint of electronic devices has decreased to a few-nm scale, increasing power consumption and limited operating speed in electronics have become a growing problem. Furthermore, because the boundary of classical operation of electronic devices has become closer due to the existence of quantum tunneling, the current design strategy of electronic transistors will not work, threatening Moore's law [191].

The field of all-optical devices [192-203] has therefore derived much attention, to substitute fermion-based electronics with boson-based photonics which allows lossless and ultrafast device operations. Although there still have been serious difficulties in the realization of all-optical devices comparable to electronic devices – such as larger footprints and restricted material properties –, related design strategies and optical structures will open a new pathway for the manipulation of the flow of light.

In this chapter, after the brief review of all-optical devices (section 4.1), we investigate all-optical devices in resonant (section 4.2, [125, 201]) and non-resonant (section 4.3, [198, 204, 205]) designs: using modal orthogonality and

slow-light dynamics respectively. We especially focus on the nonreciprocal devices including optical diode and isolator, and the functional devices such as optical switch, half-adder and A/D converter (ADC), mainly based on the Kerr-type (the 3rd harmonic) optical nonlinearity.

4.1 Introduction to all-optical devices

The linearity of chargeless Maxwell's equations enables the ultrafast, distortion-free optical communication of today. Still at the same time, this very linearity, in contrast to fermionic nonlinear interactions in electronics, has seriously hindered the development of photonic functional systems, especially missing the switching action. Because the nonlinearity is the core of logic devices, serious efforts have been applied to enhance optical nonlinearity. Although various nonlinear materials have been investigated [196, 197, 206-214], the efforts have been focused on the control of the state of light, to derive enhanced optical nonlinearity.

To derive larger optical nonlinearity, light energy should be concentrated. Resonant [193, 203] and non-resonant [214, 215] energy concentration can be applied; the former one can be achieved using high-*Q* resonators with small footprints, and photonic crystal resonant platform is one of the best platform with a huge Purcell effect; the latter one can be realized by employing surface plasmonics or slow-light dynamics.

Among many different optical nonlinearities, including the second-harmonic generation (SHG) [213, 214] and two-photon absorption (TPA) [212], optical Kerr effect [196, 197, 206-211] has attracted much attention for the realization of all-optical devices, due to its ultrafast dynamics (compared to TPA) and frequency-conserving property (compared to SHG). Figure 4.1 shows the examples of all-optical switching devices, based on various optical nonlinearities and structures.

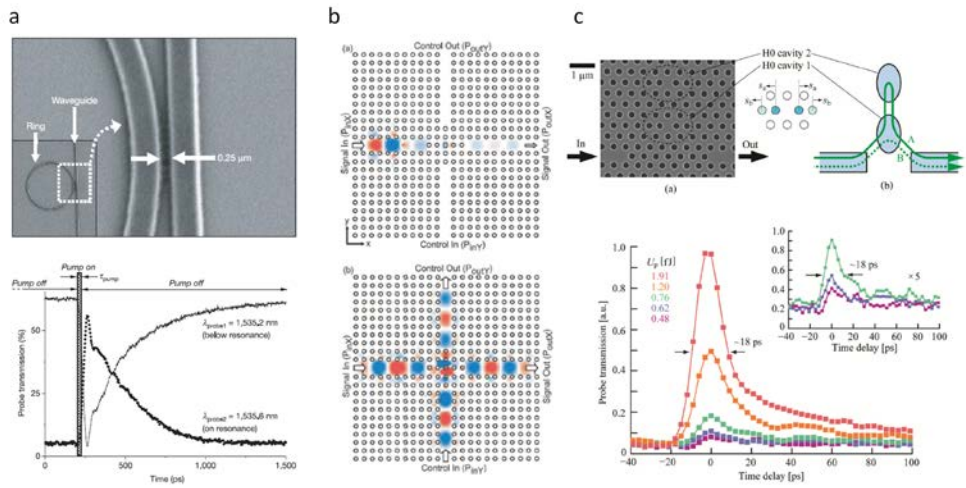

Figure 4.1. The examples of all-optical switching devices based on optical nonlinearity: (a) ring-resonator-based switch [193], (b) Kerr-effect switch based on a photonic crystal waveguide crossing structure [192], and (c) Fano-based efficient switch with coupled photonic crystal resonators [203].

Notwithstanding past efforts, the realization of digital photonics is still in an early stage. In the section 4.2, examining the similar phase in the breakthrough of electronics, we investigate the introduction of electrical junction structures for *drastic, systematic and controllable change to the asymmetric electrical potential across*. We then propose photonic junction structures [125] based on modal orthogonality with implementation examples of all-optical devices. We also study the application of slow-light dynamics [205] to all-optical devices including optical nonreciprocity in section 4.3.

4.2 Mode junction photonics

Here, taking photonics as an example, we propose a junction for wave, built upon mode-orthogonal photonic hetero-structures, as a fundamental structural unit for 'photo-tronics'. By exploiting the rich and well-defined orthogonal modes which provide abundant degrees of freedom for the choice of junctions (having different spectral mode-overlap and frequency separation), the modular construction of

highly nonlinear devices with systematic control of wave propagation is enabled. Of possible applications for the mode junction, here we provide examples of a photonic junction diode and a multi-junction half-adder, of exceptional performance metrics. Highly directional (41dB), nearly unity throughput with orders of magnitude lower threshold power (~10^3, compared to. For, external modulation power), a high quality signal regeneration at 200Gb/s, and all-optical AND, XOR operations are successfully demonstrated.

To incorporate the junction structure into the photonic domain - notwithstanding the absence of charge or reference energy, we focus our attention to the *wave* nature of photons; especially related to the orthogonality between their well-defined and plentiful eigenmodes. Through the juxtaposition of two photonic structures of each supporting different eigenmodes, a diversity of mode-orthogonal heterojunctions can be created. Explicitly, exploiting the abundant set of optical eigenmodes (~$N_a \cdot N_m \cdot N_p$ where N_i = mode number for optical atom, molecule, and polarization), variety of mode-orthogonal heterojunctions (atomic-, molecular-, polarization junctions as in Fig. 4.2a) can be created, which differ in their mode-overlap and frequency separations. To note, without loss of generality but with the ease of implementation, and also considering the range of operation frequencies, from now on we use the molecular junctions constructed of multi-atomic structures (Fig. 4.2b).

For example, let us consider the a junction juxtaposed of two structures (Fig. 4.2c), each supporting *T-* (1, $2^{1/2}$, 1) and *T0* (-$2^{1/2}$, 0, $2^{1/2}$) modes of tri-atomic resonator (the eigenvector component represents the field amplitude of each atom), *at the operation frequency*. By adjusting the permittivity (optical potential) for a specific region (here, left side of the junction), the dominant *eigenmode* at the operation frequency of the controlled region then can be dynamically switched between *T-* and *T0*, *to block* (<*T-* / *T0*> = 0) *or to authorize* (<*T0* / *T0*> = 1) *the transmission of photons across the junction* structure. To note, now onwards we denote; / *j* > as the eigenmode of the structure, $\Psi_{i\text{-}j}$ as the potential-controlled

region - supporting mode / i > in unbiased state (Fig. 4.2c in yellow), but toggling to / j > with shifted optical potential (pink in Fig. 4.2c) either by external excitation or self-induced manner.

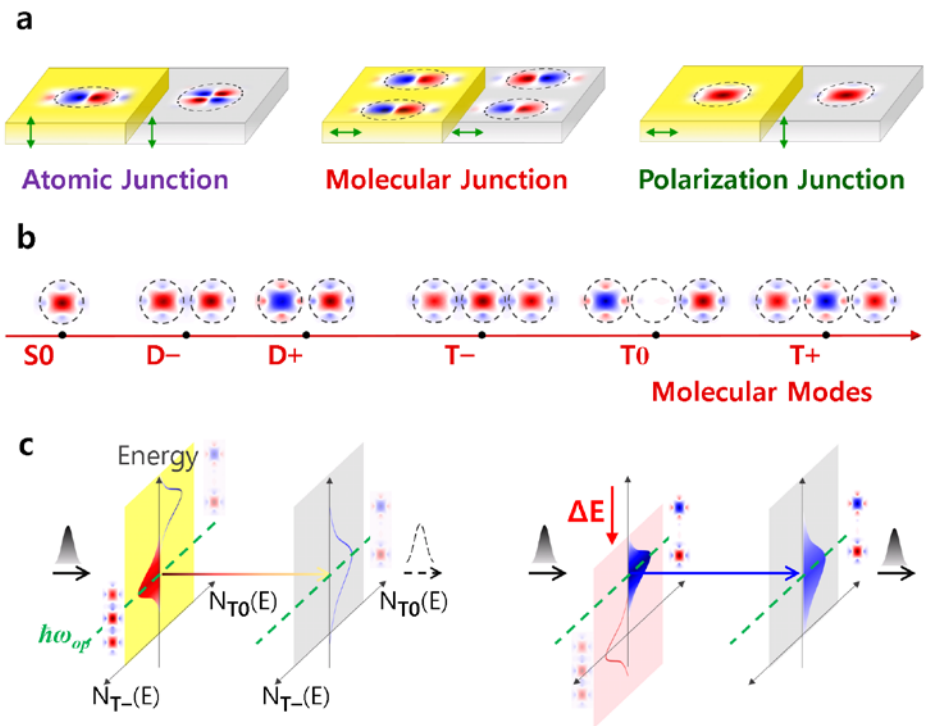

Figure 4.2. Dynamics of photonic mode junction [125]. (a) Examples of orthogonal mode junctions constructed between two orthogonal modes, providing different frequency separation and modal overlap properties. (b) Examples of molecular modes, which could be used to construct a variety of molecular mode junction (S, D, T: Single-, Di-, Tri- atomic molecular modes). A *T-* / *T0* mode junction, for example, can be constructed between two structures providing orthogonal modes of *T-* and *T0* (composed of optical atoms in single mode, sharing an identical polarization). Dashed circles in Fig. 4.2(a,b) represent optical atoms. (c) Operation principles of the mode junction. Excited modes at the operation frequency are marked with filled curves. N_{T-}(E) and N_{T0}(E) axis represents the density of states for *T-* and *T0* mode. Adjusting the optical potential, the dominant mode of the controlled region can be switched between *T-* (non-shifted, yellow) and *T0* (potential ΔE-shifted, pink) modes, to give a junction throughput of either a '0' (yellow) or '1' (pink). The coupling across the junction is determined by the inner product between eigenmodes of the left/right structures (equivalently, multiplying spatial mode profiles at the same frequency along the *identical mode axis* (*T-* or *T0*)).

4.2.1 Photonic Junction Diode

Out of the many possible functional devices that a junction can enable, we first consider the case of the photonic diode [216-224]. We note that here we define 'optical diode' as the device operated with optical isolation and additional functionality (here, the saturation and the following signal regeneration), reflecting the features of an electrical diode. For the *electrical* diode especially being highly nonlinear and asymmetric in its response providing the key functionality for current flow manipulation [225], its photonic counterpart, the photonic diode [216-224], has also attracted serious attention. Nevertheless, for the past demonstrations of photonic diode extremely costly in threshold power (~ W/μm), with the added trouble of limited throughput or directionality, it will be of worth investigating whether the proposed junction structure could provide any advantages.

As illustrated in Fig. 4.3a-4.3c, without loss of generality, let us consider a di-atomic resonator providing even- and odd- modes, separated in its frequencies (ω_e and ω_o). At the operation frequency ω_e the di-atomic resonator in the even mode forms a ψ_e-ψ_o mode junction when combined with the ψ_o odd-mode coupler (a 1 × 2 splitter and a π phase shifter in one arm). Critical to note, compared to the *right*-side low-Q ψ_o coupler, for the *left*-side high-Q di-atomic resonator enjoying a higher density of photons and thus a much enhanced, *self-induced* optical nonlinearity, the modification of the optical potential for the $\boldsymbol{\Psi}_{e\text{-}o}$-$\psi_o$ junction becomes strongly dependent on the direction of the incident wave, so as to fulfill the directionality required for diode operation. Specifically, the critical consequences are as follows. First, for the forward bias below threshold ($\boldsymbol{\Psi}_e$-ψ_o, Fig. 4.3a), the wave propagation to the other side of the junction is completely prohibited and reflected, as dictated by the mode orthogonality $< e \,/\, o > = 0$. Meanwhile, for the forward bias above threshold, with a strong on-resonance (ω_e) build-up of the field in the resonator and a corresponding optical potential shift ($n_2 I \,/\, n_0 \sim (\omega_o - \omega_e) \,/\, \omega_c$), the dominant mode in the resonator $\boldsymbol{\Psi}_{e\text{-}o}$ then gets converted from even to odd mode ($\boldsymbol{\Psi}_o$-ψ_o, Fig. 4.3b), to render full transparency to the ψ_o

coupler region (< *o* / *o* > = 1). Finally, for the reverse bias (Fig. 4.3c), the *coupling* from the odd mode coupler to even mode di-atomic resonator is suppressed by the mode orthogonality. In this case, the weakly-excited resonator will remain in the even mode, blocking the transmission, until the reverse bias reaches the breakdown - determined by the non-zero mode overlap factor (Appendix E.1).

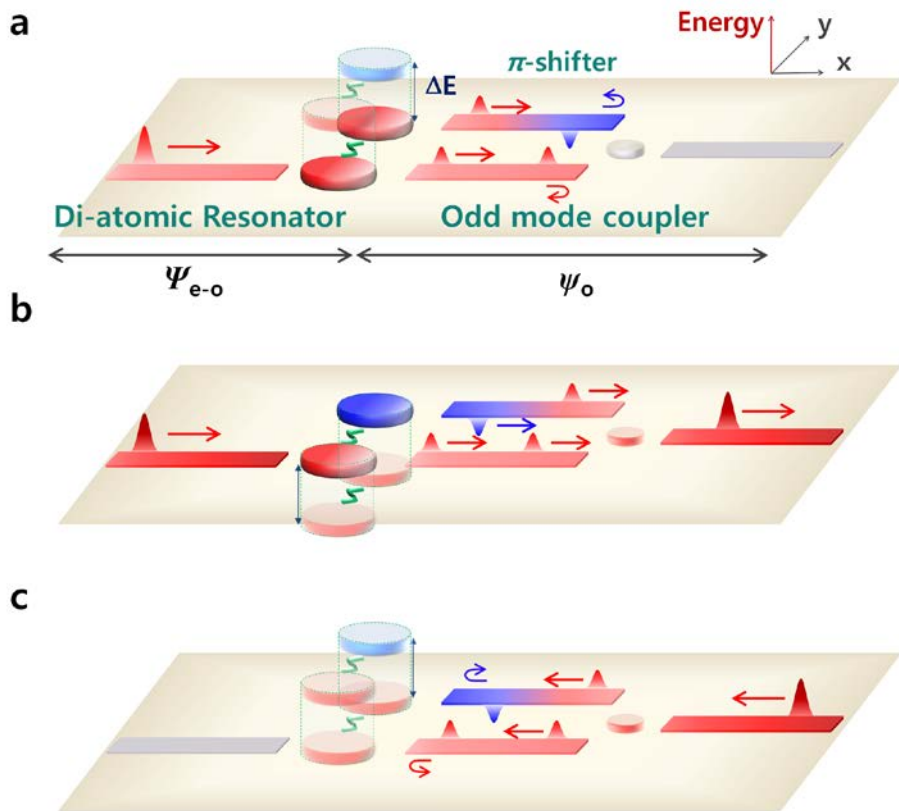

Figure 4.3. Operation of a mode junction diode [125]: under (a) Forward bias below threshold, (b) Forward bias above threshold, and (c) Reverse bias.

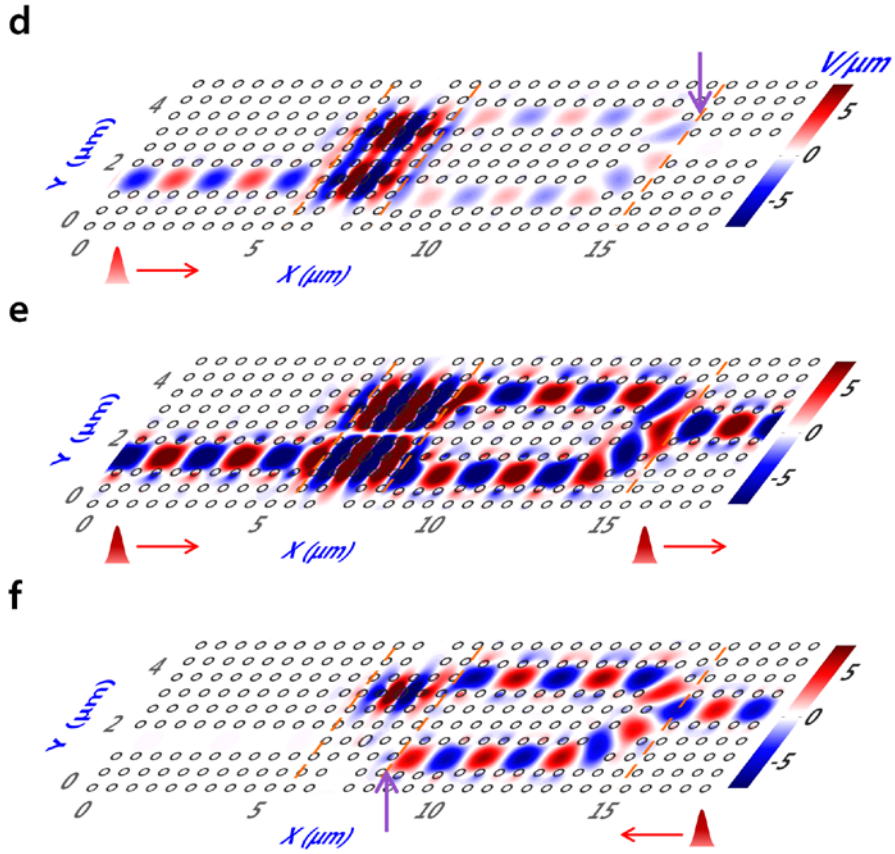

Figure 4.3 (continue). Corresponding field patterns in the photonic crystal realization are shown in (d) ~ (f) (details of numerical analysis in Appendix E.1). Unidirectional transmission of the signal is evident only for the state 4.3e, confirming the diode operation above threshold. For other states of operation, the wave propagation is inhibited; (d), at the odd-mode coupler for forward bias. (f), at the right end barrier of the di-atomic resonator, for reverse bias.

Meanwhile simple in its principle, the junction diode offers distinctive advantages. First, when compared to past approaches utilizing asymmetric potential barriers for directional operation of the diode (at the expense of severe impedance mismatch, (Fig. 4.4e, $1/\tau_L >> 1/\tau_R$) [216-224], now for the proposed junction diode, it is possible to keep the full symmetry of the potential barrier - by transferring the required diode directionality to the asymmetric arrangement of mode-orthogonal structures. As a result, an impedance-matched design can be

constructed, without any sacrifice in directionality or throughput (Fig. 4.4a, $1/\tau_L = 1/\tau_{R1} + 1/\tau_{R2}$). Furthermore, with the *orthogonal*, *two-band*, *on-resonance* operation of the $\boldsymbol{\Psi}_{e\text{-}o}$-$\psi_o$ *junction* (Fig. 4.4b-4.4d, contrast to the expensive *off*-resonance excitation for *single*-band diode operation shown in Fig. 4.4f-4.4h), it is possible to simultaneously realize; high reverse breakdown (from mode *orthogonality*), ultra-low threshold power (from the *on-resonance feeding* to the resonator in the even mode, Fig. 4.4b), and near unity throughput (with the *on-resonance releasing* of the resonator odd mode, to the ψ_o mode coupler, as in Fig. 4.4c).

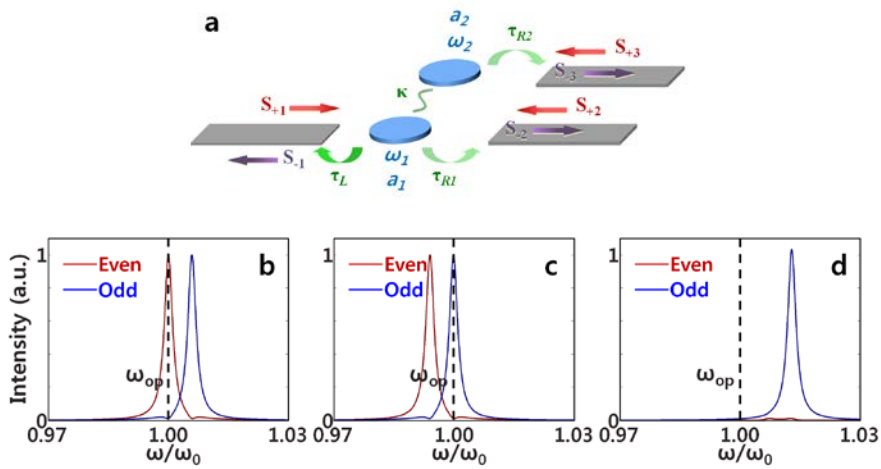

Figure 4.4. Comparison between a mode junction structure and an ordinary asymmetric structure [125]. (a) Impedance matched ($1/\tau_L = 1/\tau_{R1} + 1/\tau_{R2}$) low reflection design is achieved with a junction diode, by adjusting τ_L. Mode-dependent field intensity inside resonators (even: $|a_1+a_2|^2$, odd: $|a_1-a_2|^2$) for structures in (a) are shown for; (b) - forward bias before threshold, (c) - forward bias after threshold, (d) - under reverse bias. For two-band operation (b) at the operation frequency ω_{op} (dashed line), on resonance feeding and low power excitation of the resonator is achieved. $\kappa = 0.003\omega_{op}$, and $Q = 200$. Coupled-mode-theory was used for the calculation.

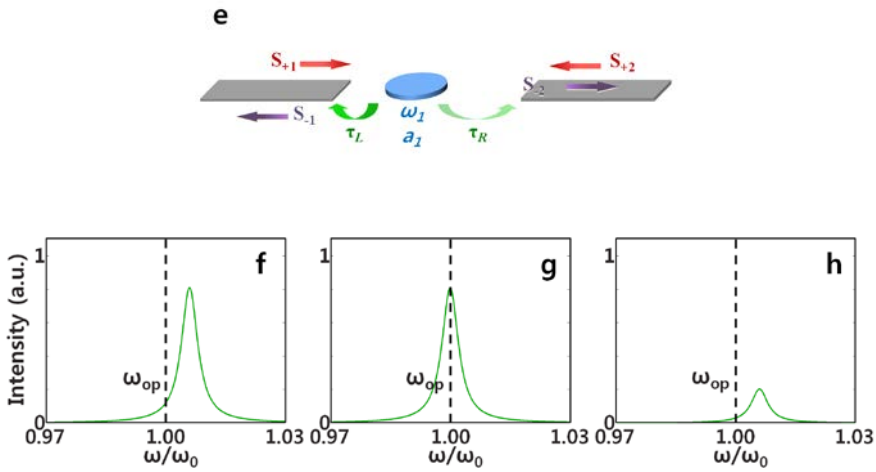

Figure 4.4 (continue). (e) Illustration of impedance imbalance, for the case of single band photonic diode (case of $\tau_R = 4\tau_L$). Mode-dependent field intensity inside resonators (even: $|a_1+a_2|^2$, odd: $|a_1-a_2|^2$) for structures in (e) are shown for; (f) - forward bias before threshold, (g) - forward bias after threshold, (h) - under reverse bias. $\kappa = 0.003\omega_{op}$, and $Q = 200$. Coupled-mode-theory was used for the calculation.

For implementation and demonstration of the proposed idea, without loss of generality, a 2D square-lattice rod-type photonic crystal platform was used [67] (structural details in the Appendix E.1). Of various optical nonlinearities, here we assume the conventional Kerr nonlinearity, to achieve a fair comparison with previous works. For the three states of the diode operation illustrated in Fig. 4.3a-4.3c, Fig. 4.3d-4.3f show the corresponding field patterns at the operating frequency ω_e of 193.24THz (1551.4nm), obtained from two dimensional Finite Difference Time Domain (2D-FDTD) analysis [226]. It is worth noting that, for the reverse operation (Fig. 4.3f), the mode orthogonality between the odd-coupler impinging wave and di-atomic resonator in the even mode resulted in a much weaker (12dB) energy build-up in the (upper) resonator, when compared to the case of forward bias. By minimizing the *spectral* overlap between the even and odd mode (Fig 4.4c), this residual build-up of the field (setting the reverse breakdown point) could be further suppressed. Blue line in Fig. 4.5a also shows the FDTD

obtained *static* response curves of the diode, as a function of input power (+ / - for forward / reverse bias). A threshold as low as 23mW/μm (~10^3 improvement over [217-221]), and a high reverse breakdown as much as 481mW/μm was observed, confirming the ultra-low power, highly unidirectional operation of the junction diode. The maximum contrast and throughput was found to be 41dB (at 142.2mW/μm. 15.7dB at peak throughput) and 0.96 (at 64.1mW/μm).

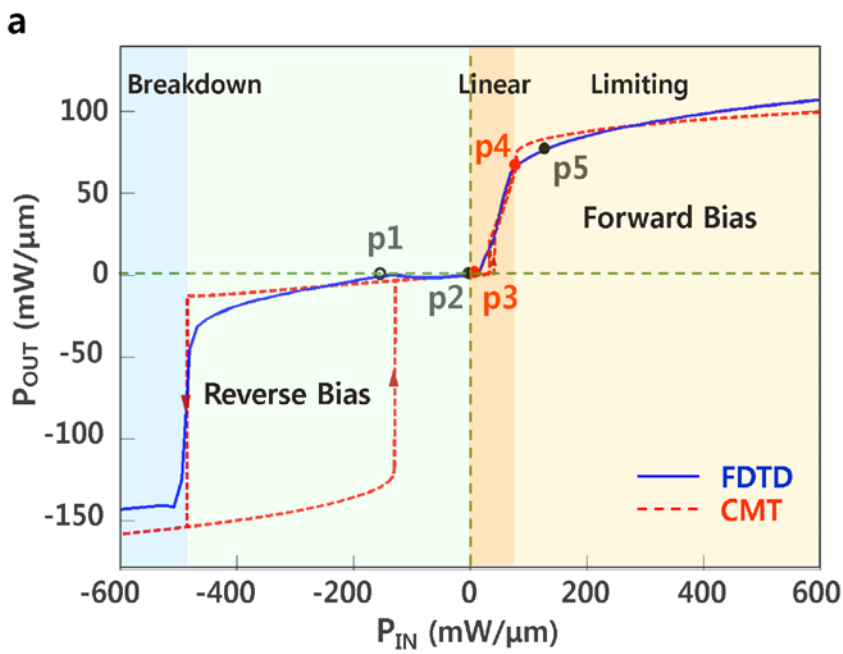

Figure 4.5. Photonic mode junction diode operation [226]. (a) Numerically (FDTD, blue lines, Appendix E.1), and analytically (CMT, red lines, Appendix E.2) obtained response curve of the $\Psi_{e\text{-}o}$-ψ_o junction diode.

Understanding that the above listed performance merits are derived from one specific example in a photonic crystal platform, it would be of interest to explore the performance boundaries of the $\boldsymbol{\Psi}_{e\text{-}o}$-$\psi_o$ junction diode having resonators of different Q factors. For this purpose, we use temporal coupled mode theory [64] (CMT, See the Appendix E.2) for its results can be used independently of implementation platform. Figure 4.5b shows the threshold, breakdown power and

bandwidth of the $\boldsymbol{\Psi}_{e\text{-}o}$-$\psi_o$ junction diode, calculated from the CMT (open circles); plotted as a function of the resonator Q, also overlaid to the results of the FDTD (solid triangles) obtained in photonic crystal platforms. The effect of introducing a higher resonator Q is twofold, but all in the same direction for achieving lower operation power; an increase in the resonator field strength, and more importantly, a smaller frequency (energy) separation between even and odd mode, enabled with the reduced spectral overlap between the orthogonal modes. Ultra-low power (4.22μW/μm ~ 73mW/μm) operation of the diode is predicted for a reasonable device speed range (1.74GHz ~ 227GHz); for its power ultimately limited by the maximum refractive index change ($n_2 I/n < 0.2\%$, [227]) assumed in the calculation, and for the operation speed limited by the resonator Q factor - bandwidth tradeoff relation [4]. Worth mentioning, by utilizing materials of higher Kerr index, or employing resonators of ultra-low modal volume [199], or by increasing spectral mode overlap across the junction, further reductions in operation power could be envisaged, down-below the μW regime.

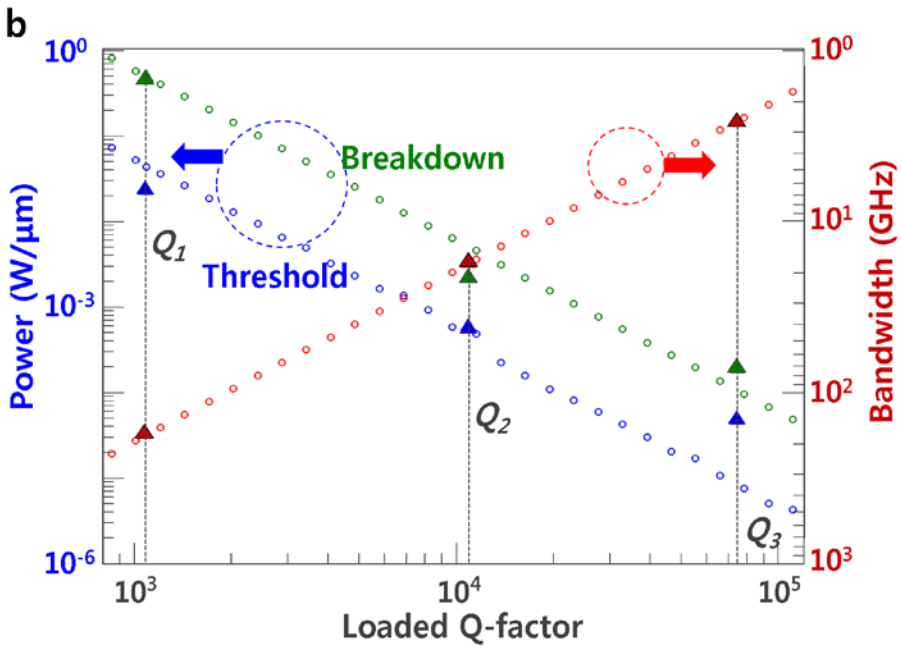

Figure 4.5 (continue). (b) Temporal-CMT calculated threshold power (blue circle), breakdown power (green circle), and operation bandwidth (red circle) as a function of the loaded *Q*-factor of a di-atomic resonator. Solid triangles overlaid to the plot are results of the FDTD, obtained with photonic diode realizations of different loaded quality factors Q_1 = 1094, Q_2 = 10945, and Q_3 = 74895 (achieved by adjusting the number of dielectric rods around the resonator).

Upon assessment of the key parameters, we also investigate the *dynamic* performance of the junction diode as a *passive* all-optical regenerator, for the application in errorless, ultra-high-speed signal processing [228]. Figures 4.5d and 4.5f show *FDTD obtained* regenerated optical eyes utilizing the highly limiting regime of the characteristic curve (p2-p3-p4-p5, in Fig. 4.5a), for the 2^7-1 PRBS (Pseudo Random Bit Sequence) NRZ (Non Return to Zero) noise-contaminated input at 100Gbit/s (Fig. 4.5c) and 200Gbit/s (Fig. 4.5e) respectively. With the all-optical signal regeneration action from the junction diode, a significant enhancement in the signal quality [4] was observed, from the optical *signal quality factor* for the input Q^i_s = 3.3 (Q^i_s = 3.9) to the output Q^o_s = 13.5 (Q^o_s = 7.0), at

100Gbit/s (200Gbit/s).

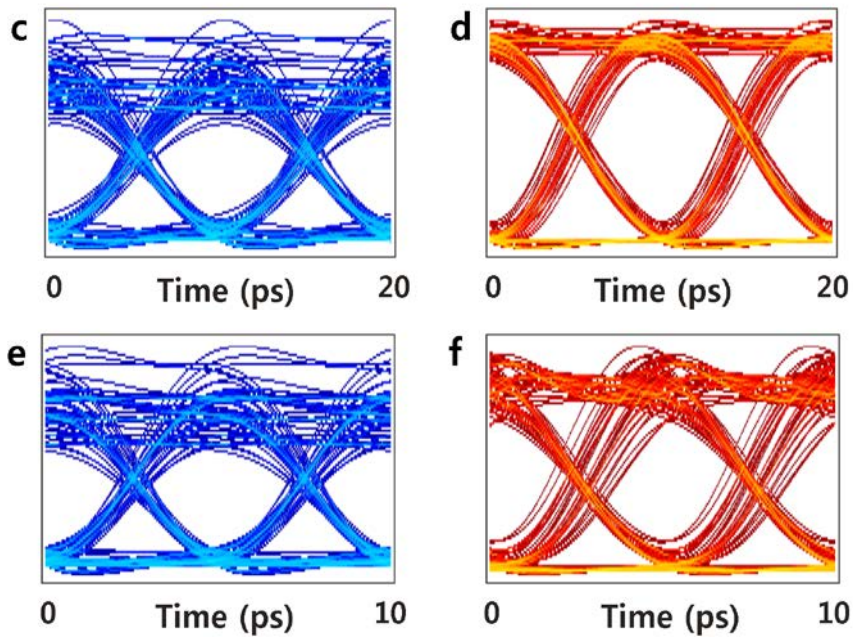

Figure 4.5 (continue). (d) and (f) show the regenerated optical eyes at the output of the junction diode, at 100Gbit/s and 200Gbit/s respectively for the input signals (c) and (e). Input signals were FDTD generated to include amplitude noise (Gaussian random distribution. for level-0, between point p2 and p3, and for level-1 between p4 and p5). For output signals from the regenerator, optical Butterworth filters were assumed to conform to the signal bandwidth.

4.2.2 Multi-Junction Half Adder

With the success in the ultra-low-power high-speed operation of photonic junction diode and all-optical regeneration using the simplest $\Psi_{e\text{-}o}$-ψ_o junction, we now consider another example for the modular application of mode junction. Half-adder, being the core building block for the Arithmetic Logic Unit (ALU) in the modern Central Processing Unit (CPU), has been often considered in the photonic domain [201, 229-231], but mostly as the combination of discrete components, and also lacking isolation properties.

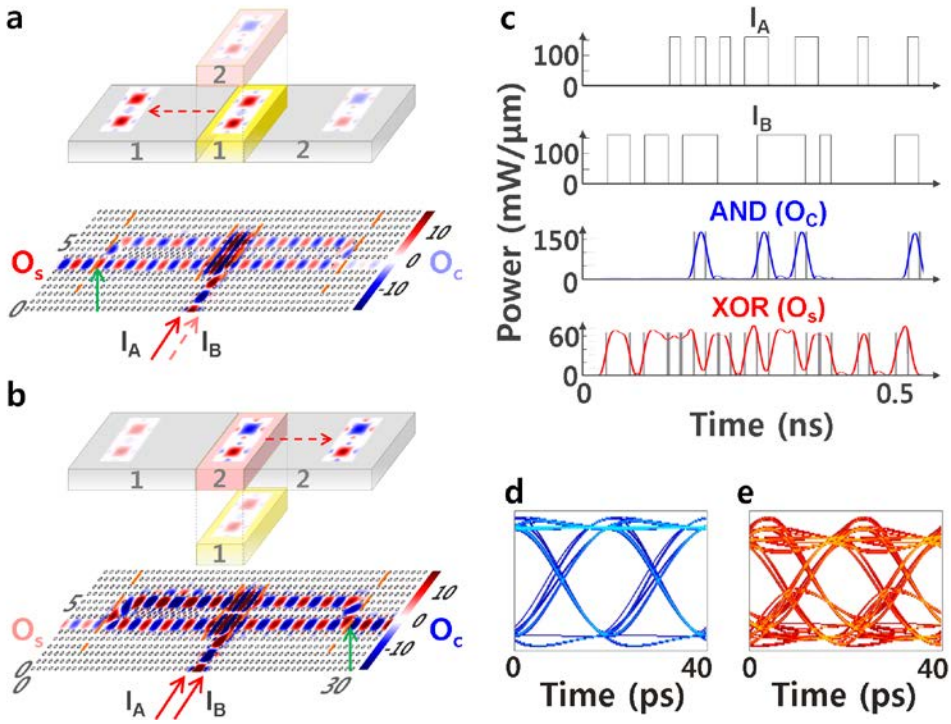

Figure 4.6. Multi-junction realization of monolithic half-adder [125]; (a) coupling to *S* (*XOR*) port with a single logic input (I_A or I_B) power below the threshold. (b) coupling to *C* (*AND*) port under two input signals ($I_A \cdot I_B$) for their total power above the threshold. Even (state 1)- / Odd (state 2)- mode excitation for the central di-atomic resonator and couplings to the even- / odd- mode coupler at the *S* / *C* port (left / right) of the half-adder is evident from the FDTD generated field amplitude plot. Figure (c) shows the logic operations of *AND* & *XOR*, under the two input signals at 50Gbps (de-correlated, PRBS). Figure (d) and (e) show the optical eye patterns for AND & XOR outputs. To note, for the generation of phase / time synchronized two input signals (I_A and I_B) for the proper logic operation, a single source was assumed, which are power divided and then separately modulated [230].

For this, we stretch our design strategy one step further, to construct a monolithic, multi-junction half-adder (ψ_e-$\boldsymbol{\Psi}_{e\text{-}o}$-$\psi_o$, shown in Fig. 4.6a); with the high-*Q* nonlinear region $\boldsymbol{\Psi}_{e\text{-}o}$ sandwiched in-between ψ_e and ψ_o structures (in this case, even- and odd- mode couplers). Setting the input power of the logic signal (I_A or I_B) for $\boldsymbol{\Psi}_{e\text{-}o}$ resonator slightly below the threshold of mode conversion, resonator

even mode coupling only to the *XOR* output port (O_S; supporting *even* mode) is enabled for a single input source (Fig. 4.6a. 1← ψ_e-$\boldsymbol{\Psi}_e$, $\boldsymbol{\Psi}_e$-ψ_o → 0), meanwhile above the threshold with two input signals ($I_A \cdot I_B$), the *AND* operation to the O_C port (supporting *odd* mode) is activated with the nonlinear conversion to the odd mode in the center resonator (0 ← ψ_e-$\boldsymbol{\Psi}_o$, $\boldsymbol{\Psi}_o$-ψ_o → 1. Fig. 4.6b). Figure 4.6c-4.6e show the *AND*, *XOR* operation and their optical eye for the multi-junction monolithic half-adder, for the input of two PRBS NRZ signals at 50Gbps. Note that, under the arrangement of the multi-junction in three-level ψ_2-$\boldsymbol{\Psi}_{(1/2/3)}$-$\psi_3$ structure, for example with Tri-atom molecule states (*T0*, *T*-, *T*+, in Fig. 4.2b), the same functionality with full input-to-output isolation could be achieved.

To summarize, we propose a mode junction for wave [125], with examples focusing on photonic applications. Rich and well-defined orthogonal modes providing ample degrees of freedom for the choice of junctions enable the modular construction of highly nonlinear devices of systematic control for wave propagation. By preferentially adjusting the optical potential, the dynamic and symmetry-breaking operation of the junction can be readily derived. For the simplest application of the formalism within a photonic crystal platform, we propose an ultra-low power photonic diode based on the $\boldsymbol{\Psi}_{e\text{-}o}$-$\psi_o$ junction, along with an application example for high speed signal regeneration. A superior performance in terms of orders has been realized when compared to previous results of photonic diode. Extending the concept further we then design a half-adder based on ψ_e-$\boldsymbol{\Psi}_{e\text{-}o}$-$\psi_o$ multi-junction, which provides all-optic *AND* and *XOR* output under a monolithic construction. The present examples operating in passive mode without external power, and providing highly nonlinear characteristics with an ultra-low threshold, we anticipate various applications beyond those demonstrated in this work.

4.3 Slow-light enhanced optical functionalities

Slow-light structure [68-71, 232-241] has been considered to be one of the key

elements for future all-optical functional devices. Many notable advantages of slow light, such as its larger group index, small footprint, and reduced power operation have been demonstrated in various forms [68-71, 232-241]. In particular, with the orders-of-magnitude enhancement of optical nonlinearities - derived from light-compression in the spatial domain [242, 243], it now became possible to seriously consider the option of optical signal processing, which has been difficult to achieve with conventional structures or materials. For instance, a slow-light enhanced nonlinear phase shift has been used to construct power-efficient and compact all-optical modulators [243], tunable buffers [244], parametric conversions [245], and optical analog-to-digital converters [204].

Still, whilst modern wavelength-division multiplexed systems and most of all-optical signal processing devices require more than one wave (for example control, signal, and clock), the slow-light structures in general, have been designed for single-band operation [68-71, 232-241] and have rarely been extended to incorporate multiband, multichannel functionalities [198]. As an example, for an all-optical, high-speed logic device based on cross phase modulation (XPM) [192, 246, 247], a multiband slow-light CROW with perfect intensity overlap and matched group velocities of its bands would be ideal.

In this section, we begin with the design of multiband slow light structures, based on the multi-atomic CROW (MA-CROW) platform (section 4.3.1, [205]). We then show the application of slow-light: optical A/D converter (ADC, section 4.3.2, [204]) and its all-optical implementation utilizing MA-CROW (section 4.3.3, [198]). Finally, we show the non-reciprocal device based on MA-CROW: all-optical slow-light-assisted isolator (section 4.3.4).

4.3.1 Multiband slow light

In this section, in order to extend our understanding of slow-light structures, we study the dispersion properties of a multi-band multi-atomic CROW [205], using coupled mode theory (CMT) [64] supported by a numerical assessment. To

incorporate the interference between multi-atomic molecular field patterns into the slow-light coupling strength, next-nearest-neighbor interaction terms are included in the CMT analysis of the multi-atomic CROW structure. By assessing the results of the CMT, a simple formula describing the origin of the band-dependent dispersion for each MA-CROW band is derived. The physical origin of the band-dependent group velocity is then explained in terms of the modification of the molecular-mode coupling strength, which is the result of the mode-dependent interference from next-nearest neighbor couplings. The result of our analysis implies that the performance limitation of multi-atomic CROW devices has to be estimated by including mode-dependent group velocity - which has been ignored in the past -, rather than using only the conventional CROW time-bandwidth relation [241]. The criteria for band separation and inter-mode intensity overlap are also discussed. Numerical assessments using a photonic crystal MA-CROW and all-optical slow-light travelling- wave Mach Zehnder switch show excellent agreement with the analytical solution developed from the coupled mode theory.

The MA-CROW unit cell is composed of multiples of single- mode atomic cavities, each at a resonant frequency of ω_0, that are tightly coupled together with an internal coupling coefficient κ_i (Fig. 4.7). When isolated, the unit cell forms a resonator molecule having orthogonal modes of non- degenerate frequency. The nearest-neighbor coupling between the atoms in neighboring molecules is also represented by an external coupling coefficient κ_o. It is critical to note that the current analysis includes a *cross-coupling coefficient* κ_c between next-nearest-neighbor resonators (dashed lines in Fig. 4.7), which has been neglected in previous studies. Under this arrangement, field amplitudes a_k^m (m=1~n, n representing the number of atomic resonators in the k-th molecule) can be written in a matrix form:

$$\frac{dA_k}{dt} = -i\omega_0 I_n A_k + i\kappa_i C_n A_k + i\kappa_o I_n (A_{k-1} + A_{k+1}) + i\kappa_c C_n (A_{k-1} + A_{k+1}) \quad (4.1)$$

where $\boldsymbol{A}_k$ is the vector with its m-th component being the field amplitude of the m-th atomic resonator in the k-th molecule ($[A_k]_m = a_k^m$), I_n is the $n \times n$ identity matrix, and C_n is the $n \times n$ matrix denoting the next nearest neighbor couplings ($C_{(p,q)} = 1$ for $|p-q|=1$, $C_{(p,q)} = 0$ otherwise).

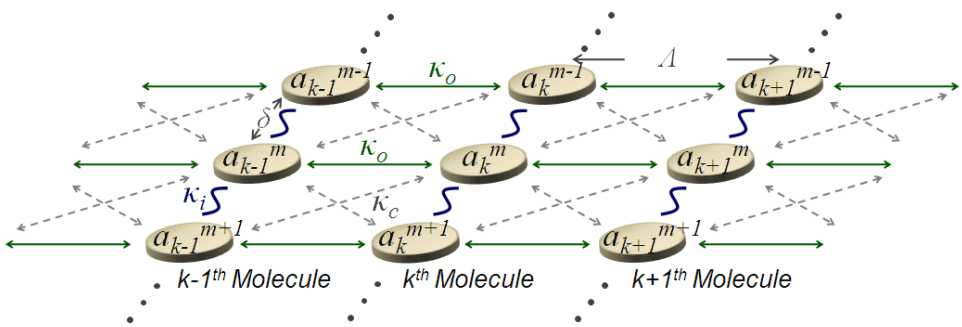

Figure 4.7. Coupled-mode theory model of a multi-atom, multi-band CROW [205]. $\kappa_{i,o,c}$: coupling constants between resonators; a_k^m : field amplitude in the m-th atomic resonator in molecule k.

By applying Bloch-wave harmonic functions $a_k^m = A_{+m}e^{-i\omega t+ik\beta\Lambda} + A_{-m}e^{-i\omega t-ik\beta\Lambda}$ (β being the propagation constant and Λ is the distance between molecules) with a periodic boundary condition, a governing equation for the dispersion relations for n-atomic CROW can be obtained,

$$M_n A_k = O \tag{4.2}$$

where, the matrix M_n is

$$M_n = \begin{bmatrix} (\omega-\omega_0)+2\kappa_o\cos(\beta\Lambda) & \kappa_i+2\kappa_c\cos(\beta\Lambda) & 0 & \cdots & 0 \\ \kappa_i+2\kappa_c\cos(\beta\Lambda) & (\omega-\omega_0)+2\kappa_o\cos(\beta\Lambda) & \kappa_i+2\kappa_c\cos(\beta\Lambda) & \cdots & 0 \\ 0 & \kappa_i+2\kappa_c\cos(\beta\Lambda) & (\omega-\omega_0)+2\kappa_o\cos(\beta\Lambda) & \cdots & 0 \\ \vdots & \vdots & \vdots & \ddots & \kappa_i+2\kappa_c\cos(\beta\Lambda) \\ 0 & 0 & 0 & \kappa_i+2\kappa_c\cos(\beta\Lambda) & (\omega-\omega_0)+2\kappa_o\cos(\beta\Lambda) \end{bmatrix}. \tag{4.3}$$

As can be seen clearly, M_n now represents the nearest and next-nearest neighbor couplings altogether. It is worth noting that by setting the diagonal / off-diagonal elements to $\Omega = (\omega - \omega_0) + 2\kappa_o \cos(\beta\Lambda)$ and $K = \kappa_i + 2\kappa_c \cos(\beta\Lambda)$, M_n can be rewritten as $M_n = \Omega \cdot I_n + K \cdot C_n$. In order to get the dispersion relations, we first derive a recurrence relation for the determinant of M_n.

$$\det(M_n) = \Omega \cdot \det(M_{n-1}) - K^2 \cdot \det(M_{n-2}) \tag{4.4}$$

Applying the initial conditions of $n = 1$ (atomic CROW, $\det(M_1) = \Omega$) and $n = 0$ (null space, $\det(M_0) = 1$), we can now write down the determinant of M_n, for n-atomic CROW as follows;

$$\det(M_n) = \frac{2^{-(n+1)}}{\sqrt{\Omega^2 - 4K^2}}[(\Omega + \sqrt{\Omega^2 - 4K^2})^{n+1} - (\Omega - \sqrt{\Omega^2 - 4K^2})^{n+1}] \tag{4.5}$$

Setting $\det(M_n) = 0$ to get non-trivial solutions, we can then obtain the following relation,

$$\frac{\Omega + \sqrt{\Omega^2 - 4K^2}}{\Omega - \sqrt{\Omega^2 - 4K^2}} = e^{i\frac{2p\pi}{n+1}}, \tag{4.6}$$

where p is an integer ($1 \le p \le n$). The closed form expression for Ω then can be obtained,

$$\Omega = \frac{1 + e^{i\frac{2p\pi}{n+1}}}{e^{i\frac{p\pi}{n+1}}} K = 2K \cos\frac{p\pi}{n+1}. \tag{4.7}$$

At this point, noting that the functional form of the matrix is $M_n = \Omega \cdot I_n + K \cdot C_n$. While $\Omega \cdot I_n$ describe the dynamics of isolated *atomic* CROW (coupled by κ_o), the

off-diagonal elements of $K \cdot C_n$ describe the rest of the interactions in MA-CROW. Meanwhile both the κ_i and $2\kappa_c \cos(\beta\Lambda)$ terms in K contribute to the modification of the eigenvalues of the molecular modes, it is critical to mention that *only the cross-coupling*-originated $2\kappa_c\cos(\beta\Lambda)$ term (with a non-zero β-differential $\partial K/\partial\beta \sim \square 2\kappa_c\Lambda \cdot \sin(\beta\Lambda)$) *modifies the group velocity*.

To get further insight into the effect of the cross- coupling κ_c to the dispersion properties of multi-atomic CROW, we now calculate in explicit the dispersion relation and group velocity. Substituting the functional forms of Ω and K into (4.7), we finally arrive at n sets of dispersion relations and group velocities (p=1~n),

$$\omega_p = \omega_0 + 2\kappa_i \cos\frac{p\pi}{n+1} - 2(\kappa_o - 2\kappa_c \cos\frac{p\pi}{n+1})\cos\beta\Lambda\,, \tag{4.8}$$

$$v_{gp} = 2(\kappa_o - 2\kappa_c \cos\frac{p\pi}{n+1})\Lambda \sin\beta\Lambda\,. \tag{4.9}$$

As can be seen from the dispersion equations (4.8) and tri-atomic example in Fig. 4.8, after the introduction of a nonzero κ_c, the *functional forms* of the n dispersion curves start to deviate from each other (Fig. 4.8a, 4.8b, (4.8)) depending on the *band* number p.

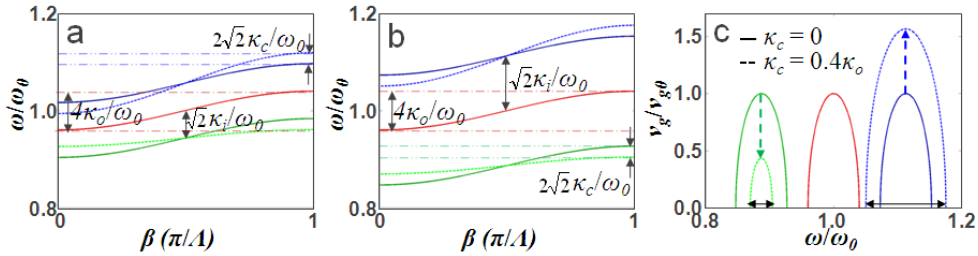

Figure 4.8. Dispersion curves of a tri-atomic CROW [205]: in (a) a weak internal coupling regime ($\kappa_i = -0.04\omega_0$, $\kappa_o = 0.02\omega_0$) and (b) a strong internal coupling regime ($\kappa_i = -0.08\omega_0$, $\kappa_o = 0.02\omega_0$). Effect of cross coupling is evident by comparing $\kappa_c = 0$ (solid line) and $\kappa_c = 0.4\kappa_o$ (dashed line). (c) Group velocities for the dispersion curves in (b). Group velocities are normalized to v_g ($\omega = \omega_0$, $\kappa_c = 0$).

This band number p-dependent deviation of dispersion curves then leads to differences in their group velocities (Fig. 4.8c, (4.9)), which would otherwise ($\kappa_c = 0$) be solely determined by κ_o. To note, in practical applications, the cross coupling strength κ_c will be dependent on both δ and Λ (Fig. 4.7), meanwhile κ_i and κ_o will be dependent only on δ and Λ respectively. Note that, by comparing Fig. 4.8a and 4.8b it is easy to see that, complete band separation can be achieved only for a regime of strong internal coupling. From (4.8), we derive the criteria for band separation between the p-1^{th} and p^{th} band as,

$$|\kappa_i| > 2 \cdot \left| \frac{\kappa_o - (\cos\frac{p}{n+1}\pi + \cos\frac{p-1}{n+1}\pi)\kappa_c}{\cos\frac{p}{n+1}\pi - \cos\frac{p-1}{n+1}\pi} \right|. \qquad (4.10)$$

Before examining dispersion properties of MA-CROW as a function of n (number of atoms in a molecule), it is better to understand the physical origin of the band- dependent group velocity. The case of a di-atomic CROW is illustrated in Fig. 4.9a. Compared to single atom CROW (where dispersion curves are determined by κ_o alone), the *effective* coupling strengths between di-atomic *molecules* become to have different values depending on the molecular mode field patterns - that is,

constructive or destructive interference between κ_o and κ_c (red- and black- arrow) directly affect the effective coupling. Similarly, for n-atomic molecules, the effective coupling between molecules ($\kappa_{eff} = \kappa_o - 2\kappa_c\cos[p\pi/(n+1)]$, from (4.9)) becomes to have different values depending on the mode field pattern (or band number p), in addition to being affected by the number of atoms, n, in a molecule. Figure 4.9b shows the calculated group velocities as a function of atomic number n, at the band centers, v_g ($\beta = 0.5(\pi/\Lambda)$, $\kappa_c = 0.2\kappa_o$). The deviation of group velocities for n-atomic CROW modes, from that of isolated ($n = 1$) CROW mode increases with n, up to a limit of $2(\kappa_o \pm 2\kappa_c)\Lambda$ (case of all- constructive or destructive interaction between κ_o and κ_c).

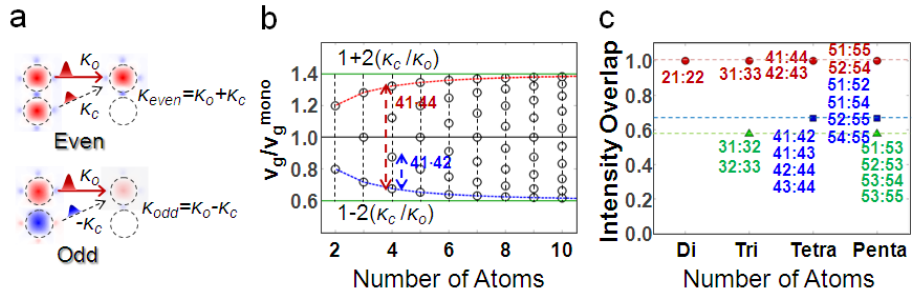

Figure 4.9. Band dynamics of MA-CROW [205]. (a) Band-dependent modification of molecular coupling strength for a di-atomic CROW; from constructive (even mode, $\kappa_{even} = \kappa_o + \kappa_c$) and destructive (odd mode, $\kappa_{odd} = \kappa_o - \kappa_c$) interferences. (b) Deviations in group velocity for each molecular mode, plotted for different n-atomic molecules. κ_c was set to $0.2\kappa_o$. v_g^{mono} denotes the group velocity of single atom CROW. (c) Intensity overlap between molecular modes p and q (marked as np:nq). Perfect intensity overlap can be obtained if $p+q=n+1$, for example, p =1 and q =4 for n = 4.

To investigate the implications of these findings for device applications, as an example here we estimate the system penalty from the group velocity walk-off [248], in cross-phase modulation devices. In the presence of signal-control walk-off, the limit of the nonlinear phase shift φ for the signal is given by [4]; $\varphi < \Delta k \cdot L_W \approx \Delta k \cdot [\Delta T / (1/v_g^{signal} - 1/v_g^{control})]$, where Δk is the XPM-induced wavevector

change, L_w is the walk-off length, and ΔT is the pulse width. Restricting the present analysis to cases of maximum XPM efficiency (i.e., p and q modes of identical $|\boldsymbol{E}(x,y)|^2$, $p + q = n + 1$ as shown in Fig. 4.9c.), now for a device using the p-th (q-th) band as a signal (control) wave for all optical modulation, the walk-off limited device bandwidth $\Delta\omega$ then can be easily estimated, using $\Delta\omega \sim 1/\Delta T$ in φ and (4.9),

$$\Delta\omega < \Delta\rho_{XPM} \cdot \frac{\sigma\omega_0}{\varphi \cdot v_{gp}} \left| \frac{1}{v_{gp}} - \frac{1}{v_{gq}} \right|^{-1} = \Delta\rho_{XPM} \cdot \frac{\sigma\omega_0}{\varphi} \cdot \frac{\kappa_o}{4\kappa_c \cos\dfrac{p\pi}{n+1}}, \quad (4.11)$$

where $\Delta\rho_{XPM}$ is the XPM-induced nonlinear refractive index change ratio, ω_0 is the signal frequency, and σ is the mode energy fraction in the nonlinear region [243].

The blue lines in Fig. 4.10a show the bandwidth (device speed) limit of a multi-atomic CROW device. With the increase of cross coupling κ_c, the walk-off (4.11) becomes the dominant factor in the bandwidth limit of the device, and gives values far below those determined by the CROW dispersion only [241] (red line in Fig. 4.10a). It is worth noting that the *maximum* bandwidth penalty is weakly dependent on the atomic number n, and saturates at a value proportional to κ_o / ($4\kappa_c$) - as expected from the maximum / minimum group velocities of $2(\kappa_o \pm 2\kappa_c)\Lambda$ (Fig. 4.9b). To verify our theory, we utilize multi-atomic CROWs on a photonic crystal platform. By assuming a 2D square-lattice, rod-type photonic crystal of lattice constant a = 528nm, rod index n_{rod} = 3.5, and radius $r = 0.2a$, CROWs made of point defect resonators ($r_d = 0.07a$, $\Lambda = 3a \sim 6a$, $\delta = 2a \sim 3a$) are constructed. Figures 4.10b and 4.10c show the group velocity walk-off, and walk-off limited bandwidth respectively for the constructed CROW. For the tested di- and also tri-atomic examples, excellent agreements between theory (CMT, lines) and numerical assessment (COMSOL, symbols) were observed, for different κ_o ($\sim \Lambda^{-1}$) and κ_c ($\sim (\Lambda^2+\delta^2)^{-1/2}$). Note that for a fixed value of δ, larger Λ results in increased walk-off and associated penalties, as the difference in strength between external coupling κ_o

and cross coupling κ_c decreases.

As an application example of *multi-band* slow-light structures, we constructed an all-optical travelling-wave Mach-Zehnder Interferometer (MZI), which could be utilized for all-optical switching [192, 199], analog-to-digital conversion [204], or parametric conversions [245, 249]. To achieve operation speed of ~100GHz, and at the same time sufficient frequency separation between control and signal wave, di-atomic CROW of $\Lambda = 4a$, and $\delta = 2a$ were used. Nonlinear Kerr index of $n_2 = 1.5\times10^{-17}m^2/W$ were assumed in the modulation region, constructed with di-atomic CROW of 200 cascaded molecule resonators. For the analysis of the switching operation, Finite Difference Time Domain (FDTD, two dimensional) method was employed. Continuous wave (CW) input signal, with 100Gbps / 200Gbps modulated control wave (2^6-1 bits pseudo- random bit sequence, of 3rd-order super-Gaussian non- return to zero pulses) was fed to the MZI to measure the bandwidth / output signal quality of the all-optical switching action. Fig. 4.10d-4.10e show the slow-light enabled low-power (10mW/μm for CW input, and maximum 30mW/μm for control) switching action of the MZI. From the FDTD-generated optical eye (Fig. 4.10f-4.10g), optical signal quality factor Q of 9.6 was obtained for the 100Gbps signal output. In contrast, at 200Gbps (near the estimated walk-off bandwidth of ~70GHz. Figure 4.9c), much worse, marginally acceptable optical quality factor Q = 3.5 were observed, supporting the signal-control walk-off limited bandwidth analysis for MA-CROW.

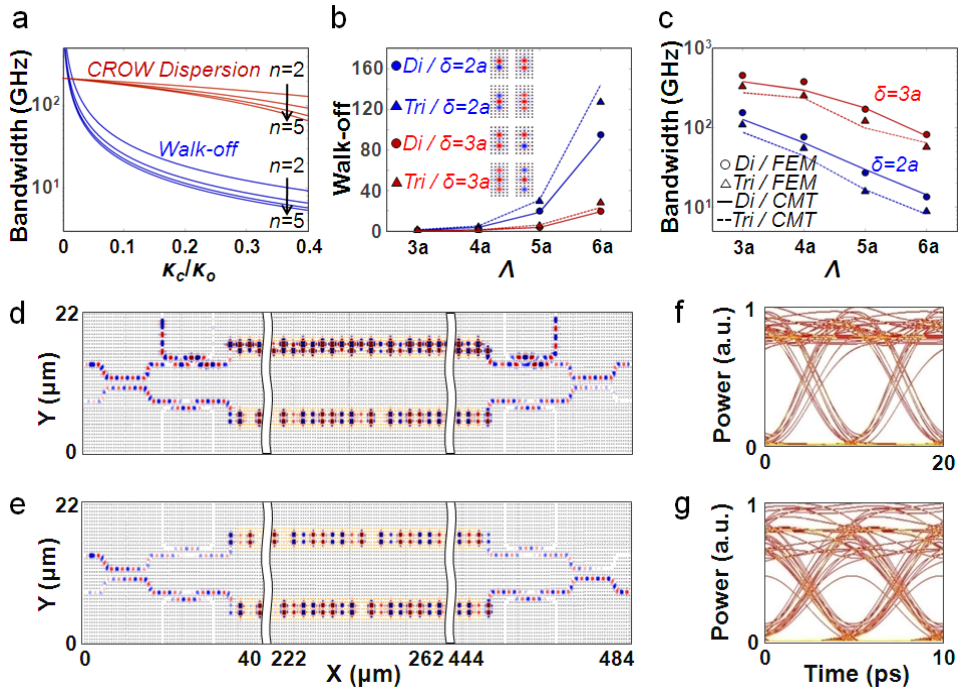

Figure 4.10. All-optical switching based on a MA-CROW Mach-Zehnder interferometer [205]. (a) Bandwidth limit of multi-atomic CROW, for different cross coupling coefficient κ_c. Blue and red lines show the walk-off- and CROW dispersion-limited bandwidth respectively, for different MA-CROW structures (n = 2~5). A plot was made for the cases of p = 1 and q = n by assuming maximum band separation and a perfect intensity overlap between the signal and control waves. $\Delta\rho_{XPM}$=0.02%, $\lambda_0=2\pi c/\omega_0$=1550nm, σ=0.6, $\varphi=\pi$, and κ_o=0.001ω_0. (b and c): A plot of the theoretically (lines) and FEM calculated (symbols) (b) walk-off parameter $\Delta n_g=c\cdot|1/v_{gp}-1/v_{gq}|$ and (c) Bandwidth limit, for di- and tri- atomic CROWs (Λ = 3a ~ 6a, for δ = 2a and 3a). Coupling coefficients for the CMT analysis were calculated from the isolated resonator modes. Switching operation of di-atomic CROW MZI for (d) On-State and (e) Off-State. Optical eye of the switched output, for PRBS control waves at (f) 100Gbps and (g) 200Gbps.

Extending our understandings on slow-light structures, we revealed the existence and origin of the band- dependent dispersion in a multi-atomic, multi-band slow light structure. By including next-nearest interaction in the CMT analysis of a multi-atomic CROW, a clear derivation of the band-dependent

dispersion equation was possible. An elucidation of its physical origin was made, in terms of the molecular field pattern interference between the κ_o (external coupling between CROW molecules) and the κ_c (cross coupling). By identifying conditions for complete band separation and also intensity overlap between different modes, our analysis provides guidelines in the design of multi-wave slow- light devices; in photonic crystal, ring resonator or plasmonic platforms. The implications of theoretical findings were elucidated in terms of the group velocity walk-off penalty, for an example of photonic crystal based XPM devices. Perfect match between theory and numerical analysis was found supporting the analysis, that the performance of the multi-atomic slow light devices has to be estimated including the effect of molecular field patterns. Our analysis addressing the physical origin of the band-dependent group velocity, it can be envisioned in the future to devise means of reducing detrimental cross-coupling effects - for example by utilizing resonance modes of anisotropic profiles.

4.3.2 Optical A/D converter

The realization of a high speed (>10GS/s) electronic analog-to-digital (A/D) converter has become a serious challenge for circuit designers [250]. With the fundamental physical limitations associated with aperture jitter, thermal noise, and comparator ambiguity [250], an increase in the universal measure of A/D converter performance (product of resolution and sampling rate) is near to the saturation regime. In this context, photonic A/D converters (PADC) have been a topic of intensive study as an attractive alternative for ultra-fast A/D converters.

Following serious research activities since early 1970s [251], PADCs of various principles and forms of operation have been suggested - which can be classified 1) in terms of the degree of photonic implementation; photonic sampled, photonic quantized, photonic sampled & quantized, and photonic assisted, and 2) in terms of de-multiplexing means for high-speed analog signal; space, wavelength, time, and interferometric.

Of these, the interferometric PADC proposed by Taylor [252] has been a structure generating most intensive follow-up studies because of its scalability (as the required number of interferometers / sources / detectors increases linearly with the ADC bits/resolutions), and its compatibility with electronic interfaces (using an input signal of *electrical* forms and providing *quantized* digital output). As an additional notable attribute, Taylor's PADC structure can be implemented with a simple, low cost single wavelength laser source instead of a multi-wavelength source of higher functionality - which is an imperative for other competing approaches [253]. Still, with the exponential dependence of the interferometer (MZI) length to the number of bits (proportional to 2^b), and correspondingly with the increase in the power consumption for the phase modulation, most of the demonstrations of Taylor's PADC have focused on a low-bit and high sampling rate, not exceeding the effective number of bits (ENOB) of 4 (at 10GS/s) so far [251].

In this section, we suggest a new and unique photonic crystal A/D converter design based on Taylor's A/D conversion concept. The uniqueness of our design, suggested here, is in the application of slow light advantages to the photonic A/D converter with the introduction of photonic crystal Coupled Resonator Optical Waveguides (CROW) [241]. By employing slow light concepts, we obtain an efficient phase change with much shorter modulation length [243], enabling the reduction in the size / power consumption of the PADC (~ by factors of tens). To our knowledge, this is a new application of slow light, quite different from the traditionally proposed ones - such as an optical buffer, optical delay line, or optical synchronizer. For investigating the properties of the suggested photonic crystal slow-light PADC, we analyze the performance limiting factors in terms of light transit time in the modulation region, as well as the pulse broadening effect (differential time delay) from the slow-light dispersion. Results show the feasibility of achieving a PADC with 20 giga-samplings per second (GS/s) and an ENOB of more than 5, under a silicon platform.

Figure 4.11 illustrates a schematic diagram of Taylor's PADC [252]. For each MZI, the necessary modulation region increases by a factor of 2 from the most significant bits. Optical outputs thus having a different period - as a function of the applied bias voltage strength (i.e, analog signal) - can be obtained from the output ports of different MZIs dedicated for each different bits, for the following conversion to a digitized gray coded output (with appropriate threshold / switch elements [254]). Worth noting that, by adjusting the amount of modulation to the MZI, it is also possible to get conventional binary output [252]. For later use, we write the relationship between the resolution (b) of the Taylor's PADC, and the required phase change ($L_{LSB}\Delta k$, L_{LSB} being the length of the modulation region for the least significant bit: LSB) in the LSB-MZI;

$$L_{LSB}\Delta k = 2^{b-1}\pi. \tag{4.12}$$

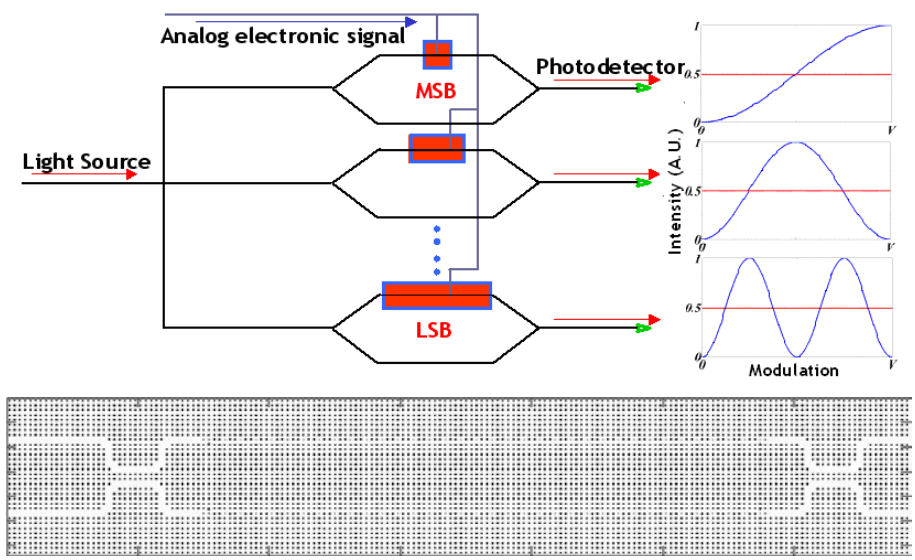

Figure 4.11. Schematics of Taylor's PADC and its ideal output (for a 3-bit A/D converter. red line: decision threshold for the digital conversion) [204]. Bottom: slow-light implementation of 2 x 2 MZI.

Meanwhile, assuming the simultaneous application of an analog signal to the

entire electrode, the net phase change felt by the optical signal is not given by the instantaneous strength of the analog signal, but is rather replaced by its averaged value over the transit time T_m (light signal propagation time in the modulated region L_m of the m-bit MZI) [255]. Different lengths of L_m and T_m for different bits of MZI thus lead to a non-uniform response to the input analog signal for its output. These non-uniform responses for different bits thus impose a limitation on the maximum signal bandwidth guaranteed for error-free operation of the ADC. As can be found in [255], writing T_b as the transit time of light for the *LSB* MZI, where b the resolution of the PADC, we now can write the maximum signal bandwidth f_s of the PADC as a function of the index change ratio $\rho = \Delta n/n$), for future reference purpose,

$$f_s < \frac{2^{2-\frac{b}{2}}}{\pi \cdot T_b} = \frac{2^{2-\frac{b}{2}} \cdot \upsilon_g}{\pi \cdot L_{LSB}} = \frac{2^{4-\frac{3}{2}b}}{\pi} \sigma\rho \cdot f_0 \qquad (4.13)$$

by using $v_g = \partial\omega / \partial k$, $(\Delta\omega / \omega_0) = \sigma(\Delta n/n) = \sigma\rho$ and Equation (4.12); here, σ is the fraction of mode energy stored in the modulated region [243], n is the refractive index of the dielectric and f_0 is the frequency of the light source. Assuming a reasonable number of 1% refractive index modulation for $\lambda_0 = 1550$nm and $\sigma = 0.6$, the PADC bandwidth becomes limited by the light propagation time T_b: to 11.5GHz at 6-bit resolution and to 1.44GHz at 8-bit resolution.

For the device size of PADC employing CROW, we now work on rewriting Equation (4.12). Utilizing the dispersion relation of light in the CROW: $\omega(k) = \omega_0(1+\kappa\cos(k\cdot\Lambda))$ and $\upsilon_g = \partial\omega / dk = \kappa\omega_0\Lambda\sin(k\cdot\Lambda)$ [256] (κ is the coupling coefficient; and ω_0 is the resonant frequency of the CROW cavity). Eq. (4.12) becomes (assuming the frequency of the signal light $\sim \omega_0$)

$$L_{LSB} = \frac{\upsilon_g}{\Delta\omega} 2^{b-1}\pi \cong 2^{b-1}\pi \frac{\kappa\Lambda}{\sigma\rho}, \qquad (4.14)$$

which is plotted in Fig. 4.12a. As can be seen, for the size reduction of Taylor's PADC based on the CROW structure (determined by the modulation length required for the LSB MZI, the longest one) it is suggested to use the smallest κ available. However, understanding that a smaller coupling coefficient in the CROW results in a narrower bandwidth [256], we naturally expect a limitation in the smallest κ accessible for the reasonable operation of the PADC.

Now, thus to analyze the penalty introduced from the restrictions in the signal bandwidth (alternatively, related to the device size, or κ), we start from the CROW dispersion equation. Focusing on the differential time delay of the signal - experienced with the CROW dispersion curve - which ultimately affects the timing jitter of the output signal of the PADC, we calculate below the differential delay in the propagation time of light after passing the modulation region. With $\Delta\omega$ being the frequency shift of the CROW structure experienced from the index change, m being the bit of the corresponding MZI (m=1~b for LSB~MSB), and L_m and T_m being the length / propagation time of light for the modulation region, the differential time delay (between modulation on / off states) of the light signal is given by, when expressed in terms of κ,

$$\begin{aligned}\Delta T_m &= \frac{dT_m}{d\omega}\Delta\omega = \frac{d}{d\omega}\left(\frac{L_m}{\upsilon_g}\right)\Delta\omega \\ &= \frac{L_{LSB}\cdot\Delta\omega}{2^{m-1}}\frac{d}{d\omega}\left(\frac{1}{\upsilon_g}\right) = 2^{b-m}\cdot\pi\frac{1}{\upsilon_g{}^2}\frac{\partial\upsilon_g}{\partial k} = \frac{2^{b-m-1}}{\kappa f_0}\frac{\cos(k\Lambda)}{\sin^2(k\Lambda)}\end{aligned} \tag{4.15}$$

Now noting that $k\Lambda \approx \pi/2$ near the center of the CROW band and writing $k\Lambda = \pi/2 + \Delta k\Lambda$, where $\Delta k\Lambda << 1$, Eq. (4.15) then can be approximated, with $\Delta k = \Delta\omega/v_g$, as

$$\Delta T_m \cong \frac{2^{b-m-1}}{\kappa f_0}\cdot\Delta k\Lambda = \frac{2^{b-m-1}\sigma\rho}{\kappa^2 f_0\sin(k\Lambda)} \cong \frac{2^{b-m-1}\sigma\rho}{\kappa^2 f_0}. \tag{4.16}$$

Treating the effect of the signal transit time (Eq. 4.13) as the bit-dependent attenuation to the input sinusoid signal [255] and then applying the differential delays (Eq. 4.16) from the CROW dispersion considerations, we can now estimate the error in the ENOB (effective number of bits) that originated from the introduction of CROW structure to Taylor's PADC platform. Applying a fast Fourier transform to the digitized output of the CROW PADC (with transit time and dispersion effects), and then calculating the signal-to-noise and distortion ratio (SINAD), we show the calculated ENOB = (SINAD-1.76)/6.02 [250, 251], in Fig. 4.12b.

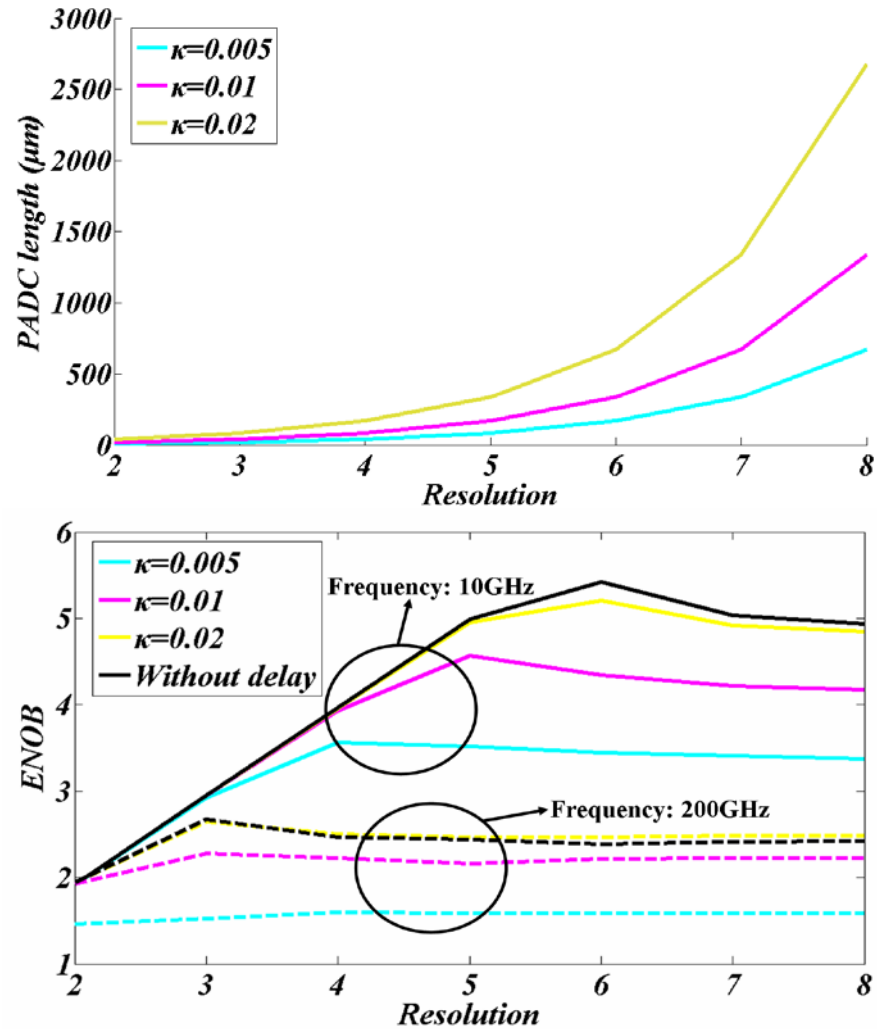

Figure 4.12. The footprint and performance of the PADC [204]. (Up) Device length and (Down) ENOB of the PADC plotted for different coupling coefficients, at various target resolutions. (1550nm, σ=0.6, ρ=1.0%, and Λ=2μm).

As can be seen, the reduction of the ENOB with smaller values of κ is evident implying the ultimate performance-size tradeoff for Taylor's PADC, resulting from the CROW bandwidth restrictions. For example, changing the coupling coefficient κ from 0.02 to 0.005, it is possible to reduce the device size / power consumption by a factor of ~ 4, but only at the accompanied expense of an ENOB reduction of ~

2 (for 10GHz, with 1 % index modulation). We also note that, from flight-time considerations only, there exists a maximum bound in the ENOB, 5 bits for 10GHz (or 20GS/s) and 2 bits for 200GHz (or 400GS/s).

Without loss of generality, two-dimensional square dielectric rod photonic crystal (PC) has been used as the basic platform, for the study of a slow-light PADC under Taylor's principle. Dielectric rod of radius r = 0.20a, with a lattice constant of a = 550nm, and an effective refractive index n^{eff} (Si) of 3.23 were adopted. For the construction of the CROW, the dispersion relation (Fig. 4.13a) was calculated using the PWEM (Plane Wave Expansion Method). The radius of the defect in the CROW cavity was set at r = 0.08a with a defect period of 3a, to provide a coupling coefficient κ of 0.0142 - considering restrictions both in the ENOB (related to differential time delay) and device size. Note that care has been taken in the wideband design of the 3dB directional splitter (Figure 4.13b) and the CROW-PC waveguide adapter (Fig. 4.13c). For the CROW-PC waveguide adapter, coupled mode theory (CMT) has been applied to give a coupling efficiency > 95%.

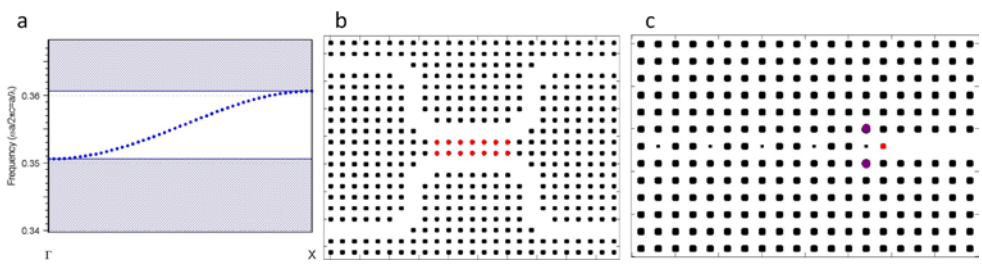

Figure 4.13. Design strategies of elements in the PADC [204]. (a) CROW dispersion relation of the achieved design. (b) 3dB splitter (red rods tuned to r = 0.18a) (c) CROW-PC waveguide adapter (purple and red rods tuned to r=0.22a and 0.15a).

With the large problem size extending to more than 100μm (=L_{LSB} for a 3bit PADC), 2D FDTD analysis was carried out employing an effective index method [257]. Push-pull index modulation (+/– 0.496%) was used to drive the MZI assuming a DC bias to both arms of the modulator, with the signal frequency set at

the CROW center frequency f = 0.3543(c/a). Figure 4.14 shows the operation of the 3-bit PADC (having different modulation lengths for each MZI), for a linearly increasing (within t = 6.88ps~27.5ps) analog input signal. To note, outputs of each MZI can be digitized by setting decision thresholds, to produce coded output. For the current example, the threshold was set at 43% of the normalized LSB peak power.

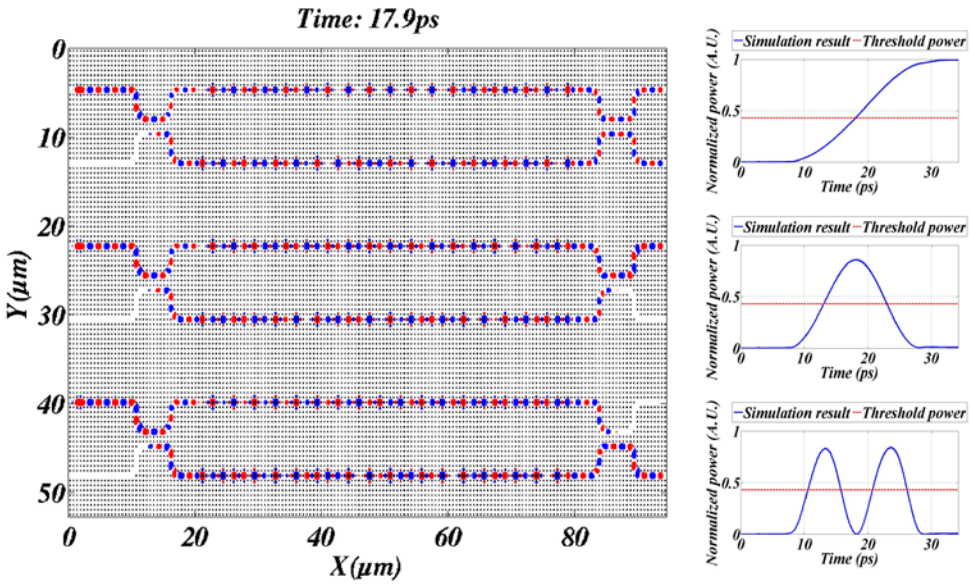

Figure 4.14. Demonstration of a 3-bit CROW PADC under a linear refractive index modulation (movie in [204]). For the figures on the right, the red dashed lines show the decision threshold.

Confirming the basic operation, now further to analyze the PADC operations at an ultra-high sampling rate, high-frequency (100 ~ 350GHz) sinusoidal analog signal has been tested to get the ENOB values at corresponding frequencies - following the procedures detailed earlier in this section. Figure 4.15a shows the 100GHz analog input signal overlaid on the digitized output. Also shown in Fig. 4.15b is the obtained ENOB of the PADC plotted together with the theoretical ENOB values. With the selection of a reasonable value for κ□= 0.0142, the differential time delay penalty from the CROW dispersion was minimized, leaving

the signal transit time as the dominant source of error in the ENOB of the CROW PADC operation. Worth to mention, to counter the signal transit time and thus to get a higher ENOB for the PADC, a traveling-wave MZI configuration can be considered, possibly using Kerr nonlinearity, and co-propagating control optical analog signals.

Finally critical to mention, for the current study assuming electrical modulation, a realistic modulation speed and the material aspects of dielectrics need to be counted. For modulating the index of silicon with an electrical signal, a plasma dispersion effect (with a response time up to 20GHz) can be used [258]. Assuming 1% of the index change ratio ρ in air-hole type Silicon PC structures, ENOB = 5 for the PADC operation was estimated at a 20GS/s sampling speed (10GHz analog signal, with $\kappa = 0.02$, resolution $b = 6$, $\sigma = 0.6$, and $\Lambda = 1.7\mu m$), with the longest MZI smaller than 600μm.

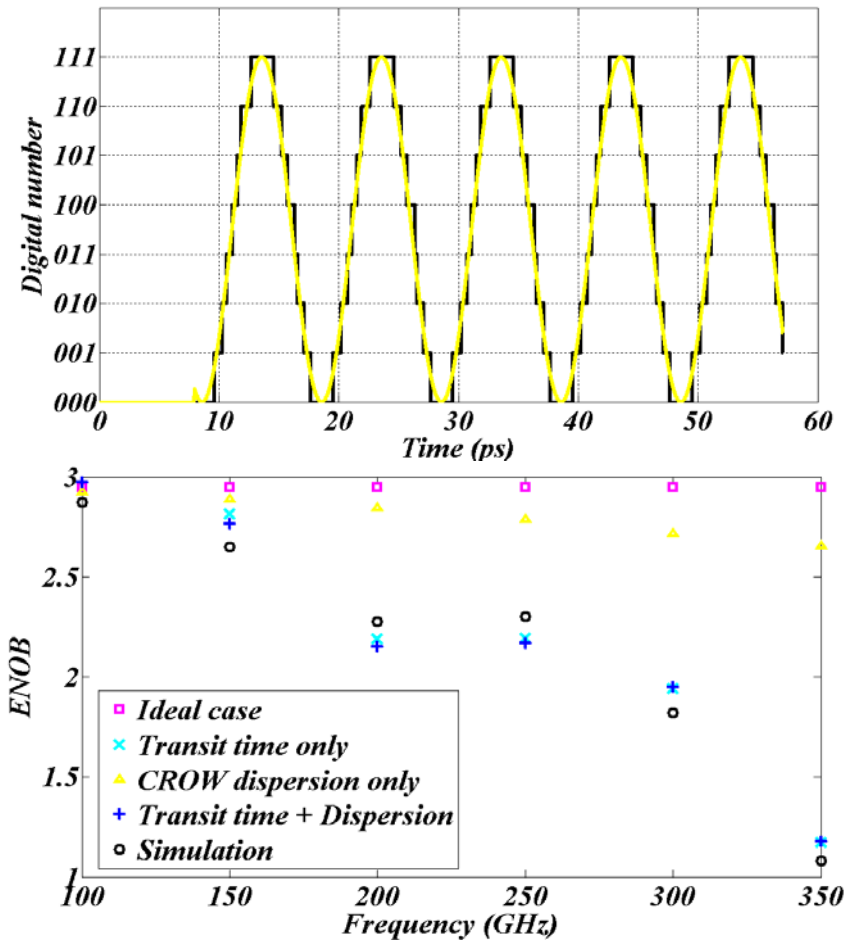

Figure 4.15. The spectral response of the CROW PADC [204]. (Up) Plot of the digitized output (black) from a 3-bit CROW PADC compared with its analog sinusoid input signal (100GHz, yellow). (Down) ENOB of the 3-bit PADC at different frequencies of analog input signals. The ENOB from the FDTD simulation (black) is compared to the ENOB values calculated from theory (in Section 2) showing excellent agreement.

We suggested and demonstrated a new and unique photonic A/D converter design using slow-light photonic crystal structures. Theoretical analysis on the performance limitation has been developed / and carried out considering both the signal transit time and CROW dispersion effect, to point out the trade-off in device size and penalties in the ENOB, associated with the differential time delay (from

the CROW dispersion). Numerical assessment of the device performance shows the feasibility of a slow-light PADC with a reduced device size (up to a factor of 10 (~v_g / c, when compared to those MZI employing a conventional waveguide) and higher ENOB / speed of operations (ENOB = 5, 20GS/s for a silicon platform using a plasma dispersion effect).

4.3.3 All-optical A/D converter

In section 4.3.2, we introduced the PADC based on electrical modulations. Yet, to achieve ultrafast dynamics (>10Gbps), all-optical scheme is required utilizing optical nonlinearity such as optical Kerr effect. Based on the contents of section 4.3.1 which enable all-optical modulations in slow-light structures, here we test the feasibility of all-optical ADC with slow-light performance enhancement [198].

Although the unit elements of all-optical ADC, travelling-wave MZI, is identical to that in Fig. 4.10 in section 4.3.1, here we introduce it in detail. The structure of the constructed travelling MZI is shown in Fig. 4.16. For the implementation, photonic crystal platform in a square lattice (lattice constant a = 528nm, rod refractive index n = 3.5, and rod radius r = 0.2a) was used. Nonlinear refractive index value of $n_2 = 1.5\times10^{-17}$m^2/W for the optical Kerr effect was also assumed for the modulation region. Coupled two-mode CROW waveguide was constructed by using paired defect rod resonators with radius r_d = 0.07a at a periodicity of 4a (section 4.3.1). The obtained central frequency of the CROW modes were 0.3407(c/a) and 0.3561(c/a) for odd mode (1550nm, control) and even mode (1483nm, signal) respectively. To maximize the Kerr nonlinearity for the reduction of control optical power, group velocity of the modes were decreased to 0.03c at the center of the modes, by setting CROW coupling coefficient κ for odd / even modes to 0.0039 / 0.0037. The phase mismatch between the odd / even mode in the ideal, infinite CROW was less than 1% with our design. The estimated CROW bandwidth with above design parameters was more than 100GHz.

Input / Output ports of the PC-MZI for signal pulse were also constructed by

using 3dB directional couplers over the photonic crystal waveguide platform. Analog modulation signal was coupled to the MZI before the Kerr modulation region, using wavelength multiplexing, photonic crystal waveguide couplers (f_{odd} = 0.3407(c/a), f_{even}= 0.3561(c/a)). For the case of 2-bit MZI, the modulation region was constructed with a CROW with 48 cascaded resonators. Overall, the total foot-print of the 2-bit PC-MZI was less than 160μm × 20μm, including every components.

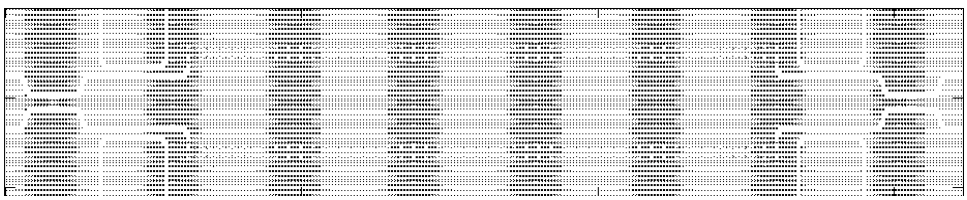

Figure 4.16. Structure of travelling-wave, two-mode, 4-ports CROW MZI [198]: composed of 2 CROW waveguide arms, 6 directional coupler, and several waveguide bending and CROW-waveguide connectors.

For the analysis, 2-D FDTD was employed without a loss of generality. Considering the sample size (length of the MZI) and computational cost of the current problem (which scales exponentially to the targeted number of bits), the switching action of the MZI only for the most significant bit (MSB) has been carried out in this study, to assess the performance of full PADC [204].

Figures 4.17a and 4.17b show the ON-OFF switching action of the MSB MZI, taken with the input signal strength of 20mW, and control analog optical modulation power of 170mW/μm (ON) and 0mW/μm (OFF) respectively. Taking the upper or lower arm of the MZI output (Fig. 4.17c) with the use of decision threshold device or a nonlinear optical element, a digitized, coded output either in electrical or optical form can be finally obtained for the full ADC operation.

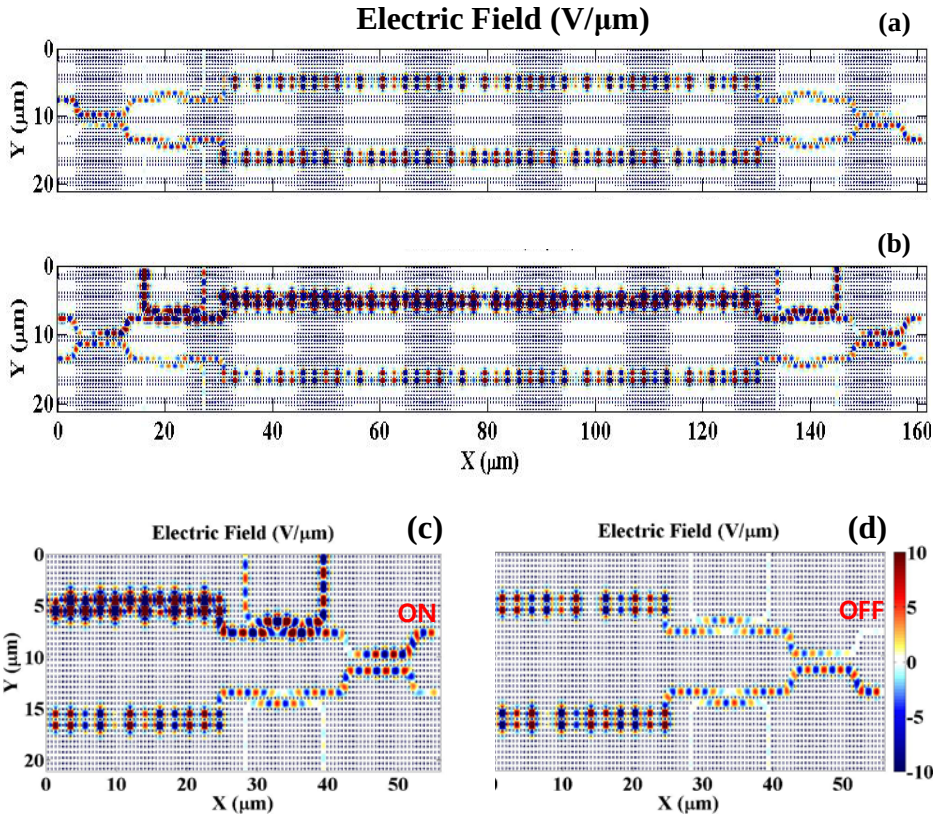

Figure 4.17. Switching action of MSB MZI of the PADC [198]. (a) ON state (control signal power = 170mW/µm). (b) OFF state (control signal power = 0mW/µm). Zoomed-in images of the wave evolution, at the output ports of the MSB MZI, for (c) ON state, and (d) OFF state.

Figure 4.18 shows the dynamic response of the two-mode *CROW* for 100GHz signal (Fig. 4.18a) and control input (Fig. 4.18b) waves respectively. Also shown is the signal wave output for the 100GHz control analog optical wave input (Fig. 4.18c) from the *MSB MZI* after the 3rd order butterworth optical bandpass filter (full-width half-maximum = 350GHz). After the initial propagation delay and power build-up time for the CROW resonator, clear sinusoidal output of the signal / control wave was observed without serious distortion. We attribute the remaining, slight distortion of the signal output to the non-optimal response of the present multiplexer design. For the output signal wave from the MSB MZI, successful

digitization can be made with a threshold level set to the middle of the peak power [204]. The observed phase mismatch (or equivalently, differential group delay, DGD) between the control and signal pulse in the two-mode non-ideal *finite* CROW was well suppressed below 10% (measured from Fig. 4.18a and Fig. 4.18b. DGD = 1.05ps for the MSB MZI having ~ 10ps of device propagation delay).

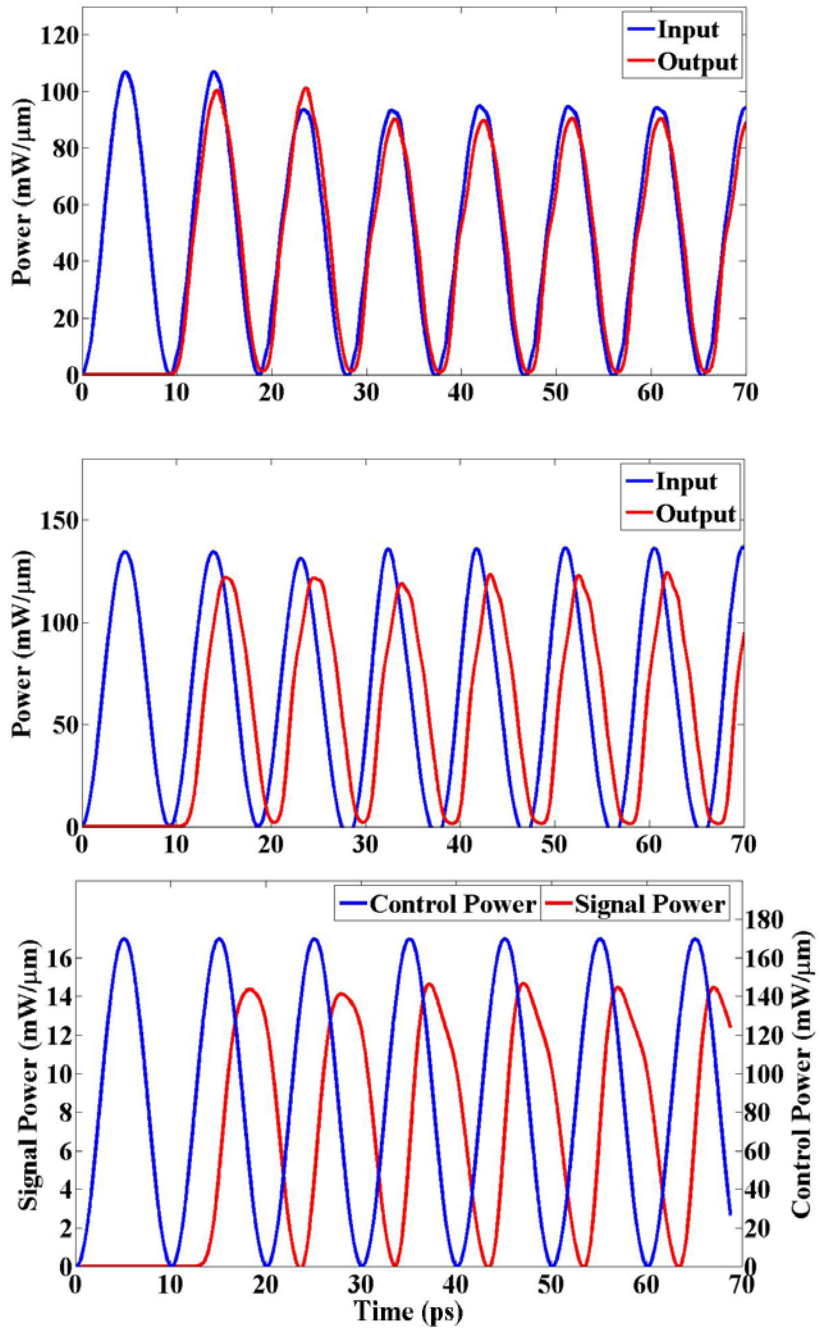

Figure 4.18. Spectral response of the two-mode CROW [198]. Response of (a) signal and (b) control wave from the two-mode CROW waveguide. (c) signal wave output from the MSB MZI, with sinusoidal control wave at 100GHz.

Using the above measured DGD between the signal and control wave, estimation on the differential time delay for the *b*-bit MZI as well can be made. Employing the effective attenuation formula in [255] now to incorporate the effect of phase mismatch for the *b*-bit MZI, the signal-to-noise and distortion ratio (SINAD), as well as corresponding ENOB for the *b*-bit PADC can be calculated at the same time considering the effect of CROW dispersion. Following the same procedure as detailed in [204], Fig. 4.19 shows the calculated ENOB for the optically modulated, travelling PADC at a 200GS/s (100GHz) operation speed. For the measured even / odd mode DGD mismatch of 10%, by using the dispersion curves of the present two-mode CROW, the difference in the ENOB between travelling, and non-travelling PADC design was estimated - to be about 0.36bit (2.58bit vs. 2.22bit). Meanwhile, using same 10% DGD value but assuming *linearized* dispersion curves [259], up to 4.9bit of ENOB was predicted for a travelling-wave optically-modulated PADC at 200GS/s - well above to that of electrically modulated PADC (2.7bit).

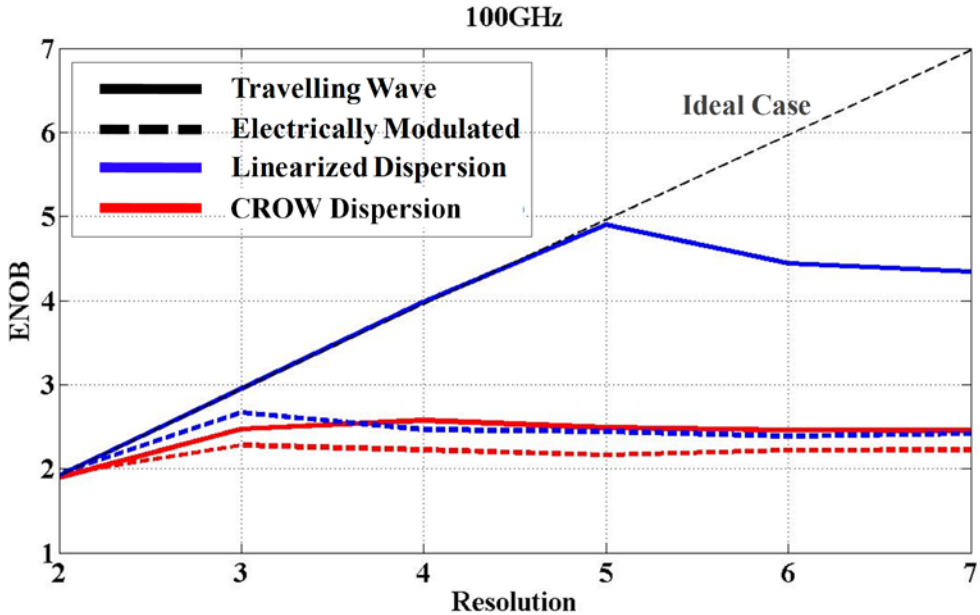

Figure 4.19. Error analysis of the all-optical PADC, based on the comparison with an electrically-modulated PADC [198]. ENOB of the travelling-wave, optically modulated PADC (solid lines, DGD = 10%) and electrically modulated PADC (dotted lines), plotted for different CROW dispersion (blue : linearized [259], red : diatomic CROW dispersion).

4.3.4 Travelling-wave all-optical isolator

In section 4.2, we showed one of the most important optical nonreciprocal devices, optical diode ('isolation + functionality'), based on resonant photonic junction structures. Despite its excellent performance, the resonant platform inherently degrades the operation speed due to its narrow bandwidth. Here we show the feasibility of a non-resonant optical nonreciprocal device, optical isolator, by employing MA-CROW slow-light structures [205].

The walk-off effect treated as the obstacle in section 4.3.2 and 4.3.3 actually involves the possibility of nonreciprocity in all-optical devices. In detail, a forward signal wave co-propagates with the control wave which gives the cross-phase modulation (XPM) $\Delta n(t)$ from optical Kerr effect. Therefore, if the group velocities

of signal and control waves are identical ($v_{g,c} = v_{g,s}$, Fig. 4.20a), photons of the forward wave are then ideally affected by $\Delta n(t_0)$ at the specific time t_0. In contrast, the backward wave counter-propagating with the control wave 'sees' the evolution of $\Delta n(t)$, deriving the effective modulation by the integration of $\Delta n(t)$ (Fig. 4.20b).

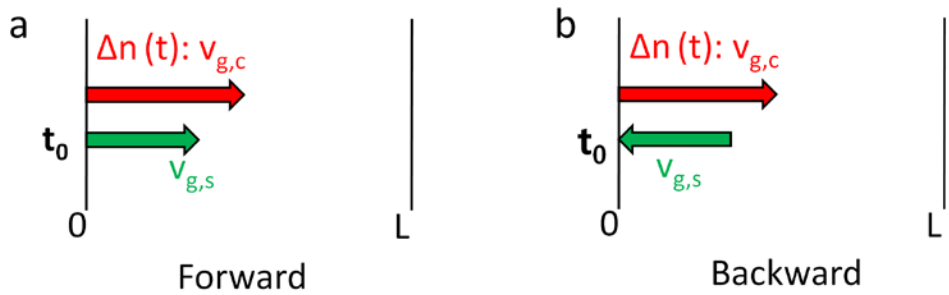

Figure 4.20. Schematics of travelling-wave all-optical isolator: (a) forward wave and (b) backward wave.

Figure 4.21a shows the all-optical isolator on the photonic crystal platform, using MA-CROW structures. Two control waves are applied to achieve the Kerr-effect XPM signal $\Delta n(t)$ while maintaining the π phase difference between two arms (by Δn_{pi} for Δk_{pi}). The type of modulations should then be square-type pulse with phase difference (Fig. 4.21b).

The operation based on Fig. 4.21b can be described briefly as follow. When $v_{g,c} = v_{g,s}$, the XPM-induced phase difference between arms is $\Delta\varphi_f = |\Delta k_1(t_0) - \Delta k_2(t_0)|L = \Delta k_{pi}L = \pi$ for the forward wave, while the XPM for the backward wave gives $\Delta\varphi_b = |[\int\Delta k_1(t)dt - \int\Delta k_2(t)dt]/T_{transit}|L = 0$ where $T_{transit}$ denotes the time for the propagation along the MA-CROW and $\Delta k_{1,2}$ is the XPM-induced wavevector shift in the 1st and 2nd path.

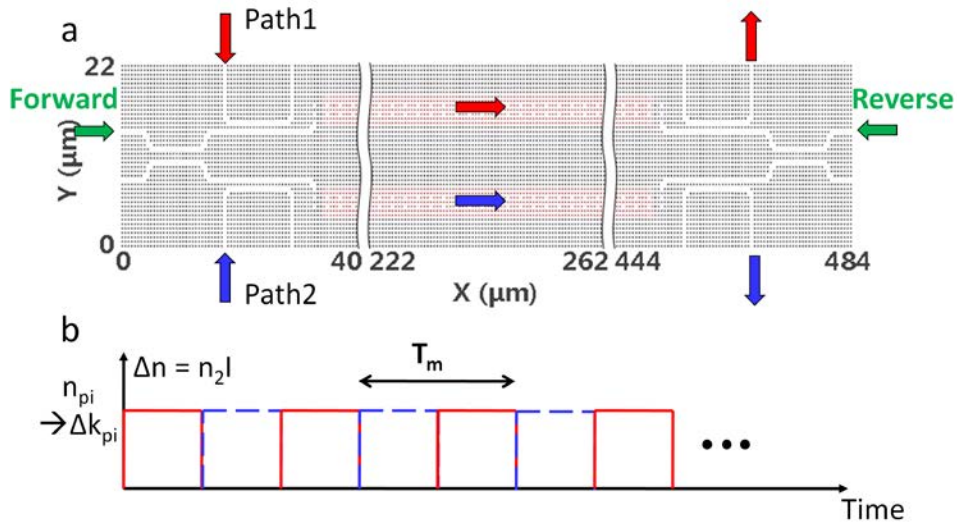

Figure 4.21. Design strategy of the travelling-wave all-optical isolator. (a) Travelling-wave all-optical isolator based on photonic crystal MA-CROWs. (b) Modulation signals for Path 1 and Path 2 in (a). T_m is a period of the square modulation and n_{pi} denotes the Kerr effect XPM for the π phase difference between two arms.

However, because there exists the group velocity walk-off between different modes of MA-CROW (section 4.3.1), more rigorous formulations are required reflecting the different group velocities between control and signal waves. For forward waves, the effective index change n_{eff} is determined as

$$\Delta n_{eff} = \frac{\left| \int_{t_0}^{t_0 + (\frac{1}{v_{g,s}} - \frac{1}{v_{g,c}})L} \Delta n(t) dt \right|}{L / v_{g,s}}, \qquad (4.17)$$

while Δn_{eff} for backward waves is

$$\Delta n_{eff} = \frac{\left| \int_{t_0}^{t_0 + (\frac{1}{v_{g,s}} + \frac{1}{v_{g,c}})L} \Delta n(t) dt \right|}{L / v_{g,s}} . \qquad (4.18)$$

To achieve the isolation, backward waves should be blocked, and then, the following relation from Eq. (4.18) is the necessary condition for all-optical isolation:

$$(\frac{1}{v_{g,s}} + \frac{1}{v_{g,c}})L = pT_m = p\frac{2\pi}{\omega_m} , \qquad (4.19)$$

where p = 1,2,…, and $\omega_m = 2\pi f_m$ is the modulation frequency. As can be seen, the modulation frequency is determined by the group velocities of signal and control waves. From Eq. (4.17), we also note that the optimum condition for the forward wave is $v_{g,s} = v_{g,c}$, minimizing the modulation sideband and deriving efficient power consumption.

Figure 4.22 shows the operation of the designed all-optical isolator. Because $v_{g,c} \sim v_{g,s} \sim 0.03c$, and L=422μm in the current structure, we can apply the ideal condition of the modulation frequency $f_m = p/[\ (1/v_{g,s}+1/v_{g,c})L\ ]$ (p=1, 2, …) from Eq. (4.19), resulting in $f_m = 10.6 \times p$ (GHz) (p=1, 2, …). We employ the modulation frequency of 43GHz (p = 4) with the time delay of 11.63ps between two arms of Mach-Zehnder modulator (Fig. 4.21b). We demonstrate that the designed isolator shows the apparent optical isolation (Fig. 4.22a vs 4.22b). In spite of power-dependent Kerr effect, the isolation condition is maintained both for 20mW/μm (Fig. 4.23, left) and 40mW/μm (Fig. 4.23, right) signal powers with about 25mW/μm modulation power. We note that due to the frequency detuning from the modulation signal, the throughput has the modulation sideband with the time domain oscillation (Fig. 4.23).

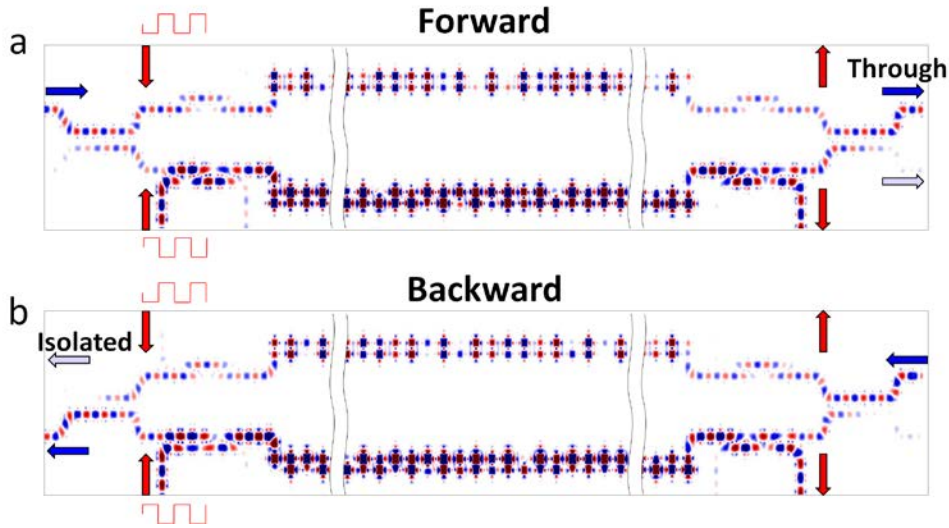

Figure 4.22. The operation of the travelling-wave all-optical isolator. (a) Forward wave, and (b) backward wave incidences. The simulation is carried out by the 2D FDTD method with optical Kerr effect.

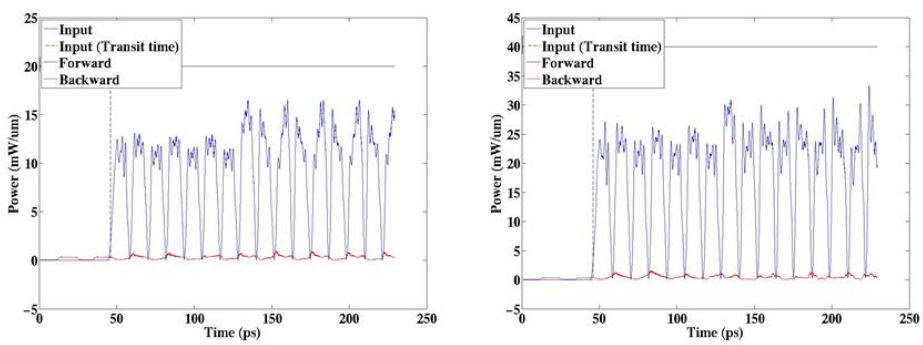

Figure 4.23. DC response of the travelling-wave all-optical isolator. Signal outputs for (left) 20mW/μm and (right) 40mW/μm signal powers, modulated by the ~25mW/μm modulation power. Blue lines for forward signals and red lines for backward signals.

The modulation sideband mainly from the high-frequency components of modulation signals becomes critical in large power signal waves which are deviated from the designed strategy (Fig. 4.24). To compensate this limit, we can remove high-frequency components by using smooth modulation pulse such as the

$\sin^2(t)$ modulation wave (Fig. 4.25). As can be seen, the unwanted backward wave throughput is sufficiently reduced (red lines in right panels of Fig. 4.24 and Fig. 4.25) even in the large power level, with the sacrifice of the forward wave throughput (blue lines in right panels of Fig. 4.24 and Fig. 4.25).

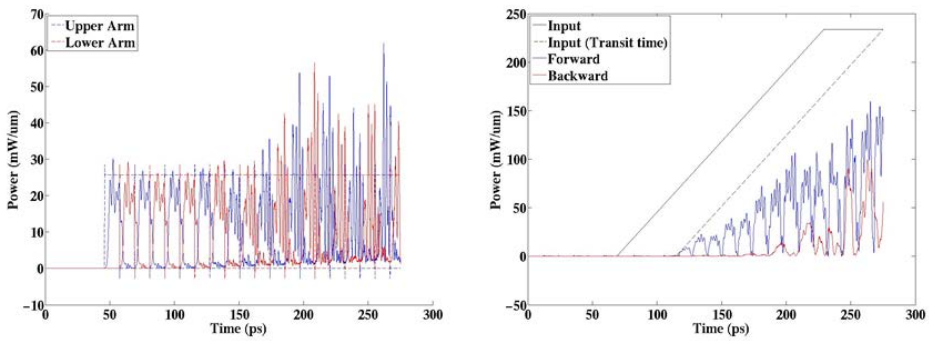

Figure 4.24. Square pulse modulation for the all-optical isolator: (left) modulation power for each arm, (right) signal output with increased power.

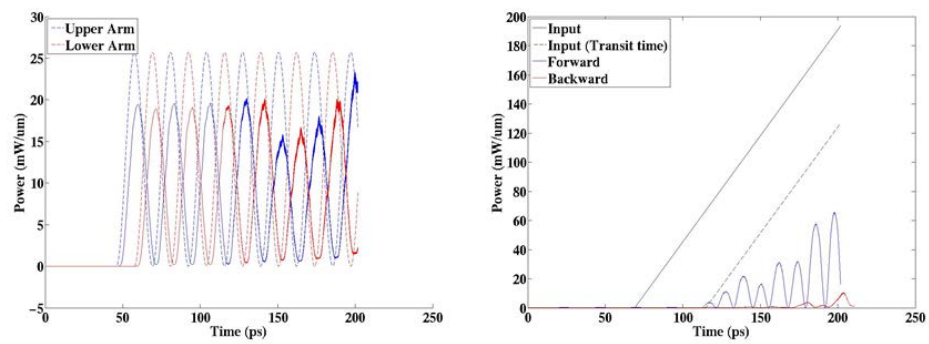

Figure 4.25. Sin^2(t) pulse modulation for the all-optical isolator: (left) modulation power for each arm, (right) signal output with increased power.

In this section, we demonstrated the all-optical nonreciprocal device with the slow-light-based non-resonant realization. Compared to the resonant realization in section 4.2.1, the level of the transmission is maintained in the operation range, because the non-resonant realization does not require the accumulation of optical power (note that in the photonic junction diode, transmission level is drastically

changed, due to the abrupt change of optical energy inside the resonator). However, the modulation sideband should be removed for the future application. Post-filtering may be the best choice.

4.4 Conclusion

In this chapter 4, we reviewed our researches in the field of all-optical devices. We handled resonant (photonic mode junction, [125]) and non-resonant (slow-light, [205]) realization of all-optical devices: including the fundamental devices of optical diode, isolator, and switch, and high-level devices such as XOR and AND logic gates, optical half-adder, and ADC. These results have been implemented on the platform of photonic crystals, due to its radiation-free design environment and superior power concentration with large Purcell effects. Yet, to achieve subwavelength design comparable to electronic devices, we believe that the design strategy should be simplified for the realization in harsher platforms such as plasmonics in metallic structures, including Ohmic loss.

Chapter 5

Conclusion

In this dissertation, we focused on 3 topics: (1) PT-symmetry linked with linear and angular momenta of light (chapter 2), (2) Disordered optics with translational symmetry breaking for controlling momentum and spectral properties of light (chapter 3), and (3) All-optical devices based on optical nonlinearity, manipulating wave flow with nonreciprocity and high-level functionality (chapter 4). All these phenomena, in an isolated or mixed manner, enable unconventional and non-classical wave dynamics by manipulating physical quantities of photons (k, ω, polarization, and amplitude), allowing novel class of optical devices as well.

Recently, a new physical axis of 'topology' [27-29] has attracted much attention in optics, inspired by the notion in condensed-matter physics. Optical implementations based on various chiral structures have been achieved as the analogy of quantum spin Hall effect, with the analysis based on the quantification with Chern number: depicting the 'topology' of wavefunction. As shown in the symmetry-broken constitution of topological insulator, which is obtained in the interface between materials of different Chern numbers (or topologies), we believe that our results in symmetry-broken optics can be extended to the field of

topological photonics: realizing scattering-free and unidirectional wave dynamics on the surface.

Appendix A

Eigenvalues in PT-Meta-molecules

At first, we derive the Eq. (2.9) in detail. Consider the $N \times N$ matrix $M_{0,N}$ of the form,

$$M_{0,N} = \begin{bmatrix} a & c & 0 & \cdots & 0 \\ c & a & c & \cdots & 0 \\ 0 & c & a & \cdots & 0 \\ \vdots & \vdots & \vdots & \ddots & c \\ 0 & 0 & 0 & c & a \end{bmatrix} \tag{A.1}$$

where $a = \beta - \beta_0$, and $c = -\kappa_o$. In order to get eigenvalues, we first derive a recurrence relation for the determinant of $M_{0,N}$.

$$\det(M_{0,N}) = a \cdot \det(M_{0,N-1}) - c^2 \cdot \det(M_{0,N-2}) \tag{A.2}$$

Applying the initial conditions of $N = 1$ (single waveguide, $\det(M_{0,1}) = a$) and $N = 0$ (null space, $\det(M_{0,0}) = 1$), we can now write down the determinant of $M_{0,N}$, for N-atomic molecule as follows;

$$\det(M_{0,N}) = \frac{2^{-(N+1)}}{\sqrt{a^2-4c^2}}[(a+\sqrt{a^2-4c^2})^{N+1} - (a-\sqrt{a^2-4c^2})^{N+1}] \quad \text{(A.3)}$$

Setting $\det(M_{0,N}) = 0$ to get non-trivial solutions, we can then obtain the following relation,

$$\frac{a+\sqrt{a^2-4c^2}}{a-\sqrt{a^2-4c^2}} = e^{i\frac{2s\pi}{N+1}}, \quad \text{(A.4)}$$

where s is an integer ($1 \le s \le N$). The closed form expression for a then can be obtained,

$$a = -\frac{1+e^{i\frac{2s\pi}{N+1}}}{e^{i\frac{s\pi}{N+1}}}c = -2c\cdot\cos\frac{s\pi}{N+1}. \quad \text{(A.5)}$$

which derives the Eq. (2.9).

Now, we derive the eigenvalues of the PT-symmetric molecule rigorously, which is treated by first setting $(\beta-\beta_0)^2$ in Eq. (2.10) as $|\beta-\beta_{r0}+i\beta_{i0}|^2$. The governing equation of M_N for the odd-number atomic molecule can be simplified as,

$$M_N = \kappa_o \cdot \begin{bmatrix} \ddots & \ddots & & & & & \\ \ddots & a & 1 & & & O & \\ & 1 & a^* & 1 & & & \\ & & 1 & b & 1 & & \\ & & & 1 & a & 1 & \\ & O & & & 1 & a^* & \ddots \\ & & & & & \ddots & \ddots \end{bmatrix} \equiv \kappa_o \cdot L_N \quad \text{(A.6)}$$

where $a=(\beta-\beta_{r0}+i\beta_{r0})/\kappa_o$ and $b=(\beta-\beta_{r0})/\kappa_o$. There are two different types for the odd-

N molecule, classified by the M_N component; 1) N=4m+1 for a and 2) N=4m+3 for a^*. We will treat the N=4m+1 case as an example (to note, the case of N=4m+3 gives an identical result through the same procedure).

In Eq. (A.6), det($L_{N=4m+1}$) can be represented as [260],

$$\begin{aligned}\det(L_N) &= \left[\begin{pmatrix} a^* & -1 \\ 1 & 0 \end{pmatrix}\begin{pmatrix} a & -1 \\ 1 & 0 \end{pmatrix}\cdots\begin{pmatrix} b & -1 \\ 1 & 0 \end{pmatrix}\cdots\begin{pmatrix} a^* & -1 \\ 1 & 0 \end{pmatrix}\begin{pmatrix} a & 0 \\ 1 & 0 \end{pmatrix}\right]_{11} \\ &= \left[\begin{pmatrix} |a|^2-1 & -a^* \\ a & -1 \end{pmatrix}^m \begin{pmatrix} b & -1 \\ 1 & 0 \end{pmatrix}\begin{pmatrix} |a|^2-1 & -a^* \\ a & -1 \end{pmatrix}^{m-1}\begin{pmatrix} |a|^2-1 & 0 \\ a & 0 \end{pmatrix}\right]_{11} \\ &\equiv \left[T^m\begin{pmatrix} b & -1 \\ 1 & 0 \end{pmatrix}T^{m-1}\begin{pmatrix} |a|^2-1 & 0 \\ a & 0 \end{pmatrix}\right]_{11}.\end{aligned} \tag{A.7}$$

To determine the T^k, matrix, T is diagonalized as,

$$\begin{aligned} T &= S\cdot T_0\cdot S^{-1} = \frac{1}{c}\begin{pmatrix} \lambda_+ +1 & a^* \\ a & \lambda_+ +1 \end{pmatrix}\begin{pmatrix} \lambda_+ & 0 \\ 0 & \lambda_- \end{pmatrix}\begin{pmatrix} \lambda_+ +1 & -a^* \\ -a & \lambda_+ +1 \end{pmatrix}, \\ S &= \begin{pmatrix} \lambda_+ +1 & a^* \\ a & \lambda_+ +1 \end{pmatrix}, \end{aligned} \tag{A.8}$$

where c=det(P), and $\lambda_\pm$ are eigenvalues of T expressed as,

$$\lambda_\pm = \frac{|a|^2 \pm \sqrt{|a|^2\left(|a|^2-4\right)}}{2} - 1. \tag{A.9}$$

To note, $\lambda_\pm$ and c are functions of $|a|^2$, not of a or a^*. Now, the k^{th} power of T is obtained as,

$$
\begin{aligned}
T^k &= \frac{1}{c^k}\begin{pmatrix} \lambda_+ +1 & a^* \\ a & \lambda_+ +1 \end{pmatrix}\begin{pmatrix} {\lambda_+}^k & 0 \\ 0 & {\lambda_-}^k \end{pmatrix}\begin{pmatrix} \lambda_+ +1 & -a^* \\ -a & \lambda_+ +1 \end{pmatrix} \\
&= \frac{1}{c^k}\begin{bmatrix} (\lambda_+ +1)^2 {\lambda_+}^k - |a|^2 {\lambda_-}^k & -a^* \cdot (\lambda_+ +1)\left({\lambda_+}^k - {\lambda_-}^k\right) \\ a \cdot (\lambda_+ +1)\left({\lambda_+}^k - {\lambda_-}^k\right) & (\lambda_+ +1)^2 {\lambda_-}^k - |a|^2 {\lambda_+}^k \end{bmatrix}
\end{aligned}
\tag{A.10}
$$

From the Eq. (A.10), T^k can be expressed by separating terms of $|a|^2$, from a or a^* as,

$$
T^k = \begin{pmatrix} P_k(|a|^2) & -a^* \cdot R_k(|a|^2) \\ a \cdot R_k(|a|^2) & Q_k(|a|^2) \end{pmatrix} \tag{A.11}
$$

and then $\det(L_N)$ is given by,

$$
\begin{aligned}
\det(L_N) &= \left[T \cdot T^{m-1}\begin{pmatrix} b & -1 \\ 1 & 0 \end{pmatrix} T^{m-1}\begin{pmatrix} |a|^2 -1 & 0 \\ a & 0 \end{pmatrix} \right]_{11} \\
&= \left[\begin{pmatrix} |a|^2 -1 & -a^* \\ a & -1 \end{pmatrix}\begin{pmatrix} P_{m-1} & -a^* R_{m-1} \\ aR_{m-1} & Q_{m-1} \end{pmatrix}\begin{pmatrix} b & -1 \\ 1 & 0 \end{pmatrix}\begin{pmatrix} P_{m-1} & -a^* R_{m-1} \\ aR_{m-1} & Q_{m-1} \end{pmatrix}\begin{pmatrix} |a|^2 -1 & 0 \\ a & 0 \end{pmatrix} \right]_{11} \\
&= \left[\begin{pmatrix} |a|^2 -1 & -a^* \\ a & -1 \end{pmatrix}\begin{pmatrix} f & -h(a^*) \\ h(a) & g \end{pmatrix}\begin{pmatrix} |a|^2 -1 & 0 \\ a & 0 \end{pmatrix} \right]_{11}
\end{aligned}
\tag{A.12}
$$

where $f = bP_{m-1}\cdot(P_{m-1}-2R_{m-1})$, $g = -bR_{m-1}\cdot(|a|^2R_{m-1}+2Q_{m-1})$, and $h(x) = -{R_{m-1}}^2x^2+bP_{m-1}R_{m-1}x+P_{m-1}Q_{m-1}$, by considering $(a + a^*)= 2b$. Then, $\det(L_N)$ becomes,

$$
\begin{aligned}
\det(L_N) &= \left(|a|^2 -1\right)^2 \cdot f - \left(|a|^2 -1\right)\cdot\left[ah(a^*) + a^* h(a)\right] - |a|^2 \cdot g \\
&= \left(|a|^2 -1\right)^2 \cdot f - \left(|a|^2 -1\right)\cdot\left[-|a|^2 bR_{m-1}(2R_{m-1} - P_{m-1}) + P_{m-1}Q_{m-1}\right] - |a|^2 \cdot g
\end{aligned}
\tag{A.13}
$$

Since P_m, Q_m, and R_m are functions of $|a|^2$, $f=f\,(|a|^2)$ and $g=g\,(|a|^2)$, and thus, $\det(L_N)$

is also a function of $|a|^2$. Because the equation for eigenvalues is obtained from $\det(M_N) = \kappa_o \cdot \det(L_N) = 0$, the set of eigenvalues in the PT-symmetric molecule is the function of $\kappa_o^2 \cdot |a|^2 = |\beta - \beta_{r0} + i\beta_{i0}|^2$. Therefore, by replacing $\kappa_o^2 \cdot |a|^2 = (\beta - \beta_{r0})^2$ in Eq. (2.10) (Hermitian case of real a) by $\kappa_o^2 \cdot |a|^2 = |\beta - \beta_{r0} + i\beta_{i0}|^2$, the Eq. (2.11) (PT-symmetric case of complex a) is finally derived.

Appendix B

Supplements for Section 2.3.1

B.1 Planewave solution of a PT-symmetric optical material

To clarify a point of importance in the chirality of a PT-symmetric optical material, here we assume the simplest case of a planewave propagating along the ***x***-axis (***E*** = $\boldsymbol{E_0}\cdot e^{i(\omega t-\beta x)}$). From the PT-symmetric permittivity tensor $\bar{\boldsymbol{\varepsilon}}_{\boldsymbol{r}}$ of the material (Eq. (2.14) in the main manuscript), Maxwell's wave equation reduces to the following 2-dimensional matrix equation:

$$\begin{bmatrix} \varepsilon_{eig} - \varepsilon_{r0} - i\varepsilon_{i0} & -\varepsilon_{\kappa 0} \\ -\varepsilon_{\kappa 0}^{\ *} & \varepsilon_{eig} - \varepsilon_{r0} + i\varepsilon_{i0} \end{bmatrix} \begin{bmatrix} E_y \\ E_z \end{bmatrix} = \mathrm{O}, \qquad \text{(B.1)}$$

where ε_{eig} is the effective permittivity of the eigenmodes ($\beta^2 = \varepsilon_{eig}\cdot(\omega/c)^2$). The effective permittivity $\varepsilon_{eig1,2}$ and the corresponding eigenmode $v_{eig1,2}$ are then obtained as

$$\varepsilon_{eig1,2} = \varepsilon_{r0} \pm \sqrt{\left|\varepsilon_{\kappa 0}\right|^2 - \varepsilon_{i0}^{\ 2}}, \qquad \text{(B.2)}$$

$$v_{eig1,2} = \eta_{1,2} \cdot \begin{bmatrix} \varepsilon_{\kappa 0} \\ -i\varepsilon_{i0} \pm \sqrt{\left|\varepsilon_{\kappa 0}\right|^2 - \varepsilon_{i0}{}^2} \end{bmatrix}, \tag{B.3}$$

where $\eta_{1,2} = [1/(\, |\varepsilon_{\kappa 0}|^2 + | \, -i\varepsilon_{i0} \pm (\varepsilon_{\kappa 0}{}^2 - \varepsilon_{i0}{}^2)^{1/2} \, |^2 \,)]^{1/2}$ is the normalization factor for each eigenmode. To define the exceptional point (EP) originating from the onset of PT symmetry breaking, we now introduce the interaction parameter $\lambda_{PT} = (|\varepsilon_{\kappa 0}|^2 - \varepsilon_{i0}{}^2)^{1/2}$, where $\lambda_{PT} = 0$ at the EP provides the geometric multiplicity of 1 (= the dimensionality of the eigenspace) for $\varepsilon_{eig1} = \varepsilon_{eig2}$. In this case, Eqs. (B.2) and (B.3) are simplified as

$$\varepsilon_{eig1,2} = \varepsilon_{r0} \pm \lambda_{PT}, \tag{B.4}$$

$$v_{eig1,2} = \eta_{1,2} \cdot \begin{bmatrix} \varepsilon_{\kappa 0} \\ -i\varepsilon_{i0} \pm \lambda_{PT} \end{bmatrix}. \tag{B.5}$$

For reference, from the condition of zero magneto-electric coupling in the present analysis, the value of $\varepsilon_{\kappa 0}$ is real ($\lambda_{PT} = (\varepsilon_{\kappa 0}{}^2 - \varepsilon_{i0}{}^2)^{1/2}$).

B.2 Density of optical chirality for complex eigenmodes

For the time-harmonic field of $\boldsymbol{E} = \boldsymbol{E_0} \cdot e^{i\omega t}$ and $\boldsymbol{B} = \boldsymbol{B_0} \cdot e^{i\omega t}$, the time-varying representation of the optical chirality density $\chi = [\varepsilon_0 \varepsilon_r \cdot \boldsymbol{E(t)} \cdot (\nabla \mathrm{x} \boldsymbol{E(t)}) + (1/\mu_0) \cdot \boldsymbol{B(t)} \cdot (\nabla \mathrm{x} \boldsymbol{B(t)})]/2$ is simplified to the time-averaged form of $\chi = \omega \cdot Im[\boldsymbol{E_0}^* \cdot \boldsymbol{B_0}]/2$. Because $\boldsymbol{E_0} = v_{eig1,2} \cdot exp(-i\beta_{1,2}x)$, where $\beta_{1,2} = 2\pi \varepsilon_{eig1,2}{}^{1/2}/\Lambda_0$, the magnetic field $\boldsymbol{B_0}$ is calculated from (B.5) as

$$\vec{B}_0 = -\frac{\eta_{1,2}\beta_{1,2}}{\omega} \cdot \begin{bmatrix} -i\varepsilon_{i0} \pm \lambda_{PT} \\ -\varepsilon_{\kappa 0} \end{bmatrix} \cdot e^{-i\beta_{1,2}x}. \tag{B.6}$$

From the definition of χ and the condition of weak coupling in the PT-symmetric system ($\varepsilon_{i0} \sim \varepsilon_{\kappa 0} << \varepsilon_{r0}$), the chirality density of each eigenmode is now expressed as

$$\chi_{1,2} = \frac{\beta_{1,2}}{2} \cdot \frac{\varepsilon_{i0}}{\varepsilon_{\kappa 0}}, \qquad \text{(B.7, before the EP)}$$

$$\chi_{1,2} = \frac{\mathrm{Re}[\beta_{1,2}]}{2} \cdot \frac{2\varepsilon_{\kappa 0} \cdot (\varepsilon_{i0} \mp \sqrt{{\varepsilon_{i0}}^2 - {\varepsilon_{\kappa 0}}^2})}{{\varepsilon_{\kappa 0}}^2 + (\varepsilon_{i0} \mp \sqrt{{\varepsilon_{i0}}^2 - {\varepsilon_{\kappa 0}}^2})^2} \cdot e^{2\,\mathrm{Im}(\beta_{1,2})x}, \text{ (B.8, after the EP)}$$

where $exp(2 \cdot Im[\beta_{1,2}]x) = |\boldsymbol{E_0}|^2 \equiv U_e$ represents the amplifying and decaying electric field intensities after the EP (Fig. 2.17b in the main manuscript, $U_e = 1$ before the EP). Herein, we adopt $\chi_{1,2}/U_e$ to express the energy-normalized chirality of the eigenmodes. It is worth mentioning that $\chi_1 \sim \chi_2$ from the condition of weak coupling (line and symbol of Fig. 2.17c in the main manuscript).

B.3 Effect of imperfect PT symmetry on the modal chirality

For completeness, here we investigate the effect of imperfect PT symmetry on the modal chirality by considering two different situations related to the condition of PT symmetry: 1) non-symmetric real parts ($\mathrm{Re}[\varepsilon_y] \neq \mathrm{Re}[\varepsilon_z]$) and 2) non-anti-symmetric imaginary parts of permittivity ($\mathrm{Im}[\varepsilon_y] \neq -\mathrm{Im}[\varepsilon_z]$).

B.3.1 Broken symmetry in the real part of permittivity

To introduce the real-part imperfection ($\mathrm{Re}[\varepsilon_y] \neq \mathrm{Re}[\varepsilon_z]$), we change Eq. (B.1), including the real part difference $\Delta\varepsilon_{r0}$, as

$$\begin{bmatrix} \varepsilon_{eig} - \varepsilon_{r0} - \Delta\varepsilon_{r0}/2 - i\varepsilon_{i0} & -\varepsilon_{\kappa 0} \\ -{\varepsilon_{\kappa 0}}^* & \varepsilon_{eig} - \varepsilon_{r0} + \Delta\varepsilon_{r0}/2 + i\varepsilon_{i0} \end{bmatrix} \begin{bmatrix} E_y \\ E_z \end{bmatrix} = \mathrm{O},$$

(B.9)

from Re[ε_y] = ε_{r0} + $\Delta\varepsilon_{r0}$/2 and Re[ε_z] = ε_{r0} – $\Delta\varepsilon_{r0}$/2. Then, the effective permittivity $\varepsilon_{eig1,2}$ and the corresponding eigenmode $v_{eig1,2}$, including the effect of the real part imperfection, are obtained as

$$\varepsilon_{eig1,2} = \varepsilon_{r0} \pm \sqrt{\left|\varepsilon_{\kappa 0}\right|^2 - \varepsilon_{i0}{}^2 + \frac{\Delta\varepsilon_{r0}}{4}(\Delta\varepsilon_{r0} + 4i\varepsilon_{i0})}\,, \tag{B.10}$$

$$v_{eig1,2} = \eta_{1,2} \cdot \left[\frac{\varepsilon_{\kappa 0}}{-\Delta\varepsilon_{r0}/2 - i\varepsilon_{i0} \pm \sqrt{\left|\varepsilon_{\kappa 0}\right|^2 - \varepsilon_{i0}{}^2 + \frac{\Delta\varepsilon_{r0}}{4}(\Delta\varepsilon_{r0} + 4i\varepsilon_{i0})}} \right], \tag{B.11}$$

where $\eta_{1,2}$ is the new normalization factor for each eigenmode satisfying $|v_{eig1,2}|^2 = 1$. It is noted that due to the complex form inside the square root of Eq. (B.10), perfect coalescence does not occur if $\Delta\varepsilon_{r0} \neq 0$, as shown in Figs. B.1a and B.1b. From Eq. (B.11), we can also calculate the modal chirality $\chi_{1,2}$ following the same process of Section B.2, which shows the effect of the imperfection on the modal chirality (Fig. B.1c). From those results, we can determine the boundary of the tolerance for the modal chirality (Fig. B.1d).

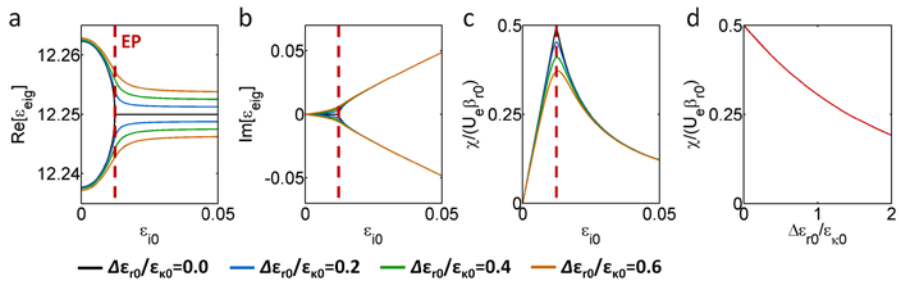

Figure B.1. The effect of the imperfection in the real part of PT symmetry. (a) The real and (b) imaginary parts of the effective permittivity $\varepsilon_{eig1,2}$. (c) The density of chirality $\chi = [\varepsilon_0\varepsilon_r \cdot \boldsymbol{E}\cdot(\nabla \mathrm{x}\boldsymbol{E}) + (1/\mu_0)\cdot\boldsymbol{B}\cdot(\nabla \mathrm{x}\boldsymbol{B})]/2$, normalized by the product of the electric field intensity $U_e = |\boldsymbol{E}|^2$ and $\beta_{r0} = \varepsilon_{r0}^{1/2}\cdot 2\pi/\Lambda_0$. (d) The density of chirality as a function of the defect $\Delta\varepsilon_{r0}$ at the EP (red dotted lines in a-c). All other parameters are the same as those in Fig. 2.17 in the main manuscript.

B.3.2 Broken anti-symmetry in the imaginary part of the permittivity

For the imaginary-part imperfection ($\mathrm{Im}[\varepsilon_y] \neq -\mathrm{Im}[\varepsilon_z]$), Eq. (B.1) is changed, including the new imaginary part $\Delta\varepsilon_{i0}$, as

$$\begin{bmatrix} \varepsilon_{eig} - \varepsilon_{r0} - i(\varepsilon_{i0} + \Delta\varepsilon_{i0}/2) & -\varepsilon_{\kappa 0} \\ -\varepsilon_{\kappa 0}^{*} & \varepsilon_{eig} - \varepsilon_{r0} + i(\varepsilon_{i0} - \Delta\varepsilon_{i0}/2) \end{bmatrix} \begin{bmatrix} E_y \\ E_z \end{bmatrix} = \mathrm{O}, \tag{B.12}$$

from $\mathrm{Im}[\varepsilon_y] = \varepsilon_{i0} + \Delta\varepsilon_{i0}/2$ and $\mathrm{Im}[\varepsilon_z] = -\varepsilon_{i0} + \Delta\varepsilon_{i0}/2$, showing the broken anti-symmetry. Then, the effective permittivity $\varepsilon_{eig1,2}$, including the effect of the imaginary part imperfection, is obtained as

$$\varepsilon_{eig1,2} = \varepsilon_{r0} + i\frac{\Delta\varepsilon_{r0}}{2} \pm \sqrt{|\varepsilon_{\kappa 0}|^2 - \varepsilon_{i0}^{\,2}} = \varepsilon_{r0} + i\frac{\Delta\varepsilon_{r0}}{2} \pm \lambda_{PT}, \tag{B.13}$$

while $v_{eig1,2}$ and the following $\chi_{1,2}$ are the same as Eq. (B.3). Therefore, it is interesting to note that the modal chirality is not influenced by the imperfect anti-

symmetry of the imaginary part. Such a result can be understood within the context of gauge transformation, which has been demonstrated in passive PT-symmetric systems ($\Delta\varepsilon_{i0} < 0$).

B.4 Transfer between RCP and LCP modes in the PT-symmetric chiral material

B.4.1 Propagation of complex eigenmodes

For an incident wave impinging upon the PT-symmetric material ($E_{inc} = A_{eig1}\cdot v_{eig1} + A_{eig2}\cdot v_{eig2}$), the transmitted wave at $x=d$ is expressed as $E_{trn} = A_{eig1}\cdot v_{eig1}\cdot exp(-i\beta_1\cdot d) + A_{eig2}\cdot v_{eig2}\cdot exp(-i\beta_2\cdot d)$, where v_{eig1} and v_{eig2} are complex eigenmodes in Eq. (B.5), $\beta_{1,2} = 2\pi\varepsilon_{eig1,2}^{1/2}/\Lambda_0$ is the propagation constant of each eigenmode, and Λ_0 is the free-space wavelength of the wave. To investigate the chiral behavior of the wave, we employ the convenient basis of RCP and LCP: $v_{R,L} = (1/2)^{1/2}\cdot(1, \pm i)^{\mathrm{T}}$. From the relation of $v_{eig1,2} = A_{R1,2}\cdot v_R + A_{L1,2}\cdot v_L \equiv [A_{R1,2}\ ,\ A_{L1,2}]_{\mathrm{CP}}{}^{\mathrm{T}}$, a transfer equation between the incident wave $E_{inc} = [E_{RI}\ ,\ E_{LI}]_{\mathrm{CP}}{}^{\mathrm{T}}$ and the transmitted wave $E_{trn} = [E_{RT}\ ,\ E_{LT}]_{\mathrm{CP}}{}^{\mathrm{T}}$ in CP bases is obtained as

$$\begin{bmatrix} E_{RT} \\ E_{LT} \end{bmatrix} = \frac{1}{A_{R1}A_{L2} - A_{R2}A_{L1}} \begin{bmatrix} A_{R1}e^{-i\beta_1 d} & A_{R2}e^{-i\beta_2 d} \\ A_{L1}e^{-i\beta_1 d} & A_{L2}e^{-i\beta_2 d} \end{bmatrix} \begin{bmatrix} A_{L2} & -A_{R2} \\ -A_{L1} & A_{R1} \end{bmatrix} \begin{bmatrix} E_{RI} \\ E_{LI} \end{bmatrix}, \tag{B.14}$$

where the explicit expression for $[A_{R1,2}\ ,\ A_{L1,2}]_{\mathrm{CP}}{}^{\mathrm{T}}$,

$$\begin{bmatrix} A_{R1,2} \\ A_{L1,2} \end{bmatrix} = \frac{\eta_{1,2}}{\sqrt{2}} \begin{bmatrix} \varepsilon_{\kappa 0} - \varepsilon_{i0} \mp i\lambda_{PT} \\ \varepsilon_{\kappa 0} + \varepsilon_{i0} \pm i\lambda_{PT} \end{bmatrix}, \tag{B.15}$$

is obtained from (B.5). By applying Eq. (B.15), Eq. (B.14) can be re-expressed using only structural (d) and material (ε_{r0}, ε_{i0}, and $\varepsilon_{\kappa 0}$) parameters in the same way as Eq. (2.15) in the main manuscript. The result shows the apparent chiral transfer

through two unequal off-diagonal terms. The magnitude of the chirality in the intermodal transfer between CP modes is quantified by C_{IM} (Eq. (2.16) in the main manuscript).

B.4.2 Strength of chiral conversion C_{CS} before the EP

Because $Re[\beta_1] \neq Re[\beta_2]$ before the EP (Fig. 2.17a, in the main manuscript), C_{CS} becomes oscillatory, in contrast to the case after the EP ($Re[\beta_1] = Re[\beta_2]$). The C_{CS} ($\varepsilon_{i0} < \varepsilon_{\kappa 0}$) is then expressed as

$$C_{CS}^{R\to L} = \left(\frac{\varepsilon_{\kappa 0}+\varepsilon_{i0}}{\varepsilon_{\kappa 0}-\varepsilon_{i0}}\right)^{1/2} \cdot \left| \tan\left(\frac{2\pi d}{\Lambda_0} \cdot \frac{\sqrt{\varepsilon_{\kappa 0}^{\,2}-\varepsilon_{i0}^{\,2}}}{\left(\varepsilon_{r0}+\sqrt{\varepsilon_{\kappa 0}^{\,2}-\varepsilon_{i0}^{\,2}}\right)^{1/2}+\left(\varepsilon_{r0}-\sqrt{\varepsilon_{\kappa 0}^{\,2}-\varepsilon_{i0}^{\,2}}\right)^{1/2}} \right) \right|, \tag{B.16}$$

$$C_{CS}^{L\to R} = \left(\frac{\varepsilon_{\kappa 0}-\varepsilon_{i0}}{\varepsilon_{\kappa 0}+\varepsilon_{i0}}\right)^{1/2} \cdot \left| \tan\left(\frac{2\pi d}{\Lambda_0} \cdot \frac{\sqrt{\varepsilon_{\kappa 0}^{\,2}-\varepsilon_{i0}^{\,2}}}{\left(\varepsilon_{r0}+\sqrt{\varepsilon_{\kappa 0}^{\,2}-\varepsilon_{i0}^{\,2}}\right)^{1/2}+\left(\varepsilon_{r0}-\sqrt{\varepsilon_{\kappa 0}^{\,2}-\varepsilon_{i0}^{\,2}}\right)^{1/2}} \right) \right|, \tag{B.17}$$

which gives the values of $C_{CS}^{R\to L} = 2\pi L_{eff}\cdot(\varepsilon_{\kappa 0}/\varepsilon_{r0})$ and $C_{CS}^{L\to R} = 0$ at the EP, equivalent to those of Eqs. (2.17) and (2.18) in the main manuscript.

Figure B.2 shows the behaviors of $C_{CS}^{R\to L}$ and $C_{CS}^{L\to R}$ with a different $\varepsilon_{\kappa 0}$ as functions of ($\varepsilon_{i0}/\varepsilon_{\kappa 0}$) before the EP ($\varepsilon_{i0} < \varepsilon_{\kappa 0}$) and after the EP ($\varepsilon_{i0} > \varepsilon_{\kappa 0}$). From the unequal strength of $C_{CS}^{R\to L} > C_{CS}^{L\to R}$, there exists an LCP-favored chiral conversion before the EP, although it is much weaker than that at the EP. It is noted that the oscillatory behavior of C_{CS} before the EP is determined by $\varepsilon_{\kappa 0}$.

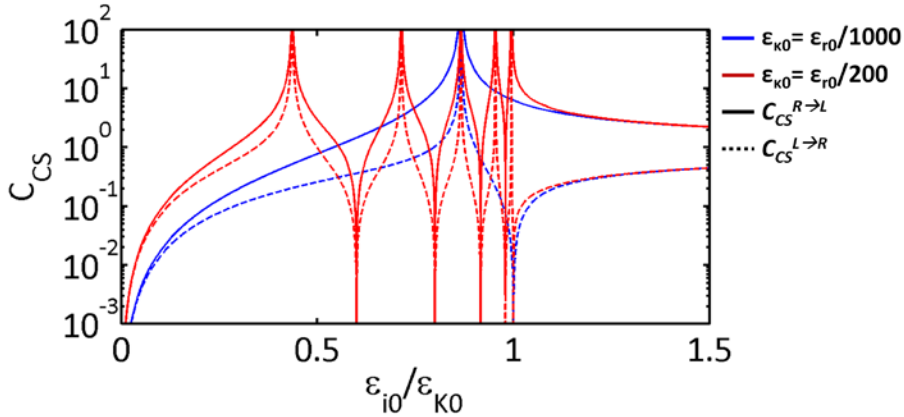

Figure B.2. $C_{CS}^{R\to L}$ and $C_{CS}^{L\to R}$ as functions of ($\varepsilon_{i0}/\varepsilon_{\kappa 0}$) for the cases of $\varepsilon_{\kappa 0} = \varepsilon_{r0}/1000$ and $\varepsilon_{\kappa 0} = \varepsilon_{r0}/200$. $\varepsilon_{r0} = 6.5$ and $L_{eff} = 10^3$.

B.5 The state of polarization (SOP) at the EP: Optical spin black hole

For the graphical representation of the SOP, here we apply the Stokes parameter expression (of S_0, S_1, S_2, and S_3) on the Poincaré sphere, which follows the relations below:

$$\begin{aligned} S_0 &= |E_x|^2 + |E_y|^2, \\ S_1 &= |E_x|^2 - |E_y|^2, \\ S_2 &= 2\,\mathrm{Re}[E_x^* E_y], \\ S_3 &= 2\,\mathrm{Im}[E_x^* E_y], \end{aligned} \tag{B.18}$$

where S_0 is the radius of the Poincaré sphere, and (S_1, S_2, S_3) is the Cartesian coordinate of the SOP on the sphere. To describe the general tendency of the SOP at the EP, we assume the 400 randomly polarized incidences ($E_x = a + bi$ and $E_y = c + di$ for the incidence where a, b, c, and d are real numbers with the uniform random distribution in [-1,1]) on the PT-symmetric optical potential for Fig. 2.18e in the main manuscript.

B.6 Giant chiral conversion in the resonant structure

To achieve a large chiral conversion within a compact footprint, a resonant structure for the effective increase of interaction length $L_{eff} = \varepsilon_{r0}^{1/2} \cdot d/\Lambda_0$ can be considered (Fig. B.3a). The resonator is composed of PT-symmetric anisotropic material at the EP (length d = 834 nm, same parameters as those of Fig. 2.18 in the main manuscript), sandwiched between two metallic mirrors (of thickness δ). Here, S-matrix analysis is utilized to calculate the frequency-dependent transmission, reflection, and field distributions inside the resonator. In detail, while the fields of the background (air) and mirrors are expressed as the linear combinations of y- and z-orthogonal bases, the field inside the PT-symmetric material is expressed by the nonorthogonal bases of $v_{eig1,2}$, as $E(x) = E_{eig1}^{+} \cdot v_{eig1} \cdot exp(-i\beta_1 \cdot x) + E_{eig1}^{-} \cdot v_{eig1} \cdot exp(i\beta_1 \cdot x) + E_{eig2}^{+} \cdot v_{eig2} \cdot exp(-i\beta_2 \cdot x) + E_{eig2}^{-} \cdot v_{eig2} \cdot exp(i\beta_2 \cdot x)$, including forward (+) and backward (–) components. From the continuity condition of the electric field across the boundary (E and $\partial_x E$), we derive the S-matrix relation of $(E_{Oy}^{+}, E_{Oz}^{+}, E_{Iy}^{-}, E_{Iz}^{-})^{T} = S \cdot (E_{Iy}^{+}, E_{Iz}^{+}, E_{Oy}^{-}, E_{Oz}^{-})^{T}$. For mirrors with thicknesses of δ = 40, 50, 60, or 70 nm, the obtained Q values of the resonators are 620, 1500, 3600, and 8200, respectively.

Figures B.3b and B.3c show the S-matrix calculated power ratio of LCP over RCP of a transmitted and reflected wave for the forward y-linear polarized incidence (E_{Iy}^{+} = 1). Also shown in Fig. B.3d are the S-matrix-calculated wave evolutions at the on-resonance condition of the 3/2 wavelength. Enhanced by the chiral standing wave in the resonator, a giant LCP-favored chirality of the transmitted wave is observed (Fig. B.3b, I_L/I_R = 20 dB within L_{eff} = 1.4 at Q = 8200; to compare, for the non-resonant structure in the main manuscript, [I_L/I_R = 0.08 dB, L_{eff} = 1.4] and [I_L/I_R = 20 dB, L_{eff} = 1450]). It is also notable that, in contrast to the non-resonant structure where the reflection is absent, *pure chiral reflection* (RCP-only) results from the backward-propagating RCP waves inside the resonator (Fig. B.3c).

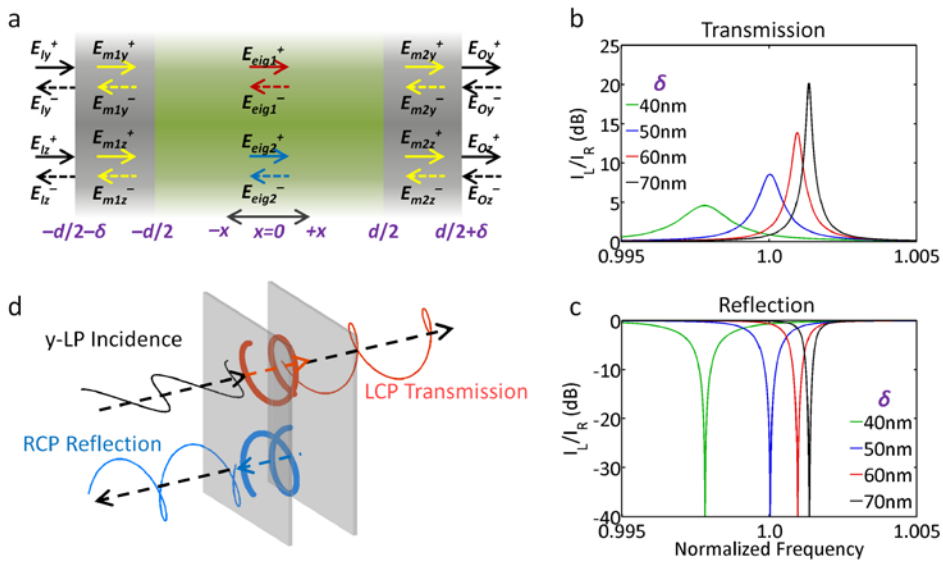

Figure B.3. Giant chiral conversion through the resonant structure. (a) Schematics of the chiral resonator for the S-matrix analysis (green: PT-symmetric anisotropic material of d = 834 nm, ε_{r0} = 6.5 and $\varepsilon_{\kappa 0} = \varepsilon_{i0} = \varepsilon_{r0}/1000$; grey: metallic mirrors, $\varepsilon_{metal} = -100$, Λ_0=1500 nm). L_{eff} = 1.4. The power ratios of LCP over RCP in the (b) transmitted and (c) reflected wave for different mirror thicknesses. (d) S-matrix-based spatial evolutions of waves through the resonator. Arrows denote the propagating direction of each wave.

B.7 Detailed information of fabrication and experiment in THz chiral polar metamaterials

B.7.1 Fabrication process of THz chiral polar metamaterials

Serving as a flexible and vertically symmetric environment of a metamaterial, a polyimide solution (PI-2610, HD MicroSystems) was spin-coated (1 μm) onto a bare Si substrate and converted into a fully aromatic and insoluble polyimide (baked at 180°C for 30 min and cured at 350°C). A negative photoresist (AZnLOF2035, AZ Electronic Materials) was spin-coated and patterned using photolithography. Then, Au (100 nm) was evaporated on the Cr (10 nm) adhesion layer and patterned as crossed 'I'-shaped array structures via the lift-off process. Repeating the polyimide coating and curing (1 μm), single-layered metamaterials

were fabricated by peeling off the metamaterial layers from the substrate.

B.7.2 THz-TDS system for the measurement of intermodal chirality

To generate a broadband THz source, a Ti:sapphire femtosecond oscillator was used (Mai-Tai, Spectra-physics, 80 MHz repetition rate, 100 fs pulse width, 800 nm central wavelength, and 1 W average power). The pulsed laser beam was focused onto a GaAs terahertz emitter (Tera-SED, Gigaoptics). The emitted THz wave was then focused onto the samples using a 2 mm spot diameter. The propagating THz radiation was detected through electro-optical sampling using a nonlinear ZnTe crystal. The THz-TDS system has a usable bandwidth of 0.1-2.6 THz and a signal-to-noise ratio greater than 10,000:1.

B.8 Realization of PT-symmetric permittivity in metamaterial platforms

To transplant the point-wise anisotropic permittivity of a PT-symmetric chiral material into the structure composed of isotropic materials, we first consider a metamaterial platform in a THz regime. As a unit element, we adopt the I-shaped patch for each polarization, which induces the enhanced light-matter interaction through the deep subwavelength (~λ_0/200) gap structure. By crossing the ***y***- and ***z***-unit elements (Fig. B.4a), we obtain the metamaterial, which supports the well-known electrical response of the Lorentz model both for ***y***- and ***z***-polarizations, as

$$\varepsilon_{ry}(\omega) = \varepsilon_{poly} + \frac{{\omega_{py}}^2}{{\omega_{0y}}^2 - \omega^2 + i\gamma_y\omega}, \qquad \varepsilon_{rz}(\omega) = \varepsilon_{poly} + \frac{{\omega_{pz}}^2}{{\omega_{0z}}^2 - \omega^2 + i\gamma_z\omega} \tag{B.19}$$

where ε_{poly} is the permittivity of the polyimide (ε_{poly} = 3.238 – 0.144*i*), $\omega_{0(y,z)}$ is the characteristic frequency, $\gamma_{(y,z)}$ is the damping coefficient, and $\omega_{p(y,z)}$ is the plasma frequency of the metamaterial for ***y***- and ***z***-polarizations. Because the near-field intensity distribution is widely separated for each polarization (Figs. B.4b and

B.4c), it is worth mentioning that the Lorentz permittivity curve of each polarization can be detuned independently to realize the required anisotropic metamaterial.

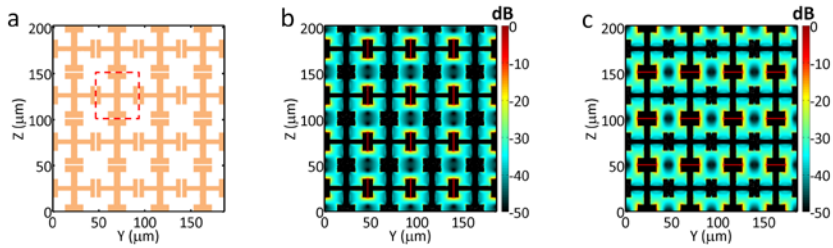

Figure B.4. Crossed I-shaped metamaterials. (a) 2D cross-sectional schematic view of the structure composed of gold (yellow) inside the polyimide (white). The tilted angle between patches is $\theta = 0°$, and all the other parameters are the same as those in Fig. 2.19 in the main manuscript. The red dashed box represents the unit-cell metamaterial. The electrical intensity distribution calculated by COMSOL ($|\boldsymbol{E}|^2$ in dB scale) is shown in (b) for a *y*-polarized and (c) a *z*-polarized planewave incidence at the peak frequency of the permittivity curves in Fig. 2.19d in the main manuscript.

As noted in the main manuscript, we utilize the low-loss ($|\mathrm{Re}[\varepsilon]| >> |\mathrm{Im}[\varepsilon]|$) and high-loss ($|\mathrm{Re}[\varepsilon]| \sim |\mathrm{Im}[\varepsilon]|$) dielectric regimes of the Lorentz response to obtain the passive PT symmetry condition of $\mathrm{Re}[\varepsilon_y] = \mathrm{Re}[\varepsilon_z]$ and $\mathrm{Im}[\varepsilon_z] < \mathrm{Im}[\varepsilon_y] < 0$ (see Section B.3.2). Because the modal chirality is critically dependent on the condition of $\mathrm{Re}[\varepsilon_y] = \mathrm{Re}[\varepsilon_z]$ (see Section B.3.1), we need to intervein the real part of the Lorentz curves. To achieve this, the effect of varying the physical quantities of the Lorentz model (ω_0, ω_p, and γ) is shown in Fig. B.5. Also corresponding to the Eq. (B.19), it is necessary to change the characteristic frequency of ω_0 for the spectral shift (Fig. B.5a), while the magnitude of the permittivity is mainly tuned with the plasma frequency ω_p (Fig. B.5b compared to B.5c).

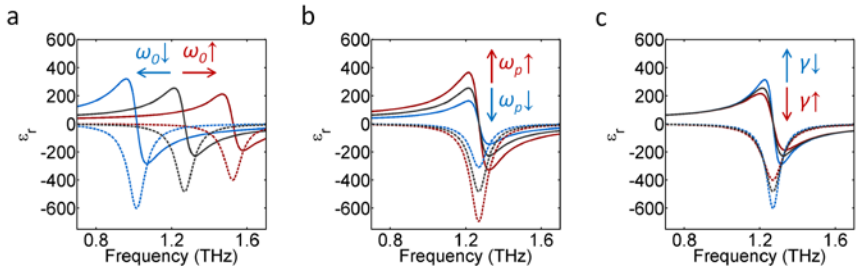

Figure B.5. The effect of changing the physical quantities (ω_0, ω_p, and γ) in the Lorentz model. The permittivities $\varepsilon(\omega)$ are shown for the changes of (a) the characteristic frequency ω_0 (black: ω_{00}, red: $1.2\cdot\omega_{00}$, blue: $0.8\cdot\omega_{00}$), (b) the plasma frequency ω_p (black: ω_{p0}, red: $1.2\cdot\omega_{p0}$, blue: $0.8\cdot\omega_{p0}$), and (c) the damping coefficient γ (black: γ_0, red: $1.2\cdot\gamma_0$, blue: $0.8\cdot\gamma_0$). ω_{00} = 1.27THz, ω_{p0} = 8.2THz, and γ_0 = 0.11THz. Solid (dotted) lines denote the Re[ε] (Im[ε]).

By considering the results of Fig. B.5, now we investigate the role of the structural parameters (*a*, *g*, *L*, and *w* of Fig. 2.19b in the main manuscript) for the design of PT-symmetric permittivity relating to the physical quantities (ω_0, ω_p, and γ). To satisfy the condition of Re[ε_y] = Re[ε_z] and Im[ε_z] < Im[ε_y] < 0 with two Lorentz curves in the dielectric regime, it is necessary to introduce the frequency shift between these curves by designing different characteristic frequencies of $\omega_{01} \neq \omega_{02}$ for I-shaped patches 1 and 2 (1, 2 represent ***y*** or ***z***). To observe the EP with the spectral stability, we consider only the cases of the broadband design of EP (black circles in Figs. B.6a,B.6b), neglecting cases that are too sensitive (green circles in Figs. B.6a,B.6b). If I-shaped patch 1 in the high-frequency regime (ω_{01}) supports a lower plasma frequency than that of I-shaped patch 2 ($\omega_{p1} < \omega_{p2}$, Fig. B.6a), the condition with broad bandwidth is satisfied at the metallic state (Fig. 2.19f in the main manuscript), which supports an evanescent mode inside the PT-symmetric metamaterial. Meanwhile, if the design satisfying $\omega_{01} > \omega_{02}$ and $\omega_{p1} > \omega_{p2}$ is applied simultaneously (Fig. B.6b), the propagating mode can be utilized to observe the low-dimensionality.

As shown in Figs. B.6c-B.6d, increasing the parameters related to the 'length' of the patch (*L* and *a*) increases the plasma frequency ω_p due to the large number of

participating electrons (note that $\omega_p^2 \sim Ne^2/(m\varepsilon_0)$, where N is the density of electrons), while the characteristic frequency decreases due to the weak restoring force. Similarly, decreasing gap g (Fig. B.6e) increases the attractive force, yielding the reversed response of $\omega_0\downarrow$ and $\omega_p\uparrow$. Therefore, the strategy for low-dimensional evanescent waves (Fig. B.6a) can be achieved with the manipulation of L, a, or g. However, by widening the patches (Fig. B.6f), we can increase the participating electrons ($\omega_p\uparrow$) and the restoring force ($\omega_0\uparrow$) simultaneously, enabling the case of Fig. B.6b, with low-dimensional propagating waves. Now, by changing the tilted angle θ (Fig. 2.19b in the main manuscript), we can obtain the low-dimensional chiral dynamics at the EP by obtaining the coupling between the ***y***- and ***z***-polarizations for both cases.

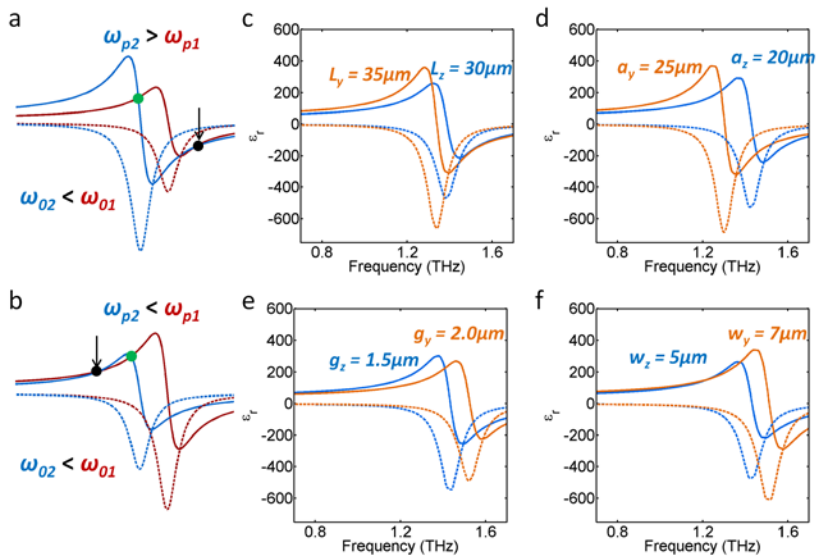

Figure B.6. The effect of changing the structural parameters. The strategy for satisfying the condition of PT symmetry with (a) $\omega_{01} > \omega_{02}$ and $\omega_{p1} < \omega_{p2}$ (low-dimensional evanescent waves) and (b) $\omega_{01} > \omega_{02}$ and $\omega_{p1} > \omega_{p2}$ (low-dimensional propagating waves). Black (or green) circles denote the condition of low-dimensional EP with broad (or narrow) bandwidths. The COMSOL-calculated permittivities $\varepsilon(\omega)$ are shown for the changes of (c) length L, (d) arm length a, (e) gap thickness g, and (f) width w. The unchanged parameters are L = 30 μm, a = 20 μm, g = 1.5 μm, and w = 5 μm.

B.9 Design parameters of chiral waveguides

For the complex-strip waveguide with isotropic materials (Fig. 2.21a in the main manuscript), the lossless Si material (ε_{Si}=12.1) is assumed to compose the strip structure on top of the lossy Ti layer (ε_{Ti}=1.66-i·30.1) above a silica substrate (ε_{SiO2}=2.07), supporting both a low-loss y-polarized mode and a high-loss z-polarized mode. The effect of the loss can be controlled by changing the depth of the Ti layer. The complex-strip waveguide satisfies PT symmetry based on the gauge transformation ($Re[\varepsilon_y]=Re[\varepsilon_z]$ and $Im[\varepsilon_z]<Im[\varepsilon_y]<0$). In Fig. 2.21a in the main manuscript, L_{11}=190 nm, L_{12}=300 nm, L_{21}=620 nm, and L_{22}=190 nm.

B.10 Low-dimensional linear polarization

Because the formulation of Eq. (B.1) is based on the general framework for two-level PT-symmetric potentials, our analysis of the low-dimensional polarization can be extended beyond the case of chirality treated in the main manuscript. For example, instead of mixing amplifying y-LP and decaying z-LP modes, consider the mixing of *amplifying RCP and decaying LCP modes*, which is possible with the recent development of active chiral materials and circular dichroism. The eigenmodes of the PT-symmetric material are then expressed as $v_{eig1,2} = \eta_{1,2} \cdot \{\varepsilon_{\kappa 0}\cdot[1,i] + (-i\varepsilon_{i0} \pm \lambda_{PT})\cdot[1,-i]\}^{\mathrm{T}} = \eta_{1,2} \cdot [\varepsilon_{\kappa 0} - i\varepsilon_{i0} \pm \lambda_{PT}\,, -i\cdot(-\varepsilon_{\kappa 0} - i\varepsilon_{i0} \pm \lambda_{PT})]^{\mathrm{T}}$, while the eigenvalues are the same as in Figs. 2.17a and 2.17b in the main manuscript.

Figure B.7 shows the corresponding profiles of the eigenpolarizations for points ***d***-***h***. For the Hermitian case (point ***d***), the eigenmodes are linearly polarized (LP) due to the even and odd couplings of the RCP and LCP modes. When ε_{i0} increases ($0 < \varepsilon_{i0} < \varepsilon_{\kappa 0}$, point ***e***), the eigenmodes begin to converge. At the EP ($\varepsilon_{i0} = \varepsilon_{\kappa 0}$, point ***f***), two LP eigenmodes have coalesced, and the reduction to a *1-dimensional LP basis* is evident. After the EP ($\varepsilon_{i0} > \varepsilon_{\kappa 0}$, points ***g*** and ***h***), each eigenmode is saturated to a CP mode (RCP, amplifying, and LCP, decaying).

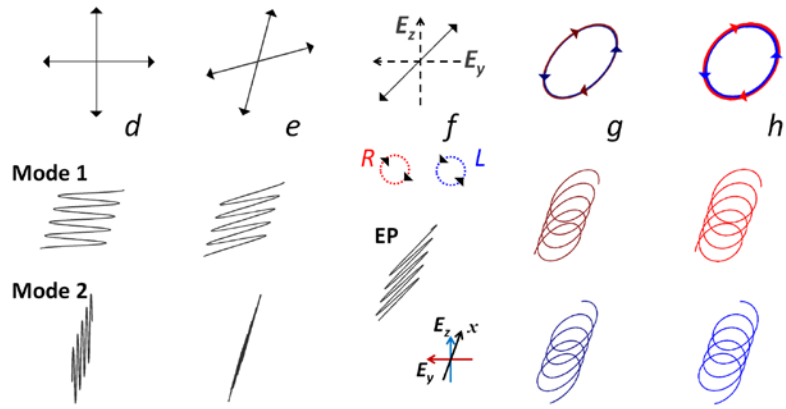

Figure B.7. Spatial evolutions of eigenmodes in the low-dimensional LP material corresponding to points *d*-*h*. At the exceptional point *f*, the complex eigenmode has the singular form of an LP state (*y*–*z*). $\varepsilon_{r0} = 12.25$, and $\varepsilon_{\kappa 0} = \varepsilon_{r0}/10^3 > 0$.

Appendix C

Detailed Derivation for Section 2.3.2

C.1 Detailed derivation of Eq. (2.20)

For spatially varying materials, the time-harmonic wave equation at a frequency ω takes the following form:

$$k_0^2 H_z = -\varepsilon_y^{-1}\partial_x^2 H_z - \varepsilon_x^{-1}\partial_y^2 H_z - \partial_x \varepsilon_y^{-1}\cdot\partial_x H_z - \partial_y \varepsilon_x^{-1}\cdot\partial_y H_z, \quad \text{(C.1)}$$

where $k_0 = \omega/c$ is the free-space wavenumber. Here, we apply two standard approximations of weakly and slowly varying modulated potentials to the time-harmonic wave equation. In the weak coupling regime ($|\Delta\varepsilon_{x,y}(x,y)| << |\varepsilon_{x0,y0}|$, where $\varepsilon_{x,y}(x,y) = \varepsilon_{x0,y0} + \Delta\varepsilon_{x,y}(x,y)$), the field can be expanded using a spatially varying envelope $\psi_{[kx,ky]}$ as follows: $H_z(x,y) = \iint \psi_{[kx,ky]}(x,y)\cdot exp(-ik_x\cdot x - ik_y\cdot y)dk_x dk_y$. Then, Eq. (C.1) becomes

$$\iint\left[k_0^2-\left(\frac{k_x^2}{\varepsilon_y}+\frac{k_y^2}{\varepsilon_x}\right)+i\left(k_x\partial_x\varepsilon_y^{-1}+k_y\partial_y\varepsilon_x^{-1}\right)\right]\psi_{[k_x,k_y]}e^{-i(k_xx+k_yy)}dk_xdk_y$$
$$=\iint 2i\cdot\left(\frac{k_x\partial_x\psi_{[k_x,k_y]}}{\varepsilon_y}+\frac{k_y\partial_y\psi_{[k_x,k_y]}}{\varepsilon_x}\right)e^{-i(k_xx+k_yy)}dk_xdk_y \quad \text{. (C.2)}$$

Assuming that the modulations are weak, i.e., $|\Delta\varepsilon_{x,y}\ /\ \varepsilon_{x0,y0}| << 1$, and the IFC relation $k_0^2 = k_x^2/\varepsilon_{y0} + k_y^2/\varepsilon_{x0}$, Eq. (C.2) can be approximated as follows:

$$\iint\left[\frac{k_x}{\varepsilon_{y0}^2}\cdot\left(\Delta\varepsilon_y k_x-i\partial_x\Delta\varepsilon_y\right)+\frac{k_y}{\varepsilon_{x0}^2}\cdot\left(\Delta\varepsilon_x k_y-i\partial_y\Delta\varepsilon_x\right)\right]\psi_{[k_x,k_y]}e^{-i(k_xx+k_yy)}dk_xdk_y$$
$$\cong\iint 2i\cdot\left[\frac{k_x\partial_x\psi_{[k_x,k_y]}}{\varepsilon_{y0}}+\frac{k_y\partial_y\psi_{[k_x,k_y]}}{\varepsilon_{x0}}\right]e^{-i(k_xx+k_yy)}dk_xdk_y \quad \text{.} \quad \text{(C.3)}$$

The left-hand side of Eq. (C.3) corresponds to the *source* of the spatially varying envelope $\partial\psi$ that appears on the right-hand side of the equation. Assuming that the modulations are slowly varying, i.e., ($|\Delta\varepsilon_y^{-1}\cdot\partial_x\Delta\varepsilon_y| << |k_x|$ and $|\Delta\varepsilon_x^{-1}\cdot\partial_y\Delta\varepsilon_x| << |k_y|$), the first-order derivatives of $\Delta\varepsilon_{x,y}$ can be neglected, and Eq. (C.3) becomes

$$\iint\left[\frac{k_x}{\varepsilon_{y0}}\cdot\frac{\Delta\varepsilon_y}{\varepsilon_{y0}}k_x+\frac{k_y}{\varepsilon_{x0}}\cdot\frac{\Delta\varepsilon_x}{\varepsilon_{x0}}k_y\right]\psi_{[k_x,k_y]}e^{-i(k_xx+k_yy)}dk_xdk_y$$
$$\cong\iint 2i\cdot\left[\frac{k_x}{\varepsilon_{y0}}\cdot\partial_x\psi_{[k_x,k_y]}+\frac{k_y}{\varepsilon_{x0}}\cdot\partial_y\psi_{[k_x,k_y]}\right]e^{-i(k_xx+k_yy)}dk_xdk_y \quad \text{. (C.4)}$$

We simplify Eq. (C.4) by introducing the ε-normalized wavevector $\boldsymbol{\beta_k} = (k_x\cdot\varepsilon_{y0}^{-1})\boldsymbol{x} + (k_y\cdot\varepsilon_{x0}^{-1})\boldsymbol{y}$ and the local modulation vector $\boldsymbol{\sigma_k}(x, y) = (k_x\cdot\Delta\varepsilon_y(x, y)/\varepsilon_{y0})\boldsymbol{x} + (k_y\cdot\Delta\varepsilon_x(x, y)/\varepsilon_{x0})\boldsymbol{y}$, which results in Eq. (2.20) in the main manuscript.

C.2 Serial calculation of discretized coupled mode equations

We apply the spatial discretization of *y*-infinite unit cells (Fig. 2.24a in the main manuscript) and the causality condition for the potential momentum (p, $q \geq 0$) to the integral form of the coupled mode equations; thus, Eq. (2.21) becomes

$$\begin{aligned} &8\pi^2 i \cdot \left(\int_{S_R} \psi_{[k_x,k_y]} \cdot \frac{k_x}{\varepsilon_{y0}} dy - \int_{S_L} \psi_{[k_x,k_y]} \cdot \frac{k_x}{\varepsilon_{y0}} dy \right) \\ &= \int_V \iint_0^\infty \left(\frac{(k_x - p)^2 \Delta\varepsilon_{ypq}}{\varepsilon_{y0}^2} + \frac{(k_y - q)^2 \Delta\varepsilon_{xpq}}{\varepsilon_{x0}^2} \right) \psi_{[k_x-p,k_y-q]} dpdqdv \end{aligned} . \quad \text{(C.5)}$$

We apply the subwavelength limit to evaluate the volume integral from the average of the values in S_L and S_R as

$$\begin{aligned} &\int_V \iint_0^\infty \left(\frac{(k_x - p)^2 \Delta\varepsilon_{ypq}}{\varepsilon_{y0}^2} + \frac{(k_y - q)^2 \Delta\varepsilon_{xpq}}{\varepsilon_{x0}^2} \right) \psi_{[k_x-p,k_y-q]} dpdqdv \\ &\cong \frac{\Delta x}{2} \cdot \left(\int_{S_L} + \int_{S_R} \right) \iint_0^\infty \left(\frac{(k_x - p)^2 \Delta\varepsilon_{ypq}}{\varepsilon_{y0}^2} + \frac{(k_y - q)^2 \Delta\varepsilon_{xpq}}{\varepsilon_{x0}^2} \right) \psi_{[k_x-p,k_y-q]} dpdqdy \end{aligned} . \quad \text{(C.6)}$$

For discretization in *k*-space with sufficiently small Δk (Fig. 2.24b in the main manuscript), Eq. (C.5) can be approximated by the following equation for the m^{th} *k*-state:

$$\begin{aligned} &\int_{S_R} \psi_m(x_R, y) dy = \int_{S_L} \psi_m(x_L, y) dy \\ &+ \sum_{n=1}^{m} \frac{\varepsilon_{y0} \Delta x \cdot \Delta p_n \Delta q_n}{16\pi^2 i k_{xm}} \cdot \left(\frac{k_{xn}{}^2 \Delta\varepsilon_{ypq}}{\varepsilon_{y0}^2} + \frac{k_{yn}{}^2 \Delta\varepsilon_{xpq}}{\varepsilon_{x0}^2} \right) \cdot \int_{S_L+S_R} \psi_n dy \end{aligned}, \quad \text{(C.7)}$$

where $p = k_{xm} - k_{xn}$, $q = k_{ym} - k_{yn}$, $\Delta p_n = k_{x(n+1)} - k_{xn}$, $\Delta q_n = k_{y(n+1)} - k_{yn}$, and n denotes

each k-state before the m^{th} state. Because the spatial boundary condition is applied to the left side of the structure, the calculation is performed from the left to the right side in space. Additionally, because of the causality condition, n has the lower limit of $n = 1$, which is defined by the k-state of an incident wave (k_{x0},k_{y0}), and the calculation in k-space should be performed from $n = 1$ to $n = m$. Therefore, we separate the unknown and known integral terms in Eq. (C.7) as

$$\begin{aligned}
&\left[1-\frac{\varepsilon_{y0}\Delta x\cdot\Delta p_m\Delta q_m}{16\pi^2 ik_{xm}}\cdot\left(\frac{{k_{xm}}^2\Delta\varepsilon_{y00}}{\varepsilon_{y0}^2}+\frac{{k_{ym}}^2\Delta\varepsilon_{x00}}{\varepsilon_{x0}^2}\right)\right]\cdot\int_{S_R}\psi_m(x_R,y)dy \\
&=\left[1+\frac{\varepsilon_{y0}\Delta x\cdot\Delta p_m\Delta q_m}{16\pi^2 ik_{xm}}\cdot\left(\frac{{k_{xm}}^2\Delta\varepsilon_{y00}}{\varepsilon_{y0}^2}+\frac{{k_{ym}}^2\Delta\varepsilon_{x00}}{\varepsilon_{x0}^2}\right)\right]\cdot\int_{S_L}\psi_m(x_L,y)dy \\
&+\sum_{n=1}^{m-1}\frac{\varepsilon_{y0}\Delta x\cdot\Delta p_n\Delta q_n}{16\pi^2 ik_{xm}}\cdot\left(\frac{{k_{xn}}^2\Delta\varepsilon_{ypq}}{\varepsilon_{y0}^2}+\frac{{k_{yn}}^2\Delta\varepsilon_{xpq}}{\varepsilon_{x0}^2}\right)\cdot\int_{S_L+S_R}\psi_n dy
\end{aligned} \quad \text{(C.8)}$$

We can now perform the serial calculation with the boundary condition $\int\psi_1(x=0)dy$. At the fixed point ($x = x_f$), all of the k-states can be obtained from Eq. (C.8) in the order $\int\psi_1(x=x_f)dy$, $\int\psi_2(x=x_f)dy$, …, $\int\psi_m(x=x_f)dy$. These results are applied to calculate the states at the next position ($x = x_f + \Delta x$). For a unity incidence wave on the boundary, the density of the envelope is directly proportional to the integral of the density of the envelope.

Appendix D

Analytical Methods for Section 3.2

D.1 Details of the FDM and FGH method

The FDM utilizes the approximation of the 2nd-derivative operator in the discrete form, and the FGH method, as a spectral method, uses a planewave basis with operator-based expressions in a spatial domain. In both methods, the Hamiltonian matrices are Hermitian because of the real-valued potentials, thus enabling the use of Cholesky decomposition to solve the eigenvalue problem. To ensure an accurate SUSY process, Rayleigh quotient iteration is also applied to obtain the ground-state wavefunction. The boundary effect is minimized through the use of a buffer region (n = 1.5) of sufficient length (30 μm = 20λ_0) on each side. Deep-subwavelength grids (Δ = 20 nm = λ_0/75) are also used for the discretization.

D.2 Calculation of the Hurst exponent

First, the discretized refractive index n_p (p = 1,2,…,N) is obtained at $x_p = x_{left} + (p\text{-}1)\cdot\Delta$, where x_{left} is the left boundary of the potential, which is of length $L = (N\text{-}1)\cdot\Delta$. Partial sequences X_q of n_p for different length scales d are then defined ($2 \le d \le N$ and $1 \le q \le d$). For the mean-adjusted sequence $Y_q = X_q - m$, where m is the mean of X_q,

we define the cumulative deviate series Z_r as

$$Z_r = \sum_{q=1}^{r} Y_q \,. \tag{D.1}$$

The range of cumulative deviation is defined as $R(d) = max(Z_1,Z_2,\ldots,Z_d) - min(Z_1,Z_2,\ldots,Z_d)$. Using the standard deviation $S(d)$ of Y_q, we can now apply the power law to the rescaled range $R(d)/S(d)$ as follows:

$$E\left[\frac{R(d)}{S(d)}\right] = c_0 d^H \,. \tag{D.2}$$

This yields $log(E[R(d)/S(d)]) = H \cdot log(d) + c_1$, where E is the expectation value and c_0 and c_1 are constants. H is then obtained through linear polynomial fitting: $H = 0.5$ for Brownian motion, $0 \leq H < 0.5$ for long-term negative correlations with switching behaviors, and $0.5 < H \leq 1$ for long-term positive correlations such that the sign of the signal is persistent.

Appendix E

Supplements for Section 4.2

E.1 Details of the device structures and numerical method used in the study

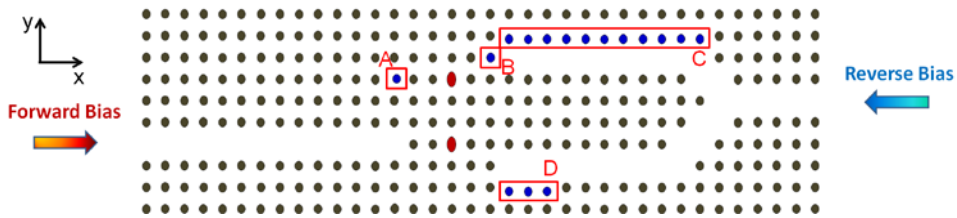

Figure E.1. Layout of the photonic junction diode (Q = 1094). Red ellipsoids are dielectric defects composing di-atomic nonlinear resonators. Blue marked rods are position shifted (parameters in Table A) in order; to introduce π-phase shift of□ between the upper and lower waveguides (Box C, D), to fine-tune the resonance of the upper resonator (Box A), and to adjust couplings into the waveguide (Box B).

Rods	Δx	Δy	Purpose
A	0.10*a*	0	Matching of $\omega_{1,2}$
B	0.05*a*	0	Matching of $\tau_{R1,2}$
C	0	- 0.15*a*	Phase shift for odd mode coupler
D	0	- 0.15*a*	

Table E.1. List of structural parameters for the photonic junction diode layout in Fig. E.1.

Square-lattice, rod-type photonic crystal platform was considered for the design of photonic junction diode and monolithic multi-junction half-adder (To note, the use of square rod platform is for the design convenience [67]. For real implementations, it is necessary to consider the vertical confinement, for example by using a line-defect waveguide with small radius rods or by adopting hole-type photonic crystal). The detailed schematics for junction diode and parameters for the photonic crystal design are illustrated and summarized in Fig. E.1 and Table E.1.

The radius of the dielectric rod was set to 0.2*a* (lattice constant a = 573nm), assuming the linear and nonlinear refractive index n = 3.5 and $n_2 = 1.5 \times 10^{-17} m^2/W$ respectively (of AlGaAs. these values are within typical number range, when compared to other Kerr medium or previous publications). In the FDTD implementation, n_2 equivalent nonlinear susceptibility value of $\chi^{(3)} = 6.50 \times 10^{-19} m^2/V^2$ were used, to treat instantaneous Kerr nonlinear polarization term. The major and minor axis of the ellipsoidal rods comprising the di-atomic resonator were set to 0.64*a* and 0.54*a* in order to support two-band resonances at 193.24THz (1551.4nm, ψ_e) and 193.55THz (1548.9nm, ψ_o) with negligible spectral mode overlap ($< e \,/\, o > = 0.16$. Note that, this residual mode overlap determines the breakdown power under reverse bias (approximately, $P_{threshold} / P_{breakdown} \sim <e/o>^2 / <e/e>^2$).

Considering both the device speed and power consumption, the loaded Q factor and modal volume V of the di-atomic resonator was set and measured to be 1094 and 0.19μm^2 for the junction diode. To note, considering the experimental realization of 3D high-Q cavity (> 10^7), and the maximum loaded Q value (<10^5) assumed here, the criteria of $Q_{intrinsic} >> Q_{loaded}$ is well met. For the design of the phase shifter in the ψ_e, or ψ_o coupler, the location of a few dielectric rods (Box C, D in Fig. E.1) were shifted toward / outward (push / pull) from the side of the photonic crystal waveguides. Both frequency domain (COMSOL Multiphysics) and time domain analysis (FDTD) was carried out in excellent agreement with the result of CMT, confirming the operation / principle of the proposed devices. For FDTD calculation, time step of 47.7 attoseconds and mesh size of $\lambda_{eff}/20$ was used for total simulation time up to 2.54ns (5.31×10^7 time step), to generate eye diagrams for diode and half adder operation. To remove the effect of reflection at the boundary, perfectly-matched layer (PML) boundary condition was applied for the simulation space of 1,320 × 480 grids (31.5 × 11.5 μm^2).

E.2 Coupled mode theory for the di-atomic photonic junction diode

E.2.1 Analytical model and coupled mode equations

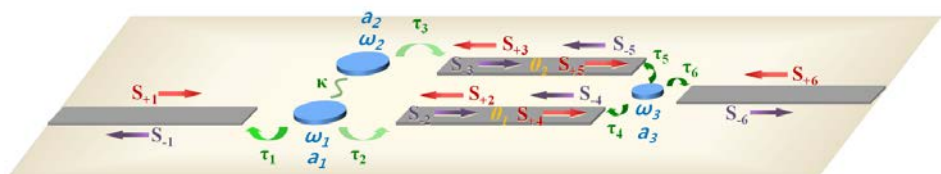

Figure E.2. Analytical model of the di-atomic mode junction diode, used in the temporal CMT analysis.

Temporal coupled mode theory was employed to assess the behavior of the proposed junction diode. First, we write down the coupled mode equations for Fig. E.2,

$$\frac{d}{dt}\begin{pmatrix} a_1 \\ a_2 \\ a_3 \end{pmatrix} = \begin{pmatrix} -i\omega_1 - (\frac{1}{\tau_1}+\frac{1}{\tau_2}) & i\kappa_{12} & 0 \\ i\kappa_{21} & -i\omega_2 - \frac{1}{\tau_3} & 0 \\ 0 & 0 & -i\omega_3 - (\frac{1}{\tau_4}+\frac{1}{\tau_5}+\frac{1}{\tau_6}) \end{pmatrix} \begin{pmatrix} a_1 \\ a_2 \\ a_3 \end{pmatrix} + \begin{pmatrix} \sqrt{\frac{2}{\tau_1}}S_{+1} + \sqrt{\frac{2}{\tau_2}}S_{+2} \\ \sqrt{\frac{2}{\tau_3}}S_{+3} \\ \sqrt{\frac{2}{\tau_4}}S_{+4} + \sqrt{\frac{2}{\tau_5}}S_{+5} + \sqrt{\frac{2}{\tau_6}}S_{+6} \end{pmatrix} \quad \text{(E.1)}$$

$$\begin{pmatrix} S_{-1} \\ S_{-2} \end{pmatrix} = -\begin{pmatrix} S_{+1} \\ S_{+2} \end{pmatrix} + \begin{pmatrix} \sqrt{\frac{2}{\tau_1}} \\ \sqrt{\frac{2}{\tau_2}} \end{pmatrix} a_1 \quad \text{(E.2)}$$

$$S_{-3} = -S_{+3} + \sqrt{\frac{2}{\tau_3}}a_2 \quad \text{(E.3)}$$

$$\begin{pmatrix} S_{-4} \\ S_{-5} \\ S_{-6} \end{pmatrix} = -\begin{pmatrix} S_{+4} \\ S_{+5} \\ S_{+6} \end{pmatrix} + \begin{pmatrix} \sqrt{\frac{2}{\tau_4}} \\ \sqrt{\frac{2}{\tau_5}} \\ \sqrt{\frac{2}{\tau_6}} \end{pmatrix} a_3 \tag{E.4}$$

$$\begin{pmatrix} S_{+2} \\ S_{+4} \end{pmatrix} = \begin{pmatrix} S_{-4} \\ S_{-2} \end{pmatrix} e^{j\theta_1} \tag{E.5}$$

$$\begin{pmatrix} S_{+3} \\ S_{+5} \end{pmatrix} = \begin{pmatrix} S_{-5} \\ S_{-3} \end{pmatrix} e^{j\theta_2} \tag{E.6}$$

E.2.2. Solution of resonator field (a_1, a_2, a_3)

Solving Eq. (E.2-E.4) and (E.5-E.6) together we now arrive at the following expressions for the wave components entering to the resonators 1, 2, and 3.

$$S_{+2} = \frac{\sqrt{\frac{2}{\tau_2}} e^{i\theta_1}}{2i\sin\theta_1} a_1 + \frac{-\sqrt{\frac{2}{\tau_4}}}{2i\sin\theta_1} a_3 \equiv \alpha_{21} a_1 + \alpha_{23} a_3 \tag{E.7}$$

$$S_{+3} = \frac{\sqrt{\frac{2}{\tau_3}} e^{i\theta_2}}{2i\sin\theta_2} a_2 + \frac{-\sqrt{\frac{2}{\tau_5}}}{2i\sin\theta_2} a_3 \equiv \alpha_{32} a_2 + \alpha_{33} a_3 \tag{E.8}$$

$$S_{+4} = \frac{-\sqrt{\frac{2}{\tau_2}}}{2i\sin\theta_1} a_1 + \frac{\sqrt{\frac{2}{\tau_4}} e^{i\theta_1}}{2i\sin\theta_1} a_3 \equiv \alpha_{41} a_1 + \alpha_{43} a_3 \tag{E.9}$$

$$S_{+5} = \frac{-\sqrt{\frac{2}{\tau_3}}}{2i\sin\theta_2} a_2 + \frac{\sqrt{\frac{2}{\tau_5}} e^{i\theta_2}}{2i\sin\theta_2} a_3 \equiv \alpha_{52} a_2 + \alpha_{53} a_3 \qquad \text{(E.10)}$$

Substituting (E.7-E.10) into (E.1), the field amplitudes in resonators $a_1 \sim a_3$ can be obtained to give,

$$a_1 = \frac{-(c_5 - \frac{c_6 M_2}{c_3})\sqrt{\frac{2}{\tau_1}} S_{+1} + (c_{12} - \frac{c_2 M_2}{c_3})\sqrt{\frac{2}{\tau_6}} S_{+6}}{(M_1 - \frac{c_{21} c_2}{c_3})(c_5 - \frac{c_6 M_2}{c_3}) - (c_4 - \frac{c_6 c_{21}}{c_3})(c_{12} - \frac{c_2 M_2}{c_3})} \qquad \text{(E.11)}$$

$$a_2 = \frac{-(c_4 - \frac{c_6 c_{21}}{c_3})\sqrt{\frac{2}{\tau_1}} S_{+1} + (M_1 - \frac{c_{21} c_2}{c_3})\sqrt{\frac{2}{\tau_6}} S_{+6}}{(M_1 - \frac{c_{21} c_2}{c_3})(c_5 - \frac{c_6 M_2}{c_3}) - (c_4 - \frac{c_6 c_{21}}{c_3})(c_{12} - \frac{c_2 M_2}{c_3})} \qquad \text{(E.12)}$$

$$a_3 = \frac{c_4 M_2 - c_{21} c_5}{c_3 c_5 - c_6 M_2} \cdot \frac{-(c_5 - \frac{c_6 M_2}{c_3})\sqrt{\frac{2}{\tau_1}} S_{+1} + (c_{12} - \frac{c_2 M_2}{c_3})\sqrt{\frac{2}{\tau_6}} S_{+6}}{(M_1 - \frac{c_{21} c_2}{c_3})(c_5 - \frac{c_6 M_2}{c_3}) - (c_4 - \frac{c_6 c_{21}}{c_3})(c_{12} - \frac{c_2 M_2}{c_3})} \qquad \text{(E.13)}$$

where

$$M_1 = i(\omega - \omega_1) - (\frac{1}{\tau_1} + \frac{1}{\tau_2}) + \sqrt{\frac{2}{\tau_2}} \alpha_{21} \qquad \text{(E.14)}$$

$$M_2 = i(\omega - \omega_2) - \frac{1}{\tau_3} + \sqrt{\frac{2}{\tau_3}} \alpha_{32} \qquad \text{(E.15)}$$

and c_{ij}'s are constant values not affected by the nonlinear frequency shift ; $c_{12} = i\kappa_{12}$, $c_{21} = i\kappa_{21}$, $c_2 = (2/\tau_2)^{1/2}\alpha_{23}$, $c_3 = (2/\tau_3)^{1/2}\alpha_{33}$, $c_4 = (2/\tau_4)^{1/2}\alpha_{41}$, $c_5 = (2/\tau_5)^{1/2}\alpha_{52}$, and $c_6 = i(\omega-\omega_3) - (1/\tau_4+1/\tau_5+1/\tau_6) + (2/\tau_4)^{1/2}\alpha_{43} + (2/\tau_5)^{1/2}\alpha_{53}$.

E.2.3 Implementation of Kerr nonlinearity and calculation of diode throughput

It is important to note that, in order to calculate the field *energy* in the resonators ($|a_1|^2$ and $|a_2|^2$) from Eq. (E.11) and (E.13), we also incorporate the resonance-red-shift from the Kerr nonlinearity for the resonator 1 and 2, using $\omega_k = \omega_k^{\,0} - \rho|a_k|^2$ (k=1, 2), where $\omega_k^{\,0}$ is the resonance frequency without nonlinearity, and ρ is $\sigma\omega_k^{\,0}(n_2/n_0)\cdot(c/n_0V_{kerr})$, σ being the fraction of the mode energy stored in the nonlinear modulated region, c is the light speed, V_{kerr} is the modal volume of the nonlinear resonator and n_2 is the nonlinear Kerr coefficient.

The transmitted optical power for the forward and reverse bias condition can then be calculated from Eq. (E.11) and (E.13), by using a simple relation, $P_O = (2/\tau_6)|a_3|^2$ for forward feeding boundary condition $|S_{+1}|^2 = P_I$, $S_{+6} = 0$, and $P_O = (2/\tau_1)|a_1|^2$ for the reverse feeding boundary condition $|S_{+6}|^2 = P_I$, $S_{+1} = 0$. Specifically, applying boundary conditions for forward bias, the expression for the stored field energy $|a_3|^2$ of resonator 3 becomes

$$|a_3|^2 = \frac{|c_1c_5 - c_4M_2|^2}{|c_3c_5 - c_6M_2|^2}|a_1|^2 \qquad \text{(E.16)}$$

where for Eq. (E.16), $M_1(|a_1|^2)$ and $M_2(|a_2|^2)$ can be calculated from (E.14,E.15) with resonance shifted frequency $\omega_k = \omega_k^{\,0} - \rho|a_k|^2$ and for $|a_1|^2$ and $|a_2|^2$ being

$$|a_1|^2 = \frac{\left|c_5 - \frac{c_6 M_2}{c_3}\right|^2 \frac{2}{\tau_1} P_I}{\left|(M_1 - \frac{c_{21}c_2}{c_3})(c_5 - \frac{c_6 M_2}{c_3}) - (c_4 - \frac{c_6 c_{21}}{c_3})(c_{12} - \frac{c_2 M_2}{c_3})\right|^2} \tag{E.17}$$

$$\frac{|a_2|^2}{|a_1|^2} = \frac{|c_3 c_4 - c_6 c_{21}|^2}{|c_3 c_5 - c_6 M_2|^2}. \tag{E.18}$$

For reverse bias boundary condition, the stored field energy $|a_1|^2$ can be reduced to give,

$$|a_1|^2 = \frac{\left|c_{12} - \frac{c_2 M_2}{c_3}\right|^2 \frac{2}{\tau_6} P_I}{\left|(M_1 - \frac{c_{21}c_2}{c_3})(c_5 - \frac{c_6 M_2}{c_3}) - (c_4 - \frac{c_6 c_{21}}{c_3})(c_{12} - \frac{c_2 M_2}{c_3})\right|^2} \tag{E.19}$$

where $M_1(|a_1|^2)$ and $M_2(|a_2|^2)$ can be calculated from, by setting $\omega_k = \omega_k{}^0 - \rho|a_k|^2$ and using,

$$\frac{|a_2|^2}{|a_1|^2} = \frac{|c_3 M_1 - c_2 c_{21}|^2}{|c_3 c_{12} - c_2 M_2|^2}. \tag{E.20}$$

The output power thus then can be obtained from $P_O = (2/\tau_6)|a_3|^2$ for forward feeding, or with $P_O = (2/\tau_1)|a_1|^2$ for reverse feeding. Using the FDTD measured resonator parameter sets $\omega_k{}^0$, ρ, τ_i, and θ_i, the transmission power and response curve of the diode (Fig. 4.5a in the main manuscript) can be finally obtained using equation for P_O separately for forward bias and reverse bias.

Bibliography

1. J. D. Jackson, *Classical electrodynamics* (Wiley, 1998).
2. M. C. Teich, and B. Saleh, *Fundamentals of photonics* (2007).
3. J. B. Pendry, D. Schurig, and D. R. Smith, "Controlling electromagnetic fields," Science **312**, 1780-1782 (2006).
4. G. P. Agrawal, *Fiber-optic communication systems* (1997).
5. E. Yablonovitch, and T. Gmitter, "Photonic band structure: the face-centered-cubic case," Physical Review Letters **63**, 1950 (1989).
6. D. Schurig, J. Mock, B. Justice, S. A. Cummer, J. Pendry, A. Starr, and D. Smith, "Metamaterial electromagnetic cloak at microwave frequencies," Science **314**, 977-980 (2006).
7. N. Fang, H. Lee, C. Sun, and X. Zhang, "Sub–diffraction-limited optical imaging with a silver superlens," Science **308**, 534-537 (2005).
8. R. A. Shelby, D. R. Smith, and S. Schultz, "Experimental verification of a negative index of refraction," Science **292**, 77-79 (2001).
9. N. Yu, P. Genevet, M. A. Kats, F. Aieta, J.-P. Tetienne, F. Capasso, and Z. Gaburro, "Light propagation with phase discontinuities: generalized laws of reflection and refraction," Science **334**, 333-337 (2011).
10. S. A. Cummer, B.-I. Popa, D. Schurig, D. R. Smith, and J. Pendry, "Full-wave simulations of electromagnetic cloaking structures," Physical Review E **74**, 036621 (2006).
11. D. N. Christodoulides, F. Lederer, and Y. Silberberg, "Discretizing light behaviour in linear and nonlinear waveguide lattices," Nature **424**, 817-823 (2003).
12. S. Longhi, "Bloch Oscillations in Complex Crystals withPTSymmetry," Physical Review Letters **103** (2009).
13. A. Block, C. Etrich, T. Limboeck, F. Bleckmann, E. Soergel, C. Rockstuhl, and S. Linden, "Bloch oscillations in plasmonic waveguide arrays," Nature communications **5** (2014).
14. F. Scheffold, R. Lenke, R. Tweer, and G. Maret, "Localization or classical diffusion of light?," Nature **398**, 206-207 (1999).
15. S. Longhi, G. Della Valle, M. Ornigotti, and P. Laporta, "Coherent tunneling by adiabatic passage in an optical waveguide system," Physical Review

B **76**, 201101 (2007).
16. S. Longhi, "Adiabatic passage of light in coupled optical waveguides," Physical Review E **73**, 026607 (2006).
17. M. Mrejen, H. Suchowski, T. Hatakeyama, C. Wu, L. Feng, Y. Wang, and X. Zhang, "Sub-wavelength critical coupling for densely integrated nano-photonics," in *Frontiers in Optics*(Optical Society of America, 2014), p. FM4A. 4.
18. H. Suchowski, M. Mrejen, T. Hatakeyama, C. Wu, L. Feng, K. OBrien, Y. Wang, and X. Zhang, "Active coupling control in densely packed subwavelength waveguides via dark mode," arXiv preprint arXiv:1501.04411 (2015).
19. B. Luk'yanchuk, N. I. Zheludev, S. A. Maier, N. J. Halas, P. Nordlander, H. Giessen, and C. T. Chong, "The Fano resonance in plasmonic nanostructures and metamaterials," Nature materials **9**, 707-715 (2010).
20. X. Piao, S. Yu, and N. Park, "Control of Fano asymmetry in plasmon induced transparency and its application to plasmonic waveguide modulator," Optics express **20**, 18994-18999 (2012).
21. X. Piao, S. Yu, S. Koo, K. Lee, and N. Park, "Fano-type spectral asymmetry and its control for plasmonic metal-insulator-metal stub structures," Optics express **19**, 10907-10912 (2011).
22. A. Grigorenko, M. Polini, and K. Novoselov, "Graphene plasmonics," Nature photonics **6**, 749-758 (2012).
23. D. R. Mason, S. G. Menabde, S. Yu, and N. Park, "Plasmonic Excitations of 1D Metal-Dielectric Interfaces in 2D Systems: 1D Surface Plasmon Polaritons," Scientific reports **4** (2014).
24. Y. Fan, Z. Wei, Z. Zhang, and H. Li, "Enhancing infrared extinction and absorption in a monolayer graphene sheet by harvesting the electric dipolar mode of split ring resonators," Optics letters **38**, 5410-5413 (2013).
25. Y. Fan, Z. Wei, H. Li, H. Chen, and C. M. Soukoulis, "Photonic band gap of a graphene-embedded quarter-wave stack," Physical Review B **88**, 241403 (2013).
26. A. Vakil, and N. Engheta, "Transformation optics using graphene," Science **332**, 1291-1294 (2011).
27. L. Lu, J. D. Joannopoulos, and M. Soljačić, "Topological photonics," Nature Photonics (2014).
28. M. Verbin, O. Zilberberg, Y. E. Kraus, Y. Lahini, and Y. Silberberg, "Observation of Topological Phase Transitions in Photonic Quasicrystals," Physical Review Letters **110** (2013).
29. A. B. Khanikaev, S. H. Mousavi, W. K. Tse, M. Kargarian, A. H. MacDonald, and G. Shvets, "Photonic topological insulators," Nature materials **12**, 233-239 (2013).
30. N. Hatano, and D. R. Nelson, "Localization transitions in non-Hermitian quantum mechanics," Physical review letters **77**, 570 (1996).
31. N. Hatano, and D. R. Nelson, "Vortex pinning and non-Hermitian quantum mechanics," Physical Review B **56**, 8651 (1997).
32. V. M. Agranovich, and V. Ginzburg, *Crystal optics with spatial dispersion*,

and excitons (Springer, 1984).
33. C. M. Bender, and S. Boettcher, "Real spectra in non-Hermitian Hamiltonians having P T symmetry," Physical Review Letters **80**, 5243 (1998).
34. X. Zhu, H. Ramezani, C. Shi, J. Zhu, and X. Zhang, "P T-Symmetric Acoustics," Physical Review X **4**, 031042 (2014).
35. V. Jakubský, "Thermodynamics of pseudo-Hermitian systems in equilibrium," Modern Physics Letters A **22**, 1075-1084 (2007).
36. M. C. Ogilvie, and P. N. Meisinger, "PT Symmetry and QCD: Finite Temperature and Density," SIGMA. Symmetry, Integrability and Geometry: Methods and Applications **5**, 047 (2009).
37. N. Chtchelkatchev, A. Golubov, T. Baturina, and V. Vinokur, "Stimulation of the Fluctuation Superconductivity by P T Symmetry," Physical review letters **109**, 150405 (2012).
38. Y. Choi, S. Kang, S. Lim, W. Kim, J.-R. Kim, J.-H. Lee, and K. An, "Quasieigenstate Coalescence in an Atom-Cavity Quantum Composite," Physical Review Letters **104** (2010).
39. C. M. Bender, D. C. Brody, H. F. Jones, and B. K. Meister, "Faster than Hermitian Quantum Mechanics," Physical Review Letters **98** (2007).
40. C. M. Bender, D. C. Brody, and H. F. Jones, "Complex Extension of Quantum Mechanics," Physical Review Letters **89** (2002).
41. A. Guo, G. J. Salamo, D. Duchesne, R. Morandotti, M. Volatier-Ravat, V. Aimez, G. A. Siviloglou, and D. N. Christodoulides, "Observation ofPT-Symmetry Breaking in Complex Optical Potentials," Physical Review Letters **103** (2009).
42. S. Longhi, "Quantum-optical analogies using photonic structures," Laser & Photonics Reviews **3**, 243-261 (2009).
43. C. E. Rüter, K. G. Makris, R. El-Ganainy, D. N. Christodoulides, M. Segev, and D. Kip, "Observation of parity–time symmetry in optics," Nature Physics **6**, 192-195 (2010).
44. S. Yu, X. Piao, D. R. Mason, S. In, and N. Park, "Spatiospectral separation of exceptional points inPT-symmetric optical potentials," Physical Review A **86** (2012).
45. S. Yu, H. S. Park, X. Piao, B. Min, and N. Park, "Chiral interactions of light induced by low-dimensional dynamics in complex potentials," arXiv preprint arXiv:1409.0180 (2014).
46. S. Yu, D. R. Mason, X. Piao, and N. Park, "Phase-dependent reversible nonreciprocity in complex metamolecules," Physical Review B **87**, 125143 (2013).
47. J. J. Sakurai, and J. Napolitano, *Modern quantum mechanics* (Addison-Wesley, 2011).
48. A. Mostafazadeh, "Pseudo-Hermiticity versus PT symmetry: The necessary condition for the reality of the spectrum of a non-Hermitian Hamiltonian," Journal of Mathematical Physics **43**, 205 (2002).
49. S. Longhi, "Talbot self-imaging inPT-symmetric complex crystals," Physical Review A **90** (2014).
50. M.-A. Miri, M. Heinrich, and D. N. Christodoulides, "Supersymmetry-

generated complex optical potentials with real spectra," Physical Review A **87**, 043819 (2013).
51. S. Yu, X. Piao, K. Yoo, J. Shin, and N. Park, "One-Way Optical Transition based on Causality in Momentum Space," arXiv preprint arXiv:1409.7031 (2014).
52. C. M. Bender, S. Boettcher, and P. N. Meisinger, "PT-symmetric quantum mechanics," Journal of Mathematical Physics **40**, 2201-2229 (1999).
53. S. Longhi, "Bound states in the continuum in PT-symmetric optical lattices," Optics letters **39**, 1697-1700 (2014).
54. A. Dasarathy, J. P. Isaacson, K. Jones-Smith, J. Tabachnik, and H. Mathur, "Particle in a box inPT-symmetric quantum mechanics and an electromagnetic analog," Physical Review A **87** (2013).
55. S. Fan, R. Baets, A. Petrov, Z. Yu, J. D. Joannopoulos, W. Freude, A. Melloni, M. Popovic, M. Vanwolleghem, D. Jalas, M. Eich, M. Krause, H. Renner, E. Brinkmeyer, and C. R. Doerr, "Comment on "Nonreciprocal light propagation in a silicon photonic circuit"," Science **335**, 38; author reply 38 (2012).
56. D. Jalas, A. Petrov, M. Eich, W. Freude, S. Fan, Z. Yu, R. Baets, M. Popović, A. Melloni, J. D. Joannopoulos, M. Vanwolleghem, C. R. Doerr, and H. Renner, "What is — and what is not — an optical isolator," Nature Photonics **7**, 579-582 (2013).
57. K. Makris, R. El-Ganainy, D. Christodoulides, and Z. H. Musslimani, "Beam dynamics in P T symmetric optical lattices," Physical Review Letters **100**, 103904 (2008).
58. A. Regensburger, C. Bersch, M. A. Miri, G. Onishchukov, D. N. Christodoulides, and U. Peschel, "Parity-time synthetic photonic lattices," Nature **488**, 167-171 (2012).
59. Z. Lin, H. Ramezani, T. Eichelkraut, T. Kottos, H. Cao, and D. N. Christodoulides, "Unidirectional Invisibility Induced byPT-Symmetric Periodic Structures," Physical Review Letters **106** (2011).
60. B. Peng, Ş. K. Özdemir, F. Lei, F. Monifi, M. Gianfreda, G. L. Long, S. Fan, F. Nori, C. M. Bender, and L. Yang, "Parity–time-symmetric whispering-gallery microcavities," Nature Physics **10**, 394-398 (2014).
61. L. Feng, Y. L. Xu, W. S. Fegadolli, M. H. Lu, J. E. Oliveira, V. R. Almeida, Y. F. Chen, and A. Scherer, "Experimental demonstration of a unidirectional reflectionless parity-time metamaterial at optical frequencies," Nature materials **12**, 108-113 (2013).
62. R. Fleury, D. L. Sounas, and A. Alù, "Negative Refraction and Planar Focusing Based on Parity-Time Symmetric Metasurfaces," Physical Review Letters **113** (2014).
63. W. D. Heiss, "The physics of exceptional points," Journal of Physics A: Mathematical and Theoretical **45**, 444016 (2012).
64. H. A. Haus, *Waves and fields in optoelectronics* (Prentice-Hall Englewood Cliffs, NJ, 1984).
65. S. Bandyopadhyay, and M. Cahay, *Introduction to spintronics* (CRC press, 2011).

66. S. G. Tikhodeev, A. L. Yablonskii, E. A. Muljarov, N. A. Gippius, and T. Ishihara, "Quasiguided modes and optical properties of photonic crystal slabs," Physical Review B **66** (2002).
67. J. D. Joannopoulos, S. G. Johnson, J. N. Winn, and R. D. Meade, *Photonic crystals: molding the flow of light* (Princeton university press, 2011).
68. Y. Shen, J. Fu, and G. Yu, "Rainbow trapping in one-dimensional chirped photonic crystals composed of alternating dielectric slabs," Physics Letters A **375**, 3801-3803 (2011).
69. K. L. Tsakmakidis, A. D. Boardman, and O. Hess, "'Trapped rainbow' storage of light in metamaterials," Nature **450**, 397-401 (2007).
70. X. P. Zhao, W. Luo, J. X. Huang, Q. H. Fu, K. Song, X. C. Cheng, and C. R. Luo, "Trapped rainbow effect in visible light left-handed heterostructures," Applied Physics Letters **95**, 071111 (2009).
71. Q. Gan, Y. J. Ding, and F. J. Bartoli, "'"Rainbow" Trapping and Releasing at Telecommunication Wavelengths," Physical Review Letters **102** (2009).
72. S. G. Johnson, P. Bienstman, M. A. Skorobogatiy, M. Ibanescu, E. Lidorikis, and J. D. Joannopoulos, "Adiabatic theorem and continuous coupled-mode theory for efficient taper transitions in photonic crystals," Physical Review E **66** (2002).
73. P. Alonso-Gonzalez, M. Schnell, P. Sarriugarte, H. Sobhani, C. Wu, N. Arju, A. Khanikaev, F. Golmar, P. Albella, and L. Arzubiaga, "Real-space mapping of Fano interference in plasmonic metamolecules," Nano letters **11**, 3922-3926 (2011).
74. N. Landy, S. Sajuyigbe, J. Mock, D. Smith, and W. Padilla, "Perfect metamaterial absorber," Physical review letters **100**, 207402 (2008).
75. M. Bayer, T. Gutbrod, J. Reithmaier, A. Forchel, T. Reinecke, P. Knipp, A. Dremin, and V. Kulakovskii, "Optical modes in photonic molecules," Physical review letters **81**, 2582 (1998).
76. P. K. Jha, M. Mrejen, J. Kim, C. Wu, X. Yin, Y. Wang, and X. Zhang, "Interacting Dark Resonance Physics with MetaMolecules," in *Frontiers in Optics*(Optical Society of America, 2014), p. FW5C. 6.
77. P. K. Jha, M. Mrejen, J. Kim, C. Wu, X. Yin, Y. Wang, and X. Zhang, "Interacting dark resonances with plasmonic meta-molecules," Applied Physics Letters **105**, 111109 (2014).
78. J. Li, and C. Chan, "Double-negative acoustic metamaterial," Physical Review E **70**, 055602 (2004).
79. S. Zhang, L. Yin, and N. Fang, "Focusing ultrasound with an acoustic metamaterial network," Physical review letters **102**, 194301 (2009).
80. A. L. Rakhmanov, A. M. Zagoskin, S. Savel'ev, and F. Nori, "Quantum metamaterials: Electromagnetic waves in a Josephson qubit line," Physical Review B **77**, 144507 (2008).
81. V. V. Cheianov, V. Fal'ko, and B. Altshuler, "The focusing of electron flow and a Veselago lens in graphene pn junctions," Science **315**, 1252-1255 (2007).
82. M. Choi, S. H. Lee, Y. Kim, S. B. Kang, J. Shin, M. H. Kwak, K.-Y. Kang,

Y.-H. Lee, N. Park, and B. Min, "A terahertz metamaterial with unnaturally high refractive index," Nature **470**, 369-373 (2011).
83. A. Szameit, M. C. Rechtsman, M. Segev, and O. Bahat-Treidel, "Complex photonic graphene: Optical tachyons, strain, and PT-symmetry," (2011).
84. Z. H. Musslimani, K. G. Makris, R. El-Ganainy, and D. N. Christodoulides, "Optical Solitons inPTPeriodic Potentials," Physical Review Letters **100** (2008).
85. T. Saitoh, and T. Mukai, "1.5 μm GaInAsP traveling-wave semiconductor laser amplifier," Quantum Electronics, IEEE Journal of **23**, 1010-1020 (1987).
86. Z. Bakonyi, H. Su, G. Onishchukov, L. F. Lester, A. L. Gray, T. C. Newell, and A. Tunnermann, "High-gain quantum-dot semiconductor optical amplifier for 1300 nm," Quantum Electronics, IEEE Journal of **39**, 1409-1414 (2003).
87. R. Laming, M. N. Zervas, and D. N. Payne, "Erbium-doped fiber amplifier with 54 dB gain and 3.1 dB noise figures," Photonics Technology Letters, IEEE **4**, 1345-1347 (1992).
88. M. K. Gaillard, P. D. Grannis, and F. J. Sciulli, "The standard model of particle physics," Reviews of Modern Physics **71**, S96 (1999).
89. A. Wang, G. J. Quigley, F. J. Kolpak, J. L. Crawford, J. H. Van Boom, G. van der Marel, and A. Rich, "Molecular structure of a left-handed double helical DNA fragment at atomic resolution," Nature **282**, 680-686 (1979).
90. Y. Tang, and A. E. Cohen, "Optical chirality and its interaction with matter," Physical review letters **104**, 163901 (2010).
91. D. M. Lipkin, "Existence of a new conservation law in electromagnetic theory," Journal of Mathematical Physics **5**, 696-700 (1964).
92. N. Yu, F. Aieta, P. Genevet, M. A. Kats, Z. Gaburro, and F. Capasso, "A broadband, background-free quarter-wave plate based on plasmonic metasurfaces," Nano letters **12**, 6328-6333 (2012).
93. E. Collett, "Polarized light. Fundamentals and applications," Optical Engineering, New York: Dekker,| c1992 **1** (1992).
94. Y. Tang, and A. E. Cohen, "Enhanced enantioselectivity in excitation of chiral molecules by superchiral light," Science **332**, 333-336 (2011).
95. T. Cao, G. Wang, W. Han, H. Ye, C. Zhu, J. Shi, Q. Niu, P. Tan, E. Wang, and B. Liu, "Valley-selective circular dichroism of monolayer molybdenum disulphide," Nature communications **3**, 887 (2012).
96. Z. Li, M. Gokkavas, and E. Ozbay, "Manipulation of asymmetric transmission in planar chiral nanostructures by anisotropic loss," Advanced Optical Materials **1**, 482-488 (2013).
97. V. Fedotov, P. Mladyonov, S. Prosvirnin, A. Rogacheva, Y. Chen, and N. Zheludev, "Asymmetric propagation of electromagnetic waves through a planar chiral structure," Physical review letters **97**, 167401 (2006).
98. S. Furumi, and N. Tamaoki, "Glass-Forming Cholesteric Liquid Crystal Oligomers for New Tunable Solid-State Laser," Advanced Materials **22**, 886-891 (2010).
99. S. Chen, D. Katsis, A. Schmid, J. Mastrangelo, T. Tsutsui, and T. Blanton,

"Circularly polarized light generated by photoexcitation of luminophores in glassy liquid-crystal films," Nature **397**, 506-508 (1999).
100. J. B. Pendry, "A chiral route to negative refraction," Science **306**, 1353-1355 (2004).
101. J. Zhou, J. Dong, B. Wang, T. Koschny, M. Kafesaki, and C. M. Soukoulis, "Negative refractive index due to chirality," Physical Review B **79** (2009).
102. S. Zhang, Y.-S. Park, J. Li, X. Lu, W. Zhang, and X. Zhang, "Negative Refractive Index in Chiral Metamaterials," Physical Review Letters **102** (2009).
103. Z. Li, M. Mutlu, and E. Ozbay, "Chiral metamaterials: from optical activity and negative refractive index to asymmetric transmission," Journal of Optics **15**, 023001 (2013).
104. E. Plum, V. A. Fedotov, and N. I. Zheludev, "Extrinsic electromagnetic chirality in metamaterials," Journal of Optics A: Pure and Applied Optics **11**, 074009 (2009).
105. Y. Cui, L. Kang, S. Lan, S. Rodrigues, and W. Cai, "Giant chiral optical response from a twisted-arc metamaterial," Nano letters **14**, 1021-1025 (2014).
106. S. Yoo, M. Cho, and Q. H. Park, "Globally enhanced chiral field generation by negative-index metamaterials," Physical Review B **89** (2014).
107. B. Wang, J. Zhou, T. Koschny, and C. M. Soukoulis, "Nonplanar chiral metamaterials with negative index," Applied Physics Letters **94**, 151112 (2009).
108. M. Liu, D. A. Powell, I. V. Shadrivov, M. Lapine, and Y. S. Kivshar, "Spontaneous chiral symmetry breaking in metamaterials," Nature communications **5**, 4441 (2014).
109. M. Li, L. Guo, J. Dong, and H. Yang, "An ultra-thin chiral metamaterial absorber with high selectivity for LCP and RCP waves," Journal of Physics D: Applied Physics **47**, 185102 (2014).
110. J. K. Gansel, M. Thiel, M. S. Rill, M. Decker, K. Bade, V. Saile, G. von Freymann, S. Linden, and M. Wegener, "Gold helix photonic metamaterial as broadband circular polarizer," Science **325**, 1513-1515 (2009).
111. M. Thiel, M. S. Rill, G. von Freymann, and M. Wegener, "Three-Dimensional Bi-Chiral Photonic Crystals," Advanced Materials, NA-NA (2009).
112. M. Reichelt, S. W. Koch, A. V. Krasavin, J. V. Moloney, A. S. Schwanecke, T. Stroucken, E. M. Wright, and N. I. Zheludev, "Broken enantiomeric symmetry for electromagnetic waves interacting with planar chiral nanostructures," Applied Physics B **84**, 97-101 (2006).
113. C. Menzel, T. Paul, C. Rockstuhl, T. Pertsch, S. Tretyakov, and F. Lederer, "Validity of effective material parameters for optical fishnet metamaterials," Physical Review B **81** (2010).
114. X. Chen, T. M. Grzegorczyk, B.-I. Wu, J. Pacheco, and J. A. Kong, "Robust method to retrieve the constitutive effective parameters of metamaterials," Physical Review E **70** (2004).
115. J. Elser, A. A. Govyadinov, I. Avrutsky, I. Salakhutdinov, and V. A. Podolskiy, "Plasmonic Nanolayer Composites: Coupled Plasmon Polaritons, Effective-Medium Response, and Subdiffraction Light Manipulation," Journal of

Nanomaterials **2007**, 1-8 (2007).
116. J. Shin, J.-T. Shen, and S. Fan, "Three-dimensional metamaterials with an ultrahigh effective refractive index over a broad bandwidth," Physical review letters **102**, 093903 (2009).
117. D. Martin, K. Neal, and T. Dean, "The optical and magneto-optical behaviour of ferromagnetic metals," Proceedings of the Physical Society **86**, 605 (1965).
118. N. Moiseyev, *Non-Hermitian quantum mechanics* (Cambridge University Press, 2011).
119. M. Moharam, and T. Gaylord, "Rigorous coupled-wave analysis of planar-grating diffraction," JOSA **71**, 811-818 (1981).
120. J. A. Schuller, E. S. Barnard, W. Cai, Y. C. Jun, J. S. White, and M. L. Brongersma, "Plasmonics for extreme light concentration and manipulation," Nature materials **9**, 193-204 (2010).
121. I. I. Smolyaninov, Y.-J. Hung, and C. C. Davis, "Magnifying superlens in the visible frequency range," Science **315**, 1699-1701 (2007).
122. Z. Liu, H. Lee, Y. Xiong, C. Sun, and X. Zhang, "Far-field optical hyperlens magnifying sub-diffraction-limited objects," Science **315**, 1686-1686 (2007).
123. T. Pertsch, P. Dannberg, W. Elflein, A. Bräuer, and F. Lederer, "Optical Bloch oscillations in temperature tuned waveguide arrays," Physical Review Letters **83**, 4752 (1999).
124. K. Chung, S. Yu, C. J. Heo, J. W. Shim, S. M. Yang, M. G. Han, H. S. Lee, Y. Jin, S. Y. Lee, and N. Park, "Flexible, Angle-Independent, Structural Color Reflectors Inspired by Morpho Butterfly Wings," Advanced Materials **24**, 2375-2379 (2012).
125. S. Yu, X. Piao, S. Koo, J. H. Shin, S. H. Lee, B. Min, and N. Park, "Mode junction photonics with a symmetry-breaking arrangement of mode-orthogonal heterostructures," Optics express **19**, 25500-25511 (2011).
126. A. Poddubny, I. Iorsh, P. Belov, and Y. Kivshar, "Hyperbolic metamaterials," Nature Photonics **7**, 948-957 (2013).
127. G. Castaldi, S. Savoia, V. Galdi, A. Alù, and N. Engheta, "Analytical study of subwavelength imaging by uniaxial epsilon-near-zero metamaterial slabs," Physical Review B **86** (2012).
128. S. L. Hahn, "Multidimensional complex signals with single-orthant spectra," Proceedings of the IEEE **80**, 1287-1300 (1992).
129. T. Bulow, and G. Sommer, "Hypercomplex signals-a novel extension of the analytic signal to the multidimensional case," Signal Processing, IEEE Transactions on **49**, 2844-2852 (2001).
130. X. Yang, J. Yao, J. Rho, X. Yin, and X. Zhang, "Experimental realization of three-dimensional indefinite cavities at the nanoscale with anomalous scaling laws," Nature Photonics **6**, 450-454 (2012).
131. P. R. West, N. Kinsey, M. Ferrera, A. V. Kildishev, V. M. Shalaev, and A. Boltasseva, "Adiabatically tapered hyperbolic metamaterials for dispersion control

of high-k waves," Nano letters **15**, 498-505 (2015).
132. J. Gear, F. Liu, S. Chu, S. Rotter, and J. Li, "Parity-time symmetry from stacking purely dielectric and magnetic slabs," Physical Review A **91**, 033825 (2015).
133. J. Han, Y. Fan, L. Jin, Z. Zhang, Z. Wei, C. Wu, J. Qiu, H. Chen, Z. Wang, and H. Li, "Mode propagation in a PT-symmetric gain–metal–loss plasmonic system," Journal of Optics **16**, 045002 (2014).
134. M. Principe, G. Castaldi, M. Consales, A. Cusano, and V. Galdi, "Supersymmetry-inspired non-Hermitian optical couplers," Scientific reports **5**, 8568 (2015).
135. H. P. Laba, and V. M. Tkachuk, "Quantum-mechanical analogy and supersymmetry of electromagnetic wave modes in planar waveguides," Physical Review A **89** (2014).
136. F. Bloch, "Über die quantenmechanik der elektronen in kristallgittern," Zeitschrift für physik **52**, 555-600 (1929).
137. C. Kittel, P. McEuen, and P. McEuen, *Introduction to solid state physics* (Wiley New York, 1976).
138. D. Levine, and P. J. Steinhardt, "Quasicrystals: a new class of ordered structures," Physical Review Letters **53**, 2477 (1984).
139. D. Weaire, and M. Thorpe, "Electronic properties of an amorphous solid. I. A simple tight-binding theory," Physical Review B **4**, 2508 (1971).
140. S. Yu, X. Piao, J. Hong, and N. Park, "Bloch-like wave dynamics in disordered potentials based on supersymmetry," arXiv preprint arXiv:1501.02591 (2015).
141. K. Vynck, M. Burresi, F. Riboli, and D. S. Wiersma, "Photon management in two-dimensional disordered media," Nature materials **11**, 1017-1022 (2012).
142. T. Schwartz, G. Bartal, S. Fishman, and M. Segev, "Transport and Anderson localization in disordered two-dimensional photonic lattices," Nature **446**, 52-55 (2007).
143. M. Kac, "Can one hear the shape of a drum?," American Mathematical Monthly, 1-23 (1966).
144. C. Gordon, D. L. Webb, and S. Wolpert, "One cannot hear the shape of a drum," Bulletin of the American Mathematical Society **27**, 134-138 (1992).
145. J. Brossard, and R. Carmona, "Can one hear the dimension of a fractal?," Communications in Mathematical Physics **104**, 103-122 (1986).
146. C. R. Moon, L. S. Mattos, B. K. Foster, G. Zeltzer, W. Ko, and H. C. Manoharan, "Quantum phase extraction in isospectral electronic nanostructures," Science **319**, 782-787 (2008).
147. T. Keilmann, S. Lanzmich, I. McCulloch, and M. Roncaglia, "Statistically induced phase transitions and anyons in 1D optical lattices," Nature communications **2**, 361 (2011).
148. P. Ramond, "Dual theory for free fermions," Physical Review D **3**, 2415 (1971).
149. F. Cooper, A. Khare, and U. Sukhatme, *Supersymmetry in quantum*

mechanics (World Scientific, 2001).
150. T. Grover, D. Sheng, and A. Vishwanath, "Emergent space-time supersymmetry at the boundary of a topological phase," Science **344**, 280-283 (2014).
151. M.-A. Miri, M. Heinrich, and D. N. Christodoulides, "SUSY-inspired one-dimensional transformation optics," Optica **1**, 89 (2014).
152. S. M. Chumakov, and K. B. Wolf, "Supersymmetry in Helmholtz optics," Physics Letters A **193**, 51-53 (1994).
153. M. Heinrich, M.-A. Miri, S. Stützer, S. Nolte, D. N. Christodoulides, and A. Szameit, "Observation of supersymmetric scattering in photonic lattices," Optics letters **39**, 6130-6133 (2014).
154. M. Heinrich, M.-A. Miri, S. Stützer, R. El-Ganainy, S. Nolte, A. Szameit, and D. N. Christodoulides, "Supersymmetric mode converters," Nature communications **5** (2014).
155. R. El-Ganainy, L. Ge, M. Khajavikhan, and D. Christodoulides, "Supersymetric laser arrays," arXiv preprint arXiv:1501.02972 (2015).
156. S. Longhi, and G. Della Valle, "Invisible defects in complex crystals," Annals of Physics **334**, 35-46 (2013).
157. S. Longhi, "Supersymmetric transparent optical intersections," arXiv preprint arXiv:1411.7144 (2014).
158. S. Longhi, "Supersymmetric Bragg gratings," arXiv preprint arXiv:1501.02063 (2015).
159. M.-A. Miri, M. Heinrich, R. El-Ganainy, and D. N. Christodoulides, "Supersymmetric optical structures," Physical review letters **110**, 233902 (2013).
160. W. Man, M. Florescu, K. Matsuyama, P. Yadak, S. Torquato, P. J. Steinhardt, and P. Chaikin, "Experimental observation of photonic bandgaps in Hyperuniform disordered materials," in *Conference on Lasers and Electro-Optics*(Optical Society of America, 2010), p. CThS2.
161. W. Man, M. Florescu, E. P. Williamson, Y. He, S. R. Hashemizad, B. Y. Leung, D. R. Liner, S. Torquato, P. M. Chaikin, and P. J. Steinhardt, "Isotropic band gaps and freeform waveguides observed in hyperuniform disordered photonic solids," Proceedings of the National Academy of Sciences **110**, 15886-15891 (2013).
162. W. Man, M. Florescu, K. Matsuyama, P. Yadak, G. Nahal, S. Hashemizad, E. Williamson, P. Steinhardt, S. Torquato, and P. Chaikin, "Photonic band gap in isotropic hyperuniform disordered solids with low dielectric contrast," Optics express **21**, 19972-19981 (2013).
163. M. Rechtsman, A. Szameit, F. Dreisow, M. Heinrich, R. Keil, S. Nolte, and M. Segev, "Amorphous photonic lattices: band gaps, effective mass, and suppressed transport," Physical review letters **106**, 193904 (2011).
164. M. Florescu, S. Torquato, and P. J. Steinhardt, "Designer disordered materials with large, complete photonic band gaps," Proceedings of the National Academy of Sciences **106**, 20658-20663 (2009).
165. K. Edagawa, S. Kanoko, and M. Notomi, "Photonic amorphous diamond

structure with a 3D photonic band gap," Physical review letters **100**, 013901 (2008).
166. J. Killingbeck, "Accurate finite difference eigenvalues," Physics Letters A **115**, 301-303 (1986).
167. C. C. Marston, and G. G. Balint-Kurti, "The Fourier grid Hamiltonian method for bound state eigenvalues and eigenfunctions," The Journal of chemical physics **91**, 3571-3576 (1989).
168. D. Egli, "Anderson localization triggered by spin disorder," (2011).
169. S. Roche, D. Bicout, E. Maciá, and E. Kats, "Long range correlations in DNA: scaling properties and charge transfer efficiency," Physical review letters **91**, 228101 (2003).
170. H. E. Hurst, "{Long-term storage capacity of reservoirs}," Trans. Amer. Soc. Civil Eng. **116**, 770-808 (1951).
171. D. S. Wiersma, "Disordered photonics," Nature Photonics **7**, 188-196 (2013).
172. Z. V. Vardeny, A. Nahata, and A. Agrawal, "Optics of photonic quasicrystals," Nature Photonics **7**, 177-187 (2013).
173. C. E. Zachary, Y. Jiao, and S. Torquato, "Hyperuniform long-range correlations are a signature of disordered jammed hard-particle packings," Physical review letters **106**, 178001 (2011).
174. S. Torquato, and F. H. Stillinger, "Local density fluctuations, hyperuniformity, and order metrics," Physical Review E **68**, 041113 (2003).
175. M. Florescu, P. J. Steinhardt, and S. Torquato, "Optical cavities and waveguides in hyperuniform disordered photonic solids," Physical Review B **87**, 165116 (2013).
176. M. Hejna, P. J. Steinhardt, and S. Torquato, "Nearly hyperuniform network models of amorphous silicon," Physical Review B **87**, 245204 (2013).
177. Y. Jiao, T. Lau, H. Hatzikirou, M. Meyer-Hermann, J. C. Corbo, and S. Torquato, "Avian photoreceptor patterns represent a disordered hyperuniform solution to a multiscale packing problem," Physical Review E **89**, 022721 (2014).
178. M. A. Klatt, and S. Torquato, "Characterization of maximally random jammed sphere packings: Voronoi correlation functions," Physical Review E **90**, 052120 (2014).
179. R. Dreyfus, Y. Xu, T. Still, L. A. Hough, A. Yodh, and S. Torquato, "Diagnosing hyperuniformity in two-dimensional, disordered, jammed packings of soft spheres," Physical Review E **91**, 012302 (2015).
180. N.-h. Liu, "Propagation of light waves in Thue-Morse dielectric multilayers," Physical Review B **55**, 3543 (1997).
181. M. Dulea, M. Johansson, and R. Riklund, "Trace-map invariant and zero-energy states of the tight-binding Rudin-Shapiro model," Physical Review B **46**, 3296 (1992).
182. M. K. Hedayati, M. Javaherirahim, B. Mozooni, R. Abdelaziz, A. Tavassolizadeh, V. S. K. Chakravadhanula, V. Zaporojtchenko, T. Strunkus, F. Faupel, and M. Elbahri, "Design of a perfect black absorber at visible frequencies using plasmonic metamaterials," Advanced Materials **23**, 5410-5414 (2011).

183. T. Sun, C. F. Guo, F. Cao, E. M. Akinoglu, Y. Wang, M. Giersig, Z. Ren, and K. Kempa, "A broadband solar absorber with 12 nm thick ultrathin a-Si layer by using random metallic nanomeshes," Applied Physics Letters **104**, 251119 (2014).
184. S. Kinoshita, S. Yoshioka, and K. Kawagoe, "Mechanisms of structural colour in the Morpho butterfly: cooperation of regularity and irregularity in an iridescent scale," Proceedings of the Royal Society of London B: Biological Sciences **269**, 1417-1421 (2002).
185. R. A. Potyrailo, H. Ghiradella, A. Vertiatchikh, K. Dovidenko, J. R. Cournoyer, and E. Olson, "Morpho butterfly wing scales demonstrate highly selective vapour response," Nature Photonics **1**, 123-128 (2007).
186. P. Vukusic, J. Sambles, C. Lawrence, and R. Wootton, "Quantified interference and diffraction in single Morpho butterfly scales," Proceedings of the Royal Society of London. Series B: Biological Sciences **266**, 1403-1411 (1999).
187. E. Shevtsova, C. Hansson, D. H. Janzen, and J. Kjærandsen, "Stable structural color patterns displayed on transparent insect wings," Proceedings of the National Academy of Sciences **108**, 668-673 (2011).
188. Y. Zhao, Z. Xie, H. Gu, C. Zhu, and Z. Gu, "Bio-inspired variable structural color materials," Chemical Society reviews **41**, 3297-3317 (2012).
189. I. Woo, S. Yu, J. S. Lee, J. H. Shin, M. Jung, and N. Park, "Plasmonic structural-color thin film with a wide reception angle and strong retro-reflectivity," Photonics Journal, IEEE **4**, 2182-2188 (2012).
190. A. R. Parker, and H. E. Townley, "Biomimetics of photonic nanostructures," Nature nanotechnology **2**, 347-353 (2007).
191. L. B. Kish, "End of Moore's law: thermal (noise) death of integration in micro and nano electronics," Physics Letters A **305**, 144-149 (2002).
192. M. F. Yanik, S. Fan, M. Soljačić, and J. D. Joannopoulos, "All-optical transistor action with bistable switching in a photonic crystal cross-waveguide geometry," Optics letters **28**, 2506-2508 (2003).
193. V. R. Almeida, C. A. Barrios, R. R. Panepucci, and M. Lipson, "All-optical control of light on a silicon chip," Nature **431**, 1081-1084 (2004).
194. J. Dintinger, I. Robel, P. V. Kamat, C. Genet, and T. W. Ebbesen, "Terahertz All-Optical Molecule- Plasmon Modulation," Advanced Materials **18**, 1645-1648 (2006).
195. D. Pacifici, H. J. Lezec, and H. A. Atwater, "All-optical modulation by plasmonic excitation of CdSe quantum dots," Nature Photonics **1**, 402-406 (2007).
196. X. Hu, P. Jiang, C. Ding, H. Yang, and Q. Gong, "Picosecond and low-power all-optical switching based on an organic photonic-bandgap microcavity," Nature Photonics **2**, 185-189 (2008).
197. C. Koos, P. Vorreau, T. Vallaitis, P. Dumon, W. Bogaerts, R. Baets, B. Esembeson, I. Biaggio, T. Michinobu, F. Diederich, W. Freude, and J. Leuthold, "All-optical high-speed signal processing with silicon–organic hybrid slot waveguides," Nature Photonics **3**, 216-219 (2009).
198. S. Yu, S. Koo, X. Piao, and N. Park, "Application of slow-light photonic

crystal structures for ultra-high speed all-optical analog-to-digital conversion," Microoptics Group (OSJ/JSAP) (2009).
199. K. Nozaki, T. Tanabe, A. Shinya, S. Matsuo, T. Sato, H. Taniyama, and M. Notomi, "Sub-femtojoule all-optical switching using a photonic-crystal nanocavity," Nature Photonics **4**, 477-483 (2010).
200. A. Ciattoni, C. Rizza, and E. Palange, "All-optical active plasmonic devices with memory and power-switching functionalities based onε-near-zero nonlinear metamaterials," Physical Review A **83** (2011).
201. X. Piao, S. Yu, and N. Park, "All-optical half-adder based on photonic mode junction," in *Quantum Electronics Conference & Lasers and Electro-Optics (CLEO/IQEC/PACIFIC RIM), 2011*(IEEE, 2011), pp. 488-489.
202. E. N. Bulgakov, and A. F. Sadreev, "All-optical manipulation of light inX- andT-shaped photonic crystal waveguides with a nonlinear dipole defect," Physical Review B **86** (2012).
203. K. Nozaki, A. Shinya, S. Matsuo, T. Sato, E. Kuramochi, and M. Notomi, "Ultralow-energy and high-contrast all-optical switch involving Fano resonance based on coupled photonic crystal nanocavities," Optics express **21**, 11877-11888 (2013).
204. S. Yu, S. Koo, and N. Park, "Coded output photonic A/D converter based on photonic crystal slow-light structures," Optics express **16**, 13752-13757 (2008).
205. S. Yu, X. Piao, and N. Park, "Slow-light dispersion properties of multiatomic multiband coupled-resonator optical waveguides," Physical Review A **85**, 023823 (2012).
206. Y. C. Chen, N. R. Raravikar, L. S. Schadler, P. M. Ajayan, Y. P. Zhao, T. M. Lu, G. C. Wang, and X. C. Zhang, "Ultrafast optical switching properties of single-wall carbon nanotube polymer composites at 1.55 μm," Applied Physics Letters **81**, 975 (2002).
207. M. Dinu, F. Quochi, and H. Garcia, "Third-order nonlinearities in silicon at telecom wavelengths," Applied Physics Letters **82**, 2954 (2003).
208. H. Kang, and Y. Zhu, "Observation of Large Kerr Nonlinearity at Low Light Intensities," Physical Review Letters **91** (2003).
209. Y. Xu, and G. Xiong, "Third-order optical nonlinearity of semiconductor carbon nanotubes for third harmonic generation," Chemical Physics Letters **388**, 330-336 (2004).
210. K. Ikeda, and Y. Fainman, "Material and structural criteria for ultra-fast Kerr nonlinear switching in optical resonant cavities," Solid-State Electronics **51**, 1376-1380 (2007).
211. T. Hasan, Z. Sun, F. Wang, F. Bonaccorso, P. H. Tan, A. G. Rozhin, and A. C. Ferrari, "Nanotube"Polymer Composites for Ultrafast Photonics," Advanced Materials **21**, 3874-3899 (2009).
212. M. Albota, D. Beljonne, J.-L. Brédas, J. E. Ehrlich, J.-Y. Fu, A. A. Heikal, S. E. Hess, T. Kogej, M. D. Levin, and S. R. Marder, "Design of organic molecules with large two-photon absorption cross sections," Science **281**, 1653-1656 (1998).
213. K. O'Brien, H. Suchowski, J. Rho, A. Salandrino, B. Kante, X. Yin, and X.

Zhang, "Predicting nonlinear properties of metamaterials from the linear response," Nature materials **14**, 379-383 (2015).
214. H. Kollmann, X. Piao, M. Esmann, S. F. Becker, D. Hou, C. Huynh, L.-O. Kautschor, G. Bösker, H. Vieker, and A. Beyer, "Toward plasmonics with nanometer precision: nonlinear optics of helium-ion milled gold nanoantennas," Nano letters **14**, 4778-4784 (2014).
215. H. Suchowski, K. O'Brien, Z. J. Wong, A. Salandrino, X. Yin, and X. Zhang, "Phase Mismatch–Free Nonlinear Propagation in Optical Zero-Index Materials," Science **342**, 1223-1226 (2013).
216. L. Fan, J. Wang, L. T. Varghese, H. Shen, B. Niu, Y. Xuan, A. M. Weiner, and M. Qi, "An all-silicon passive optical diode," Science **335**, 447-450 (2012).
217. C. Lu, X. Hu, H. Yang, and Q. Gong, "Ultrahigh-contrast and wideband nanoscale photonic crystal all-optical diode," Optics letters **36**, 4668-4670 (2011).
218. R. Philip, M. Anija, C. S. Yelleswarapu, and D. Rao, "Passive all-optical diode using asymmetric nonlinear absorption," Applied Physics Letters **91**, 141118 (2007).
219. K. Gallo, and G. Assanto, "All-optical diode based on second-harmonic generation in an asymmetric waveguide," JOSA B **16**, 267-269 (1999).
220. M. D. Tocci, M. J. Bloemer, M. Scalora, J. P. Dowling, and C. M. Bowden, "Thin-film nonlinear optical diode," Applied physics letters **66**, 2324-2326 (1995).
221. K. Gallo, G. Assanto, K. R. Parameswaran, and M. M. Fejer, "All-optical diode in a periodically poled lithium niobate waveguide," Applied Physics Letters **79**, 314-316 (2001).
222. Y. Fan, J. Han, Z. Wei, C. Wu, Y. Cao, X. Yu, and H. Li, "Subwavelength electromagnetic diode: One-way response of cascading nonlinear meta-atoms," Applied Physics Letters **98**, 151903 (2011).
223. E. Bulgakov, and A. Sadreev, "All-optical diode based on dipole modes of Kerr microcavity in asymmetric L-shaped photonic crystal waveguide," Optics letters **39**, 1787-1790 (2014).
224. W. Aroua, F. AbdelMalek, and A. A. Kamli, "Optical diode based on plasmonic nanosphere chains," Optics Communications **332**, 25-30 (2014).
225. J. Scaff, and R. Ohl, "Development of silicon crystal rectifiers for microwave radar receivers," Bell System Technical Journal **26**, 1-30 (1947).
226. A. Taflove, and S. C. Hagness, *Computational electrodynamics* (Artech house, 2005).
227. X. Hu, Q. Zhang, Y. Liu, B. Cheng, and D. Zhang, "Ultrafast three-dimensional tunable photonic crystal," Applied physics letters **83**, 2518-2520 (2003).
228. R. Slavík, F. Parmigiani, J. Kakande, C. Lundström, M. Sjödin, P. A. Andrekson, R. Weerasuriya, S. Sygletos, A. D. Ellis, and L. Grüner-Nielsen, "All-optical phase and amplitude regenerator for next-generation telecommunications systems," Nature Photonics **4**, 690-695 (2010).
229. P.-l. Li, D.-x. Huang, X.-l. Zhang, and G.-x. Zhu, "Ultrahigh-speed all-optical half adder based on four-wave mixing in semiconductor optical amplifier,"

Optics express **14**, 11839-11847 (2006).
230. Q. Liu, Z. Ouyang, C. J. Wu, C. P. Liu, and J. C. Wang, "All-optical half adder based on cross structures in two-dimensional photonic crystals," Optics express **16**, 18992-19000 (2008).
231. S. C. Xavier, K. Arunachalam, E. Caroline, and W. Johnson, "Design of two-dimensional photonic crystal-based all-optical binary adder," Optical Engineering **52**, 025201-025201 (2013).
232. Q. Gan, and F. J. Bartoli, "Surface dispersion engineering of planar plasmonic chirped grating for complete visible rainbow trapping," Applied Physics Letters **98**, 251103 (2011).
233. A. Kocabas, S. S. Senlik, and A. Aydinli, "Slowing Down Surface Plasmons on a Moiré Surface," Physical Review Letters **102** (2009).
234. B. Corcoran, C. Monat, C. Grillet, D. J. Moss, B. J. Eggleton, T. P. White, L. O'Faolain, and T. F. Krauss, "Green light emission in silicon through slow-light enhanced third-harmonic generation in photonic-crystal waveguides," Nature Photonics **3**, 206-210 (2009).
235. M. Notomi, E. Kuramochi, and T. Tanabe, "Large-scale arrays of ultrahigh-Q coupled nanocavities," Nature Photonics **2**, 741-747 (2008).
236. S. Mookherjea, J. S. Park, S.-H. Yang, and P. R. Bandaru, "Localization in silicon nanophotonic slow-light waveguides," Nature Photonics **2**, 90-93 (2008).
237. Q. Gan, Z. Fu, Y. J. Ding, and F. J. Bartoli, "Ultrawide-Bandwidth Slow-Light System Based on THz Plasmonic Graded Metallic Grating Structures," Physical Review Letters **100** (2008).
238. R. J. P. Engelen, D. Mori, T. Baba, and L. Kuipers, "Two Regimes of Slow-Light Losses Revealed by Adiabatic Reduction of Group Velocity," Physical Review Letters **101** (2008).
239. Z. Shi, R. W. Boyd, R. M. Camacho, P. K. Vudyasetu, and J. C. Howell, "Slow-Light Fourier Transform Interferometer," Physical Review Letters **99** (2007).
240. B. M. Möller, U. Woggon, and M. V. Artemyev, "Bloch modes and disorder phenomena in coupled resonator chains," Physical Review B **75** (2007).
241. A. Yariv, Y. Xu, R. K. Lee, and A. Scherer, "Coupled-resonator optical waveguide: a proposal and analysis," Optics letters **24**, 711-713 (1999).
242. M. Ebnali-Heidari, C. Monat, C. Grillet, and M. Moravvej-Farshi, "A proposal for enhancing four-wave mixing in slow light engineered photonic crystal waveguides and its application to optical regeneration," Optics express **17**, 18340-18353 (2009).
243. M. Soljačić, S. G. Johnson, S. Fan, M. Ibanescu, E. Ippen, and J. Joannopoulos, "Photonic-crystal slow-light enhancement of nonlinear phase sensitivity," JOSA B **19**, 2052-2059 (2002).
244. C. J. Chang-Hasnain, P.-c. Ku, J. Kim, and S.-l. Chuang, "Variable optical buffer using slow light in semiconductor nanostructures," Proceedings of the IEEE **91**, 1884-1897 (2003).
245. J. B. Khurgin, "Slowing and stopping photons using backward frequency conversion in quasi-phase-matched waveguides," Physical Review A **72**, 023810

(2005).
246. Y. J. Jung, C. W. Son, Y. M. Jhon, S. Lee, and N. Park, "One-level simplification method for all-optical combinational logic circuits," IEEE Photonics Technology Letters **20**, 800 (2008).
247. Y. J. Jung, S. Yu, S. Koo, H. Yu, S. Han, N. Park, J. H. Kim, Y. M. Jhon, and S. Lee, "Reconfigurable all-optical logic AND, NAND, OR, NOR, XOR and XNOR gates implemented by photonic crystal nonlinear cavities," in *Conference on Lasers and Electro-Optics/Pacific Rim*(Optical Society of America, 2009), p. TuB4_3.
248. R. Danielius, P. Di Trapani, C. Solcia, P. Foggi, A. Andreoni, and A. Piskarskas, "Matching of group velocities by spatial walk-off in collinear three-wave interaction with tilted pulses," Optics letters **21**, 973-975 (1996).
249. Y. Ding, and J. Khurgin, "Backward optical parametric oscillators and amplifiers," Quantum Electronics, IEEE Journal of **32**, 1574-1582 (1996).
250. R. H. Walden, "Analog-to-digital converter survey and analysis," Selected Areas in Communications, IEEE Journal on **17**, 539-550 (1999).
251. G. C. Valley, "Photonic analog-to-digital converters," Optics express **15**, 1955-1982 (2007).
252. H. F. Taylor, "An optical analog-to-digital converter-design and analysis," IEEE Journal of Quantum Electronics **15**, 210-216 (1979).
253. F. Kärtner, R. Amatya, M. Araghchini, J. Birge, H. Byun, J. Chen, M. Dahlem, N. DiLello, F. Gan, and C. Holzwarth, "Photonic analog-to-digital conversion with electronic-photonic integrated circuits," in *Proc. SPIE*(2008), pp. 689806-689815.
254. R. A. Becker, C. Woodward, F. J. Leonberger, and R. C. Williamson, "Wide-band electrooptic guided-wave analog-to-digital converters," Proceedings of the IEEE **72**, 802-819 (1984).
255. F. Leonberger, C. Woodward, and D. Spears, "Design and development of a high-speed electrooptic A/D converter," Circuits and Systems, IEEE Transactions on **26**, 1125-1131 (1979).
256. J. Scheuer, G. T. Paloczi, J. K. Poon, and A. Yariv, "Coupled resonator optical waveguides: toward the slowing and storage of light," Optics and photonics news **16**, 36-40 (2005).
257. L. Yang, J. Motohisa, and T. Fukui, "Suggested procedure for the use of the effective-index method for high-index-contrast photonic crystal slabs," Optical Engineering **44**, 078002-078002-078007 (2005).
258. F. Gan, and F. X. Kartner, "High-speed silicon electrooptic modulator design," Photonics Technology Letters, IEEE **17**, 1007-1009 (2005).
259. S. Kubo, D. Mori, and T. Baba, "Low-group-velocity and low-dispersion slow light in photonic crystal waveguides," Optics letters **32**, 2981-2983 (2007).
260. L. G. Molinari, "Determinants of block tridiagonal matrices," Linear algebra and its applications **429**, 2221-2226 (2008).

Abstract in Korean

매질 내 빛의 흐름은 통상적으로 거시적 맥스웰 방정식에 의해 정의된다. 동질성 및 등방성을 가지고, 선형적이며, 시간에 대해 일정한 광학 매질 변수를 갖는 이상적인 매질에서는 광파의 양상이 페르마의 원리의 직접적인 예인 진동하는 전자기장의 직진 형태로, 간단하며 직관적이다. 이러한 평면파적 특성은 기하 광학의 바탕이며, 슈뢰딩거 방정식 형태의 파동 방정식이 갖는 다양한 대칭성 (병진 대칭, 키랄 대칭, 에르미트 대칭, 로렌츠 대칭 및 시간 반전 대칭)의 보존에서 그 원리을 찾을 수 있다.

렌즈, 거울 및 프리즘과 같은 고전적인 방식에서조차, 빛의 흐름을 조절키 위해서는 일부 광학적 대칭성의 붕괴를 필요로 한다. 비균질 매질에서의 병진 대칭의 붕괴는 굴절, 반사, 회절과 같은 산란 기반 빛 제어를 위한 고전적인 방법이다. 전파 시의 빛 에너지의 소모 또는 증폭은 파동 방정식의 비에르미트 헤밀토니안에 의해 정량화된다. 키랄 분자로 이루어진 매질은 광학 활성, 즉 빛의 편광을 돌릴 수 있도록 한다. 천문학에서 별 및 은하 움직임의 관찰에 이용되는 광학적 도플러 효과는 로렌츠

대칭성을 붕괴시키는 광원의 시간에 따른 변화에 기반한다.

비직관적인 이론적 결과물 및 향상된 공정 기술을 포함하는 광학 분야의 최근 성과들은 이제 비고전적인 빛의 흐름을 이끌어내기 위한 광학적 퍼텐셜 제어의 새로운 영역을 개척하고 있다. 메타 물질 개념과 연계된 나노 스케일 기술은 단방향 빛 전파, 변형된 스넬의 법칙, 음굴절율, 투명 망토, 완전 흡수체와 같은 특이한 빛의 흐름을 지원하는, 이론적으로 증명된 인조 매질의 설계를 가능케 한다. 광 증폭 기술의 발전은 양자역학적 개념인 패리티-시간 대칭성의 구현에 적용되어, 복소 퍼텐셜에서의 새로운 종류의 광학을 탄생시켰다. 이러한 성취물들은 맥스웰 방정식에서의 더 넓고 급격한 형태의 대칭성 붕괴에 기반하기 때문에, 의도된 빛의 흐름 조절을 위해서는 다양한 대칭성 붕괴에 관한 심도있는 연구가 필요하다.

본 학위 논문에서는 복소, 불규칙, 비선형 광학 퍼텐셜과 같은 다양한 플랫폼에서의 대칭성 붕괴에 대하여 살펴보고자 한다. 본 연구는 패리티-시간 대칭성, 키랄 특성, 인과율, 초대칭, 생물 모방 기술, 모드 경계 광학 및 느린 빛 원리와 연계된 빛의 특이한 흐름에 집중한다. 본 연구진이 이끌어낸 비직관적인 개념 및 광소자의 새로운 설계 기법 관련 결과들은 비고전적인 빛의 흐름에 기반한 미래 광학 발전에 도움이 될 것이다.

주요어: 대칭성 붕괴, 패리티-시간 대칭, 불규칙성, 전광 소자, 광학, 파동

학번: 2007-21026